LEABHARLANN CHOLÁISTE NA TRÍONÓIDE, BAILE ÁTHA CLIATH | TRINITY COLLEGE LIBRARY DUBLIN
Ollscoil Átha Cliath | The University of Dublin

Terms and Conditions of Use of Digitised Theses from Trinity College Library Dublin

Copyright statement

All material supplied by Trinity College Library is protected by copyright (under the Copyright and Related Rights Act, 2000 as amended) and other relevant Intellectual Property Rights. By accessing and using a Digitised Thesis from Trinity College Library you acknowledge that all Intellectual Property Rights in any Works supplied are the sole and exclusive property of the copyright and/or other IPR holder. Specific copyright holders may not be explicitly identified. Use of materials from other sources within a thesis should not be construed as a claim over them.

A non-exclusive, non-transferable licence is hereby granted to those using or reproducing, in whole or in part, the material for valid purposes, providing the copyright owners are acknowledged using the normal conventions. Where specific permission to use material is required, this is identified and such permission must be sought from the copyright holder or agency cited.

Liability statement

By using a Digitised Thesis, I accept that Trinity College Dublin bears no legal responsibility for the accuracy, legality or comprehensiveness of materials contained within the thesis, and that Trinity College Dublin accepts no liability for indirect, consequential, or incidental, damages or losses arising from use of the thesis for whatever reason. Information located in a thesis may be subject to specific use constraints, details of which may not be explicitly described. It is the responsibility of potential and actual users to be aware of such constraints and to abide by them. By making use of material from a digitised thesis, you accept these copyright and disclaimer provisions. Where it is brought to the attention of Trinity College Library that there may be a breach of copyright or other restraint, it is the policy to withdraw or take down access to a thesis while the issue is being resolved.

Access Agreement

By using a Digitised Thesis from Trinity College Library you are bound by the following Terms & Conditions. Please read them carefully.

I have read and I understand the following statement: All material supplied via a Digitised Thesis from Trinity College Library is protected by copyright and other intellectual property rights, and duplication or sale of all or part of any of a thesis is not permitted, except that material may be duplicated by you for your research use or for educational purposes in electronic or print form providing the copyright owners are acknowledged using the normal conventions. You must obtain permission for any other use. Electronic or print copies may not be offered, whether for sale or otherwise to anyone. This copy has been supplied on the understanding that it is copyright material and that no quotation from the thesis may be published without proper acknowledgement.

A STUDY OF THE HEAT TRANSFER PROCESSES AND RELATED FLOWS OF A SYNTHETIC JET IMPINGING PERPENDICULAR TO A HEATED SURFACE

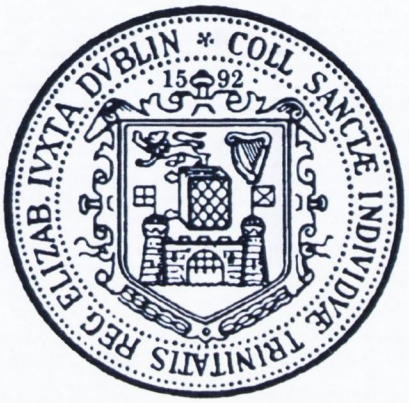

Thomas Alan McGuinn

Department of Mechanical & Manufacturing Engineering

Parsons Building

Trinity College

Dublin 2

Ireland

May 2011

A thesis submitted to the University of Dublin in partial fulfilment of the requirements for the degree of Ph.D.

TRINITY COLLEGE
11 SEP 2012
LIBRARY DUBLIN

Declaration

I declare that this thesis has not been submitted as an exercise for a degree at this or any other university and it is entirely my own work.

I agree to deposit this thesis in the University's open access institutional repository or allow the library to do so on my behalf, subject to Irish Copyright Legislation and Trinity College Library conditions of use and acknowledgement.

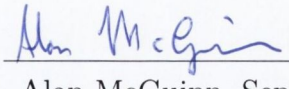

Alan McGuinn, September 2011

Abstract

To maintain the development of modern technology and its thermally intensive processes, versatile methods of enhancing localised heat transfer are continually required. This need has resulted in an on-going drive to achieve greater levels of heat dissipation through the implementation of active and passive cooling technologies. Many of these techniques aim to dissipate heat by either supplying the thermally saturated area with an ever increasing volume of cooler fluid or by using a form of turbulence enhancement to disrupt the thermal boundary layer. One of the most promising technologies of this type is the synthetic jet. It has been shown that this technology can provide significant levels of heat transfer enhancement without many of the penalties which hamper other methods of cooling such as scalability, complexity, power consumption and cost. While the synthetic jet's ability to provide cooling has been documented to some degree, a more in-depth investigation into the turbulent mechanisms and their influence on heat transfer is required.

A thorough investigation has been undertaken into a synthetic air jet impinging perpendicular to a heated surface. Extensive measurements have been performed to determine flow characteristics of the impinging jet and the corresponding effects on heat transfer from the surface. This investigation pays particular attention to the level of fluctuating heat transfer achieved with varying jet parameters.

A comprehensive investigation has been carried out combining detailed local heat transfer, velocity and air temperature measurements with high speed flow visualisation to examine what effects varying the synthetic the jet operational parameters has on the flow structure and resulting heat transfer profile. With respect to synthetic jet operational parameters the primary quantities of interest are Reynolds number, jet

dimensionless stroke length and spacing between jet and impingement surface. This investigation found that although Reynolds number has a direct bearing on heat transfer magnitude, adjusting the dimensionless stroke length can significantly change the characteristic of the impinging flow, by increasing or decreasing this parameter it is possible to alter the state of jet development upon impingement. In addition, a number of different jet flow regimes and impinging heat transfer regimes were identified with varying height above the impingement surface. Stagnation point heat transfer correlations were developed correlating Nusselt number to axial spacing, Reynolds number and dimensionless stroke length.

Further analysis was undertaken on the experimental data using signal decomposition to separate out the periodic nature of the synthetic jet flow from the random. This process was necessary so as to identify genuine turbulent fluctuation in the various signals rather than the regular oscillatory nature of the synthetic jet flow itself. The results of this analysis make it possible to identify under which conditions the jet flow degrades from large scale coherent structures to smaller scale turbulent mixing.

Through the use of multiple data acquisition and post processing techniques this investigation has clearly shown that heat transfer to an impinging synthetic jet is highly dependent on a number of parameters. The careful selection of the dimensionless stroke length, Reynolds number and axial spacing in particular can have a great influence on the maximum level of heat transfer achievable by the synthetic jet.

Acknowledgments

First and foremost I would like to express my enormous gratitude to my supervisor, Professor Darina Murray for all her support and guidance right from day one of this project. When needed, she provided direction through the voice of experience as well as encouragement to find my own way with the project. I'd like to thank Dr. Tim Persoons in particular, his encyclopaedic knowledge of everything got me out of many a tough situation. My eternal gratitude to Mr. Gerry Byrne whose practical skills and advice around the thermo lab know no bounds, you were always on hand with much needed banter. Thanks to Dr. Tadhg O'Donovan whose help at the beginning of the project was invaluable. I'd also like to thank the other members of staff I've had the pleasure of working with over the past few years, in particular Joan Gillen, Mick Reilly and the rest of the lads down in the workshop, without them my project would be held together with even more Sellotape and Blu-Tack.

To my friends and colleagues in the thermo group, I couldn't have managed the past few years without their constant interruptions, abuse and unsolicited advice. In particular Seamus O'Shaughnessy, Brian Donnelly, Brian Whelan, Tom Lupton, Rayhaan Farrelly, Gerrard McGranaghan, Karl Brown and David O'Donoghue.

To my family who provided me with continual support and encouragement throughout my studies at every level. Thanks to you I have achieved the otherwise unachievable.

To Niamh, I'm eternally grateful for your unwavering support and patience over the past few years which has been invaluable to me throughout.

Finally, I would like to acknowledge the CTVR and SFI for the continued funding of this project.

Contents

1 Introduction **1**

1.1 Background 2

1.2 Research Objectives 4

1.3 Dimensionless Numbers 5

1.3.1 Nusselt number 5

1.3.2 Reynolds number 5

1.3.3 Stokes number 6

1.3.4 Strouhal number 6

1.3.5 Dimensionless stroke length 7

1.3.6 Prandtl number 7

2 Literature Review **9**

2.1 Continuous Jets 9

2.1.1 Self-Similarity 11

2.2 Free Synthetic Jet Flow Structure 12

2.3 Impingement Synthetic Jet Flow Structure 14

2.4 Synthetic Jet Formation 14

2.4.1 Velocity Calculation 19

2.4.2 Computational and Analytical Modelling for Synthetic Jet Formation 23

2.4.3 Orifice effects 27

2.4.4 Near Field Evolution 29

2.4.5 Saddle Point 40

2.4.6 Far Field Evolution 42
2.4.7 Flow Control 47
2.4.8 Energy Separation 50
2.5 Synthetic Jet Heat Transfer 53
2.5.1 Motivation for Novel Cooling Systems 53
2.5.2 Heat Transfer Characteristics 56
2.5.3 Local Fluid Temperature Measurement 64
2.5.4 Orifice Geometry Effects on Synthetic Jet Heat Transfer 67
2.5.5 Novel Applications 69
2.6 Analytical Techniques 70
2.6.1 Spectral Analysis 71
2.6.2 Proper Orthogonal Decomposition 75
2.7 Conclusion 78

3 Experimental Considerations and Techniques **81**
3.0.1 Design of Apparatus 81
3.0.1.1 Nozzle Design 82
3.0.1.2 Impingement Surface 82
3.0.1.3 Confinement 83
3.0.1.4 Design for Varying Reynolds Number 84
3.0.1.5 Orientation 85
3.0.2 Experimental Techniques 85
3.0.2.1 Heat Transfer Measurement 86
3.0.2.2 Thermo-Chromatic Liquid Crystals 87
3.0.2.3 Infrared Camera & Image Diagnostic Equipment . . . 88
3.0.2.4 Naphthalene Sublimation Technique 88
3.0.2.5 Micro-Foil® Heat Flux Sensor 90
3.0.2.6 Hot-Film Sensors 90
3.0.2.7 Thermal Test Die 90
3.0.2.8 Flow Measurement 91
3.0.2.9 Hot-Wire 91

3.0.2.10 Laser & Flow Visualisation Techniques 92
3.0.2.11 Schlieren Visualisation Technique 93
3.0.2.12 Smoke Visualisation Technique 93
3.0.3 Conclusion 94

4 Experimental apparatus **95**
4.1 Apparatus Parameters 96
4.1.1 Nozzle to Surface Axial Spacing 96
4.1.2 Jet Velocity 97
4.1.3 Position within the Impingement Flow 97
4.1.4 Impingement Surface 98
4.1.5 Jet Design 99
4.1.6 Simultaneous Measurements 100

5 Instrumentation **103**
5.1 Speaker Amplifier & Cavity Pressure Measurement 103
5.2 Mass Flow Controller 106
5.3 T-Type Thermocouples 107
5.4 RdF Micro-Foil® Heat Flux Sensor 111
5.5 Constant Temperature Anemometry (CTA) 115
5.6 Senflex Hot-Film Sensor 119
5.7 Hot-wire Probe & Dantec CTA Control 123
5.8 Hot-wire Probe Calibration 123
5.9 Temperature Probe & Control Module 127
5.10 Data Acquisition & Processing 130
5.11 Particle Image Velocimetry (PIV) 132

6 Analysis Techniques **137**
6.1 Proper Orthogonal Decomposition (POD) 137
6.2 Swirl and Shear 140
6.3 Spectral Analysis 141
6.4 Spectral Decomposition 142

7 Results and Discussion **147**

7.1 Jet Evolution 149

7.1.1 Instantaneous Flow Fields 152

7.1.1.1 H/D=8 152

7.1.1.2 H/D=4 157

7.1.1.3 H/D=12 162

7.1.1.4 Findings 166

7.1.2 Vortex Strength & Path 166

7.1.2.1 H/D=4 168

7.1.2.2 H/D=8 170

7.1.2.3 H/D=12 171

7.1.2.4 Findings 175

7.1.3 Volume Flux 176

7.1.3.1 H/D=4 176

7.1.3.2 H/D=8 178

7.1.3.3 H/D=12 179

7.1.3.4 Findings 180

7.1.4 Mean Velocity Profiles 181

7.1.4.1 H/D=4 182

7.1.4.2 H/D=8 185

7.1.4.3 H/D=12 187

7.1.4.4 Findings 189

7.1.5 POD Analysis 190

7.1.5.1 H/D=4 193

7.1.5.2 H/D=8 197

7.1.5.3 H/D=12 200

7.1.5.4 Findings 204

7.2 Heat Transfer 205

7.2.1 Stagnation Point Measurements 205

7.2.1.1 Findings 216

7.2.2 Spectral Decomposition 216

7.2.2.1 Findings . . . 226
7.2.3 Spectral Reconstruction . . . 228
7.2.4 Stagnation Point Power and Coherence Spectra . . . 230
7.2.4.1 H/D=2 . . . 231
7.2.4.2 H/D=4 . . . 233
7.2.4.3 H/D=6 and 8 . . . 235
7.2.4.4 H/D=12 and 16 . . . 237
7.2.4.5 Findings . . . 239
7.3 Radial Decomposition . . . 239
7.3.1 Re=3000 . . . 239
7.3.1.1 H/D=2 . . . 240
7.3.1.2 H/D=4 . . . 244
7.3.1.3 H/D=8 . . . 248
7.3.1.4 H/D=16 . . . 253
7.3.1.5 Findings . . . 256
7.3.2 Effect of Reynolds number on radial decomposition . . . 257
7.3.2.1 H/D=2, Re=1000 . . . 257
7.3.2.2 H/D=2, Re=2000 . . . 260
7.3.2.3 H/D=8, Re=1000 . . . 262
7.3.2.4 H/D=8, Re=2000 . . . 264
7.3.2.5 Findings . . . 265
7.4 Summary . . . 265

8 Conclusions **271**
8.1 Conclusions . . . 271
8.2 Further Work . . . 274

A Appendix **291**
A.1 Additional Figures . . . 291
A.2 Instrument Specification & Calibration Documentation . . . 294

List of Figures

1.1 Schematic diagram of the synthetic jet 2

2.1 Continuous impinging jet 10
2.2 Turbulent jet schematic 12
2.3 Formation schematic 13
2.4 Impinging synthetic jet flow structure 14
2.5 Coupled resonance 16
2.6 Axial numerical and experimental velocity profiles 25
2.7 Transition map 26
2.8 Flow through orifice 27
2.9 Vortex celerity and trajectory 30
2.10 Vortex formation limit 33
2.11 Vortex ring circulation 34
2.12 Vortex circulation with increasing Reynolds number 35
2.13 Flow visualisation for increasing Reynolds number and constant stroke length 37
2.14 Flow visualisation of vortex ejection from synthetic jet nozzle over one cycle for increasing stroke length with constant Reynolds number . . . 38
2.15 Temporal variations of instantaneous streamwise centreline velocity . . 40
2.16 Saddle point 41
2.17 Velocity profiles for synthetic and continuous jet 42
2.18 Time averaged centreline velocity comparison 44
2.19 Self-similarity at the half-velocity 46

2.20 Vortical structures formed in crossflow 49
2.21 Energy separation schematic 51
2.22 Energy separation with increasing Mach number in a turbine nozzle . . 52
2.23 Heat transfer coefficients for various coolants 54
2.24 Die size vs. cost and application 55
2.25 Continuous jet heat transfer profiles 57
2.26 Heat transfer profile 58
2.27 Velocity and vorticity fields for slot jet 62
2.28 Velocity power spectra 72
2.29 POD reconstruction of time resolved velocity data and velocity spectra 75

3.1 Nozzle confinement 84

4.1 Experimental Apparatus 96
4.2 Synthetic jet assembly 99
4.3 Hot-film, hot-wire and temperature probe setup 100

5.1 Impingement cooling section for acoustic coil 104
5.2 Microphone and amplifier 105
5.3 Mass flow controller 106
5.4 Ambient air temperature calibration 108
5.5 Cavity temperature calibration 109
5.6 Micro-Foil ® temperature calibration 109
5.7 Hot-Film temperature calibration 110
5.8 Image of Micro-Foil® heat flux sensor 111
5.9 Micro-Foil® heat flux calibration 114
5.10 Micro-Foil® Regression Uncertainty 115
5.11 Wheatstone bridge schematic 115
5.12 Image of a hot-film sensor 119
5.13 Hot-film calibration data 122
5.14 Hot-wire probe 123
5.15 Hot-wire calibrator 124

5.16 Hot-wire calibration curve 125
5.17 Hot-wire calibration residual error 126
5.18 Temperature probe 127
5.19 Temperature probe calibration 129
5.20 Temperature probe regression uncertainty 130
5.21 DAQ modules 131
5.22 Raw PIV image 132
5.23 PIV schematic 134

6.1 Schematic of diaphragm displacement vs. phase angle φ 138
6.2 POD of synthetic jet flow field 139
6.3 Conversion of raw data to frequency domain 143
6.4 Frequency isolation 143
6.5 Signal reconstruction 144

7.1 Jet formation with stroke length 151
7.2 Instantaneous flow field; $H/D = 8, Re = 3000, L_0/D = 3$ 152
7.3 Instantaneous flow field; $H/D = 8, Re = 3000, L_0/D = 4$ 153
7.4 Instantaneous flow field; $H/D = 8, Re = 3000, L_0/D = 8$ 154
7.5 Instantaneous flow field; $H/D = 8, Re = 3000, L_0/D = 16$ 155
7.6 Instantaneous flow field; $H/D = 8, Re = 3000, L_0/D = 32$ 156
7.7 Instantaneous flow field; $H/D = 4, Re = 3000, L_0/D = 3$ 157
7.8 Instantaneous flow field; $H/D = 4, Re = 3000, L_0/D = 4$ 158
7.9 Instantaneous flow field; $H/D = 4, Re = 3000, L_0/D = 6$ 159
7.10 Instantaneous flow field; $H/D = 4, Re = 3000, L_0/D = 8$ 160
7.11 Instantaneous flow field; $H/D = 4, Re = 3000, L_0/D = 16$ 161
7.12 Instantaneous flow field; $H/D = 12, Re = 3000, L_0/D = 3$ 162
7.13 Instantaneous flow field; $H/D = 12, Re = 3000, L_0/D = 6$ 163
7.14 Instantaneous flow field; $H/D = 12, Re = 3000, L_0/D = 18$ 164
7.15 Instantaneous flow field; $H/D = 12, Re = 3000, L_0/D = 32$ 165
7.16 Vortex path; $H/D = 4$, $Re = 3000$ 168
7.17 Vortex path; $H/D = 8$, $Re = 3000$ 170

7.18 Vortex path; $H/D = 12$, $Re = 3000$ 171
7.19 Flow regime map 172
7.20 Average volume flux; $H = 4D$, $Re = 3000$ 176
7.21 Average volume flux; $H = 8D$, $Re = 3000$ 178
7.22 Average volume flux; $H = 12D$, $Re = 3000$ 179
7.23 Average velocity profiles; H/D=4, Re=3000 182
7.24 Average velocity profiles; H/D=8, Re=3000 185
7.25 Average velocity profiles; H/D=12, Re=3000 187
7.26 Streamwise velocity profile; $Re = 2500$ 188
7.27 POD mode energy; $Re = 3000$ 191
7.28 POD eigenmode flow fields; $Re = 3000$, $H/D = 4$ 194
7.29 POD eigenmode flow fields; $Re = 3000$, $H/D = 8$ 198
7.30 POD eigenmode flow fields; $Re = 3000$, $H/D = 12$ 199
7.31 POD eigenmodes; $Re = 3000$, $H/D = 12$ 201
7.32 POD eigenmodes; $Re = 3000$, $H/D = 12$ 203
7.33 Maximum saddle point location 204
7.34 Time averaged stagnation point Nusselt number, velocity, and temperature; $Re = 3000$ 206
7.35 Scaled time averaged stagnation point Nusselt number, velocity, and temperature; $Re = 3000$ 207
7.36 Stagnation point Nusselt number; $Re = 1000$ 211
7.37 Stagnation point Nusselt number; $Re = 2000$ 212
7.38 Stagnation point heat transfer correlation; $H = 2D$ 213
7.39 Stagnation point heat transfer correlation; $3D \leq H \leq 12D$ 214
7.40 Stagnation point Nusselt number; $Re = 2000$ 215
7.41 Stagnation point fluctuating Nusselt number, velocity, and temperature; $Re = 3000, H/D = 2$ 218
7.42 Stagnation point fluctuating Nusselt number, velocity, and temperature; $Re = 3000, H/D = 3$ 219
7.43 Stagnation point fluctuating Nusselt number, velocity, and temperature; $Re = 3000, H/D = 4$ 220

7.44 Stagnation point fluctuating Nusselt number, velocity, and temperature; $Re = 3000, H/D = 6$ 221

7.45 Stagnation point fluctuating Nusselt number, velocity, and temperature; $Re = 3000, H/D = 8$ 222

7.46 Stagnation point fluctuating Nusselt number, velocity, and temperature; $Re = 3000, H/D = 10$ 223

7.47 Stagnation point fluctuating Nusselt number, velocity, and temperature; $Re = 3000, H/D = 12$ 224

7.48 Stagnation point fluctuating Nusselt number, velocity, and temperature; $Re = 3000, H/D = 16$ 225

7.49 Reconstructed periodic time resolved data; $Re = 3000$ 227

7.50 Time resolved and power spectra plots of sine and square waves 231

7.51 Power and coherence spectra of Nusselt number, velocity and temperature; $Re = 3000, H/D = 2$ 232

7.52 Power and coherence spectra of stagnation point Nusselt number, velocity and temperature; $Re = 3000, H/D = 4$ 233

7.53 Power and coherence spectra of stagnation point Nusselt number, velocity and air temperature; $Re = 3000, H/D = 6$ 235

7.54 Power and coherence spectra of stagnation point Nusselt number, velocity and air temperature; $Re = 3000, H/D = 8$ 236

7.55 Power and coherence spectra of stagnation point Nusselt number, velocity and air temperature; $Re = 3000, H/D = 12$ 237

7.56 Power and coherence spectra of stagnation point Nusselt number, velocity and air temperature; $Re = 3000, H/D = 16$ 237

7.57 Decomposed Nusselt number and air temperature profiles; $Re = 3000$, $H/D = 2$ 240

7.58 Power and coherence spectra of Nusselt number and air temperature; $Re = 3000$, $H/D = 2$, $L_0/D = 2, 4, 8$, $r/D = 0, 2, 4$ 243

7.59 Decomposed Nusselt number and air temperature profiles; $Re = 3000$, $H/D = 4$ 245

7.60 Power and coherence spectra of Nusselt number and air temperature; $Re = 3000$, $H/D = 4$, $L_0/D = 2, 4, 8$, $r/D = 0, 2, 4$ 247

7.61 Decomposed Nusselt number and air temperature profiles; $Re = 3000$, $H/D = 8$ 248

7.62 Power and coherence spectra of Nusselt number and air temperature; $Re = 3000$, $H/D = 8$, $L_0/D = 4, 8, 16$, $r/D = 0, 2, 4$ 251

7.63 Decomposed Nusselt number and air temperature profiles; $Re = 3000$, $H/D = 16$ 254

7.64 Power and coherence spectra of Nusselt number and air temperature; $Re = 3000$, $H/D = 16$, $L_0/D = 8, 24, 48$, $r/D = 0, 2, 4$ 255

7.65 Decomposed Nusselt number profiles; $Re = 1000$, $H/D = 2$ 257

7.66 Nusselt number power spectra; $Re = 1000$, $H/D = 2$, $L_0/D = 3, 4, 8$ . . 258

7.67 Decomposed Nusselt number profiles; $Re = 2000$, $H/D = 2$ 260

7.68 Nusselt number power spectra; $Re = 2000$, $H/D = 2$, $L_0/D = 3, 4, 8$ . . 261

7.69 Decomposed Nusselt number profiles; $Re = 1000$, $H/D = 8$ 262

7.70 Nusselt number power spectra; $Re = 1000$, $H/D = 8$, $L_0/D = 4, 8, 16$. 263

7.71 Decomposed Nusselt number profiles; $Re = 2000$, $H/D = 8$ 264

7.72 Nusselt number power spectra; $Re = 2000$, $H/D = 8$, $L_0/D = 4, 8, 16$. 265

A.1 Decomposed Nusselt number profiles, $Re = 2000$, $H/D = 4$ 292

A.2 Nusselt number power spectra, $Re = 2000$, $H/D = 4$, $L_0/D = 4, 8, 16$. 292

A.3 Decomposed Nusselt number profiles, $Re = 2000$, $H/D = 12$ 293

A.4 Nusselt number power spectra, $Re = 2000$, $H/D = 12$, $L_0/D = 4, 8, 16$. 293

List of Tables

2.1 Comparison of synthetic and continuous jet rates of spread 45

2.2 Stagnation Nusselt number correlations for synthetic jets 59

2.3 POD mode energy 77

4.1 Dimensionless cavity measurements 100

5.1 Thermocouple uncertainties 110

5.2 DAQ module specifications 130

7.1 Synthetic jet operational parameters 148

7.2 Stagnation point regimes 213

==========

Nomenclature

α_0	temperature coefficient of resistance $[\Omega/K]$
$\bar{U}$	spatial and time-averaged velocity $[m/s]$
β	added mass coefficient $[-]$
$\dot{m}$	mass flow rate $[kg/s]$
ϵ	porosity $[-]$
Γ_0	circulation $[m^2/s]$
Γ_{nd}	dimensionless circulation $[-]$
κ	thermal diffusivity $[m^2/s]$
κ_e	isentropic expansion factor $[-]$
μ	dynamic viscosity $[Ns/m^2]$
ν	kinematic viscosity $[m^2/s]$
ω	angular frequency $[Rad/s]$
ρ	density $[kg/m^3]$
ρ_A	area density $[kg/m^2]$
τ	time of discharge $= 1/2f$ $[s]$
φ	phase angle $[^o]$

A	area $[m^2]$
C	speed of sound $[m/s]$
C_{aC}	cavity acoustic compliance $= V_c/\rho C^2$ $[s^2m^4/kg]$
C_{aD}	diaphragm compliance $= \Delta V_c/P$ $[s^2m^4/kg]$
C_m	rate of entrainment $[-]$
C_p	specific heat capacity $[kJ/kgK]$
D	diameter $[m]$
D_m	mass diffusivity $[m^2/s]$
E	voltage $[V]$
E_S	sensor voltage $[V]$
f	frequency $[Hz]$
f_d	diaphragm resonant frequency $[Hz]$
f_H	cavity (Helmholtz) resonant frequency $[Hz]$
h	heat transfer coefficient $[W/m^2K]$
h_c	cavity height $[m]$
I_0	impulse $[m^2/s^2]$
K	mass transfer coefficient $[m/s]$
k	thermal conductivity $[W/mK]$
K_p	pressure stiffness $[Pa/m]$
l	characteristic length $[m]$
L_0	stroke length $[m]$

l_o orifice length $[m]$

M mass $[kg]$

M_{aD} diaphragm acoustic mass $= \frac{2\pi}{\Delta V_c^2} \int_0^{R_2} \rho_A [w(r)]^2 r dr$ $[kg/m^4]$

M_{aN} orifice acoustic mass $= 4\rho L/3\pi r^2$ $[kg/m^2]$

M_{aRad} orifice acoustic radiation mass $= 8\rho/3\pi^2 r$ $[kg/m^4]$

M_o mass of fluid in orifice $[kg]$

Nu Nusselt number $= \frac{hl}{k}$ [-]

Nu' fluctuating Nusselt number $[-]$

Nu_0 stagnation point Nusselt number $[-]$

P pressure $[N/m^2]$

Pr Prandtl number $= \frac{C_p \mu}{k}$ $[-]$

Q volumetric flow rate $[m^3/s]$

q heat flux $[W/m^2]$

R resistance $[\Omega]$

r radius $[m]$

R_a active sensor resistance $[\Omega]$

r_c cavity radius $[m]$

R_S ambient sensor resistance $[\Omega]$

Re Reynolds number $= \frac{\rho U l}{\mu}$ $[-]$

$Re_{\bar{U}}$ spatial and time-averaged Reynolds number $[-]$

Re_{Γ_0} circulation Reynolds number $[-]$

Re_{I_0} impulse Reynolds number $[-]$

Re_{U_0} area averaged Reynolds number $[-]$

S Stokes number $= \frac{\tau_r U}{l}$ $[-]$

S_u decay constant $[-]$

Sc Schmidt number $= \nu / D_m$ $[-]$

Sh Sherwood number $= \frac{KL}{D_m}$ $[-]$

St Strouhal number $= \frac{fl}{U}$ $[-]$

T temperature $[K]$

t time $[s]$

T' fluctuating temperature $[K]$

$T^{*'}$ fluctuating dimensionless temperature $= \frac{T'}{T_{surf} - T_{cav}}$ $[-]$

T^* dimensionless temperature $= \frac{T_{surf} - T_{air}}{T_{surf} - T_{cav}}$ $[-]$

T_{inf} jet temperature $[K]$

T_{air} local air temperature $[K]$

T_{cav} cavity temperature $[K]$

T_{surf} surface temperature $[K]$

T_S sensor temperature $[K]$

U mean velocity $[m/s]$

U_0 area averaged velocity $[m/s]$

$u_0(t)$ instantaneous velocity at time t $[m/s]$

U_{cl} centreline velocity $[m/s]$

U_m momentum flow velocity $[m/s]$

V' fluctuating velocity $[m/s]$

V_c cavity volume $[m^3]$

$w(r)$ transverse diaphragm displacement $[m]$

x, y streamwise and radial directions $[m]$

τ_r relaxation time $[s]$

b slot length $[m]$

F_D damping force $[N]$

w slot width $[m]$

Chapter 1

Introduction

The focus of this research is on the convective heat transfer and flow characteristics of an impinging synthetic air jet with a view to applications such as localised cooling in manufacturing and industrial processes, microelectronics, integrated circuitry and in particular microprocessors. Many of these applications prove to be challenging environments to implement traditional methods of cooling. It is for this reason that significant research has been undertaken into the impinging synthetic jet for purposes of heat dissipation. The configuration of the synthetic jet is detailed in figure 1.1 and operates on a simple principle where a flexible membrane, diaphragm or piston forms one side of a partially enclosed chamber. Opposite to the membrane is an opening, such as a jet nozzle or orifice plate. An oscillator such as a piezoelectric diaphragm or a mechanical or electromagnetic actuator causes the membrane to oscillate in a sinusoidal motion; it is this oscillation which periodically forces air into and out of the opening which results in the formation of a non-zero mean streamwise pulsating jet in front of the orifice known as a synthetic jet. This jet can be directed at heated surfaces to enhance heat transfer. Impinging synthetic air jets are a relatively new technology and as such have so far had limited use in commercial applications. However, they have shown great promise in a number of practical applications ranging from flow control through active boundary layer mixing [1], the cooling of a manufacturing process [2], the thermal management through forced convection of electronics and in particular microprocessors [3].

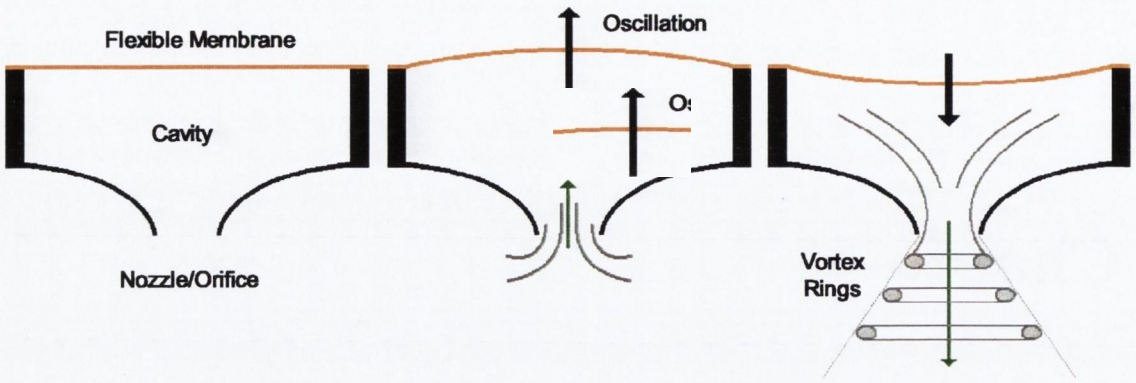

Figure 1.1: Schematic diagram detailing the operational principle of the synthetic jet

It is well established that effective rates of cooling can be achieved using conventional steady flow impinging jets [4, 5]. However, it has also been shown that synthetic jets can deliver cooling effects of similar magnitude without the need for an external air supply system [6, 7, 8]. As highlighted in a review article by Glezer and Amitay [9], impinging synthetic jets are therefore an extremely promising technology for applications in electronics cooling. In these, and in other cases, research has been conducted specifically with an application in mind but there have also been a number of fundamental investigations into fluid flow and heat transfer. These have led to the identification of several parameters which have significance for the enhancement of heat transfer from the impingement surface. Thus, the main variables for synthetic jet impingement heat transfer are the dimensionless stroke length, the jet Reynolds number and the height of the nozzle above the impingement surface.

1.1 Background

The operation of microprocessors, as with many types of electronics, generates very high local heat fluxes. In the past twenty years the cooling requirement for microprocessors has increased dramatically; where at one stage natural convection provided sufficient cooling for the most powerful chips, it is now the case that the limiting factor in processor power has become the extent to which heat can be dissipated from the chip surface [10]. Excessive temperatures have an adverse effect on the performance and lifespan of microprocessors to the point that loss of cooling may lead to the sudden

failure of the chip.

In most cases microprocessor cooling is achieved via an axial fan mounted on a large heat sink. Fans are used for their ability to produce relatively high volume flow rate within a confined environment; when combined with a heat sink, which essentially spreads the heat produced by the chip over a greater area, this solution has only proven adequate to a point for the industry's cooling needs. In an attempt to keep up with ever increasing heat flux densities, heat sinks are being designed larger and manufactured out of more expensive materials, the fans used are also larger, noisier and more power-hungry; as a result this technology is reaching its practical, operational and economical limits. It has reached the stage where some manufacturers are employing extravagant and expensive new technologies. Therefore there are a number of motivations for using synthetic jets including cooling performance, power consumption, size, noise, complexity and cost. Unfortunately, as of yet the maximum heat transfer potential of the synthetic jet is unknown. It is for this reason that much research is required to characterise and optimise heat transfer to an impinging synthetic air jet.

In recent years with the development of highly advanced flow visualisation techniques much of the research into synthetic jets has been focused on the flow characteristics; however minimal research has been performed investigating the link between fluid flow and heat transfer. The flow characteristics of a synthetic jet are highly complex; consequently the heat transferred from a surface subject to such a flow is highly variable. Numerous jet configurations have been studied and various experimental parameters have been established which influence both the fluid flow and the heat transfer. Significant research has been conducted into the area of impinging synthetic jet heat transfer by, among others, Campbell *et al.* [11], Mahalingam and Glezer [12], Pavlova and Amitay [8] and Travnicek and Tesar [13]. However, this research is limited in scope, as few studies have been conducted into fluctuating heat transfer or into the relationship between the fluid flow and surface heat transfer. The overall objective of the current research is to conduct a fundamental investigation into the heat transfer mechanisms for an impinging synthetic air jet.

1.2 Research Objectives

The current research is concerned with a single synthetic air jet impinging normal to a flat, heated surface for a range of impingement parameters. Tests have been conducted to determine both mean and fluctuating heat transfer distributions in combination with local air temperature and velocity measurements. Of particular interest to the current investigation is how the stagnation point heat transfer magnitude changes with varying jet parameters. A primary goal of this research is to identify the fundamental mechanisms relating the various heat transfer regimes to the corresponding synthetic jet flow field.

One potentially important application of the synthetic jet is the cooling of integrated circuitry and microelectronics such as personal computers, amplifiers and power supplies. It can prove quite difficult to obtain high levels of heat transfer due to the high degree of confinement and elevated ambient temperatures commonly found within these devices. It is for this reason that local air temperature measurements have been combined with local velocity and surface heat flux measurements. This technique can provide a greater understanding as to whether fluid temperature or velocity is the primary driving force behind surface heat transfer and how this relationship changes with various flow regimes.

Objectives:

- Document and analyse various synthetic jet flow regimes using flow visualisation.
- Use stagnation point and radial heat flux measurements to identify the modes of heat transfer which correspond to the respective flow regimes.
- Correlate levels of heat transfer to fluid velocity and temperature using simultaneous local measurements.
- Identify the key mechanisms involved in driving heat transfer to the impinging synthetic jet.

1.3 Dimensionless Numbers

As jets, and flows in general, can have such a broad range of parameters and characteristics, groups of dimensionless numbers have been established to help describe the state of the flow and allow easy comparison across a broad range of parameters. This section describes and defines the main dimensionless numbers relevant to the synthetic jet.

1.3.1 Nusselt number

The Nusselt number corresponds to a dimensionless temperature gradient at a heated surface and is a characteristic of the effectiveness of the convection process.

$$Nu = \frac{hl}{k} \tag{1.1}$$

where h is the convective heat transfer coefficient, l is the characteristic length and k the thermal conductivity of the fluid. For round jets, the characteristic length is generally taken to be the exit diameter while for rectangular jets the exit width is used. The Nusselt number can provide a good comparison of the level of heat transfer achieved across a range of scales and fluids.

1.3.2 Reynolds number

The concept of the Reynolds number was originally introduced by George Gabriel Stokes in 1851 and can be defined as the ratio of inertia force to viscous force:

$$Re \equiv \frac{Inertia force}{Viscous force} = \frac{\rho U l}{\mu} \tag{1.2}$$

where ρ and μ are fluid density and viscosity respectively, U the relative fluid velocity and l the characteristic length, which in jets is usually chosen to be the diameter of the nozzle. Reynolds number is commonly used to identify whether a flow is dominated by viscous forces ($Re << 1$), inertial forces ($Re >> 1$) or if the two forces

are in equilibrium ($Re \approx 1$). It is also used to identify different flow regimes and the onset of turbulence.

1.3.3 Stokes number

The Stokes number also introduced by and named after George Gabriel Stokes, provides a description of the characteristic response time of a fluid compared to that of a particle suspended in the fluid flow. In other words it gives an idea of the ability of the suspended particle to follow the fluid flow and is defined as a ratio of stopping distance of a particle to a characteristic dimension of an object:

$$S = \frac{\tau_r U}{l} \tag{1.3}$$

where τ is the relaxation time of the particle, U is the mean flow velocity and l is the characteristic length of the object. For $S >> 1$ particles will continue in a straight line and impact upon the object as the fluid flows around it and for $S << 1$ particles will follow the path of the fluid closely as it flows around the object. The main relevance of the Stokes number to this study is in its use for the choice of seeding particles used in PIV flow visualisation. It is necessary to choose a substance which will follow the motion of the fluid closely rather than maintain its own trajectory.

1.3.4 Strouhal number

The Strouhal number is a dimensionless parameter used across a broad range of fluid mechanics applications, the purpose of which is to provide a description of the oscillating mechanisms within a flow. It can be defined as follows:

$$St = \frac{fl}{U} \tag{1.4}$$

where f is the primary frequency, commonly that of vortex shedding, l is the characteristic length and U is the fluid velocity. In jets the primary application of the

Strouhal number is to help identify the presence of phenomena such as vortex rollup, shedding and pairing. Other experiments involving vortex shedding from a circular cylinder in cross flow have shown that the value of St remains close to 0.21 for a large range of Reynolds numbers.

1.3.5 Dimensionless stroke length

The dimensionless stroke length is a relatively new parameter devised to help characterise the formation and evolution of pulsatile flows dependent on intermittent fluid ejections such as those produced by synthetic jets and pulse jets. The stroke length L_0 can be defined as the effective length of fluid extruded through the jet orifice during a single ejection phase of the ejection cycle and can be calculated by dividing the average jet velocity U (as outlined by equation 2.10) by the pulsation frequency f:

$$L_0 = \frac{U}{f} \tag{1.5}$$

this parameter can subsequently be nondimensionalised by dividing by the diameter of the jet exit, D, thereby giving the value of dimensionless stroke length. This value can be seen to be inversely proportional to the Strouhal number, since $L_0/D = \frac{1}{2}(fD/U)^{-1}$. The formation and flow characteristics of many intermittent jets are highly dependent on this parameter and it has been shown to provide an easily comparable and more transparent unit of comparison.

1.3.6 Prandtl number

The Prandtl number is a nondimensional parameter in flows involving heat conduction and is defined as follows:

$$Pr = \frac{\nu}{\kappa} = \frac{C_p \mu}{k} \tag{1.6}$$

where ν is the kinematic viscosity, κ is the thermal diffusivity, C_p the specific heat capacity, μ is the dynamic viscosity and k the thermal conductivity. It is significant

that unlike other dimensionless numbers such as the Reynolds and Nusselt number, the Prandtl number contains neither length nor velocity scales and as such is a fluid property and not a flow variable.

Chapter 2

Literature Review

A comprehensive review of the published literature regarding the formation and structure of free and impinging synthetic jets is presented in this section. Primary factors involved in the analysis of synthetic jet flows include vortex formation, Reynolds number, pulsation frequency, dimensionless stroke length, turbulence, flow regimes, jet spread, recirculation effects, etc. With so many highly influential factors, analysis of the flow structure of an impinging synthetic air jet has proven to be highly complicated. However, as synthetic jets have already shown enormous potential for application in many disciplines from heat transfer to flow control it is essential that the fundamental formation and flow mechanisms are understood in order to ensure maximum potential is achieved.

2.1 Continuous Jets

The basis for the formation of any type of jet is the ejection of fluid through a nozzle or orifice into another fluid filled domain. The consequential interaction between the jet and the fluid occupying the ejection domain can be controlled so as to suit the desired application, be it to provide thrust, heat transfer, flow control or otherwise. The most common type of jet is known as a continuous jet where a stream of constant velocity fluid exits a jet nozzle, this type of jet has been the subject of much research for many years with some of the most notable research undertaken into heat transfer to impinging continuous jets by authors such as Gardon and Akfirat [14] and Liu and

Sullivan [15].

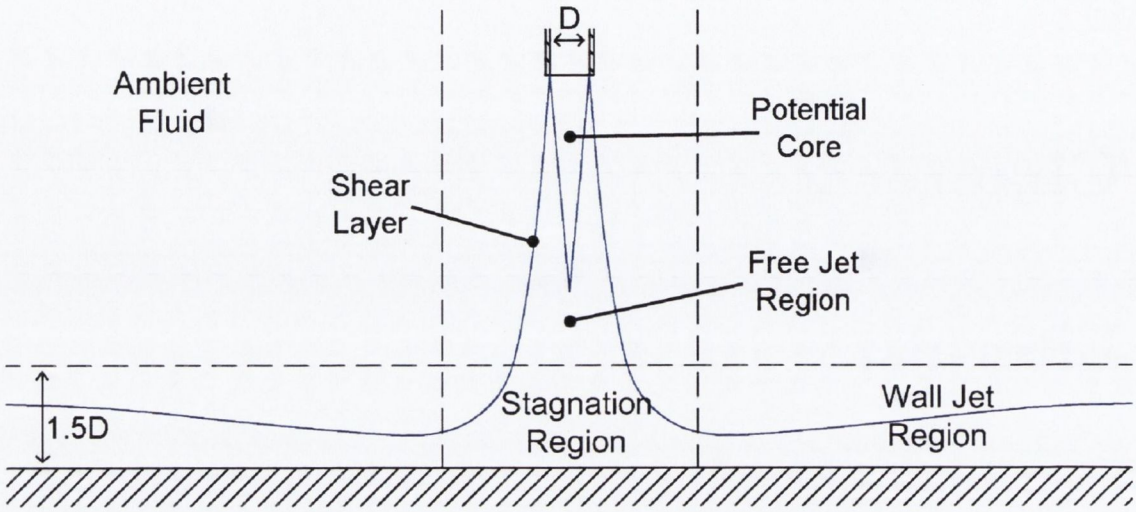

Figure 2.1: Continuous impinging jet

Figure 2.1 shows a schematic of an impinging continuous jet with the three primary flow regions. Once a net mass flux has been established the first region formed by the jet is the free jet region; this is a region where the jet develops and up to approximately 1.5 diameters above the impingement surface is largely unaffected by its presence. In the centre of the free jet region exists what is known as a potential core; this is a core of undiminished velocity and low turbulence intensity and exists for approximately 4 diameters from the jet exit. Between the potential core and the ambient fluid exists a shear layer in which vortex formation, rollup, fluid entrainment and mixing occurs, resulting in a relatively high level of turbulence. Shear layer velocity is less than that within the potential core and reduces further with the spreading of the jet. At the jet centerline, maximum turbulence intensity is experienced at the point where the shear layer penetrates to the centreline of the jet; a corresponding decrease in the local velocity occurs. Impinging jets also have a region known as a stagnation zone, prior to entering this region the axial component of the fluid velocity is very much greater than the radial component, however as the flow approaches the surface the velocity component normal to the surface begins to decrease while the velocity parallel to the surface increases. If the jet impinges upon the surface while the potential core is still in existence a true stagnation point in the flow velocity may exist. The final region is that of the wall jet, where the flow changes direction as it extends beyond the stagnation

zone and the mean flow continues parallel to the impingement surface.

2.1.1 Self-Similarity

Figure 2.2 shows the most simplistic schematic of an axisymmetric turbulent jet. For a round jet issuing from a nozzle of diameter D, the potential core, which occupies most of the nozzle exit plane, is maintained up to about $x = 4D$. Beyond this, and up to a distance of $x = 30D$ there is a more moderate change in the shape of the velocity profiles as well as other aspects such as entrainment and Reynolds stresses[1]. Further afield once again, a region where the velocity profiles become independent of x (self-similar) is commonly found when suitably scaled. Sherman [16] provides a comprehensive explanation of the conditions required to achieve self-similarity in a jet. From figure 2.2, jets are characterised by the velocity of the domain into which they are issuing U_1, with the velocity of the jet profile being $U_0(x)$ and the local width of the profile $\delta(x)$. With these parameters, the self-similar form of the velocity profile can be expressed as:

$$U(x, y) = U_1 + U_0(x) f'(\eta) \tag{2.1}$$

where $\eta = y/\delta(x)$. Using the continuity equation the corresponding expression in V can be found for plane flow:

$$V(x, y) = -f(\eta)\frac{d(U_0\delta)}{dx} + \eta f'(\eta) U_0 \frac{d\delta}{dx} \tag{2.2}$$

To achieve self-similarity these normalised jet velocity profiles must be fully collapsible onto one another. Examples of self-similarity in continuous jets have been documented by Hussein *et al.* [17] and Panchapakesan and Lumley [18].

[1]Reynolds stresses are the mean forces (per unit area) imposed on the mean flow by turbulent fluctuations.

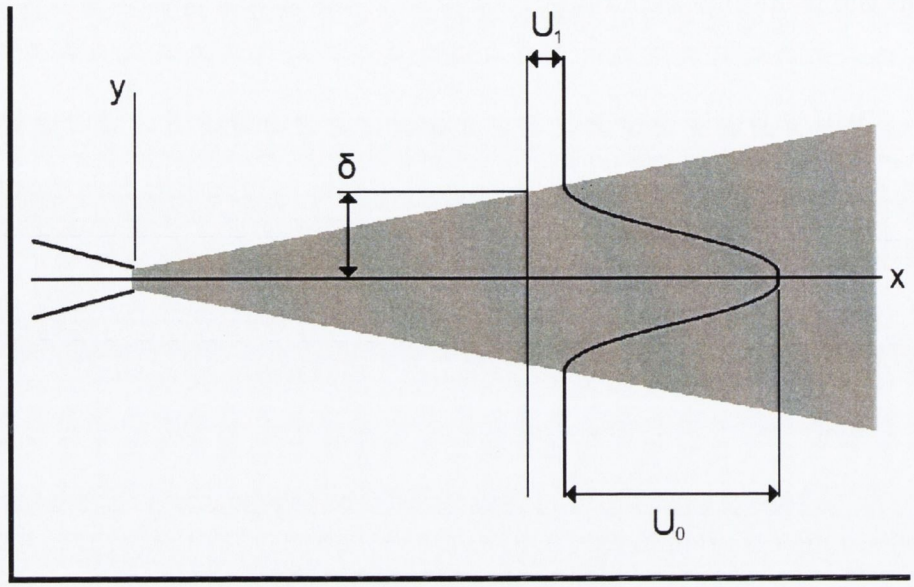

Figure 2.2: Turbulent jet schematic [16]

2.2 Free Synthetic Jet Flow Structure

The synthetic jet was first observed over 60 years ago by Ingard and Labate [19] while investigating what at the time was referred to as an acoustical streaming phenomenon around orifices; the authors noted that three flow regions exist. The first was a laminar region of low fluid velocity with a flow direction which was reversible above a certain level. A pulsatory medium velocity flow was experienced in the second region, where the pulsations were superposed upon actuation signal. The third, high velocity region was seen to be only pulsatory, forming jets and vortex rings. These three regions are now recognised as essential components in the formation of the synthetic jet. Work published by Holman *et al.* [20] presented a synthetic jet where the formation criterion for the jet was proposed and validated. The authors state that a vortex escapes or a jet is formed only when the Strouhal number is below a critical value; this is detailed further in section 2.4.2. Referring to the schematic of a typical synthetic jet shown in figure 2.3, during the expulsion part of the cycle fluid exits the nozzle at a velocity V_I and a vortex ring is formed at the sides of the ejected fluid. Once formation conditions have been fully satisfied, sufficient momentum is imparted to the vortex so that it will convect away from the orifice; repeated oscillations will result in a train of high-momentum vortex rings propagating away from the orifice. A turbulent jet is

synthesised as these vortex rings interact downstream.

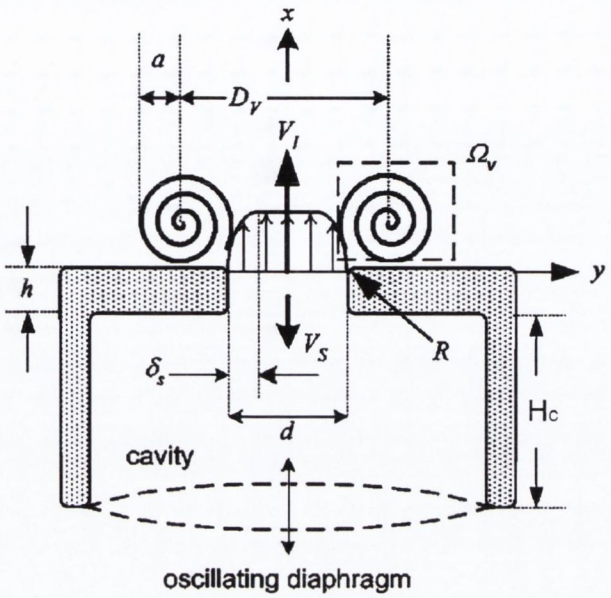

Figure 2.3: Synthetic jet formation, δ_s is boundary layer thickness, h height of orifice, H_c depth of orifice, a vortex radius, V_I jet velocity, D_V distance between vortices, Ω_ν vortex strength and R orifice edge radius of curvature. [20]

Smith and Swift [21] have shown that the flow structure of synthetic jets has much in common with continuous jets, but where continuous jets have a constant exit flow velocity synthetic jets have a time-varying, periodic velocity V_I. After exiting the nozzle, the structure of both types of jets consists of a potential core and a mixing layer; the potential core is the area within the jet flow that due to its high momentum resists mixing with the ambient fluid. For continuous jets it is normal to have a very low fluctuating velocity within this potential core, however due to the periodic nature of the synthetic jet flow this is the region of the jet which experiences the greatest velocity fluctuation. With increased distance from the nozzle exit the potential core reduces in size due to interaction with the mixing region; for the parameters tested by Smith and Swift this continues until the potential core is no longer visible at a distance of approximately $x = 5D$. Up to this point the flow velocity within the potential core is very close to that of the jet exit velocity. As the distance from the jet exit is increased farther, interactions between vortices cause the breakdown of the once coherent vortices resulting in small scale mixing and high turbulence intensities.

Smith and Swift [22] found that in the far field, synthetic jets bear much resemblance to continuous jets in that the self-similar velocity profiles are identical; however the study also found that the spread rate and volume flux of synthetic jets are substantially greater than that of continuous jets, attributing this to the fact that synthetic jets are dominated by vortex pairs which entrain greater amounts of fluid.

2.3 Impingement Synthetic Jet Flow Structure

The impinging jet flow structure for the synthetic jet is more complex than that of the free jet. Figure 2.4 shows the schematic of the flow structure. As with continuous jets the synthetic jet flow structure can be broken down into the same three regions, however significant differences in substructure exist depending on formation parameters, specifically that of stroke length.

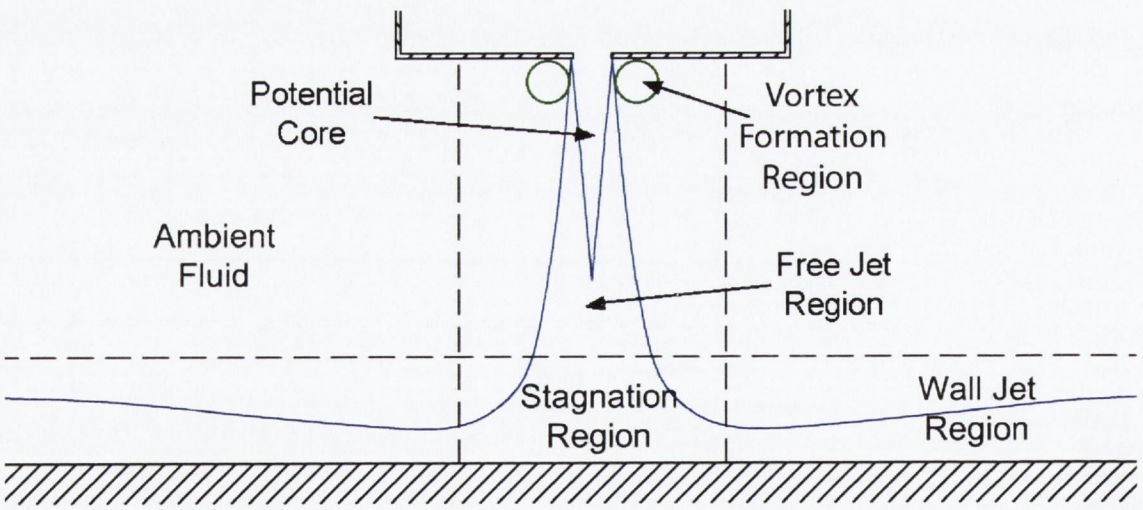

Figure 2.4: Impinging synthetic jet flow structure

2.4 Synthetic Jet Formation

An isolated synthetic jet is formed in quiescent fluid as a result of alternating pressure fluctuations across an orifice. Fluid is periodically entrained in through the orifice upon a negative pressure gradient and expelled once again from the orifice as the

pressure is reversed. This pressure oscillation produces a streamwise flux in front of the orifice in the form of a train of vortices, subsequent downstream vortex interaction and breakdown form the jet flow itself. The fluid ejection and suction across the orifice is such that it produces a net mass flux equal to zero.

The primary vortex synonymous with synthetic jets is formed during the momentary ejection phase. The sudden increase in flow velocity through the orifice causes flow separation at the sharp edge of the orifice resulting in the formation of a vortex sheet for orifices of slot geometry, and vortex ring for round geometry either side of the main stream flow. Under normal operating conditions the vortex produced is convected away from the surface due to its own self-induced velocity, hence forming a time averaged jet. This phenomenon was observed by Ingard and Labate [19] who went on to define it as a type of jet flow.

As noted previously, synthetic jets are typically formed by applying a time periodic alternating pressure drop across an orifice. In past investigations various methods have been employed in producing this effect; mechanically driven pistons were one of the first methods employed, being used by Cater and Soria [23], Xu *et al.* [24], Crittenden and Glezer [25], Di Cicca and Iuso [26] amongst others. Generally driven by an electric motor, the use of a piston to form a synthetic jet can prove very simple and highly effective as a wide range of stroke lengths and Reynolds numbers can easily be achieved. As the piston stroke length is dictated by the length of the crank shaft it is easy to maintain a constant stroke length while Reynolds number can be changed by increasing or decreasing the driving frequency of the jet. However, disadvantages include the reliability of the electric motor, the relatively large size and complexity of the assembly and the requirement to change the crank shaft to alter the stroke length.

Acoustic speakers are also a common tool in synthetic jet assemblies, having been used by many authors including Smith and Swift [21], Holman *et al.* [20] and Wu *et al.* [27]. Others have used custom built electromagnetic actuators such as Gillespie *et al.* [28] and Campbell *et al.* [11]. As acoustic speakers are normally capable of producing relatively large diaphragm deflections it is possible to produce a wide range of stroke lengths and Reynolds numbers. These parameters are easily controllable by adjusting the frequency or amplitude of the driving signal. However, calibration can prove

complex as each acoustic speaker has its own mechanical resonance and impendence, also, the use an electromagnetic coil raises the issue of long term reliability.

The vast majority of research undertaken into synthetic jets has made use of piezoelectric actuators. The attractiveness of this type of actuator is attributed to their small size, cost, power consumption and performance, making them perfect for use in both the electronics industry for thermal dissipation and aeronautics industry for active flow control. As the piezoelectric actuator is a solid state device it possesses excellent reliability. However, a complex calibration similar to that required by the acoustic speaker is required and diaphragm displacement is highly dependent on operating the actuator at its resonant frequency. Consequently, maximum diaphragm deflection is substantially less than that produced by either an acoustic speaker or a piston, therefore the range of stroke lengths achievable is severely limited . Numerous investigations in both fields have implemented piezoelectric actuators including Smith and Glezer [29], Mallinson *et al.* [30], Gomes *et al.* [1] and Pavlova and Amitay [31].

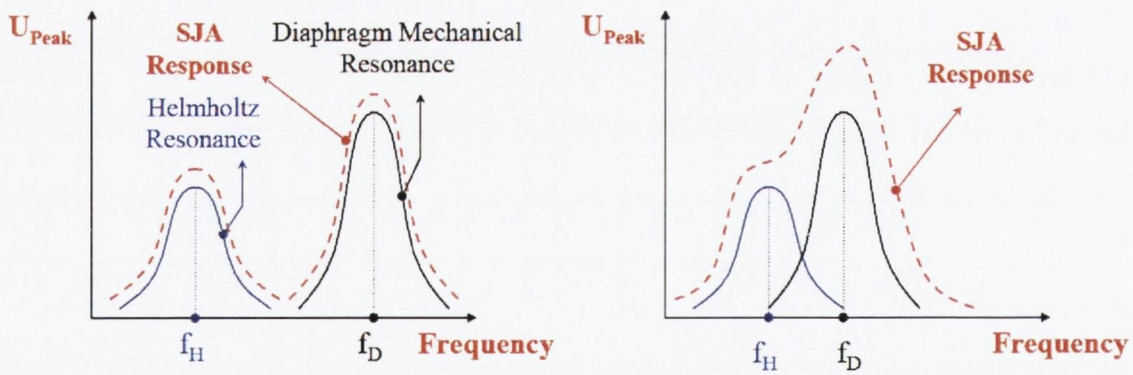

Figure 2.5: Helmholtz and diaphragm mechanical resonance overall SJA response: a) uncoupled case; b) coupled case [32]

Pavlova and Amitay [8] found that if a synthetic jet is driven at its natural resonant frequency significant performance benefits can be gained with minimal modification; similar results by Arik [33], Gomes *et al.* [32] and McGuinn *et al.* [34] have confirmed this. In a synthetic jet there are two primary influential sources of resonant frequency, the resonant frequency of the diaphragm, f_D, and that of the cavity, f_H; the latter is known as the Helmholtz frequency. These are defined as:

$$f_D = \frac{1}{2\pi}\sqrt{\frac{1}{M_{aD}C_{aD}}} \tag{2.3}$$

$$f_H = \frac{1}{2\pi}\sqrt{\frac{1}{(M_{aN}M_{aRad})C_{aC}}} \tag{2.4}$$

where M_{aD} and C_{aD} refer to diaphragm acoustic mass[2] and diaphragm compliance respectively and M_{aN}, M_{aRad} and C_{aC} are orifice acoustic mass, orifice acoustic radiation mass and cavity acoustic compliance respectively. The acoustic mass M through a membrane or orifice, as defined by Cox and D'Antonio [35] can be calculated as follows:

$$M_{aN} = \frac{\rho}{\epsilon}\left[t + 2\Delta r + \sqrt{\frac{8\nu}{\omega}\left(1 + \frac{t}{2r}\right)}\right] \tag{2.5}$$

Where ρ is fluid density, ϵ material porosity, t thickness, δ end correction factor, r perforation radius, ν kinematic viscosity of air and ω angular frequency. A simpler and often more useful form of Helmholtz frequency can be calculated using the following equation:

$$f_H = \frac{C}{2\pi}\sqrt{\frac{A}{V_c l_{eff}}} \tag{2.6}$$

where C is the speed of sound, A is the orifice area, V_c is the cavity volume and l_{eff} the effective orifice length ($l_{eff} = l_o + 0.85l_o$).

The acoustic nonlinearity of an orifice was investigated as far back as 1967 by Ingard and Ising [36]. It was these researchers who first identified the relation between pressure and velocity amplitudes as being almost linear at sufficiently low pressures and as approaching a square law relation at large velocity amplitudes. This square law is reflected in equation 2.6 above. A paper was presented by Gomes *et al.* [1] in which

[2]The acoustic mass refers to the effect of inertia in an acoustic system, an impeding of the transmission of sound through that system.

the theoretical Helmholtz frequency of a cavity was compared to an experimentally measured frequency. Gomes found that although the results showed good agreement with the inverse square relationship in equation 2.6, Helmholtz theory consistently over predicted the frequency of the cavity resonance by approximately 18%. The authors also investigated the effect of driving a synthetic jet with uncoupled diaphragm and cavity frequencies. It was shown that although performance gains were experienced at both cavity and diaphragm resonant frequencies, driving the synthetic jet actuator at the diaphragm mechanical resonance provides a peak velocity of at least an order of magnitude higher than at the cavity resonance; this is illustrated in figure 2.5. The presence of uncoupled resonance for both cavity and diaphragm was present in the results of other authors [6, 37, 38], where Gallas *et al.* [38] went on to use the coupling of the resonant frequencies to optimise the performance of the jet.

A number of authors [39, 40, 41] have implemented a technique called Lumped Element Modelling (LEM) to simulate synthetic jet frequency response. This technique effectively approximates the synthetic jet and its components as a circuit model whereby the energy storage and dissipation mechanisms are represented by their electronic equivalents, i.e. resistors, capacitors and inductors. Gallas *et al.* [38] presented a paper employing this technique to predict the jet exit velocity. The system was split into two parts by separately optimising the cavity volume and the piezoelectric diaphragm. It was revealed that the frequency response of a synthetic jet actuator is consistent with that of a damped fourth order coupled oscillator where one oscillator is a Helmholtz resonator and the second is the flexible diaphragm; a finding later confirmed by Gomes *et al.* [1]. Both papers highlight the fact that optimum performance can be achieved through coupling between the cavity and the diaphragm mechanical resonances; this coupling effect has a constructive effect on the resulting actuator jet velocity, as shown in figure 2.5. While the LEM approach has the potential to give good insight into the basic dynamic interaction between the materials that make up the synthetic jet and the predicted fluidic reaction it may prove somewhat idealistic. Significant validation would be required to test the limitations of this approach. It would also prove difficult to ensure all assumptions are achieved over a wide range of testing parameters.

A parametric study was undertaken by Kordik *et al.* [42] to model the resonant frequency of a synthetic jet actuator. Four models were implemented and compared, 2 one mass oscillation models, a two mass model with two degrees of freedom and also a model based on a solution to the wave equation. Results showed that the simpler one mass model proved the closest match for the first harmonic of the synthetic jet actuator; however two limits were identified for this model. Firstly Π_i, which can be considered as an expression of the dimensionless cavity depth, must be very small:

$$\Pi_1 = \frac{h_c K_p}{\kappa_e P_b} << 1 \tag{2.7}$$

where h_c is the cavity height, K_p is the diaphragm pressure stiffness, κ_e is the isentropic expansion factor and P_b is the external barometric pressure. The cavity mass effect, Π_2, must also be very small

$$\Pi_2 = \left(\frac{M_D}{M_o}\right)\left(\frac{r}{r_c}\right)^4 << 1 \tag{2.8}$$

where M_D and M_o are the mass of the diaphragm and the mass of the oscillating column of gas in the orifice, r_c and r are the cavity and orifice radii respectively. Although the more complex model based on the wave equation did not perform as well, the author states that it could give better results for the second, and possibly even higher resonant frequencies, although further validation of the results is required.

2.4.1 Velocity Calculation

Over the years numerous authors have proposed methods of calculating jet velocity and hence Reynolds number for a synthetic jet. Some of these calculations have ranged from the simplistic, involving single point centreline velocity measurement [43, 44, 28], to the more complex involving the average momentum flow velocity [45, 23]. However due to the zero net-mass-flux characteristic of the flow, no definitive calculation has been established to date. The most widely used method for calculating Reynolds number is based on a "slug-velocity-profile" model which has been used by authors

such as Smith and Glezer [46], Glezer and Amitay [9], Pavlova and Amitay [8] and Gillespie *et al.* [28]. This slug-velocity model is described by the following equation:

$$Re_{U_0} = \frac{U_0 D}{\nu} \tag{2.9}$$

Where U_0 is the area averaged jet discharge velocity across the orifice, D is the nozzle diameter and ν is the kinematic viscosity. For this particular case U_0 is only calculated over the duration of ejection:

$$U_0 = fL_0 = f\int_0^{\tau} u_0(t)dt \tag{2.10}$$

where U_0 is the experimentally measured flow velocity, f is the frequency of oscillation of the actuator, $\tau = 1/2f$ is the blowing period of the jet and L_0 is the distance that the slug of fluid travels away from the orifice during the ejection phase of the cycle, and is also known as the stroke length. This parameter is often non-dimensionalised by dividing by the diameter D to produce a term which is inversely proportional to the Strouhal number, since $L_0/D = \frac{1}{2}(fD/U_0)^{-1}$. Although the value $u_0(t)$ should ideally be measured across the profile of the jet to obtain an area averaged value, the majority of investigations use the velocity measured at a point on the centreline of the jet at or close to the jet exit. While this is often done for practical reasons such as geometric constraints due to small diameter orifice or to reduce the complexity of analysis, it can lead to substantial error in flow rate and Reynolds number calculation. The deficiency in this model is in the assumption that the flow velocity $u_0(t)$ is uniform across the width of the orifice. Smith and Swift [21] argued that because the spatial velocity profile can deviate significantly from the assumed slug shape the centreline velocity profile $u_0(t)$ is more generally replaced by the spatial-averaged velocity at the exit. As mentioned previously this proposal was validated by Nae [47] when the author presented numerical results showing that velocity profiles could deviate from top-hat distribution for up to 50% of the ejection stroke; a result that was confirmed experimentally by both Shuster and Smith [48] and Di Cicca and Iuso [26].

An alternate method for Reynolds number calculation was proposed by Utturkar *et al.* [49]. The method was defined in terms of a spatial and time-averaged exit velocity during the expulsion stroke, $Re_{\bar{U}} = \bar{U}D/\nu$ where

$$\bar{U} = \frac{1}{\tau}\frac{1}{A}\int_A \int_0^\tau u(t,y)dtdA \tag{2.11}$$

With A being the exit area and y the cross-stream coordinate. Utturkar shows that the two velocity scales are related by $\bar{U} = 2U_0$ since the ejection duration $\tau = 1/2f$. Hence, equation 2.11 is only calculated over the ejection phase of the jet, whereas equation 2.10 is time averaged over the whole cycle; a Reynolds number of twice the magnitude for the exact same flow parameters is calculated with equation 2.11.

Yet another method of calculating Reynolds number was used in a paper by Cater and Soria [23]. The authors argued that since the flow generation mechanism (diaphragm or piston) has a constant mean position there is no net mass injected in to the system. However, the fact that there is energy transferred to the environment resulting in a net momentum flow through the exit plane suggests a velocity should be calculated using mean momentum flow. Consequently, Cater and Soria implemented a derivation of an equation commonly used in steady flow emanating from axisymmetric continuous jets. This equation calculates what is termed the momentum flow velocity:

$$U_m = \left[\frac{4}{\pi D^2 \tau}\int_0^\tau \int_0^{D/2} 2\pi r u(r,t)u(r,t)\, dr\, dt\right]^{1/2} \tag{2.12}$$

Utturkar *et al.* [49] used the same equation for steady flow emanating from an axisymmetric orifice to calculate a constant, N. This value describes the ratio of the jet centreline velocity to the average velocity, where $N = u_0/\bar{U}$, with u_0 being the instantaneous centreline velocity. Significantly, it was found that N is higher for an axisymmetric orifice than for a two-dimensional slot. When related back to the constant for the jet formation criterion where $K < Re/S^2$, this suggests that a synthetic jet is more likely to be formed at a lower Reynolds number for an axisymmetric orifice than for a two dimensional slot. It was found that a value of $K > 2$ and $K > 0.16$

was required for the formation of a two dimensional and an axisymmetric synthetic jet respectively.

A further method of calculating Reynolds number has been outlined by Glezer and Amitay [9] and is based on the impulse imparted, or momentum associated with the jet discharge, $Re_{I_0} = I_0/\mu D$, where

$$I_0 = \rho \int_0^{\tau} \int_A {u_0}^2(\bar{x}, t)\, dA\, dt \tag{2.13}$$

with ρ and μ representing the fluid density and viscosity, respectively.

A more recent method for the estimation of the flow velocity was developed by Persoons and O'Donovan [50]. The method developed is based on the laws of simplified gas dynamics, and requires the measurement of internal cavity pressure to estimate synthetic jet velocity and actuator deflection. When the equation for conservation of momentum is applied at the orifice it is found that

$$M_o \frac{d\bar{U}}{dt} + F_D(\bar{U}) = pA \tag{2.14}$$

where M_o is the mass of gas in the orifice, p is the varying cavity pressure relative to the unloaded condition and $F_D(\bar{U})$ represents a damping force where F_D is a function of $\bar{U}$. Calibration for this method requires a centreline velocity measurement similar to that used for equation 2.10, this is required only to characterise an added mass coefficient, β and a pressure loss coefficient, K_p, for a steady flow through the orifice for the specific geometry which is incorporated into the mass of gas in the orifice, M_o, and the damping force F_D respectively. As the velocity calculation itself is dependent on simplified gas dynamics and on the momentum equation the velocity calculated is more similar to that of equation 2.11. Other authors such as Crittenden and Glezer [25] and Kercher *et al.* [6] also used pressure measurement based estimates to calculate the average velocity of the synthetic jet. In a paper presented by Kercher *et al.* [6] a miniature total pressure tube was used to extract the average jet velocity from the pressure differential ΔP, which is the difference between the pressure within the jet

and the local static pressure. The average jet velocity is therefore given by:

$$\bar{U} = \sqrt{\frac{2\Delta P}{\rho}} \tag{2.15}$$

There is merit in using either equation 2.11 or 2.10 to calculate synthetic jet Reynolds number. Equation 2.11 provides a good idea of the peak velocities and the state of the fluid expelled through the orifice during the ejection phase of the synthetic jet cycle. This provides a good measure of the maximum fluid velocities reached in and near the jet exit, and may better describe quantities important when discussing aspects of the synthetic jet such as vortex formation, kinetic energy or imparted impulse. However, equation 2.10 more accurately reflects the time averaged mass flux of fluid produced by the synthetic jet. Smith and Glezer [46] argued in favour of the use of U_0 in comparison with $\bar{U}$ for a continuous jet. They believed that in the far field, the average downstream volume flux is more analogous to a continuous jet as this is what controls the important jet phenomena. While neither method stands out as being more valid, equation 2.11 does lend itself more to far field analysis and comparison with continuous jets, whereas equation 2.10 may be more suitable for formation analysis and near field evolution. For this work the Reynolds number has been calculated using the method as outlined by Utturkar *et al.* [49] in equation 2.11.

2.4.2 Computational and Analytical Modelling for Synthetic Jet Formation

Many numerical investigations have been undertaken for synthetic jets. Wu and Leschziner [51] showed that large eddy simulation (LES) could be used to realistically capture the flow field of an isolated, turbulent, round, synthetic jet injected from a cavity into a quiescent environment. Two different types of meshes and orifice geometries were tested; a deformed and a square cell mesh on a round orifice and a square celled mesh on a square orifice. Rather surprisingly it was concluded that the deformed mesh did not produce the optimum results; a non-circular flow field near the orifice was returned because of the strong deformation of the cells. The authors concluded that the rather simple solid cell mesh produced the best results as it proved

adequate at capturing all essential features of the evolution of the jet when compared to experimental data.

Another widely used approach in recent years has been that of the unsteady Reynolds-averaged Navier-Stokes (RANS) numerical solver. Recently Le Song and Prudhomme [52] used a RANS model with steady boundary condition to successfully predict the formation of coherent structures in the exit flow field for an impinging synthetic jet. The authors found that using the unsteady averaging approach previously used by Ha Minh [53] they were able to reproduce from steady state boundary conditions the coherent vortices produced experimentally by the impinging synthetic jet. Nae [54] was one of the first authors to implement a RANS solver on a synthetic jet. Work published by Nae [47] used an unsteady compressible RANS model to analyse not only a synthetic jet but also its cavity and surrounding domain. Using these parameters Nae found that compressibility effects meant it was necessary to apply a pressure correction for low Mach numbers to improve convergence and alleviate instability problems. Results were compared to both experimental data and numerical studies from other papers. Nae showed that a simple constant velocity profile is only valid for approximately 70% of the nozzle area in suction and less than 50% in the ejection phase; this can have significant implications for velocity and flow rate calculations. Similar trends can be seen in figure 2.6 (*a*) which shows experimental phase locked velocity exit profiles presented by Shuster and Smith [48]. These data confirmed what had previously been established through the use of numerical modelling by Gallas *et al.* [55] as shown in figure 2.6 (*b*); significant deviation from the top-hat profile is present through most of the suction and ejection phases. Unfortunately, a number of other authors including Gomes *et al.* [1] overlooked the same phenomenon by assuming a top-hat like velocity profile for their data. Using an incompressible Navier-Stokes solver Kotapati *et al.* [56] undertook a comprehensive investigation where the entire domain of a synthetic jet with slot geometry was modelled, including the flow within the cavity, through the orifice and into the main flow field. The authors showed that within the orifice and during both ingestion and expulsion phases there is significant deviation from the ideal top-hat velocity profiles, indicating that the flow in the slot is highly un-developed.

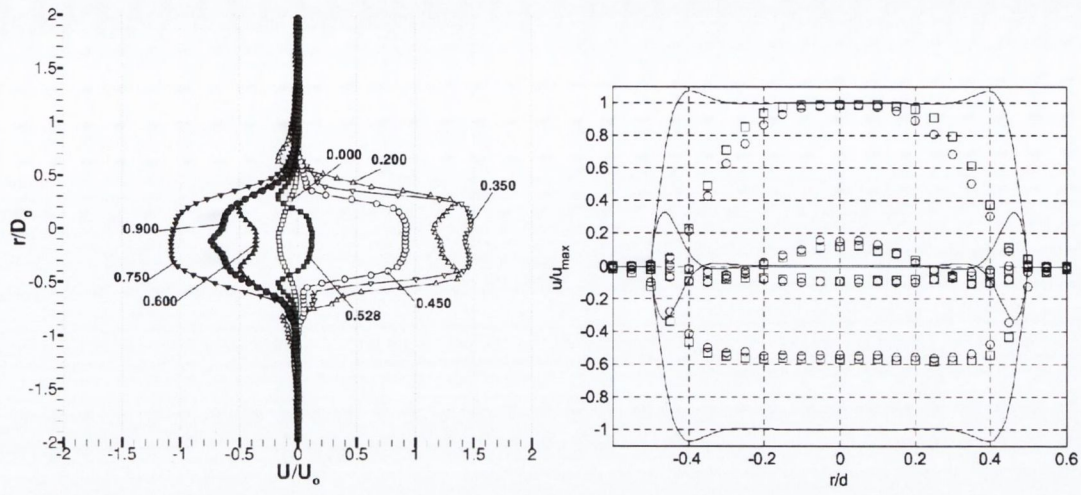

(a) (b)

Figure 2.6: (a) Cross-stream profiles of the streamwise component of the velocity at the orifice $L_0/D = 3$, $Re_{U_0} = 2500$ [48] (b) Normalized axial velocity profiles at four phases during a cycle for $S = 8$, (◯) $Re = 45.5$, (□) $Re = 94$, (−) solution for pipe flow with an oscillating Δp [55].

As outlined in section 2.4.1, Persoons and O'Donovan [50] used an analytical model to estimate synthetic jet velocity and actuator deflection. Their model was derived from simplified gas dynamics and used cavity pressure measurements to estimate jet velocity for a frequency range which extends from zero up to a frequency limit governed by the geometry of the synthetic jet actuator. Applied to the test case presented in their paper the resulting analytical model shows good agreement with experimental data and is valid from $0Hz$ up to 1.5 times its Helmholtz resonance frequency. Although the model was only validated for one specific orifice, its generic basis allows for pressure based velocity estimation for other synthetic jets, requiring only limited calibration.

The idea of a theoretical criterion for synthetic jet formation has been explored and validated by Utturkar *et al.* [49] and Holman *et al.* [20] using both numerical and experimental investigations. Numerical simulations were performed using an extensively validated Cartesian grid solver to simulate an unsteady, viscous, incom-

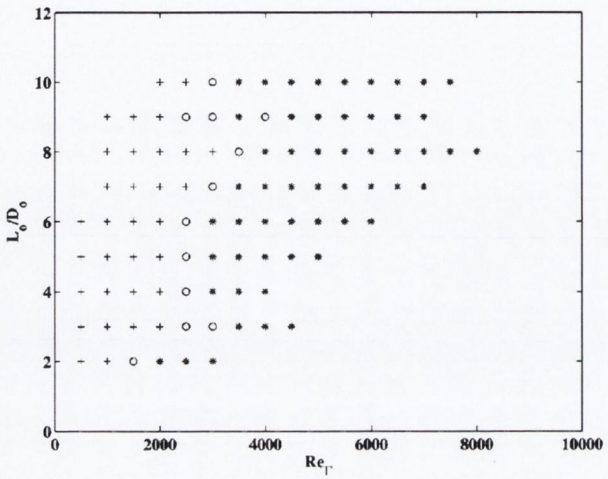

Figure 2.7: Transition map for vortex rings formed in the synthetic jet: +, laminar; ○, transitional; *, turbulent.[48]

pressible flow combined with a multigrid algorithm for solving the pressure Poisson equation. In common with Nae [47] these simulations were performed both on the cavity volume and surrounding domain. The data collected suggested that vortex formation is dependent on the dimensionless stroke length (i.e. Strouhal number). These data support the formation criterion $Re/S^2 > K$ proposed by Utturkar *et al.* [49], where $Re/S^2 \approx \bar{U}/2\pi fd$ and the formation constant K is approximately equal to 1 and 0.16 for two-dimensional and axisymmetric jets respectively. The dimensionless stroke length is related to the formation criterion as follows:

$$L_0/D = \frac{\bar{U}}{2fD} = \pi \frac{Re}{S^2} \tag{2.16}$$

These results are in accordance with the previous findings of Smith and Swift [21] who found that, for a two dimensional jet, a minimum stroke length of $L_0 = 5.5D$ exists below which no synthetic jet is formed. As the dimensionless stroke length is increased beyond $L_0/D = 5.5$ the jet momentum is increased and so the vortex pair escapes the influence of the suction stroke. Similar results were presented in a paper by James *et al.* [57] for jet formation in water, although no stroke lengths were reported upon. Shuster and Smith [48] investigated a synthetic jet flow field for much smaller dimensionless stroke lengths between $1 \leq L_0/D \leq 3$ for a round orifice over a range of Reynolds numbers. A transition map was presented indicating the state of the vortex

at various values of stroke length and Reynolds number; this map is shown in figure 2.7. These results show that a synthetic jet can be formed at stroke lengths as small as $L_0 = 2D$, far below that reported by Smith and Swift for an orifice of slot geometry.

A slug flow model used by Holman *et al.* [20] to identify scaling parameters in the jet flow field identified the lowest value of $L_0/D \approx 0.5$ to be close to the limiting synthetic jet formation condition. Although no actual criterion was proposed a similar conclusion was arrived at by Mittal *et al.* [58]. The authors stated that the vortex pair must be separated from the orifice edge by a minimum distance before the start of the ingestion stroke, a separation distance dependent on jet velocity and vorticity. This proved to be a proposal that was not strictly accurate. Shuster and Smith [48] observed that vortex rings were unable to escape the orifice for $L_0/D \leq 0.6$, in which case the vortex ring which was formed during the expulsion phase of the actuator cycle was subsequently reingested into the orifice during the suction phase of the cycle.

2.4.3 Orifice effects

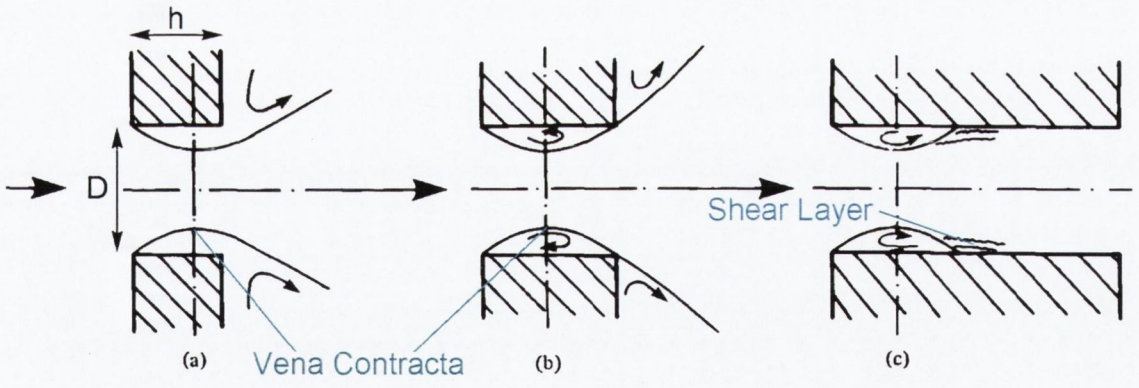

Figure 2.8: Flow through a constant diameter cylindrical orifice with increasing depth **(a)** Separated flow $h/D < 0.75$ **(b)** Marginally reattached flow $h/D \approx 0.75$ **(c)** Fully reattached flow $h/D > 0.75$ [59]

The characteristics of cylindrical nozzles with sharp upstream edges have been discussed at length by Ward-Smith [59]. Gomes *et al.* [32] subsequently applied the findings of Ward-Smith to the flow through a synthetic jet orifice. Gomes *et al.* identified two specific effects acting on the flow travelling through the orifice which are

of importance in understanding the influence of increasing orifice depth. Firstly, the greater the orifice length h, the bigger the damping effect on the flow curvature will be. It can be seen in figure 2.8 a) above that flow curvature occurs due to the boundary layer forming between the jet flow and the orifice walls. This has an acceleration effect on the flow up to the point of minimal effective cross sectional area, which in this case is the location of the vena contracta. Figure 2.8 *c*) indicates that due to shear action of the slow fluid moving near the wall and the fast moving flow in the core, the boundary layer displacement thickness grows with length. The result of this is a slowdown of the overall flow and hence a reduced area-averaged peak velocity. Although a greater nozzle length may provide a more developed flow, it will also increase deviation from a top-hat velocity profile. This finding is confirmed numerically by results presented by Mittal *et al.* [58] in which velocity profiles for orifices of $h_o/D = 1$ and $h_o/D = 3$ are compared. Gomes [32] goes on to state that a compromise exists between the two phenomena presented in figure 2.8 (*a*) and (*c*) at which an optimum is reached. As such, the minimum orifice length, h required for the flow to exit uniformly without the curvature caused by flow separation is $h_o \approx D/2$ and the optimal orifice depth would be the summation of the lengths required to achieve marginally attached flow (i.e. $h_o \approx 0.75D$) plus the required extension to achieve a measure of uniform flow $h_o \approx D/2$, resulting in a total orifice depth of around $1.25D$ and is depicted in figure 2.8 (*b*). The presence of vena contracta were also noted by Kotapati *et al.* [56] for simulated flow within an orifice, where for an orifice of length $2.6D$ the high turbulence intensity associated with the boundary layers formed on the slot walls caused the boundary layers themselves to separate and form a vena contracta at the slot openings. However, in practice vortical structures which are ingested into the slot from the internal and external cavity quickly destabilise the separated boundary layer.

Experimental investigations in the same study by Gomes *et al.* [32] showed that although this ideal orifice length $h_o \approx 1.25D$ may well achieve uniform flow, it is not the optimum for the nature of the flow within the synthetic jet orifice. A wide range of parameters were tested to ascertain what arrangement of orifice length and cavity depth would achieve maximum jet velocity. The authors identified an optimum di-

mensionless length and depth of $h_o/d \approx 2.1$ and $H_c/d \approx 0.6$ respectively. The cavity depth was shown to have a much more significant effect on peak velocity; this was attributed to the decoupling of the Helmholtz and diaphragm resonant frequencies as the volume changed. These results broadly agree with numerical data presented by Gallas *et al.* [55], where the author states that qualitatively, the flow produced remained the same with a doubling of orifice depth from $h_o/d = 1$ to 2. Much like Gomes *et al.* [32], Chaudhari *et al.* [37] also investigated the effect on jet velocity of varying the cavity and orifice dimensions. Tests were conducted across a wide range of frequencies at constant input voltage; this setup meant the jet performance was highly dependent on natural resonant frequencies. This study used varying orifice diameter, effectively changing h_o/d, it is therefore hard to interpret the effect of this dimensionless parameter as consequently H_c/d changes proportionally. Inadvertently, what the investigation does is confirm the previous findings of constructive coupling, as it was shown that as the orifice diameter and cavity depth are increased the cavity resonance is pushed further up the frequency range and away from that of the diaphragm.

2.4.4 Near Field Evolution

In the near field the defining difference between steady jets and synthetic jets is the nature of the flow. A continuous jet by its own definition produces a constant, continuous flow issuing from an orifice or nozzle; the result of this is a uniform velocity field low in turbulent fluctuation. The synthetic jet provides a contrasting flow field, in large part because of its inherent pulsatile nature which gives rise to velocity fluctuations which are commonly larger than the mean velocity. Synthetic jets are also highly dependent on the formation and subsequent advection of discrete vortices formed at the periphery of the orifice, consequently the near field of a synthetic jet can only be analysed once a net mass flow has been established. Much literature has been published regarding both vortex formation and the proceeding flow field. Smith and Glezer [46] undertook a comprehensive investigation into the formation and evolution of a synthetic jet in which they reported on the celerity (or propagation velocity) of a vortex pair.

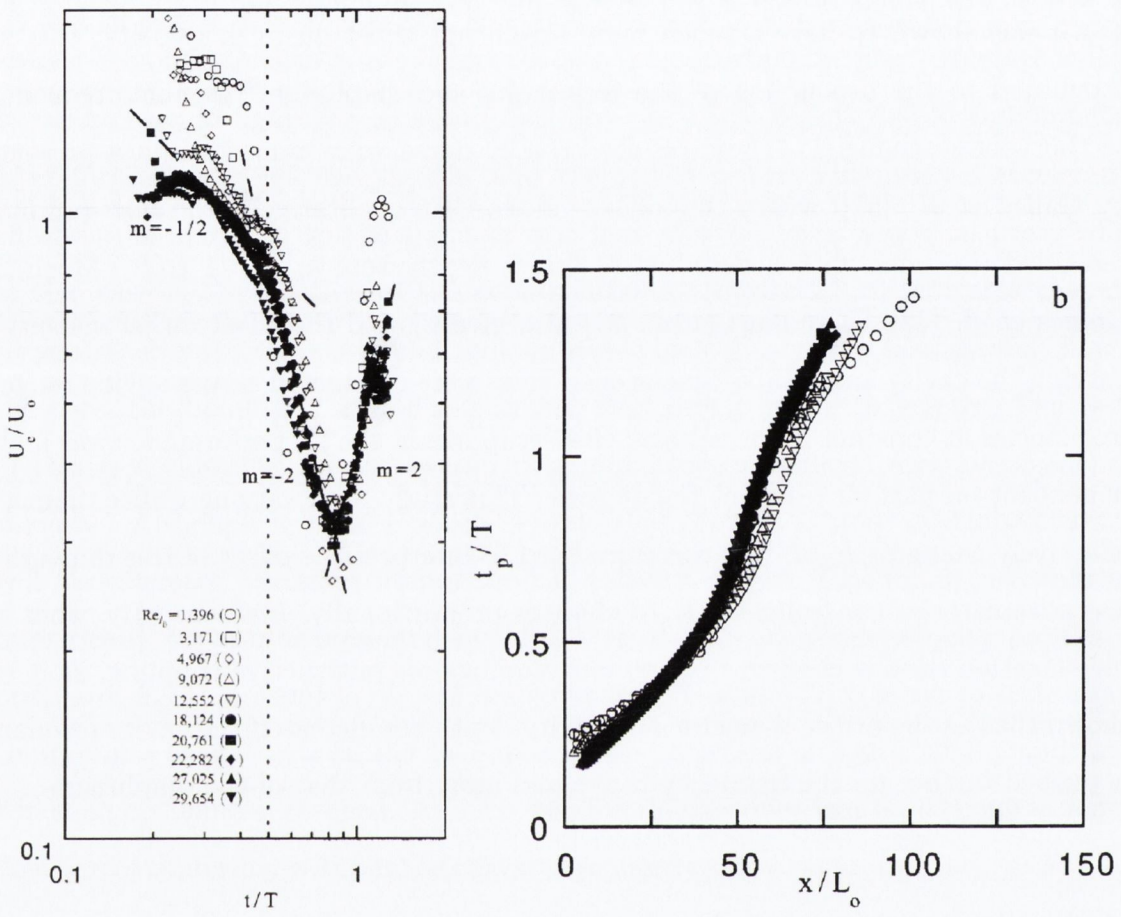

(a) (b)

Figure 2.9: (a) Variation of vortex pair celerity with time. (b) Individually normalised vortex pair trajectories, where t_p is the time corresponding to the passage of the velocity peak on the jet centerline during the passage of the vortex pair at a given measurement station and $T = 2\tau$ [46]

Results show that the vortex propagation and subsequent degradation to turbulence is highly influenced by the suction phase of the jet. Smith and Glezer present data from a synthetic jet with increasing impulse ($1400 \leq Re_{I_0} \leq 30000$) and dimensionless stroke length $5.3 < L_0/D < 25$ which shows the mean trajectory of vortex pairs at a fixed actuation frequency ($1140Hz$). It was found that, regardless of impulse magnitude, the resulting trajectories are very similar and are comprised of three distinct domains characterized by changes in slope (or celerity); this can be seen in

figure 2.9 (*b*). Similar trends were observed in research published by Xu *et al.* [24]. Significantly, Xu *et al.* noted that beyond $t/T > 0.1$ the vortex core is consistently located downstream of the centerline velocity peak. This indicates that for the parameters tested, the self-induced velocity of the vortex pair is greater than the convective velocity of the fluid itself. Unfortunately Xu *et al.* only presented data for one parameter of $100Hz$ (unknown Re and L_0/D), but the detachment of the vortex pair from the trailing jet has been reported previously by Gharib *et al.* [60] for discrete, constant velocity impulses rather than repeated oscillations. From figure 2.9 (*a*) it can be seen that at approximately $t/T \approx 0.6$ the vortex pair begins to slow down, it is at this point that the flow begins to undergo a transition to turbulence; these results can be correlated with the data presented in figure 2.9 (*b*) where the existence of three distinct streamwise domains are shown. The first domain corresponds to the formation of the vortex pairs and their laminar advection away from the orifice. As the flow progresses in the streamwise direction the transition to turbulence corresponds to the change in slope. Finally, the emergence of the turbulent jet can be seen as the slope changes once again. This third domain corresponds to $t/T \approx 0.9$ in figure 2.9 (*a*), where the vortex pair speeds up once more until it loses its phase coherence and becomes part of the mean jet flow. It is noted that the sudden reduction in velocity and transition to turbulence at $t/T \approx 0.6$ starts immediately after the beginning of the actuator's suction cycle. Smith and Glezer surmised that the transition may be triggered by core instabilities associated with the reversal of the streamwise velocity near the exit plane. It is worth noting that regardless of the impulse imparted to the jet, no vortices were phase locked to the actuator driving frequency much beyond $t/T \approx 1.3$. Shuster and Smith [48] reported on a round jet with much lower dimensionless stroke lengths of $1 \leq L_0/D \leq 3$; results showed that the mean centreline velocity peaked near $x/L_0 = 1$ for all stroke lengths and monotonically decreased after this distance. The decay law was found to be similar to that of a conventional turbulent jet with $U/U_{cl} = 0.46x/D$ for all three stroke lengths, however with a faster rate of spread. These results are in clear contrast to the findings of Smith and Glezer [46] who reported that for a two dimensional jet the mean centerline velocity of the jet increases until it reaches a local maximum at $x/h = 7$ and subsequently decays monotonically, which unlike the

findings of Shuster and Smith is independent of dimensionless stroke length. It can be concluded that the reason for the very different results may primarily be down to the vastly different dimensionless stroke lengths investigated although the effects of differing orifice geometry can also not be discounted. Although Shuster and Smith [48] report that a jet is formed at a stroke length as low as $L_0 = 1D$ it is evident that it is significantly different to those formed at greater stroke lengths. At such low stroke lengths the jet is significantly diminished; this is down to two reasons: (i) a minimum stroke length for complete vortex formation is not reached, as a result vortex circulation is diminished, (ii) the beginning of the suction stroke occurs before the vortex is fully formed and has reached the necessary distance from the orifice; as such it is unable to escape the effects of flow reversal and a significant amount of the convection fluid is reingested into the orifice. Muller *et al.* [61] reported that for $L_0/D \leq 3$ a significant amount of vorticity imparted during the expulsion stroke can be reingested during the suction stroke. The authors identified that the thrust coefficient in this regime is proportional to $(L_0/D)^4$. For the regime $L_0/D > 3$ the thrust was found to equal the positive momentum flux at the orifice and was proportional to $(L_0/D)^2$.

Research undertaken by authors such as Gharib *et al.* [60] and Rosenfeld *et al.* [62] has looked at the formation of vortex rings generated through impulsively started jets. Although this research was not undertaken specifically with synthetic jets in mind, it becomes highly relevant in this context as much of the processes such as vortex formation, convection and subsequent interaction remain more or less the same. Both of the above papers used an impulsively started piston to eject a single column of fluid from a round orifice, this was done for various velocity profiles. The ejected fluid subsequently produced a number of flow formations, depending on stroke length, which were studied in depth. While these flow formations are analysed independently of any flow reversal experienced by the synthetic jet suction stroke and any preceding flow, the findings themselves define the fundamental principle upon which the synthetic jet is founded; vortex formation. Significantly, the paper by Gharib *et al.* [60] identifies a time scale, or formation number, which characterises the formation of vortex rings. The time scale is the time beyond which larger rings are not possible; this equates to $L_0/D \approx 4$ for an impulsively started jet.

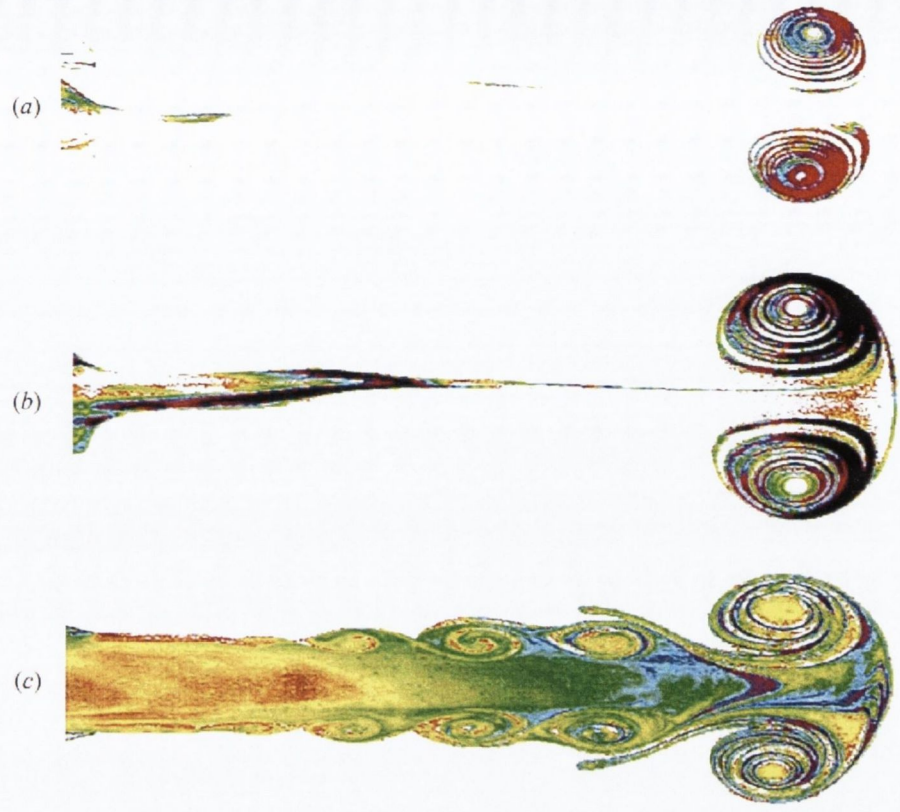

Figure 2.10: Visualization of vortex rings for (*a*) $L_0/D = 2$, (*b*) $L_0/D = 3.8$ and (*c*) $L_0/D = 14.5$ [60]

Prior to reaching the limiting formation number Gharib finds that all discharged fluid becomes entrained in the vortex ring, this is evident from figure 2.10 (*a*) and (*b*). It is noted that as the stroke length increases up to the formation limit, the size and circulation of the vortex also increase linearly; this is reflected in data presented in figure 2.11 (*a*). Figure 2.10 (*c*) depicts the effect on the jet when the stroke length is increased beyond the formation number; in this particular case to $L_0/D = 14.5$. The author describes this case as a leading vortex ring followed by a trailing jet where the shear layer of the trailing jet forms into a series of vortices similar to the Kelvin-Helmholtz instability[3]. Importantly, the size of the vortex in (*b*) and (*c*) appear similar. It is revealed in figure 2.11 (*b*) that this is indeed the case and that although total

[3]Kelvin-Helmholtz instability occurs when velocity shear is present within a continuous fluid, or when there is sufficient velocity difference across the interface between two fluids to cause vortex rollup in the shear layer.

circulation continues up the point where the piston stops, the vortex has long since reached its maximum circulation. In the case of figure 2.10 (c), once the formation of the vortex ring has been completed, the vortex ring appears to separate itself from the trailing jet and vorticity is no longer entrained from its shear layer region.

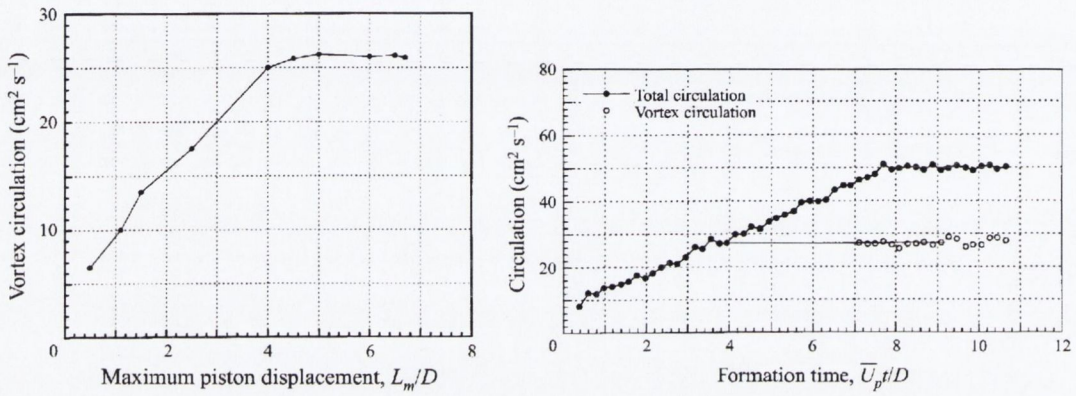

(a) (b)

Figure 2.11: Vortex ring circulation as a function of (a) stroke length L_0/D and (b) formation length for the case $L_0/D = 8$ [60]

While this behaviour of detachment of vortex and trailing jet appears to indicate that, once formed, the two phenomena should be treated as two completely separate regimes, this is not necessarily the case. The authors have documented the behaviour of the vortex for a fast-ramp case which more closely resembles the ejection stroke of the synthetic jet. In this case it is observed that the trailing jet can indeed catch up and interact with the preceding vortex. Gharib *et al.* noted that as the primary vortex in the trailing jet impacted with the primary vortex, merging occurred and the circulation level was increased in a step-like manner. However, the excess vorticity was subsequently shed and the circulation of the leading vortex returned to that dictated by the formation number. More vigorous and frequent mergers between the primary vortex and the trailing jet resulted in destruction of the primary vortex. The authors concluded that this was due to the inability of the primary vortex to shed a sufficient amount of fluid required to maintain its formation number; as such the vortex became unstable and destruction ensued.

Gharib *et al.* [60] went on to vary the velocity programs further with implementation of exponential, logarithmic and triangle programs. Results showed that all of these programs only served to delay the formation length of the vortex beyond that of an impulsive program. A number of other authors explored this topic further [62, 63, 64], with Rosenfeld *et al.* [62] undertaking an approach combining both numerical and experimental research. Like Gharib *et al.* all three studies investigated the effect of varying the velocity program, employing impulsive, trapezoidal and linear ramp programs. Results presented from all authors confirmed the existence of a formation number previously documented by Gharib *et al.* [60].

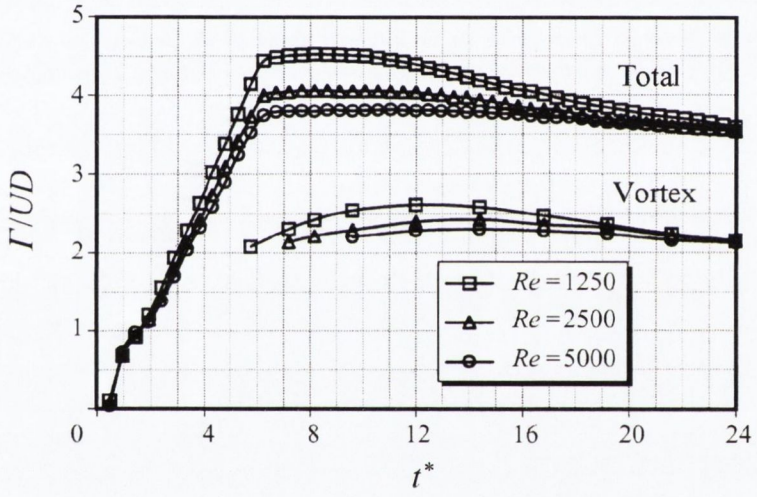

Figure 2.12: The effect of Reynolds number on the evolution of the total and vortex circulations for an orifice [62]

Rosenfeld *et al.* [62] observed that there is a small yet noticeable increase in total circulation as Reynolds number decreases; this is shown in figure 2.12. This is attributed to the dependence of the discharge velocity profile on Re, because the boundary layer is thicker due to the more dominant viscous effects at low Reynolds numbers it results in a larger centreline velocity; a consequential increase in total circulation is experienced.

Krueger *et al.* [63] presented data showing impulse imparted by the various stages of the flow formation. The experimental studies showed that the forming vortex ring contributes proportionally more impulse per unit L_0/D than that for the subsequent trailing jet. This leads to the conclusion that propulsive quantity is optimised by

starting jets at L_0/D just after pinch off occurs and before a trailing jet has been formed. This finding is at odds with that of Muller *et al.* [61], one of the few studies to document the distinction between the primary vortex ring and the subsequent trailing vorticity for synthetic jets. Muller *et al.* state that with increasing stroke length this vorticity does not influence the thrust coefficient scaling for $L_0/D > 3$, which was found to be proportional to $(L_0/D)^2$. Krueger *et al.* go on to suggest that this research may be useful in design strategies for pulsed-jet technologies, where the primary goal is to impart momentum to the flow.

Shusser *et al.* [64] define a theoretical dimensionless vortex ring circulation:

$$\Gamma_{nd} = \sqrt[3]{\frac{\pi}{16b^4B^2}} \approx 1.26 \tag{2.17}$$

where B and b are defined using Fraenkel's [65] second order formulae which are based on the dimensionless thickness of the ring, ϵ. Comparing this result to data computed from Rosenfeld *et al.* [62] it was observed that Γ_{nd} remained consistently close to theoretical predictions, implying that the dimensionless circulation of the ring is indeed a universal quantity.

Recently, Shan and Wang [66] studied the direct influence of both Reynolds number and stroke length on the flow characteristics produced from a discrete ejection from a synthetic jet orifice of round geometry. The authors presented the flow visualisations shown in figure 2.13 as part of their results depicting the evolution of vortex rings at three different Reynolds numbers for fixed stroke length and phase. Reynolds numbers were calculated using conventional jet exit velocity, Re_{U_0}, as well as a number based on the vortex ring circulation, Re_{Γ_0}, and are displayed beside the images. Circulation Reynolds number is calculated as follows:

$$Re_{\Gamma_0} = \frac{\Gamma_0 D}{\nu} \tag{2.18}$$

$$\Gamma_0 = \int_0^T \frac{u_0^2(t)}{2} dt = \frac{\bar{u}_0^2 T}{2} \tag{2.19}$$

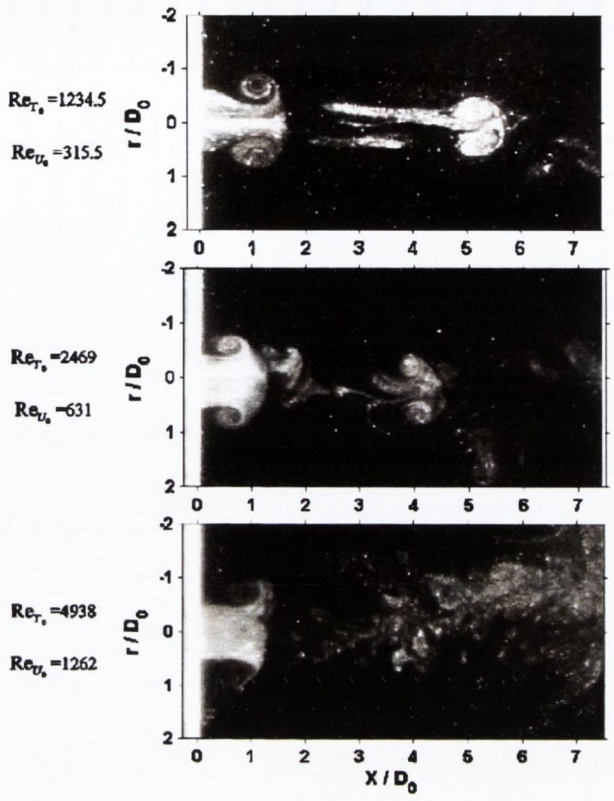

Figure 2.13: Flow visualizations at different Reynolds numbers, $t/T = 0.25$, L_0/D=6.3 [66]

where $u_0(t)$ is defined as the instantaneous mean velocity at the jet exit, $T = 1/f$ is the cycle duration. The three Reynolds number levels displayed in figure 2.13 were selected to span the transition map presented by Shuster and Smith [48] from a laminar to turbulent flow. It is evident that although the Reynolds numbers presented are quite different, the position of the first vortex ring ejected from the synthetic jet nozzle is the same in all three images, albeit the formation of the higher Reynolds number vortices appears more unstable. Looking further into the flow fields a distinct difference can be seen across them. While the vortex formation and advection appears quite uniform at $Re_{\Gamma_0} = 1234.5$, with increasing Reynolds number breakdown begins to occur until all coherency appears to be lost in the far field at $Re_{\Gamma_0} = 4938$. Shan and Wang concluded that the increase in Reynolds number does indeed have a direct bearing on vortex ring breakdown and that if the vortex ring formed at the jet exit

is turbulent, breakdown will occur earlier in the resulting flow. These results confirm the findings of Shuster and Smith [48] in this respect.

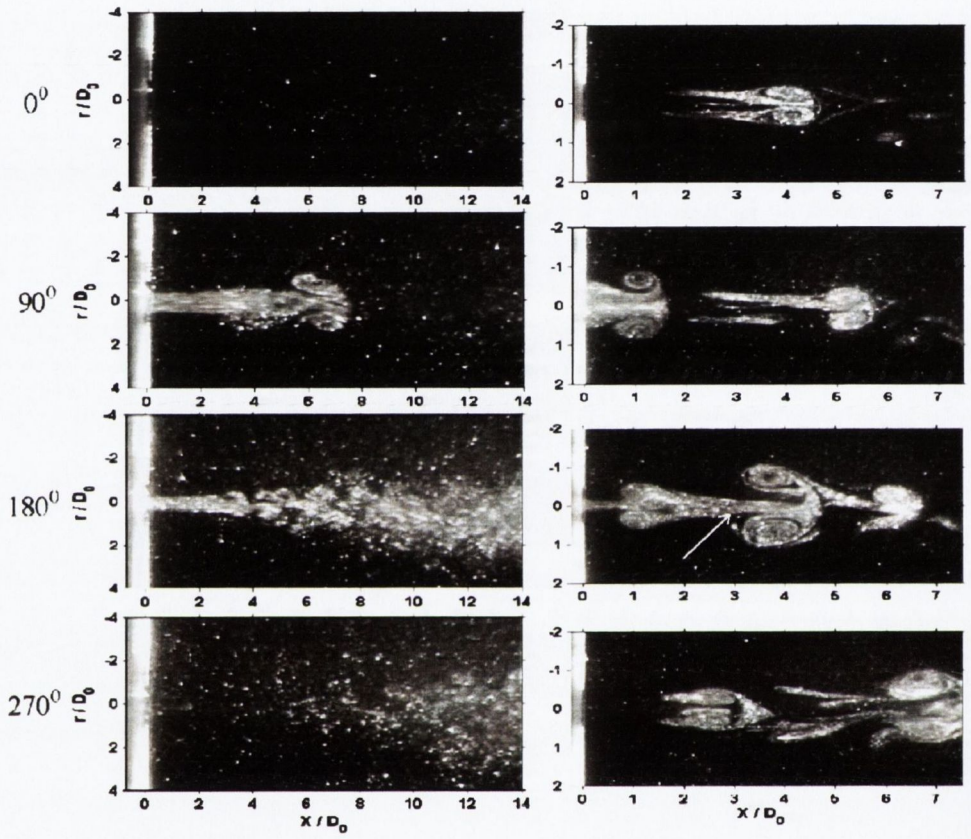

(a) $L_0/D = 50.7$ (b) $L_0/D = 6.3$

Figure 2.14: Flow visualisations for two different stroke lengths at $Re_{U_0} = 315.5$ [66]

Further investigation by Shan and Wang [66] into the effect of stroke length for a fixed Reynolds number was undertaken in the same paper. Figure 2.14 shows flow visualisations obtained by the authors. The contrast in the two different types of flow produced is clearly evident. While both stroke lengths produce vortices at the beginning of the ejection phase, it can be seen that in figure 2.14 (*b*) for a stroke length of $L_0/D = 6.3$ the flow field is dominated by the vortex formation and advection with good coherence and minimal interaction. The same detachment of the trailing jet from the primary vortex observed by Gharib *et al.* [60] can be seen at 180°, as indicated by the arrow. The flow field for the larger stroke length of $L_0/D = 50.7$ presented

in figure 2.14 (*a*) is almost unrecognisable compared to that in (*b*). Like that of the shorter stroke length, a vortex is formed at the beginning of the ejection phase, but this is where the similarities end. With progression through the phases, the flow field becomes dominated by the trailing jet, at 180°; the vortex no longer exists as the continual acceleration of the trailing jet past the vortex formation length leads to impact between the two, and consequential destruction of the leading vortex occurs. A significant amount of vorticity manifesting through the Kelvin-Helmholtz instability in the trailing jet at 180° is observable, a phenomenon that was also noted by Gharib *et al.* [60].

It is thought that for a synthetic jet, vortex interaction and viscous dissipation alone are not the primary contributors to the degradation of the flow, which results ultimately in a developed turbulent jet. While these mechanisms, which are manifested in the near field of the synthetic jet, do indeed play a major role in the transition to turbulence, there is some evidence to suggest that a not insignificant amount of velocity fluctuation is present prior to the flow exiting the jet orifice. Figure 2.15 shows time traces of the centreline streamwise velocity at various points from $x = -4D$, which is inside the cavity, to $x = 2.89D$ in front of the orifice, these results were presented in a paper by Kotapati *et al.* [56]. Unsurprisingly, turbulent velocity fluctuations u_2''/V_j can be seen in front of the jet orifice at $x/D = 2.89$ in 2.15 (*a*). Notably, these fluctuations dominate the blowing phase and are almost non-existent in the suction phase. While they might commonly be attributed to the natural evolution and degradation of the jet one would expect these fluctuations to subside with closer proximity to the orifice exit, however this is not the case. Looking at the velocity at $x/D = 0$ in 2.15 (*b*) it can be seen that the fluctuations do not originate in the near field of the jet and are in fact present prior to exiting the orifice. The fact that the fluctuations are still only present in the blowing phase suggests that they originate at a stage prior to exiting the orifice. Moving deeper into the jet at 2.15 (*c*) and (*d*) reveals that these fluctuations are also present prior to the fluid entering the orifice. Kotapati *et al.* conclude that originally the turbulence is associated with the detached shear layers formed during both suction and ejection. However, due to the high levels of confinement present within the cavity the vast majority of the fluctuations are

initiated there, with fluctuations being subsequently convected into the slot during the expulsion stroke. Conversely, less turbulence is present during the suction stroke as the majority of the turbulent fluctuation produced during expulsion has convected a sufficient distance from the orifice prior to the beginning of the suction phase so as re-entrainment does not occur.

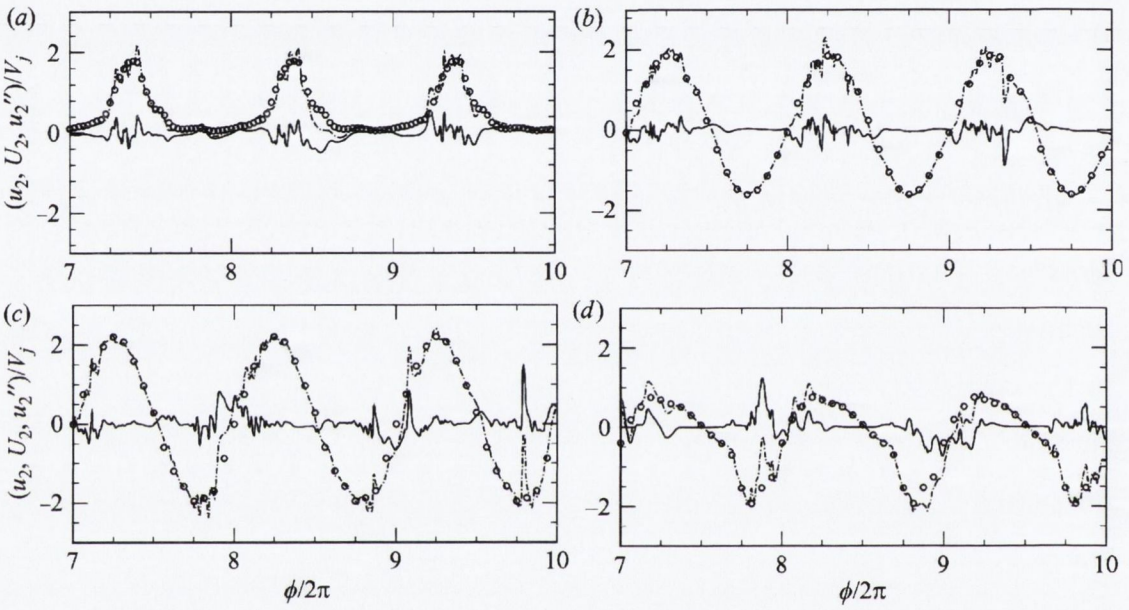

Figure 2.15: Temporal variations of instantaneous streamwise centreline velocity u_2/V_j $(-\cdot-)$, phase-averaged streamwise velocity U_2/V_j $(\circ)$, and turbulent fluctuation u_2''/V_j $(-)$, slot $h = 2.6D$ and orifice exit at $x = 0D$; (a) $x/D = 2.89$ (b) $x/D = 0$ (c) $x/D = -2$ (d) $x/D = -4$. [56]

2.4.5 Saddle Point

One of the more significant features observed in the near field of the synthetic jet is that of the saddle point. The saddle point is caused by the time-periodic directional reversal of synthetic jet flow, where alternate blowing and suction strokes lead to a time averaged stagnation (saddle) point in the flow.

Figure 2.16 shows the presence of a saddle point, in a phase-averaged streamline map of a two-dimensional jet that was computed from PIV data. It can be seen that a stagnation point exists at $x/b = 5$, above which point the motion is always directed

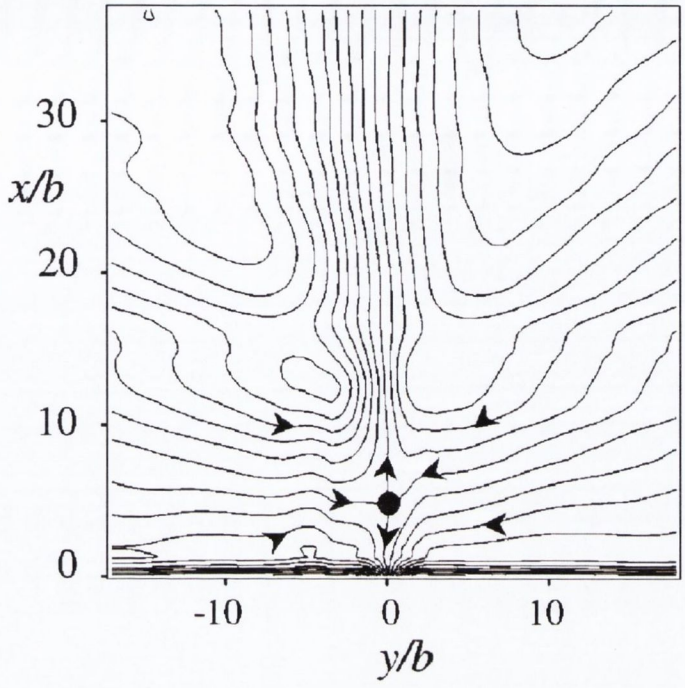

Figure 2.16: Phase-averaged streamline maps from PIV data; $\varphi = 270°$, $f = 300Hz$, $Re_{U_0} = 300$, $L_0/D = 29.1$ [29]

downstream, while below the flow is directed towards the orifice. Saddle points have also been documented by Xu *et al.* [24] and Di Cicca and Iuso [26], with the latter reporting the existence of a saddle point for an instantaneous velocity vector field at $x/b = 2$. The saddle point only appears during the suction stroke with its position being dependent on the instant of the suction phase. The saddle point begins initially at the mouth of the orifice, but as suction proceeds, the point moves progressively downstream until it completely disappears, and so the cycle starts again. The presence of a saddle point in confined flow was reported by McGuinn *et al.* [67], who found that confinement significantly affects the location of the saddle point. As confinement is increased the saddle point can be seen to move closer to the orifice exit until it becomes undetectable due to the strong recirculation between the plate and orifice. It is thought that the maximum distance extended by the saddle point is related to the dimensionless stroke length L_0/D, and confinement H/D, however there appears to be limited research available on the exact nature of the relationship. Smith and Glezer [29] reported that it was possible to affect the symmetry of the flow that is transported

towards the orifice during the suction stroke by extending one edge of the jet orifice in the downstream direction. This reduces intake confinement and moves the position of the saddle point closer to the orifice. Di Cicca and Iuso [26] also observed a decaying centreline velocity region in the near field; this was found to obey the law $1/x^m$, for $m \neq 1$.

2.4.6 Far Field Evolution

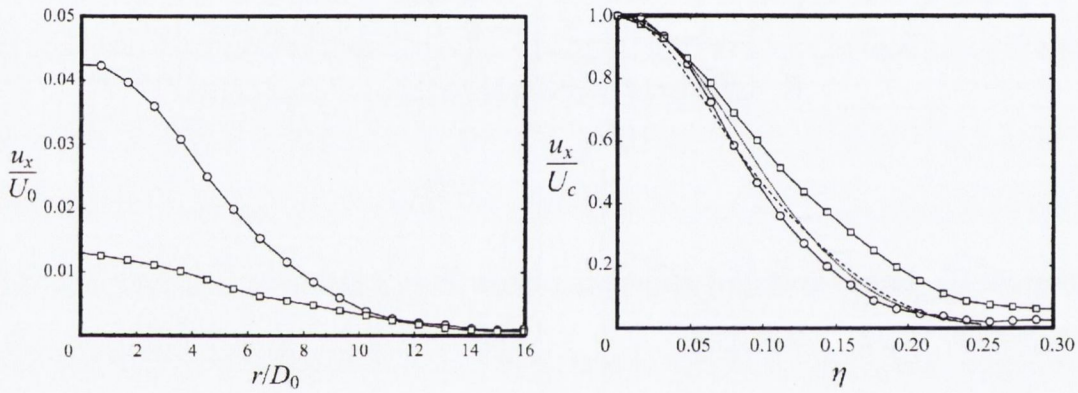

(a) (b)

Figure 2.17: (a) Non-dimensionalised and (b) Normalised profiles of axial velocity at $x = 60D$ for jets at $Re = 10^4$. Continuous jet (◯), ZNMF jet (□), Gaussian distribution ($\cdots$), Hussein *et al.* ($--$) [23]

It has been reported by numerous authors that the far field of a synthetic jet is very similar in many ways to that of a continuous turbulent jet [68, 23], this can be seen in figure 2.17. Although the shape of the mean velocity profiles is similar to that of a continuous jet in the far field, the mean streamwise gradients and magnitudes can be significantly different. A study by Cater and Soria [23] presented much data comparing the flow field properties of both types of jets. It was demonstrated that a round turbulent synthetic jet has a similar cross stream velocity distribution to that of a conventional continuous jet. Figure 2.17 (*b*) shows the same data as in 2.17 (*a*), but normalised by the centerline velocity and the radial coordinate non-dimensionalised by the axial location $\eta = r/(x - x_0)$, also known as the similarity

variable. An identical spread rate was observed up to $x = 30D$, beyond which the authors observed a reduction in the spread of the continuous jet while that of the synthetic jet was maintained; this is reflected in figure 2.17 (*b*), where the synthetic jet velocity profile is shown to remain significantly wider than that of the continuous jet. The rate of entrainment for a continuous jet was measured to be $\alpha_\epsilon = 0.089$ which taking testing conditions into account, was in reasonable agreement with a study by Hussein *et al.* [17] which obtained a value of $\alpha_\epsilon = 0.08$. This compares with the spread rate of the synthetic jet, $\alpha_\epsilon = 0.107$, which is over 33% larger. Muller *et al.* [61] reported that the rate of entrainment for a round synthetic jet was comparable to that of a conventional axisymmetric jet where

$$C_m = \frac{\dot{m}}{\rho D^2 f} = 0.155\left(\frac{L_0}{D}\right)^2 \tag{2.20}$$

with C_m being the rate of entrainment. This behaviour differs from that found by Smith and Glezer [46] where the entrainment for a two dimensional synthetic jet was found to have a slope of $Q \propto x^{0.35}$, significantly greater than that of the comparable continuous jet which had a slope of $Q \propto x^{0.5}$. Dimensional analysis of a synthetic jet using the principle of conservation of momentum leads us to expect a linear growth of the jet at a rate that depends on the jet Reynolds number. Also, a decrease in the centreline velocity with x^{-1} is expected, such that for a self-preserving jet the relationship for the centreline velocity becomes:

$$\frac{U_0}{U_{cl}} = S_u\left(\frac{x - x_0}{D}\right) \tag{2.21}$$

where S_u is a decay constant, U_0 is the area averaged orifice velocity, U_{cl} is the centreline velocity and x_0 is a velocity virtual origin[4]. Data presented by Smith and Glezer [46] showed the evolution of the synthetic jet mean centreline velocity which progressed from zero at the orifice exit, to a maximum as the flow becomes fully devel-

[4]The virtual origin is the coordinate at which the jet width goes to zero using the approximated relationship.

oped, and again reduced to zero as it degrades into a fully turbulent flow. It was found that this degradation to turbulence occurred at a distance of approximately $x = 25D$, whereas it would be expected to be much farther downstream for an equivalent continuous jet. In fact a synthetic jet velocity decay rate seven times larger than of a conventional jet was observed. This dramatic difference in the rate of decay can be attributed to the nature of the flow, the intermittency of the synthetic jet flow means that it has a potential core of diminished velocity, unlike its continuous counterparts.

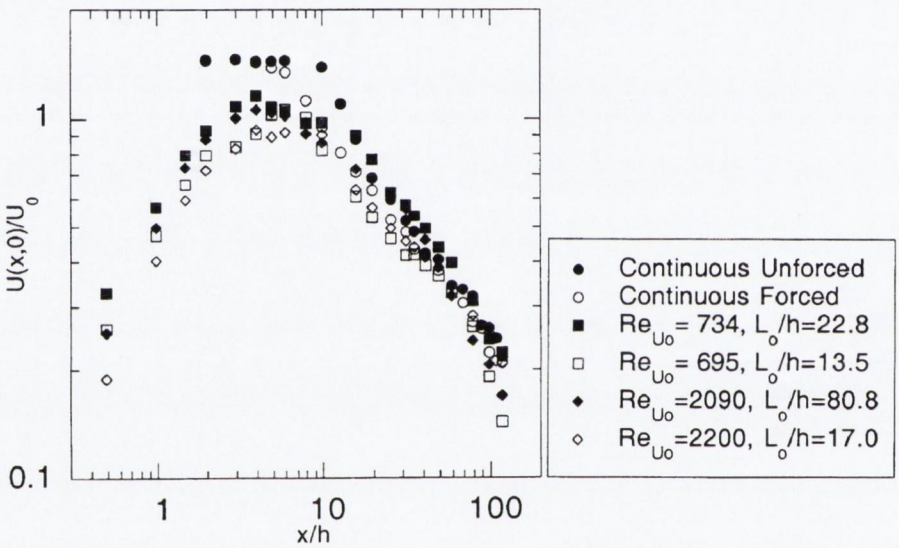

Figure 2.18: Time-averaged centerline velocity versus downstream distance [22]

Smith and Swift [22] published an article detailing the differences between synthetic and continuous jets where numerous parameters were compared. Figure 2.18 depicts the mean streamwise evolution of the jet velocities. Although the velocity decay rates follow the typical $-1/2$ power law and not the x^{-1} as expressed by Cater and Soria [23] this may be attributed to the difference in flow produced between two dimensional and axisymmetric jets. It is noteworthy that the synthetic jets all begin transition well before the continuous jet, as early as $x = 4h$ compared with $x = 10h$. Smith and Swift also measured each velocity profile a distance downstream where the centreline velocity U_{cl} is half that of $\bar{U}$ (continuous jets) or U_0 (synthetic jets). The velocity profiles of each jet were found to collapse onto a single curve for all cases. It was concluded that at these downstream distances the time-averaged features of the jets show little or no reflection of how the jets were generated. Smith and Swift also presented data

Experimenters	Jet type	Geometry	Re	Spread rate db/dx	L_0/D
Cater & Soria [23]	SJ	round	10^4	0.107	150
Cater & Soria	CJ	round	10^4	0.092	N/A
Di Cicca & Iusso [26]	SJ	round	$1290 - 3400$	0.098	23
Smith & Glezer [46]	SJ	2D	$104 - 489$	0.194	$5.3 - 25$
Smith & Swift [22]	SJ	2D	$734 - 2200$	$0.174 - 0.213$	$17 - 22$
Smith & Swift	CJ	2D	2200	0.125	N/A
Smith & Swift	forced CJ	2D	2200	0.149	N/A

Table 2.1: Comparisons of spread rates for synthetic and continuous jets as obtained from experiments.

comparing the width of the jet versus downstream distance, in accordance with Cater and Soria [23]. It was noted that the spreading rate is larger for synthetic jets than for continuous jets, especially for those with large dimensionless stroke length. The authors concluded that as a result of the unsteady vortex formation at the synthetic jet origin the increased growth was due to greater entrainment and hence volume flux in the near field.

A table of experimentally measured spread rates for synthetic and continuous jets are presented in table 2.1. Cater and Soria [23] compared the spread rate of synthetic jets to that of continuous jets by presenting the evolution of the jet half-width as a function of axial distance db/dx, where b is the cross stream half-width of the jet from the centre. It was found that the synthetic jet had a spread rate of $db/dx \approx 0.107$, 20% higher than what they observed a continuous jet to be; it was also noted that the spread rates for both jets increased linearly up to $x = 30D$. Cater and Soria surmised that the reason that synthetic jets spread differently throughout the domain compared to equivalent continuous jets is down to structural differences present in the near field, the primary one being the differing mean streamwise velocity gradient. Di Cicca and Iuso [26] also present data for a non-dimensional jet half width, but for a distance limited to $x = 7D$. Two regions, each of which were characterised by an almost constant rate of spread were clearly identifiable, with the first region extending up to $x = 3D$ at a $db/dx \approx 0.017$. The spreading rate for the secondary region was greater at 0.098, appeared constant and was almost independent of the Reynolds number. These values

of jet growth rate seem to be quite similar to the typical value of steady turbulent jets ($db/dx \approx 0.1$) and are in good agreement with the results reported by Cater and Soria [23] ($db/dx = 0.096$).

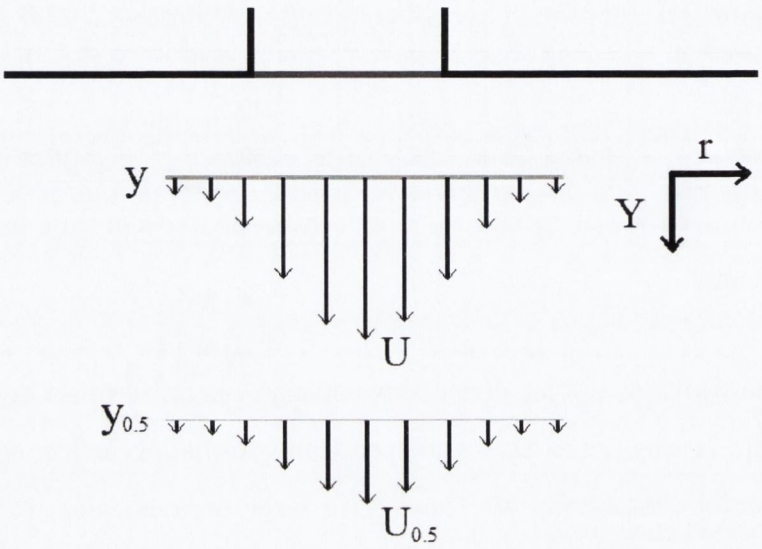

Figure 2.19: Axial locations for the self-similariy of the half-velocity

Cater and Soria [23], Smith and Swift [22] and Xu *et al.* [24] have examined other aspects of synthetic jets and conventional continuous jets. While Cater and Soria compared jets from circular orifices, Smith and Swift compared jets from high-aspect-ratio rectangular slots. In all these cases, the authors found self-similar velocity profiles in the far field that were comparable to continuous jets. The majority of authors reported this self-similarity to exist from $x = 10D$, however Di Cicca and Iuso [26] reported self-similarity for a distance as close as $4D$. Xu *et al.* found that all velocity profiles beyond the location of the saddle point at $x/D > 2$ coincide with each other and agree well with the self-similarity equation $U/U_{max} = exp[-(Y/Y_{0.5})^2]$, where Y and $Y_{0.5}$ are the y coordinate values at which point the velocity is equal to the half of the centerline velocity at the same downstream section, i.e. the Y and $Y_{0.5}$ locations where $U_{0.5} = U/2$; as in figure 2.19. Agrawal *et al.* [69] undertook a similarity analysis of a planar synthetic jet in which a scaling relationship for self-similarity was developed. The governing equations proved to be much more involved for the synthetic jet compared to those of the continuous jet, revealing the difference in complexity. The results agreed favourably with previous literature and the authors

went on to identify that the most fundamental characteristic differentiating the two types of jets is the inherently larger spreading rate of the synthetic jet. Agrawal *et al.* propose that the role of pressure in the self-similar region is negligible, a claim that has yet to be verified.

2.4.7 Flow Control

Flow control can mean a number of different things, but as far as the application of the synthetic jet is concerned Gomes et al. [1] described it as: *"the achievement of making a flow behave in a way that it would not ordinarily do so by the application of a minimum amount of energy or effort"*. While the application of flow control does not have any direct relation to synthetic jet heat transfer, it is important to recognise that much of the research undertaken into the formation and evolution of the synthetic jet was motivated by and completed with the objective of using the knowledge obtained to improve its performance in dynamic flow situations. Many authors in this field, including Nae [70] and Wu and Leschziner [51], have focused on numerical modelling to capture the resulting synthetic jet flow field, results which have contributed significantly to the understanding of how heat transfer processes may be affected by the flow generated. Other authors such as Jabbal and Zhong [71] documented important flow characteristics which went previously unobserved by authors investigating heat transfer. It is for this reason that, although not directly related, it is important to review the literature available for synthetic jets in flow control applications.

There has been much interest particularly by the aerospace industry in the application of the synthetic jet for the delay and possible prevention of flow separation over aerofoils. It is believed that significant aerodynamic gains can be achieved in this way, and so, much research has been undertaken into the potential effectiveness of the synthetic jet. Research into this area only really began about the year 2000 when a number of authors looked at the operation of the jet in a simple crossflow. Crook *et al.* [72] performed dye visualisation experiments and noted that the key factors governing the behaviour of the jet were both the ratio of jet velocity to bulk flow velocity and

also the separation distance between the vortex rings. Nae [70, 54] pioneered some early work in this field, although the author's primary goal was concerned with establishing the validation of employing numerical flow solvers to the problem. This was successfully accomplished, with Nae concluding that the simulations proved flow control is possible using the synthetic jet actuator, and in fact an increase in aerodynamic stability can be achieved with higher actuator speeds.

Some early experimental work was undertaken by Lee *et al.* [73] looking at the effect of operating a synthetic jet within a boundary layer. The authors found that the jet was most effective in disturbing the boundary layer when operated at the boundary layer's natural instability frequency, which in this case was caused by the Tollmien-Schlichting[5] wave, rather than the frequency at which the jet produces the maximum velocity which was a significantly higher frequency. Further investigation into this phenomenon has recently been done by Ozawa *et al.* [74]; the investigations were mainly focused on the lower frequency range of the Tollmien-Schlichting instability, referred to previously by Lee *et al.* [73] as the natural instability frequency. Results obtained using large eddy simulation agreed with those of Lee *et al.*, suggesting that the forcing frequency had greater influence, however Ozawa *et al.* were able to attribute the increase in performance to the effective elimination of the separation bubble.

Wu *et al.* [27] went on to expand the area of research to include that of the near field of two synthetic jets operating within a turbulent boundary layer. Results showed that there appeared to be two operational regimes. At low amplitude, pairs of closely spaced actuators were found to act independently with the net effect being linearly additive. Higher amplitudes showed that interactions were much stronger and produced notable distortion. The differences were attributed to the stronger pressure field produced by the higher amplitude, particularly in the suction phase. Results obtained using large eddy simulation by Wu and Leschziner [51] revealed that the separation upstream of the jet was also prevented by the suction stroke as the entrainment of the high velocity fluid upstream of the jet caused an acceleration in the flow. Wu and Leschziner also

[5] A Tollmien-Schlichting wave is caused by a disturbance to a viscous laminar channel flow in which the wave grows in amplitude due to the destabilising effects of the no-slip boundaries conditions and viscous effects in the bulk flow

went on to state that the effectiveness of the jet does not depend specifically on the injection velocity, but, since the shear stress $\overline{u'v'}$ was found to be the main agency for momentum transfer effectiveness, was dependent on the ability of the streamwise vortices to survive over a significant distance in the wake.

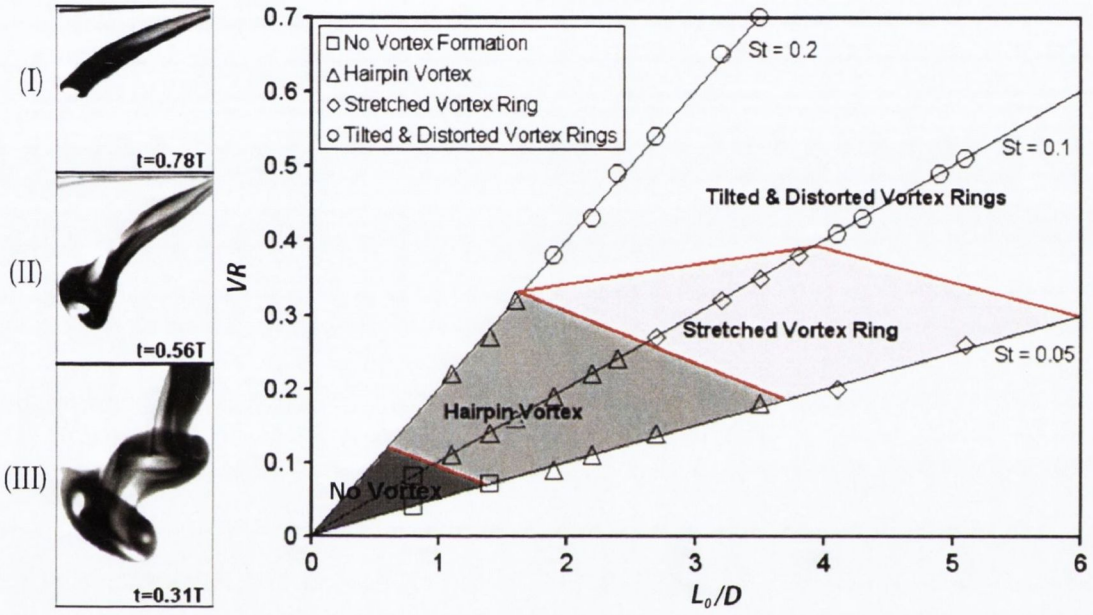

(a) (b)

Figure 2.20: (a) Close-up view of synthetic jet formation and roll up for (i) hairpin vortices, (ii) stretched vortex rings and (iii) distorted vortex rings (b) Parameter map of the different vortical structures seen as a result of the interaction between a synthetic jet and a boundary layer [71].

Jabbal and Zhong [71] performed dye visualisations for various synthetic jet to free stream velocity ratios, VR, in which three distinct vortical structures were identified. Figure 2.20 shows the three different types of vortices formed and the relationship between velocity ratio VR and Reynolds number. Hairpin vortices were observed to be formed at the lower end of both stroke length and velocity ratio. With an increase in both parameters the formation structure was observed to change to a stretched vortex ring. The upper limits of these parameters, above a velocity ratio $VR > 0.4$, revealed what was described as a tilted and distorted vortex ring, a formation that seems to be

dependent on velocity ratio rather than either dimensionless stroke length or Reynolds number. Although the authors Bonnet *et al.* [75] came to similar conclusions, they went on to state that while a synthetic jet that perturbs the mixing layer is desirable, the velocity ratio of synthetic jet to the mixing layer should not be so big that the jet penetrates the mixing layer completely. It is worth noting that figure 2.20 (*b*) indicates that as the velocity ratio increases the stroke length required to form a vortex becomes less, indicated by the red boundary line between the "No Vortex" zone and the "Hairpin Vortex" zone. Extending this line down to a velocity ratio $VR = 0$, i.e. a synthetic jet in quiescent fluid, results in an interception at $L_0/D = 2.6$. While this research does not present results directly linked to heat transfer, the versatility of the synthetic jet and the fact that it can be implemented in a wide range of environments means these results may well have relevance; such environments may include thermal boundary layers or induced cross flows designed to enhance heat transfer.

The potential implementation of this technology to delay flow separation was looked at by Gomes *et al.* [32, 1]. In the first paper [32] the authors looked at optimising the piezoceramic diaphragm so as to achieve the maximum possible performance; a mean peak velocity of 130 m/s was obtained. The second paper [1] showed that it is possible to design a synthetic jet flow control system within the performance limits of an aircraft. The aircraft evaluated for potential cost-benefits was an Airbus A321. The authors concluded that the lowest weight and power penalties were present when synthetic jets were implemented on the flaps of the aircraft. While the concept was validated no conclusion was arrived at as to whether or not the performance gains are greater than the system costs in terms of weight, power and fuel.

2.4.8 Energy Separation

Limited research has been undertaken into the occurrence and effect of instantaneous energy separation in steady jets and no reviewed papers to date have addressed this phenomenon in synthetic jet flows. A two part paper by Han and Goldstein [77] describes energy separation as the re-distribution of the total energy in a fluid flow without external work or heat so that some portion of the fluid has higher and another

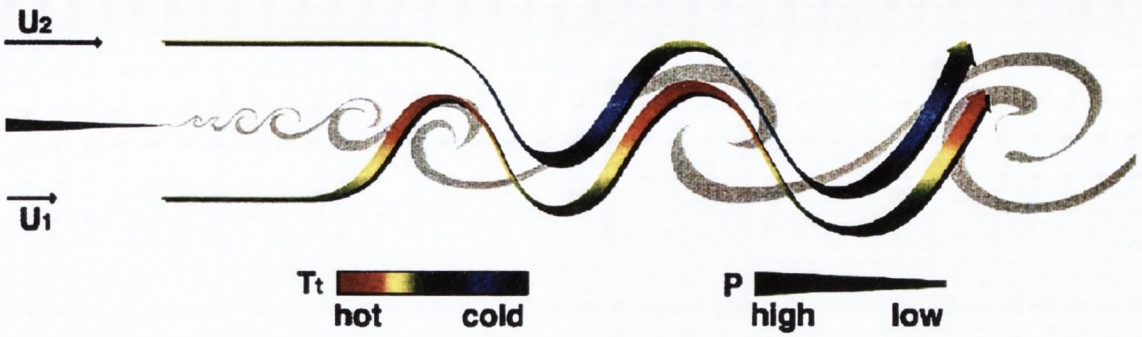

Figure 2.21: Schematic diagram of pressure and total temperature variation along path lines in a shear layer; colour denotes the total temperature, and thickness denotes the pressure [76]

portion has lower total energy (temperature) than the remaining fluid, hence having the potential to heat or cool a fluid without using a conventional heating or cooling system. A schematic diagram of this phenomenon describing pressure and temperature variation in the shear layer is depicted in figure 2.21. A study by Han and Goldstein used acoustic excitation at various frequencies as a method to enhance energy separation in a free jet. It is understood that in flow through disturbed pressure fields which generate large-scale coherent vortical structures, such as jet flow or cylinder crossflows, pressure fluctuation is caused by moving vortices and is the dominant mechanism of energy separation; Han *et al.* [76] state that this is a much stronger process than that due to the shear work and heat conduction. Han and Goldstein [78] reported that with acoustic excitation to a free jet there was notable enlargement of the temperature difference in the jet, indicating an increase in energy separation. The frequencies of dominant total temperature fluctuation unsurprisingly coincide with fluctuations in velocity, resulting from the shedding of vortices at a particular frequency. It was confirmed that this energy separation in a free jet was caused by the motion of these coherent vortical structures generating pressure fluctuations within the flow field. The authors observed a consistent intensification in the level of energy separation with active acoustic excitation, regardless of excitation frequency, but also noted that, in particular for $Sr = 0.9$, energy separation is greater in the region $1D \leq y \leq 4D$.

As the fundamental operation of the synthetic jet is dependent on the formation and

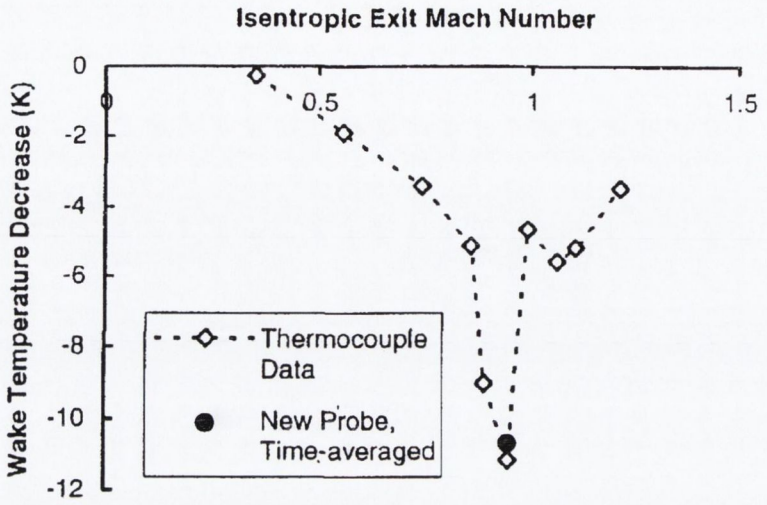

Figure 2.22: Phase-averaged temperature measurements in the Vortical Wake Flow of a Turbine Nozzle Cascade [79]

advection of large coherent vortices, it is reasonable to consider that energy separation may take place in the flow field of the synthetic jet; however the intensity level that might be expected is unknown. Significant effects of energy separation have been noted in other areas of fluid flow, especially for high velocity flows such as those experienced in aerospace applications. Thus, Carscallen *et al.* [79] reported significant energy separation occurring in a wake flow of a turbine nozzle cascade with increasing effects at high velocities; maximum separation was experienced at Mach 0.95 as can be seen in figure 2.22. These temperature fluctuations were found to be a manifestation of Eckert-Weise[6] effect energy separation in the shed vortex street. Results showed that across the wide velocity range tested energy separation was only detectable from a Mach number of 0.4 upwards. Few, if any, synthetic jets researched have even approached velocities of this magnitude, with only applications of flow control reporting maximum velocities of approximately 130 m/s, (Mach 0.38) as described by Gomes *et al.* [1]. While energy separation may occur at and below these velocities, the effect on heat transfer is likely to be negligible for the operational range of a standard synthetic jet designed for a heat transfer application. Consequently, this topic will not be discussed further in this work.

[6]The Eckert-Weise effect occurs when temperatures are suppressed in the centre of the flow and discrete 'hot spots' appear towards the edges of the wake flow

2.5 Synthetic Jet Heat Transfer

As previously asserted, there is little research available that satisfactorily correlates the fluid flow with heat transfer between an impinging synthetic jet and a heated surface. Nevertheless, parameters such as geometric arrangement and novel implementations have been investigated and their influence on heat transfer has been reported. This section reports on such investigations of synthetic jet heat transfer. Data in this area have proven particularly difficult to compare due to the numerous different methods that authors have used to quantify synthetic jet operational parameters. The reporting of standardised parameters such as Reynolds number, dimensionless stroke length and Nusselt number has only been established within this area of research in recent years and it is quite common for previous literature to report in terms of parameters such as jet driving frequency, diaphragm displacement, heat transfer enhancement or relative temperature reduction. While Reynolds number is included commonly in the documented data in one form or another, the omission of stroke length in favour of frequency, a parameter which is more easily measureable, makes it difficult to assess the nature of the flow and hence draw comparisons between various studies. Nevertheless, an attempt has been made and is presented in the following sections.

2.5.1 Motivation for Novel Cooling Systems

Zero-net-mass flux jets have many potential applications and uses in the field of heat transfer, specifically cooling; however the major area of interest recently has been their potential application in the cooling of electronics. Gunther *et al.* [80] presented a comprehensive paper which addresses both the current and future requirements of power dissipation in microprocessors. The authors report that the power dissipation of modern processors has been rapidly increasing along with increasing transistor count, density and clock frequencies. At the same time, there is a growing disparity between the maximum power consumption of a processor and the typical power consumed by that processor; i.e., power consumed while running typical applications. This disparity has resulted in the necessity for the integrated thermal management systems to dissipate and redistribute very high heat fluxes intermittently, a requirement which

continually threatens to exceed system limits. This is particularly important because, as chip power increases, there is a non-linear relationship between the cooling capabilities and the cost of the solution as more complex configurations are implemented. Ranges of achievable heat transfer coefficients for various fluids can be seen in figure 2.23, however any fluid other than air requires the implementation of relatively expensive hardware. This emphasises the importance of developing new methods of achieving the effective, high rates of cooling required by the industry while maintaining or even driving down the respective costs.

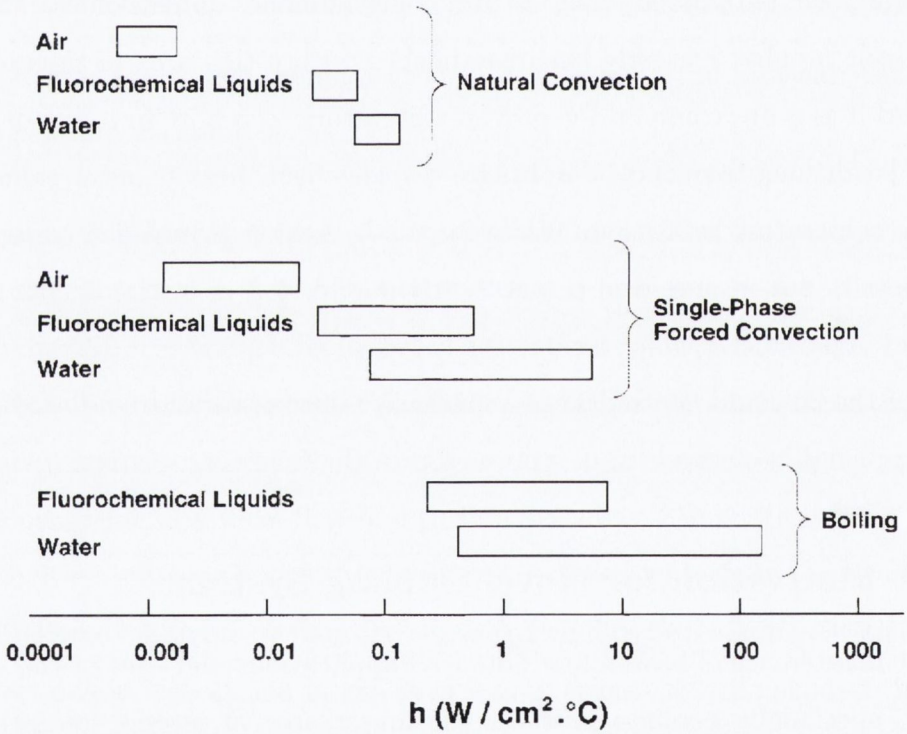

Figure 2.23: Heat transfer coefficients attainable with natural convection, single-phase liquid forced convection and boiling for different coolants. [81]

In the past, advancement in microelectronic systems has developed in accordance with the well-known "Moore's Law" [82] which states that processor speed will double every 18 months, however this must also be facilitated by the availability of adequate thermal management systems. In a review article by Bar-Cohen [10] it was noted that up to as recently as the late-1980's air cooled modules provided cost-effective thermal packaging solutions for the electronics industry. Although the majority of high

performance electronics require some form of forced cooling, the "low-cost" product category, including disk drives, displays, micro-controllers, digital video and audio devices rarely go beyond reliance on buoyancy-induced natural circulation of air, however this is mainly due to cost considerations. Similar cost constraints severely limit the options for battery-operated hand-held products, including devices such as tablet PCs, smart phones and regular mobile phones; in these cases clever use of heat spreaders generally make it possible to cool the required 1-2W integrated circuits. In many current applications the fan-on-sink solution of chip cooling has already reached its limit and more expensive solutions have had to be implemented.

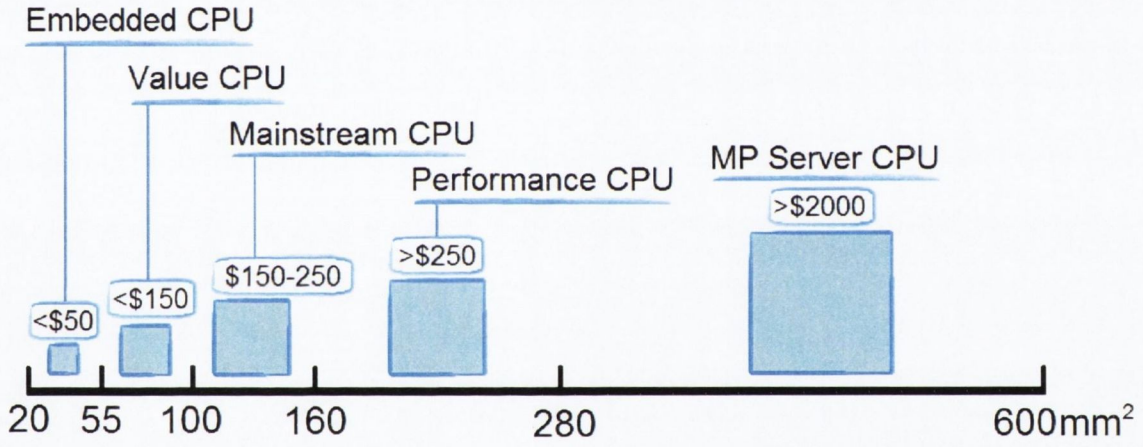

Figure 2.24: Cost and application of processor vs. die size for $45nm$ transistor architecture [83].

Figure 2.24 shows how processor application and cost varies with die size. Since the early 1990's an annual publication has been issued by an independent international committee whose job it is to foresee the future requirements and limitations of the semiconductor industry and also to set goals pertaining to such things as transistor densities and thermal design. In the most recent of these reports entitled *"International Technology Roadmap For Semiconductors"* [84] it has been identified that, with the continual surge in integrated circuit power consumption, the power requirements for high performance processors will rise above $161W$ to a projected maximum of $198W$; this equates to a projected maximum heat flux of $92.5W/cm^2$ by the end of 2011; for a regular sized chip of $214mm^2$. The current maximum thermal design package for a commercially available processor stands at $150W$ for an Intel©Core™Extreme

Processor QX9775. The upper limit of $198W$ was not set by technological constraints; significantly, power will be limited more by system level cooling and test constraints rather than by packaging [85]. In recent years, to accommodate the power requirements of high performance computing, manufacturers have had to continually increase processor die size from a standard of about $80mm^2$ to dies as large as $596mm^2$; this effectively reduces heat flux density in an attempt to achieve more realistic operational temperatures, however this has serious ramifications for the cost of manufacture. Larger dies require larger silicon wafers, the cost of obtaining larger wafers with suitably low defect levels increases disproportionately with size, as is highlighted by figure 2.24. As such, to reduce costs there is a continual drive towards smaller die size and methods of achieving higher levels of heat dissipation. Consequently, improvements in thermal packaging technology are necessary. While the synthetic jet cannot be expected to reach heat transfer rates near $90W/cm^2$, these figures show the magnitude of the challenge facing engineers; serious consideration is required when implementing effective cooling solutions right across the range, from integrated microchips all the way up to multicore processors. Although the synthetic jet may not be the sole solution, it is envisaged that, when implemented on various scales, and in conjunction with other technologies, synthetic jets can provide an efficient and highly effective method of local heat dissipation where required. To achieve this, optimisation is essential; this will only truly be possible once a greater understanding of the relationship between heat transfer, fluid temperature and the flow mechanisms is achieved.

2.5.2 Heat Transfer Characteristics

When considering heat transfer to the synthetic jet there are a number of parameters of particular interest. Stagnation point heat transfer can be a parameter of great importance, as when implementing cooling technologies such as impinging jets the centre of the jet is commonly directed at a location which requires the greatest level of cooling. Although this may seem intuitive, it has been documented that for some configurations of continuous jets it may not coincide with the location of maximum heat transfer [4], which is also an important factor to consider when analysing the

heat transfer characteristics of an impinging jet. Many investigations present a mean Nusselt number value for heat transfer. While this may give a good idea of the average performance of the jet, it lacks the detailed information about local heat transfer coefficients such as regions where heat transfer drops below a specific level and the presence of local maxima and minima. Such information can prove pertinent when it is necessary to obtain certain minimum levels of heat dissipation, especially when working within a limiting thermal environment or packaging configuration.

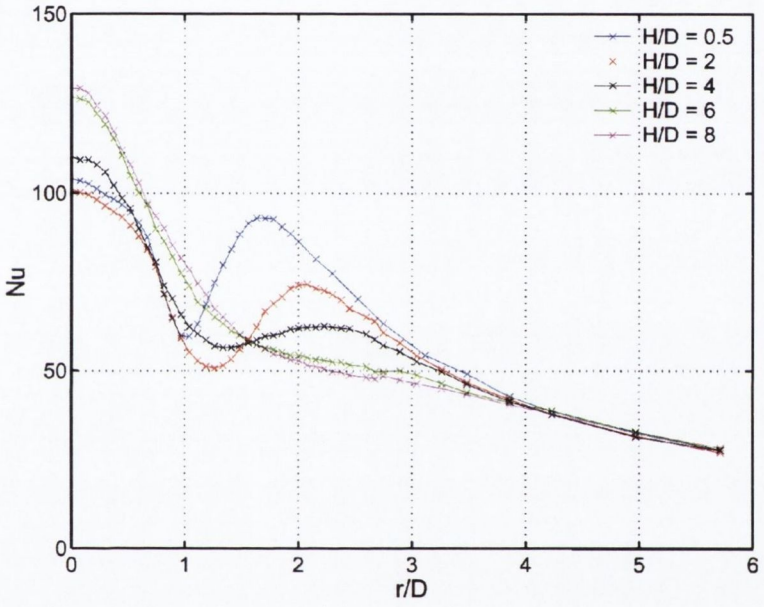

Figure 2.25: Continuous jet heat transfer profiles, $Re = 30000$ [4]

Figure 2.25 shows local heat transfer profiles for a continuous jet of Reynolds number 30000 impinging normal to a heated surface at a number of axial spacings. At larger heights above the surface the peak heat transfer typically occurs at the jet's geometric centre, or stagnation point. The trend has been described by Gillespie *et al.* [28] as Gaussian, where the heat transfer then goes into a steep decline monotonically or even exponentially with increasing radial position. This is what is intuitively expected for impinging jets and in general is the case. At lower spacings it is quite common to observe secondary peaks in heat transfer. Referring back to figure 2.1, as the potential core impinges upon the plate a high-pressure, low-turbulence, stagnation zone is formed, as this flow changes direction and travels along the wall a transition to turbulence is experienced, causing the observed secondary peak in heat transfer.

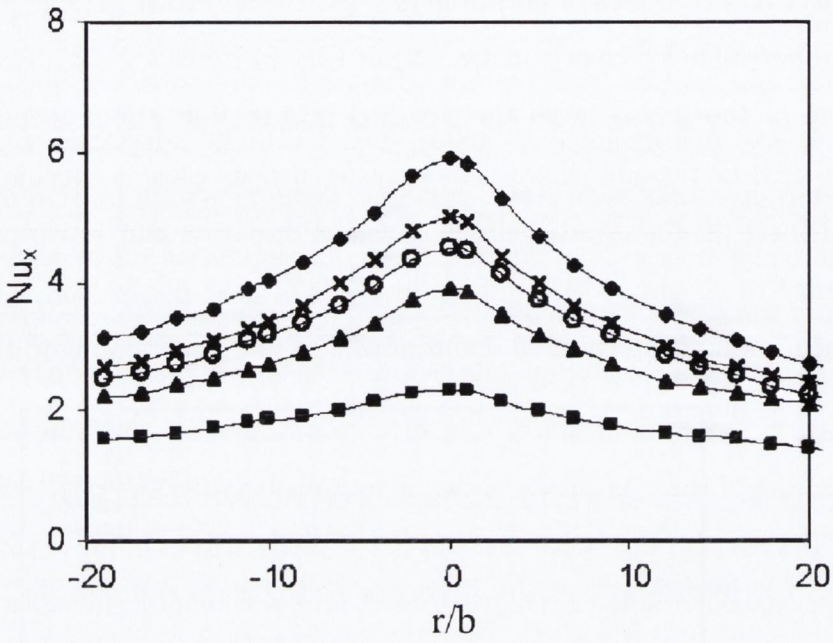

Figure 2.26: Local Nusselt number distributions for a 2D synthetic jet; $H/b = 3.6$, $Re =$ ■108, ○254, ▲309, ×367, ♦396 [28].

Figure 2.26 shows the radial variation in local Nusselt number for a two dimensional impinging synthetic jet for Reynolds numbers varying from 108 to 396, height above impingement surface of $H/b = 6$ and dimensionless stroke lengths varying from $L_0 = 8.1b$ to $10.3b$. While these radial profiles may look quite similar to those produced by a conventional continuous jet at similar spacings, the factors influencing local Nusselt number are far more complex. For normal impingement, continuous jets have two primary driving parameters affecting the heat transfer profile, namely the Reynolds number and impingement height. Not only is heat transfer for a synthetic jet highly influenced by stroke length also, but confinement plays a much greater role than in the case of the conventional jet. The very periodic nature of the synthetic jet means there are many influential factors interacting together when considering a heat transfer profile. Collectively, these not only change the magnitude of the profile but also aspects such as the slope, localised peaks and even the minimum heat transfer.

A number of studies have been undertaken into heat transfer to an impinging synthetic jet. Although certain trends are common to these studies, some inconsistencies in the reported findings highlight this need for further research into this area. Li and

Source	Jet type	Instrumentation (D_s = spatial resolution)	Re	H/D	Nu correlation in normalised form (Eq. 2.23)
Chaudhari *et al.* [44]	sharp orifice (R,C,T)	heater-average $D_s \approx 3.8D$	1150–4180	3 – 25	$0.203 Re_{U_0}^{0.792} Pr^{0.333} (H/D)^{-0.63}$ (+)
Chaudhari *et al.* [88]	sharp orifice $(2D,C,T)$	heater-average $D_s \approx 3.8D$	950–4000	3 – 25	$0.086 Re_{U_0}^{0.912} Pr^{0.333} (H/D)^{-0.56}$ (+)
Valiorgue *et al.* [89]	sharp orifice (R,C,Q)	IR thermography $D_s \approx 0.03D$	500–2150	2	$2.182 Re_{U_0}^{0.32} Pr^{0.4}$ (for $L_0/H > 2.5$)
Persoons *et al.* [90]	sharp orifice (R,C,T)	const. temp. hot-film $D_s < 0.02D$	500–1500	2 – 16	$0.168 Re_{U_0}^{0.686} Pr^{0.4} f(H)$ (for $L_0/H > 2$)

Table 2.2: Overview of stagnation Nusselt number correlations for a synthetic jet, impinging perpendicularly onto a flat surface. R = axisymmetric, 2D = two-dimensional, C = confined, T = isothermal heating, Q = constant heat flux $^+$ These correlations represent averages over an isothermal heater surface of about $40 \times 40\ mm^2$. Table as from Persoons *et al.* [90].

Zhong [86] presented a study of the heat transfer characteristics of a round synthetic jet impinging normal to a surface which approximates a uniform wall flux boundary condition. It was found that, for a nozzle height above the plate of $H/D = 8$, increasing the diaphragm oscillating amplitude (effectively increasing both Reynolds number and stroke length) increased the heat transfer to the jet at the geometric centre. Below this height there is a slight decrease in heat transfer for the same increments. Li and Zhong [86] also identified an optimal jet to surface spacing for this particular jet at $H/D = 14$ for all diaphragm oscillation frequencies; streamwise velocity magnitude and power spectra data presented in the paper suggest that this spacing corresponds to the streamwise location where the jet flow becomes fully turbulent. Similar findings have been well established for conventional continuous jets; for example, the authors Ashforth-Frost and Jambunathan [87] stated that the point of maximum heat transfer was observed to coincide with the end of the potential core, where the absolute turbulence level begins to increase and to compensate for the loss in axial momentum. For the synthetic jet, the transition to local turbulence is difficult to establish due to its periodic nature. As such the development of new analytic techniques may be needed to identify more clearly the real onset of turbulence in the synthetic jet.

Black *et al.* [3] investigated a round synthetic jet using a heat transfer module

which simulated the cooling required in electronic packages. It was found that the heat transfer effectiveness decreases at both small and large nozzle-to-surface distances, and that for their experimental setup an optimum spacing occurred near $H/D = 8$, a result that disagrees with the finding of Li and Zhong [86], at $H/D = 14$, but is in good agreement with the findings of a large number of other authors including Kercher *et al.* [6], Arik [33] and Pavlova and Amitay [8]. Black *et al.* stated that at large spacing the decrease in heat transfer is related to the decrease in the jet centreline velocity and to the reduced stagnation pressure at the centre of the impingement surface. This result was confirmed in the same year by Smith and Glezer [46] who observed that the jet mean centerline velocity increases until it reaches a local maximum at $x/H = 7$ and then decays monotonically. Black *et al.* found that at small H/D there was a noticeable decrease in heat transfer, this was attributed to recirculation of warm fluid back into the synthetic jet; these results are in accordance with the findings of a number of authors [34, 6], with Kercher *et al.* [6] confirming this effect with smoke visualisations. While there is no clear reason why there is such variation in the H/D at which maximum heat transfer occurs, one possible reason for discrepancies may be attributed to the type of thermal boundary conditions implemented in the tests, as McGuinn *et al.* [34] and Black *et al.* [3] used a constant wall temperature impingement surface whereas Li and Zhong [86] used constant wall heat flux (which may not suffer from thermal saturation to the same extent at lower axial spacing). Black *et al.* [3] concluded that synthetic jet modules are capable of providing localised cooling and also have great potential for the redistribution of heat within sealed enclosures. Kercher *et al.* [6] compared the heat transfer performance of both a single and a multi-orifice synthetic jet driven at resonant frequency to that of various fan-and-sink combinations. Kercher *et al.* provide a qualitative comparison to conventional impinging jet flow by comparing heat transfer results to previous studies into continuous jets. For single circular continuous air jet impingement Nusselt Number can be expressed by:

$$Nu \propto Re^{a} \tag{2.22}$$

where the characteristic exponent $a = f(r/D, H/D)$ is typically in the range from

0.5 to 0.8 for conventional jets. For a synthetic jet when situated at the optimum height above the impingement surface, the characteristic component was found to be approximately 0.2. A table of experimentally acquired heat transfer correlations from Persoons *et al.* [90] is presented in table 2.2 where the original Nusselt number correlation is reoriented in the standard formulation:

$$Nu_0 = cRe^m Pr^n (H/D)^p \tag{2.23}$$

where m, n and p are correlation exponents extrapolated from experimental data. The findings of Persoons *et al.* [90] compare well with other synthetic jet studies by Chaudhari *et al.* [44, 88], particularly with the Reynolds exponent ($m \cong 0.686$) and at large axial spacing ($Nu_0 \propto (H/D)^{-0.487}$). The authors identify four heat transfer regimes dependent on stroke length and axial spacing with that of the largest stroke length generally providing the greatest level of heat transfer, although a local maximum is achieved at a lower stroke length. The authors state that operating at the inherently lower operational frequencies associated with some of the larger stroke lengths can prove inefficient for certain actuators with high resonant frequencies, as such it may be possible to take advantage of the local maxima experienced at a smaller stroke lengths.

Gillespie *et al.* [28] presented a paper on convective heat transfer to an impinging synthetic jet with slot geometry in which three different regimes of near, intermediate and far-field flow were presented. Similar results to those presented by Black *et al.* [3] and Kercher *et al.* [6] were found regarding re-ingestion of the flow in the near-field and diminished velocity in the far-field. In the intermediate-flow regime the increased jet velocity coupled with a more effective mixing with ambient air produced improved local heat transfer rates. Average Nusselt numbers were maximized when the dimensionless plate spacing was between 14 and 18; it is proposed that this deviation from the majority of literature is due to the slot geometry. As the jet evolves it has a tendency to converge along the y-axis with increasing distance from the slot exit, as can be seen in figure 2.27 (*a*), and diverge along the x-axis as in figure 2.27 (*b*).

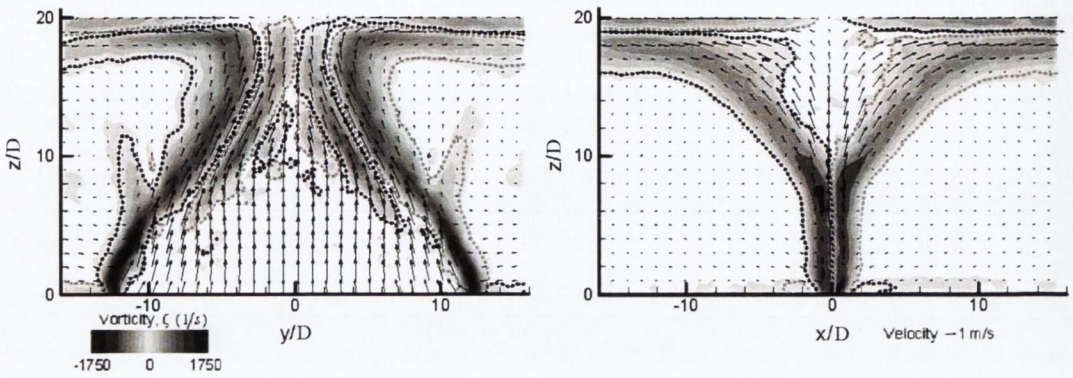

(a) major axis

(b) minor axis

Figure 2.27: Time averaged velocity field and spanwise vorticity concentrations for a slot jet impinging at $H = 20b$, $Re = 400$, $L_0 = 9.96b$ [28].

As such the "focal point" where the jet has maximum centreline momentum appears at a greater dimensionless distance from the nozzle exit than it does for a round orifice. Spectral analysis of the jet centreline velocity presented by Gillespie *et al.* [28] revealed the rapid evolution of small-scale motions within the jet, indicating strong mixing and producing high turbulence that results in thermal dissipation; these are key factors in applications required for small-scale heat removal from solid surfaces. Significantly, Gillespie *et al.* found that flow from the synthetic jet is fully turbulent even at Reynolds numbers far below the critical Reynolds number for steady jets and that the fully turbulent nature of the jet at low velocities can be exploited when small-scale heat transfer is desired.

The efficiency and convective mechanism of cooling a constant heat flux surface by an impinging synthetic jet was investigated by Pavlova and Amitay [8] in a study which examined both a high frequency of $1200Hz$, and a low frequency of $420Hz$. It was found that for a constant Reynolds number the higher frequency jet (and hence smaller stroke length) achieved greater heat transfer for $4 \leq H/D \leq 11$ before degrading rapidly. In contrast, the lower frequency jet did not reach as high a peak in heat transfer, although it did maintain its maximum level up to $H/D \approx 11$. The authors state that this behaviour is related to the wavelength of the coherent structures asso-

ciated with the synthetic jets, i.e. the stroke length. When the synthetic jet is driven at the low operating frequency, the vortex rings impinge on the surface individually; thus, these large-scale coherent structures are responsible for the enhanced heat removal (compared to a continuous jet). At the high operating frequency, the vortex rings merge and break into smaller secondary structures before reaching the surface; hence, the heat removal is enhanced by mixing of smaller scale structures, this also results in the loss of momentum at greater heights above the plate. An investigation undertaken by Travnicek *et al.* [91] into impinging flow mass transfer for a novel annular synthetic jet came to similar conclusions with respect to the effect of frequency on jet flow. The authors found that at lower frequencies, the vortices generated by individual outflows retain their identity for a considerable distance. At higher frequencies, a rather rapid break-up of the vortices takes place. In most cases investigated, at low excitation frequencies, the flow field was dominated by a large recirculation bubble of a separated flow, originating at the annulus, and reaching up to the impingement wall. At the higher excitation frequencies, the character of the flow field was found to be different, the bubble collapsed into a relatively small one right at the nozzle body wall. The transition between these two types of flow was attributed to what was described as a spectacular instability.

It is worth noting that in the investigation by Pavlova and Amitay [8] heat transfer to the synthetic jet was reported to be up to three times greater than that of the equivalent continuous jet; this finding is at odds with that of a number of other authors. Farrelly *et al.* [7] undertook a comparison of local heat transfer characteristics between synthetic and steady jets at low nozzle to surface spacing. It was concluded that while the performance of the equivalent synthetic jet may approach that of a steady jet at some of the larger spacings tested, the synthetic jet's performance suffered significantly at closer spacing due to fluid recirculation caused by the high degree of confinement, an effect which was previously documented by McGuinn *et al.* [92].

2.5.3 Local Fluid Temperature Measurement

While the majority of studies undertaken into heat transfer to an impinging synthetic jet focus primarily on the effects of jet velocity and turbulence intensity, another very important parameter often overlooked is local fluid temperature. A common way of increasing heat transfer from a heated surface is to increase the velocity of the fluid flowing across that surface. Similarly, an equivalent increase in heat transfer can be achieved by increasing the temperature differential between the heated surface and the cooling fluid, with the converse of this also holding true. It is usually found that, for a fully developed jet, once the jet has impacted upon the surface there is a significant decrease in jet velocity with increasing radial distance; a corresponding decrease in heat transfer is also experienced. While this may well be an intuitive relationship, this decrease in heat transfer can also be attributed to an increase in the local temperature of the fluid. As heat is transferred from the surface to the fluid the temperature differential is also decreased, thereby reducing the potential for further heat transfer.

Although fluid temperature plays just as large a role in convective heat transfer as fluid velocity, few papers, if any have been published investigating the effect it has on heat transfer to the impinging synthetic jet; as such there is a need to obtain data revealing the extent of the influence that local fluid temperature has on heat transfer. Research into methods of obtaining high frequency, local air temperature measurements was conducted as far back as 1947 when Corrisin [93] published a thesis on what was referred to at that time as extended applications of hot-wire anemometry. Today this technique is better known as cold-wire anemometry and is described at length in section 5.9. Corrisin showed that the cold-wire technique was capable of acquiring local fluid temperature data with high temporal frequency and spatial resolution by applying the principles developed for the operation of hot-wires. Corrisin [93] went on to perform a detailed investigation of the flow in a slightly heated, round, turbulent air jet where it was found that the lateral rate of heat transfer in a turbulent shear flow was significantly greater than that of momentum transfer. The author also noted that, for the same jet, both velocity and temperature fluctuations were of the same order of magnitude. Torkelsson [94] presented a paper outlining the implementation of

a type of resistance thermometer for measurements of fluctuating and mean temperature which was capable of operating in high gradient thermal boundary layers. The thermometer was based on conventional cold-wire techniques and was implemented using a probe with three prongs bridged by two platinum-plated tungsten wires of different length. The advantage of this unique configuration was that the error caused by the temperature difference between the tip of the prongs and the gas was effectively reduced by an order of magnitude. However, a significant trade-off exists in that, at $4.91mm$ in length, the probe is over twelve times the length of a standard moderen Dantec $55P31$ temperature probe, resulting in a temperature reading averaged over a much larger area which may not be suitable for the type of small scale, high frequency temperature fluctuations associated with small diameter and high velocity jets. Han and Goldstein [78] also employed an alternative two-wire technique in order to measure local fluid temperature fluctuation caused by energy separation in a continuous jet. Two identical $5\mu m$ diameter tungsten wires were operated parallel to one another, at a separation of $1mm$ and at two different overheats. By knowing the velocity of the flow and using King's Law, outlined in section 5.5, the total temperature of the flow was determined. Significantly, Han and Goldstein [78] were able to show that the dominant frequencies present in the temperature fluctuation spectrum coincided with those in the velocity spectrum. Although this method was proven successful at measuring temperature fluctuations in a free jet, its operation within a boundary layer for an impinging jet may prove difficult. Due to the large velocity gradients present within a boundary layer it would be incorrect to assume that both probes experience the same velocity; as such, fluid temperature cannot be calculated using this method.

A number of other authors including Burattini and Djenidi [95] and Drobniak *et al.* [96] have combined both local fluid velocity and temperature measurements to aide with the analysis of jet flow. Both authors implemented constant current anemometry in conjunction with a fine metal wire to obtain temperature measurements and three component hot-wire anemometry to obtain velocity measurements. Burattini and Djenidi [95] used a custom made Wollaston wire[7] to measure temperature; veloc-

[7]The Wollaston wire was invented in the 19th century. Consisting of a very fine silver coated platinum wire less than $0.01mm$ in diameter it is manufactured by drawing it through successively

ity was measured using two hot-wire probes, one single and one dual element, with the dual being of x-wire configuration to measure flow velocity in U and V directions. These instruments were used in the analysis of a heated, free, round jet with obstructing grids at the nozzle exit. Mean and fluctuating temperature data were used to analyse the behaviour of the jet; temperature spectra revealed a $-5/3$ slope indicating viscous dissipation present due to turbulent flow. These temperature data are relevant in revealing the actual interaction and mixing of the heated and ambient fluids and hold relevance in the context of the spreading of contaminants. Drobniak *et al.* used a commercially available $1\mu m$ Dantec P31 probe, similar to the one used in the present work, to obtain local temperature data; a triple-wire gold-plated Dantec 55P91 probe was also used to acquire velocity data. This setup resulted in a spherical measurement volume occupied by the wires of approximately $2mm$ in diameter. This setup was implemented in a free, round jet, heated to $40°C$ above ambient temperature. Significantly, the author concluded that although there was a mutual phase relation between the velocity and temperature data for both oscillatory and random components, the intensification of radial heat transport was much greater, especially within the area dominated by the coherent motion. This was not found to be the case for the longitudinal direction, where no significant changes in the presence of coherent structures were found.

Heist and Castro [97] described a technique for determining turbulent heat flux in flows with high levels of turbulence and temperature fluctuation using a combination of three component LDA and a $5\mu m$ cold-wire anemometer. Experiments were performed within a heated, turbulent boundary layer where it was found that no limitations were imposed by high turbulence intensity or instantaneous flow reversals which commonly prove problematic in such a setup. To minimise the effects of spatial separation and blockage of the cold-wire it was concluded that separation distance between the cold-wire and the LDA measuring volume should be below about seven Kolmogorov[8] length scales.

smaller dies. For most uses the silver cladding is etched away leaving the platinum core exposed.

[8]The Kolmogorov scale is a measure of the smallest eddies that are present in a turbulent flow at high Reynolds number.

There is very little research available documenting local fluid temperatures for impinging flows, however there are a number of papers which present results combining both local fluid temperature and heat transfer. Both Rydholm [98] and Jovanovic *et al.* [99] presented papers documenting the ejection of jets from a hole in a planar surface into crossflows of a different temperature. In the paper by Rydholm [98] local mean fluid temperature measurements were used to document the difference in position between the velocity wake of the jet, measured by LDA, and the actual core position, measured by a high precision thermocouple. Rydholm observed that a greater heat transfer magnitude is present farther downstream of the jet due to reduced turbulence; this lower level of turbulence reduced mixing allowing the cooler core maintain coherence to a greater distance from the orifice, resulting in the cooler fluid effecting a greater level of heat transfer due to the larger temperature differential. Jovanovic *et al.* [99] observed a similar phenomenon. Using liquid crystals to obtain heat transfer measurements from the planar surface in crossflow in combination with PIV measurements and local temperature measurements acquired using a thermometer, Jovanovic *et al.* showed that increased turbulence resulting from hole imperfections resulted in lower local heat transfer, but higher overall heat transfer was observed due to the mixing of the jet with the ambient fluid. Both papers stop short of taking fluctuating heat transfer measurements, however it is likely they would contribute greatly to the overall understanding of the type of flow mechanisms involved in heat transfer. None of the papers reviewed here provide time-resolved or simultaneously acquired velocity and temperature data for impinging flows, let alone include local heat flux measurements. As such, there is a real need to investigate more closely the cause and effect between local surface heat transfer and the local fluid velocity and temperature to which it is attributed.

2.5.4 Orifice Geometry Effects on Synthetic Jet Heat Transfer

Although the performance of different types of orifice geometry has been researched and documented, it is still the case that little information is available comparing the

influence of these geometries on the resulting heat transfer. Throughout the vast quantity of literature published on synthetic jets there are two dominant types of orifice geometries; circular with varying diameter D, and rectangular or slot, with varying aspect ratio $b : w$, where b and w are slot length and width respectively. One recent paper by Chaudhari *et al.* [44] investigates the effect of orifice geometry on heat transfer from a heated surface. Both circular and rectangular orifices with various aspect ratios and identical hydraulic diameters are investigated. Significantly, for $H > 5D$ a square geometry outperforms the equivalent circular and rectangular geometry, however for closer spacing a rectangular orifice of aspect ratio $3 < b/w < 5$ outperforms all others. It is proposed that the increased performance of the square geometry compared to that of the circular nozzle at high axial spacing is down to the larger entrainment rate resulting in a significant increase in the mass flux at the same distance from the nozzle. The effect of square vs. circular geometry was numerically modelled by Wu and Leschziner [51]. Although no heat transfer data were presented it was shown that a square jet of the same hydraulic diameter produced significantly higher levels of turbulence due to the increased straining at the corners of the orifice; this might also contribute to the increase in heat transfer observed by Chaudhari *et al.* [44]. It might be expected that this effect should be enhanced with an increase in aspect ratio, but this is not necessarily the case. Chaudhari *et al.* surmise that while the slot shaped orifices can achieve a higher degree of heat transfer at low axial distances, due to the larger entrainment rate, the vortex pair from a rectangular orifice is less stable than that of a square or circular vortex. Thus, breakdown occurs much sooner than for the other geometries resulting in a loss of momentum and a drop in performance at smaller axial distances than for circular nozzles.

A number of more unusual types of orifice geometries have been investigated by other authors. Travnicek and Tesar [13] tested the heat transfer performance of an annular impinging synthetic jet for a fixed power input and across a range of frequencies. As both Reynolds number and stroke length are highly dependent on the frequency response of the acoustic speaker used to drive the jet and also on the chamber geometry, it is likely that both parameters varied significantly across the testing range. Two distinct types of flow resulting in contrasting heat transfer profiles were identi-

fied. The first type of flow appeared at the lower driving frequency which consisted of relatively large stroke lengths; this flow impinged on the surface and produced, as expected, two peaks in heat transfer consistent with the annular geometry. Smoke visualisations identified a small recirculation bubble right at the nozzle body wall. At the higher driving frequencies and low impingement height the heat transfer profile was significantly different, with a single peak occurring at the centre. The authors suggest that the change in flow structure and in heat transfer characteristics is associated with stability, bistability and hysteretic behaviour. Travnicek *et al.* went on to investigate a further, more complex nozzle in a two part paper [91, 100]. This system consists of a combined central and annular nozzle which operates on both actuation strokes, effectively achieving twice the fluid displacement for the same work input. Although no heat transfer evaluation was reported it was concluded that at large axial distance the jet performance was comparable to that of a conventional fully developed turbulent jet.

2.5.5 Novel Applications

While a vast amount of research has been published on the synthetic jet, only a small minority of it is related directly to the analysis of heat transfer and the mechanisms by which it is effected. The majority of papers investigating heat transfer address unique implementations, many with a particular application in mind, and assess them on their own merits. A number of authors have investigated the integration of synthetic jets into heat sinks in order to increase their performance, these authors include Mahalingam *et al.* [101, 102], Beratlis and Smith [103] and Gerty *et al.* [104]. Many of these papers boast impressive results and show that synthetic jets have a promising future in the cooling of electronics. In fact Mahalingam *et al.* [102] showed that with the combined use of both a synthetic jet and fan on a heat sink, a very significant reduction in ambient noise is achievable while effecting the same level of heat transfer; similar results were arrived at by Campbell *et al.* [11] for a combined setup. These results are without doubt important in proving the technology in real life applications, but do not elucidate the fundamental nature of the jet's performance. Other authors such

as Kercher *et al.* [6], Black *et al.* [3] and Wang *et al.* [105, 106] integrated the synthetic jet directly onto the circuit board. Again these papers may validate the potential application of the jet but many of them are merely optimising one particular jet in a specialised application. It is for this reason that the synthetic jet needs to be investigated in universal terms; a fundamental understanding needs to be achieved so that it can be optimised before implementation in any potential application.

Pavlova *et al.* [31] used a synthetic jet with a slot geometry operated at a 30° angle at the side of an atomised spray to control the spray behaviour so as to obtain flow vectoring. While the exact flow from the angled synthetic jet was not documented it was shown to be successful at significantly altering the vector of the atomised spray. Ritchie *et al.* [107] investigated a similar application where nine circumferentially placed synthetic jets were used to enhance mixing in a continuous coaxial jet. This application proved highly effective in manipulating both the inner and outer mixing layers of the annulus.

2.6 Analytical Techniques

Many different analytic, decompositional and interpretive techniques have been employed over the years in the pursuit of gaining a better understanding into the fundamental mechanisms which govern the operation of the synthetic jet. There is a continual requirement to both update current methods and develop new techniques in order to analyse and interpret the vast amounts of data commonly recorded. As technology has advanced, new experimental instrumentation and computational processing power have delivered increasingly sophisticated computational fluid dynamics software, and more accurate, higher resolution, experimental data. Extraction of the relevant information and trends can prove quite challenging; as such, the selection of a suitable method of analysis can reveal information that may otherwise remain unseen.

2.6.1 Spectral Analysis

The main purpose of spectral analysis is to break a discrete-time signal down into its component frequencies and estimate the signal power distributed throughout the spectrum. Spectral analysis and correlation techniques were originally developed to help with the interpretation of recorded signals so as to provide insight into the systems that generate them. These methods have been employed across a wide range of disciplines including communications, geophysics, medicine and vibration analysis. The most efficient method of applying spectral analysis is through the use of the fast Fourier transform (FFT). First used by Gauss in 1805 [108] the FFT was rediscovered in the 1960s by Cooley and Tukey [109], and since then has seen widespread use throughout the scientific community.

The very first use of spectrum analysis in the field of synthetic jets was by the pioneers of the synthetic jet, Ingard and Ising [36]. The authors presented a spectrum of the pressure wave transmitted through the orifice plate. It was noted that while the fundamental excitation frequency was the dominant harmonic, there were also overtones present, predominantly of odd order. The presence of these harmonics was attributed to the non-linearity of the orifice. Although an oscillating pressure gradient of specific frequency is fundamentally required for the formation of a synthetic jet, it is the case that since this initial publication, spectral analysis has played a surprisingly minor role in the analysis of the synthetic jet.

Using measurements acquired with laser Doppler anemometry (LDA) James *et al.* [57] presented spectra for the centreline velocity of a round turbulent jet produced by an oscillating diaphragm at one diameter from the orifice. Spectral peaks were observed at integer orders to the driving frequency, similar to those seen in the pressure measurements by Ingard and Ising. Unusually, James *et al.* also documented a sub harmonic, below the excitation frequency; this was attributed to the coupling of the natural resonant frequency of the diaphragm and the third harmonic of the excitation frequency. This phenomenon has not been observed in any other literature to date. Smith and Glezer [46] also presented spectra of jet centerline velocity for a free two dimensional synthetic jet acquired using hot-wire anemometry, seen in figure 2.28.

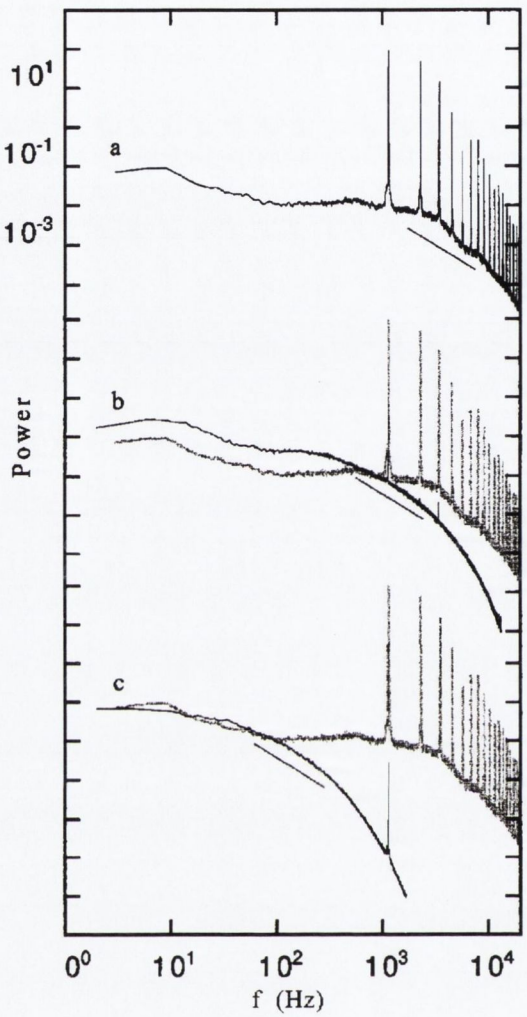

Figure 2.28: Power spectra of the centerline velocity for a free two dimensional synthetic jet. Each curve is successively displaced 7 decades: (a) $x/b = 5.9$, (b) $x/b = 19.7$, (c) $x/D = 177.2$; $Re_{U_0} = 383$, $L_0 = 10.1b$. [46]

Near the jet exit, 2.28 (a), the spectrum is once again dominated by the excitation frequency of the vortex pairs and its higher harmonics; unlike the jet investigated by James *et al.* no frequency peaks below that of the fundamental frequency are evident across any axial spacings, although it is quite evident that with increasing axial distance a significant increase in this spectral band occurs; this is indicative of the development of the jet flow and a decay of the vortex pairs. This decay is also confirmed by the rapid attenuation of the spectral peaks and a reduction in the total turbulent kinetic energy. Smith and Glezer [46] argue that following the time harmonic formation of discrete vortex pairs, a transfer of energy occurs from

these large scale structures, resulting in a developed flow through coalescence. The mean flow cascades down to smaller scales, and hence higher frequencies, at which dissipation ultimately occurs; a similar conclusion was also arrived at by Gillespie *et al.* [28]. A slope of approximately $-5/3$ evident in figures 2.28 (*b*) and (*c*), suggests the presence of an inertial subrange[9] which is limited by the low Reynolds number of the flow, this has been observed by a number of other authors, [30, 37]. Similar results were presented by Li and Zhong [86] but for an impinging synthetic jet; like the free jet, results also showed the attenuation of the jet harmonics with increasing axial distance. While the same transfer of energy from the driving frequency to lower frequencies was clearly visible, the results differed to those of Smith and Glezer [46] in that there were no discernable peaks at the formation frequency beyond $H/D = 10$, whereas figure 2.28 (*c*) shows remnants of the excitation frequency at $x = 177.2D$. This rapid attenuation of the driving frequency experienced by Li and Zhong [86] may well be as a result of the deceleration and subsequent degradation of the flow caused by the immediate presence of the impingement surface. The authors conclude that a fully turbulent flow is established when the jet loses its periodicity, and both the peak, and mean, velocity are almost identical at the same location. Gillespie *et al.* [28] also presented velocity spectra at various axial distances; results showed that similar trends to those mentioned above were present. Gillespie *et al.* [28] note that, with the spectral decay experienced at the formation frequency and its harmonics, an increase in the magnitude of broadband high frequency components is evident, manifesting in a slope of $-5/3$. This indicates both viscous dissipation and a greater level of small scale mixing, producing the type of flow which is ideal for thermal dissipation and heat removal from solid surfaces.

More recently the authors Tesar and Kordik [110] undertook an investigation into the character and structure of a free synthetic jet which employed spectral analysis as

[9]Inertial subrange refers to an intermediate range of turbulent scales or wavelengths that is smaller than the primary energy-containing eddies, but larger than the viscous eddies. In the inertial subrange, the net energy coming from the energy-containing eddies is in equilibrium with the net energy cascading to smaller eddies where it is dissipated. Thus the slope of the energy spectrum in this range remains constant.

the primary investigative technique. A definite change in the character of the velocity spectra confirmed the existence of a phenomenon which was observed to occur at the axial distance of 50 diameters from the jet exit. The phenomenon identified a change in the frequency spectra as the flow transitioned from a regime dominated by coherent vortical structures into one dominated by stochastic turbulence. Although no operational stroke length was reported the authors stated that a jet $4mm$ in diameter was operating at a Reynolds number $Re_{U_0} = 2920$ and frequency of $f = 30Hz$, as such the stroke length can be calculated at $L_0 = 42D$ which is generally considered to be quite large. The authors do not go on to validate their findings at other operational parameters but do state that it is necessary to perform additional investigations under different conditions to gain confidence in these findings.

No authors reviewed in this thesis have presented spectra of surface heat flux, this may be due to the difficulty in implementing instrumentation with sufficiently high spatial resolution and frequency required to perform such measurements. Consequently, there are no known spectral heat flux data present for the synthetic jet. Scholten and Murray [111] did, however, present time-resolved, simultaneous, heat transfer and velocity data for a staggered tube array. Suitably high frequency heat flux data ($3200Hz$) was measured using a hot-film sensor in conjunction with a constant temperature anemometer (CTA) while the velocity measurements were obtained with laser Doppler anemometry (LDA). Significantly, both heat flux and velocity signals showed peaks at the same frequencies corresponding to vortex shedding; good correlation between the heat flux and velocity was found at these frequencies. O'Donovan and Murray [112] also presented simultaneous heat transfer and velocity data, but for an obliquely impinging continuous air jet. The authors showed that good correlation existed between velocity and heat flux, more so for velocity normal to the impingement surface than for radial velocity. Maximum coherence was consistently observed at frequencies corresponding to vortex rollup and vortex pairing.

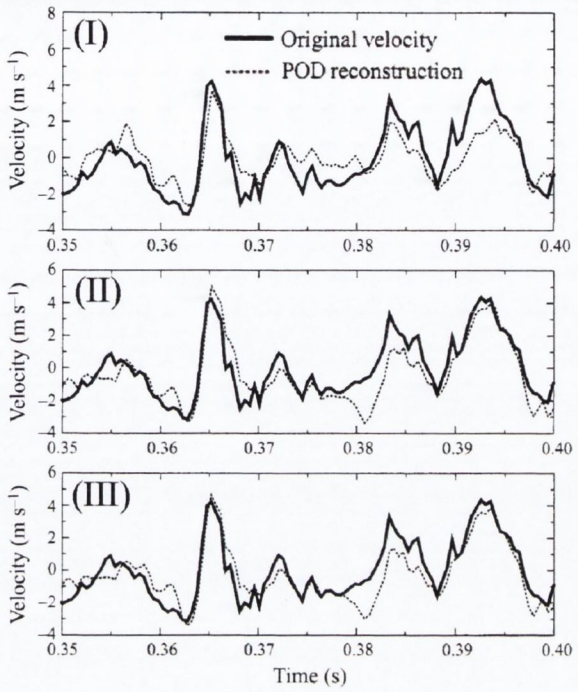

(a) POD reconstruction of the instantaneous velocity in a mixing layer for (i) the first POD mode, (ii) the first two POD modes and (iii) the first three POD modes [113].

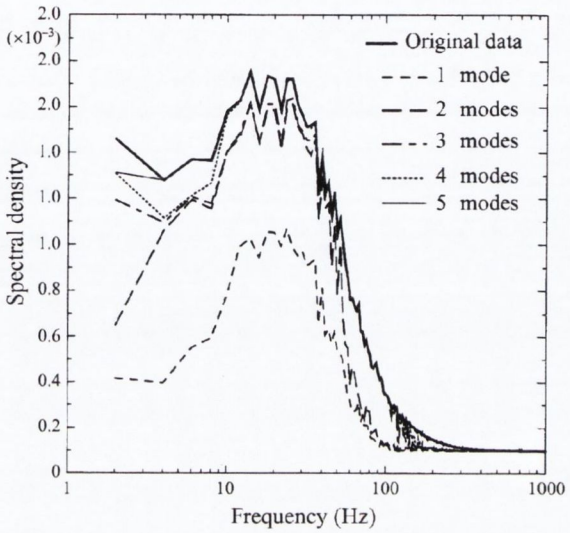

(b) POD reconstruction of the spectrum in the mixing layer for the first five POD modes [113].

Figure 2.29: POD reconstruction of time-resolved velocity data and velocity spectra for a free continuous jet; $x/D = 3$, $r/D = 0.54$, $Re = 80000$

2.6.2 Proper Orthogonal Decomposition

Proper orthogonal decomposition (POD) also known as Karhunen Loève expansion and principal components analysis is a form of low order modelling which has its origins in signal processing. It has been used for a wide variety of applications from thermal chemical processing to derivation of reduced-order dynamical models. Currently POD is most commonly used in the analysis of fluid flows measured by PIV. While the mathematics behind POD prove to be quite complex the objective is to seek out and isolate most energetic fluctuations in a vector field. This is achieved by defining the proper orthogonally decomposed basis functions, $\varphi_i(x,t)$, by the maximisation of their normalised mean-square projection on the velocity vector:

$$\frac{\left\{\int u_i(x,t)\varphi_i^*(x,t)dxdt \int [u_j(x',t)\varphi_j^*(x',t)]^* dx'dt\right\}}{\int \varphi_l(x,t)\varphi_l^*(x,t)dxdt} = \lambda \tag{2.24}$$

where the curly brackets represent resemble averaging and $*$ complex conjugation. By normalising the projection in this way any amplitude dependence on the resulting function is eliminated, thereby emphasising the degree of the projection. The calculus of variations is used to maximise λ with the result being a type of Fredholm integral eigenvalue equation:

$$\int R_{i,j}(x,x',t,t') = \varphi_j(x',t')dx'dt' = \lambda\delta_i(x,t) \tag{2.25}$$

where the symmetric kernel of this equation is the two point correlation tensor:

$$R_{i,j}(x,x',t,t') = \langle u_i(x,t)u_j(x',t')\rangle \tag{2.26}$$

For problems such as vector fields which can be considered statistically inhomogeneous fields containing finite total energy the solution to equation 2.24 is governed by the eigenfunction expansion theorem, also known as the Hilbert-Schmidt theorem of linear integral equations.

By implementing these equations time resolved POD enables the breakdown, or decomposition, of the flow field by isolating, in decreasing order of magnitude, the most energetic, coherent structures. As a result it is possible to decouple the small-scale turbulence, commonly hidden in mixing layers and periodic flows, from large-scale vortical structures and their spatial and temporal evolution. Traditionally, the acquisition frequencies of most PIV systems have not been large enough to resolve the temporal evolution of the flow structures required to effectively employ POD; ideally the acquisition frequency should be in the kilohertz range. This is especially true for fine-scale turbulence, which typically exists on a much smaller spatial and temporal scale than traditional PIV systems can accommodate. In the past number of years both PIV hardware and POD analysis techniques have advanced to a stage where both can operate on a complimentary level.

While POD can be a very powerful analysis tool when implemented correctly, it is still an interpretive technique to be used at the discretion of the author to help

POD mode	Mode energy (%)	Summed energy (%)
1	68.5	68.5
2	14.4	82.9
3	10.3	93.2
4	2.8	96.0
5	3.6	99.6

Table 2.3: Percentage of energy contained in the first five radial POD modes from a single position in the mixing layer of a free continuous jet; $x/D = 3$, $r/D = 0.54$, $Re = 80000$ [113].

reveal the flow mechanisms present in the flow field. The energy content of each mode can vary greatly depending on the type of data analysed. Although POD has been employed very little in the analysis of synthetic jets, a number of authors have used it for control and simulation [114, 115, 116]. It was found that as few as 4 or 5 principal modes can accurately describe the response of synthetic jet flows. POD has been widely used to great effect over the years in the analysis of regular continuous jets and has proved very successful at separating fluctuations in shear layers and turbulence from the mean flow [117, 118, 119]. The authors Citriniti and George [113] used POD as the primary investigative tool while analysing the mixing layer of a round continuous jet. In this paper, data acquired using an array of hot-wires was used to characterise fluid velocity at three diameters from the nozzle exit. There are two techniques used by these authors of particular relevance to synthetic jets, namely time-resolved velocity reconstruction and spectral reconstruction. Figure 2.29 (a) shows how powerful POD can be at capturing the most energetic parts of the flow with few modes; the corresponding energy levels for each mode are presented in table 2.3. Looking at figure 2.29 (a) (i) it can be seen that reconstruction with just one mode can approximate the most significant and coherent features of the flow very well. Translated into the frequency spectrum, figure 2.29 (b), the power of POD is equally impressive, with the most dominant frequencies being, by and large, accounted for by the second mode. The majority of the higher frequencies associated with more turbulent, small-scale fluctuations in the flow can be seen to be accounted for in the third mode, at which stage a flow energy approximation of 96.0% has been

achieved. For a synthetic jet, it can prove difficult to separate turbulent fluctuation from coherent periodicity; it is for this reason that the type of deconstructive analysis provided by POD can prove highly suitable and effective in the analysis of the flow field. As was seen above, POD may provide a means of decoupling the periodicity and coherent vortices produced by the synthetic jet from the genuine small-scale mixing subsequently produced by the jet's degradation to turbulence.

2.7 Conclusion

This literature review has so far highlighted the necessity for further research to be undertaken into the heat transfer characteristics of the synthetic air jet. A number of factors may have great influence on the heat transfer performance of the jet, in particular Reynolds number and dimensionless stroke length. While most types of jets use the sole parameter of velocity, and hence Reynolds number, to help describe the state of the fluid flow upon ejection, the synthetic jet is quite different in that it is a reciprocating flow by its very nature operating at a specific driving frequency. This fact has resulted in many authors reporting synthetic jet operational parameters in terms of frequency and velocity. While these parameters are perfectly valid and easily measureable they provide no direct indication as to what the dimensionless stroke length, L_0/D, of the jet is, a parameter which has significant importance in the formation and evolution of the synthetic jet. This parameter has been shown to be neglected throughout literature; it is the fundamental parameter which characterises the operation of the synthetic jet therefore it is necessary to document how the flow field is affected and what this means for the corresponding impingement heat transfer. There are a number of experimental methods and analytic techniques which have been used by previous authors, which have shown significant merit. However, it is believed that further investigation has the potential to reveal far more information about the operational mechanisms of the synthetic jet and its respective flow and heat transfer regimes. In particular, the simultaneous measurement of local heat flux, fluid velocity and fluid temperature, together with flow visualisation and time averaged heat flux measurements can provide greater insight into the mechanisms which affect heat

transfer.

Chapter 3

Experimental Considerations and Techniques

Much research has been carried out in the area of jet impingement heat transfer and many different experimental setups have been designed. In an attempt to characterise the heat transfer to an impinging synthetic jet the following parameters have been varied and extensively tested:

- Distance between jet exit and impact surface, H/D
- Dimensionless stroke length, L_0/D
- Reynolds number, Re

3.0.1 Design of Apparatus

The experimental apparatus is designed so that all the required test parameters are variable. In some investigations, the experimental apparatus is required to simulate the specific application by which the research is motivated. In general, however, the motivation for any jet cooling study is the enhancement of heat transfer to or from an impinging jet. The following geometric design variables have been considered to that end.

3.0.1.1 Nozzle Design

Nozzle design is possibly one of the most important aspects of rig design for synthetic jet investigations. The nozzle geometry influences jet formation, cavity resonance frequency and the jet flow condition. All of these can have a great influence on the local and area averaged heat transfer. It is for these reasons that such a wide variety of nozzle geometries and designs have been employed in heat transfer studies.

The majority of investigations undertaken into synthetic jets concern jet formation and flow characteristics, as such nearly all data reported is for the case of a synthetic jet formed with a cavity and orifice. Investigations have typically concerned themselves with two types of orifices; the more common type is the circular cross-section with this type of nozzle being investigated by many researchers including, Smith and Swift [21], Gordon and Soria [45] and Travnicek and Tesar *et al.* [13]. The other type of exit geometry most commonly investigated is that of the asymmetric slot jet also known as a two dimensional jet; due to their large aspect ratio these may be more suited to certain applications, and substantial research has been undertaken by Glezer and Amitay [9], Holman *et al.* [20] and Gillespie *et al.* [28] among others.

Jet arrays have also been investigated by several researchers including Wu and Breuer [27], Chaniotis *et al.* [2] and Campbell *et al.* [11]. Here the jet flows may interact with each other before impingement and result in a highly complicated flow structure as well as complex heat transfer profiles. Various jet arrangements have been studied, from a simple inline jet pair by Chaniotis *et al.* [2] to the more complex arrangement of five orifices in one plate presented by Campbell *et al.* [11].

3.0.1.2 Impingement Surface

Several methods have been implemented to achieve the required thermal boundary conditions. The design of the impingement surface is highly dependent on the boundary condition as the impact plate is usually a composite of test surface, heat transfer measurement instrumentation, heat source and insulation.

There are two standard thermal boundary conditions for convective heat transfer measurements, namely Uniform Wall Temperature (UWT) and Uniform Wall Flux

(UWF) boundary conditions. The choice of boundary condition for a given study is determined largely by the application for which the study is being conducted. Thus, in a study by Chaniotis *et al.* [2], the cooling of electronic components was simulated by a uniform wall flux boundary condition.

In an attempt to achieve a UWT boundary condition one method employed by Papel [120] was to have a test cylinder consisting largely of a thick-walled copper tube; it is essential to use materials with high thermal conductivity such as copper to achieve as uniform a temperature as possible. It is necessary to provide a constant thermal input to achieve the heating required for the UWT, the use of resistance heaters is quite common, while Papel used thermofoil heaters adhered to the copper tubing. Others have striven for a boundary condition of uniform wall flux; Gillespie *et al.* [28] and others have been satisfied that they achieved this by the use of a thin, stainless steel heating foil as the impingement surface.

It is often the case that while an investigator may strive for an ideal boundary condition, material constraints dictate a fully uniform wall flux or temperature is not realistically achievable under experimental conditions. However, for the purposes of heat transfer investigation it is reasonable to say that many experimental setups come close enough to the desired conditions to justify approximation; in reality the boundary condition achieved will lie somewhere between that of UWF and UWT.

The impingement plate is, in its simplest form, flat with little surface roughness. Geometry of the impingement plate however does tend to vary significantly from investigation to investigation. These include mosaic surfaces to simulate electronic components mounted on circuit boards, as used by Black *et al.* [3], to a jet impinging on a surface with a shallow cavern of sharp edges to investigate the effect on secondary and tertiary vortex formation, Tchavdarov [121].

3.0.1.3 Confinement

The degree of confinement of the jet flow is an experimental parameter that warrants investigation, because many of the applications that motivate synthetic jet research are confined to some extent. The most common example of this is synthetic jet impingement cooling of electronic components that are confined within the casing of

a computer or other electronic device. Two degrees of confinement are commonly investigated, these are illustrated in figure 3.1.

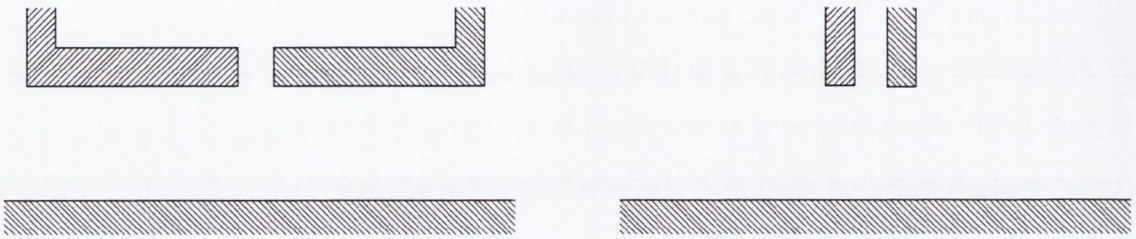

Figure 3.1: Schematic of semi-confined impinging jet (left) and unconfined impinging jet (right).

If a channel is formed between the nozzle plate and the impacting surfaces this is termed semi-confinement. An aspect ratio for a semi confined jet is defined as the length, or diameter, of the plate to the diameter of the nozzle. A further restriction at some distance along the wall jet would lead to a fully confined system. Due to the nature of the synthetic jet operating within the working fluid, only semi-confined conditions are investigated in this research. Varying degrees of confinement have a significant influence on fluid flow and heat transfer. Very few studies into synthetic jets have broached the subject of confinement, but it has been addressed by Campbell *et al.* [11] and Gillespie *et al.* [28].

3.0.1.4 Design for Varying Reynolds Number

The Reynolds number is a parameter of significant importance for synthetic jet heat transfer. Some of the more rigorous investigations vary Reynolds number in one of two ways. Firstly, by increasing the oscillating amplitude of the driver a corresponding increase in stroke length is achieved; this results in a greater Reynolds number. A similar increase in Reynolds number can be achieved by increasing the driving frequency while maintaining the stroke length constant. It has been shown that these two methods of changing the Reynolds number can result in significantly different flow characteristics, Pavlova and Amitay [8].

3.0.1.5 Orientation

Only one investigation surveyed to date, by Arik *et al.* [122], has investigated the influence of angle of jet impingement relative to the plate. It was concluded that the jet was not particularly sensitive to orientation, with results only varying by ±20%, except for normal impingement (90°) wherein performance was significantly enhanced. Arik [33] has also investigated heat transfer to an impingement surface orientated in the vertical plane but solely with normal impingement. No investigation has commented on the effect of the orientation of the combined impingement surface and the jet. The only possible effects that could be considered are those of gravitation and buoyancy. While normally it could be argued that the effects of buoyancy on the heat transfer to an impinging air jet would be minimal, this may not be the case for the synthetic jet. As confinement can play such a significant role at low nozzle to surface spacings, any mechanism which can provide an increase in the exchange of air across the confinement boundary could potentially have a major effect on the level of heat transfer obtainable.

3.0.2 Experimental Techniques

Throughout the literature surveyed many variables have been identified and thus a range of measurement instrumentation is used. This instrumentation is used not only to measure the heat transfer parameters, but also to quantify parameters that are not properly regulated, such as the turbulence intensity within the jet. Relating the fluid flow to the heat transfer has been one of the more difficult objectives of a complete impingement heat transfer study. Measurement instrumentation options for the various aspects of a complete study are described in this section.

Methods using metal foil surface heating use electrical power dissipation in the material as a way of determining the heat flux. The principle is as follows; an electrical current is passed through an ohmic material such as a heating foil. The power is dissipated through the electrical resistance of the material. Heat is generated and is subsequently transferred to the surroundings.

The equation for convective heat transfer can be written as:

$$q = h(T_{surf} - T_{\infty}) \tag{3.1}$$

where T_s and T_{∞} are surface and jet fluid temperature respectively and h the heat transfer coefficient. For compressible flows T_{∞} is replaced by the adiabatic jet temperature. Depending on the desired boundary condition the heat transfer coefficient h can be determined in two ways. Heat transfer measurement using Uniform Wall Flux is determined by maintaining the heat flux q constant and measuring the local surface temperature T_s. Alternatively, it is possible to determine h by applying a Uniform Wall Temperature boundary condition in which T_s is maintained constant through the use of a thick, highly conductive material such as a copper plate, while q is measured locally.

For continuous air jets the fluid temperature T_{∞} is usually measured by placing a thermocouple in the air flow prior to exiting the nozzle. However, the synthetic jet is synthesised directly from the ambient fluid, which under certain conditions can suffer considerably from thermal saturation due to high levels of confinement, consequently this may prove to be a far more complex problem. To date no literature reviewed has addressed the issue of whether to use internal cavity temperature or ambient air temperature for the jet temperature T_{∞}. Work undertaken by Gillespie *et al.* [28] showed evidence to suggest that the internal cavity temperature may in fact be substantially higher than that of the ambient surroundings because the jet is inclined to re-ingest the working fluid. This effect becomes more pronounced as confinement is increased and recirculation cells are established; as such there is reason to support the use of the internal cavity temperature, however further research into this area is needed.

3.0.2.1 Heat Transfer Measurement

There are a multitude of heat transfer measurement techniques that have been employed previously in synthetic jet heat transfer studies, as described in this section.

3.0.2.2 Thermo-Chromatic Liquid Crystals

This is a simple method of temperature-contour visualisation and for this reason has been employed by many researchers such as Li and Zhong [86] and Jabbal and Zhong [71]. A good description of this technique is available in a two-part paper by Anderson and Baughn [123, 124].

The liquid crystal phase is a phase that occurs between the solid (crystalline) and liquid (isotropic) state, and is characteristic for certain organic compounds. In the mesophase the molecules are movable but still ordered. There are three different kinds of mesophase known as the smectic, the nematic and the cholesteric. The cholesteric liquid crystal system can change through the complete colour spectrum with changes in temperature. In its solid state the crystal is transparent but as it melts it changes to reflect red from incoming white light. As the temperature is increased further the reflected colour continues to change through the spectrum from red to yellow and so on until it becomes blue; past this state the crystal will return to being transparent.

The position of the colour contours, given a uniform heat flux boundary condition, correspond to isotherms and enable the calculation of the heat transfer profile of a jet. The acquisition of the results is usually in the form of digital photographs, but some studies concerned with the transient heat transfer to an impinging air jet record the gradual movement of contours. Results obtained in image format will require hue, saturation and value processing by calibrated computer software such as MATLAB. While this technique can prove simple and effective when implemented correctly, certain characteristics of liquid crystals also make them problematic. Drift in the temperature-colour calibration with time is common so it is prudent to test immediately after calibration; heating and cooling of the liquid crystals will accelerate this drift. Calibration and testing must be completed in controlled lighting conditions so as to obtain consistent results when converting colour to temperature. Any alteration in lighting conditions can significantly change results.

3.0.2.3 Infrared Camera & Image Diagnostic Equipment

This technique has been employed by authors such as Wang *et al.* [105], Chang *et al.* [125] and Arik [33] to find the heat transfer to an impinging synthetic jet. The infrared camera detects and records the radiosity of the impingement surface. With the detected radiosity, and knowing the emissivity of the surface and the ambient temperature, the infrared camera determines the local surface temperature distribution across the plate. The thermal image can either be recorded onto digital media such as a hard drive, or onto videotape. A thermal image processing system is then used to extract the local temperatures to calculate the heat transfer coefficients between the impingement surface and the jet (for a UWF boundary condition). The implementation of this technique requires in situ calibration and knowledge of the target material's emissivity. Complications may arise when the target is composed of a number of materials with varying emissivities, however this problem can often be overcome by coating the target object with a uniform layer of paint with a known (high) emissivity.

3.0.2.4 Naphthalene Sublimation Technique

The naphthalene sublimation technique is an experimental mass transfer technique which has been employed for many years to measure heat transfer coefficients from convective flows. A number of review papers detail the theory and fundamentals upon which the naphthalene sublimation technique is based, and also present the basic characteristics and implementation procedure [126, 127]. Although this technique has seen somewhat limited use in synthetic jets, employed primarily by Travnicek and Tesar [13], its use in other heat transfer analyses such as continuous jets has been widespread [128, 129, 130]. This technique works by first performing the mass transfer experiment in the lab; results are converted into heat transfer coefficients through the relationship between heat transfer and mass transfer.

Naphthalene, $C_{10}H_8$, is the substance chosen for this technique due to its unique properties, such as the fact that it sublimes at room temperature, its low toxicity and its good casting and machining properties. To use this technique for the measurement of heat transfer a flat naphthalene surface is cast to the required dimensions; this

surface will sublime in accordance with both natural and forced convection effects. After the convection has taken place for a set amount of time the resulting cast is contoured. Measurements of the naphthalene plate are made before and after the jet impact to determine the mass transfer from the plate. These contours can be measured by instrumentation that converts the movement of a sensor tip into a voltage proportional to the depth of contour. A value called the mass transfer coefficient K is calculated using the change in mass $\dot{m}$ during the sublimation process:

$$K = \frac{\dot{m}/A}{\Delta t_s(\rho_s - \rho_b)} \tag{3.2}$$

where A is the naphthalene sublimation area, Δt_s duration of sublimation process, ρ_s naphthalene density at the transfer surface and ρ_b is the bulk naphthalene vapour density which can normally be taken to be equal to zero. This value for mass transfer coefficient is then used to calculate the Sherwood number:

$$Sh = \frac{KL}{D_m} \tag{3.3}$$

where L the characteristic length, D_m is the mass diffusivity. Finally, the Schmidt number is also required:

$$Sc = \nu/D_m \tag{3.4}$$

where ν is the kinematic viscosity of the air. The Nusselt number can then be obtained by combining equations 3.3 and 3.4 as follows:

$$Nu = (Pr/Sc)^n Sh \tag{3.5}$$

where Pr is the Prandtl number, and for most forced convection problems $n \approx 0.34$.

3.0.2.5 Micro-Foil® Heat Flux Sensor

Used in investigations by Scholten and Murray [111] and O'Donovan *et al.* [4] for cylinders in cross flow and impinging continuous jets respectively, this sensor directly measures local surface heat flux. The sensor is a composite of three layers of Kapton insulating material. These are bonded together with copper/constantan thermocouple piles or thermopiles either side of the central layer. An applied heat flux causes a temperature difference across the central layer that produces an output e.m.f. from the thermopiles proportional to the heat flux through the sensor. This type of sensor also includes an integrated thermocouple for local temperature measurement and is used generally with Uniform Wall Temperature boundary conditions.

3.0.2.6 Hot-Film Sensors

This type of sensor was originally designed for the identification of flow features such as laminar to turbulent transition, boundary layer instabilities, stagnation points, flow separation, reattachment and shock in wind tunnels and in flight. In more recent investigations however, the hot-film sensor is used for heat transfer measurement requiring both good temporal response, and local resolution. Used by Scholten and Murray [131] to measure fluctuating heat transfer of cylinders in cross flow and by O'Donovan *et al.* [132, 133] to measure fluctuating heat transfer for an impinging continuous jet, these sensors involve complex calibration. This calibration involves the calculation of the effective surface area, a correction for the overheat of the film and a shear stress correction. This type of sensor is used in the current research and its operating principle is described in section 5.6.

3.0.2.7 Thermal Test Die

This method of evaluating heat transfer characteristics and performance has been used by a number of authors investigating synthetic jets such as Beratlis and Smith [103], Mahalingam and Glezer [12] and Wang *et al.* [105]. This sensor measures average heat flux through the use of thermal diodes and heating resistors. Thermal test dies are uniquely-designed for package characterisation and design comparison. Integrated into

each die are a number of separate diodes, strategically placed for temperature sensing in key areas of the die. Thermal input is provided using a number of ohmic heating resistors situated on each die which can be operated in series or parallel to match the capabilities of available power supplies or thermal test instruments. While these devices can accurately simulate the operation of a processor chip and the corresponding thermal dissipation achieved under test conditions, the results obtained represent an average heat transfer across the whole chip; as such no local heat transfer data are acquired.

3.0.2.8 Flow Measurement

As with all convective heat transfer situations, variations in the flow characteristics have significant influence on heat transfer in a jet impingement situation. Because of this, many techniques have been employed to measure every aspect of the flow.

3.0.2.9 Hot-Wire

The hot-wire sensors work on the principle that the rate of heat transfer from a cylinder in cross flow is dependent on the velocity across it. It can operate in a constant temperature or constant current mode. Similar to the hot-film sensor detailed earlier, this is a highly responsive process and rapid fluctuations in the fluid flow can be observed. The development and propagation of flow structures can also be identified. Hot-wires were used in investigations by Smith and Glezer [46], Pavlova and Amitay [8] and Shuster and Smith [48], amongst others, to map the velocity profile of a synthetic jet. While the implementation of a single hot-wire is only capable of measuring velocity in a one direction, the combined implementation of up to three orientated orthogonal to one another can provide velocity measurements in all three planes. The disadvantage of hot-wire probes is that due to their intrusive nature they may not be suitable for implementation in certain situations, particularly in flows which rely on a small characteristic length scale and often for flows with a high temperature gradient, unless local temperature measurement is possible.

Turbulence intensity can also be calculated from the information acquired when

using the hot-wire; this information is essential when analysing fluid flow regimes. For example, transition to turbulence in the free jet can be detected by a sharp increase in turbulence. The hot-wire technique has also been used by Gillespie *et al.* [28] to measure the velocity of the reversible flow across the synthetic jet orifice and hence to calculate average jet velocity.

3.0.2.10 Laser & Flow Visualisation Techniques

Flow visualisation is a very useful tool for both flow structure identification and flow regime determination. Flow velocities can also be determined using optical measurement. Although some techniques such as Laser Doppler Anemometry (LDA) are limited to point velocities, other laser techniques such as Particle Image Velocimetry (PIV) can produce instantaneous flow field information. A thorough explanation of the PIV flow visualisation technique is given in section 5.11.

Laser Doppler Anemometry (LDA) can be used to perform local velocity measurements. LDA systems commonly employ a two component measurement system measuring the velocity in orthogonal directions. The laser is split into two pairs of beams of differing wavelengths emanating from a single lens; where the two beams intersect interference generates a set of constructive and destructive fringes aligned perpendicular to the flow direction. It is necessary to seed the fluid flow with smoke particles for this velocity measurement technique, particles are generally introduced through the use of a glycol based smoke generator. As these particles pass through the fringes they reflect light from the regions of constructive interference which is reflected into a photodetector. The velocity of the seeding particle can then be calculated by measuring the Doppler frequency shift of the reflected light. In this way time varying coincident velocity measurements can be acquired in orthogonal directions. Depending on the type of flow and geometric constraints LDA systems are capable of acquiring data in two operational modes, forward-scatter and back-scatter. The signal is acquired and processed by a Base Spectrum Analyser (BSA) which computes the instantaneous velocity of the fluid. As the system is dependent on a seeding particle passing through the measurement volume the frequency of acquisition is arbitrary and erratic.

Yao *et al.* [134] and Holman and Utturkar [20] used both LDA and PIV measurements to form part of a synthetic jet flow field database which was subsequently used to validate a computational fluid dynamic model of a synthetic jet. As with all laser analysis, the flow is seeded and a technique such as backscatter acquires the necessary data for flow measurement.

3.0.2.11 Schlieren Visualisation Technique

The word Schlieren comes from the German word "Schliere", meaning "streak". The basic optical schlieren system uses light from a single collimated source shining on, or from behind, a target object. Variations in refractive index caused by density gradients in the fluid distort the collimated light beam. This distortion creates a spatial variation in the intensity of the light; this light deviation effectively produces areas of shadow and brightness which can be visualised directly with a shadowgraph system. Schlieren visualisation has been used in many papers on conventional jet flow and has proved extremely useful in investigations into synthetic jets. Smith and Glezer [46] used the schlieren visualisation technique to identify various regimes in the jet flow. Other authors such as Glezer and Amitay [9], Smith and Swift [22] and Crittenden and Glezer [25] have implemented the schlieren visualisation technique in their studies.

3.0.2.12 Smoke Visualisation Technique

Similar to schlieren visualisation techniques smoke visualisation can be used to identify flow regimes within a jet. Many authors including Travnicek and Tesar [13] have used smoke-wire techniques for the visualization of the air jet downstream from the nozzle. This technique involves coating high resistance heater wire with paraffin oil before each test. When DC current is passed through the wire the joule effect[1] causes it to heat up and vaporise the paraffin producing a steady stream of smoke when positioned in or near the jet flow. By using a contrasting black background the flow effects in the form

[1]Joule's first law, also known as the Joule effect, is a physical law expressing the relationship for the heat generated by the current flowing through a conductor. $Q = I^2Rt$, where Q is the heat generated by a constant current I flowing through a conductor of electrical resistance R for a duration t

of white streak lines can be observed and photographed. Other authors who use this technique in the analysis of synthetic jets include Smith and Glezer [46], Mahalingam *et al.* [135] and Gilarranz *et al.* [136, 137].

3.0.3 Conclusion

Taking all of the above techniques into consideration a suitable experimental apparatus was designed to conduct an investigation into the heat transfer and flow characteristics of an impinging synthetic jet. The original design considerations for the experimental apparatus were twofold. Firstly the experimental rig needed to approximate loosely the air jet impingement cooling which might be found in a manufacturing process or electronics application, and secondly it needed to replicate baseline published results for the calibration of heat transfer instrumentation. The choice of instrumentation and the ranges of test variables were dictated by what might be required by an electronics cooling application. A complete description of the apparatus design for this project is presented in chapter 4.

Chapter 4

Experimental apparatus

The experimental apparatus was designed to investigate heat transfer between a synthetic jet and an impingement surface. The eventual goal of this investigation is to apply the heat transfer knowledge gained from the measurements to applications such as the cooling of electronics or manufacturing processes. To this end it was decided that the impingement surface be heated and the jet serve as a mechanism of cooling.

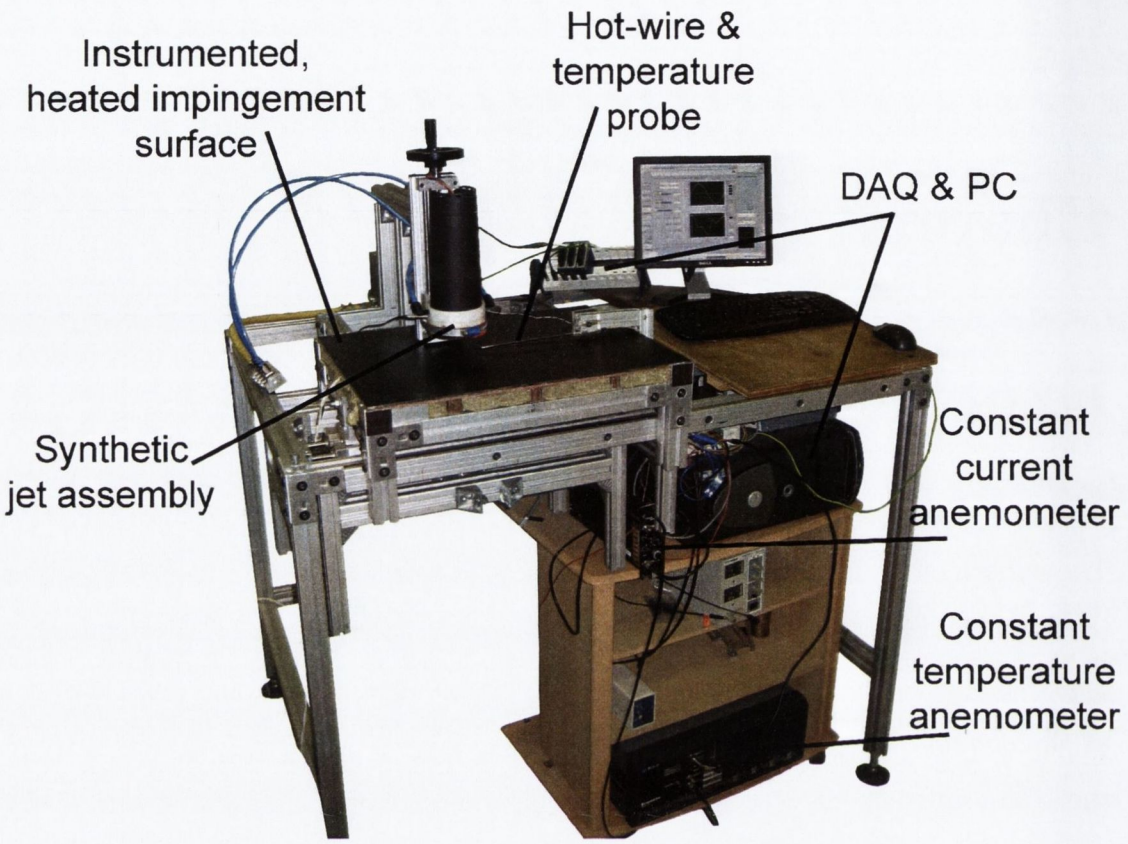

Figure 4.1: Overview of Experimental Apparatus

4.1 Apparatus Parameters

There are many parameters that can affect heat transfer to the impinging synthetic jet, and so the apparatus used was designed to facilitate the variation of all relevant parameters in a sufficiently wide range. The parameters are listed and discussed in the following sub-sections:

4.1.1 Nozzle to Surface Axial Spacing

The synthetic jet assembly is clamped at a fixed position above the impingement plate. It is possible to adjust the height of the jet above the impingement surface using the hand operated lead screw which provides a high degree of control and accuracy. It has been reported in literature that the maximum heat transfer to an impinging synthetic jet is typically at a nozzle to surface spacing of 8 to 12 diameters; as reported by

Gillespie *et al.* [28]. The apparatus has been designed with large height adjustability in both the x and y axis to accommodate measurements for the current jet nozzle and if necessary those of larger nozzle diameters.

4.1.2 Jet Velocity

As discussed previously, effective jet velocity is highly dependent on a number of factors, such as Reynolds number Re and stroke length L_0; however the maximum average jet velocity U_0 is constrained primarily by the design and components that make up the synthetic jet. The current research uses a coil and magnet type Visaton FR-8 audio speaker with a 10W power rating, where the coil provides the driving mechanism for the synthetic jet and the cone forms the oscillating diaphragm. The operational limit of the synthetic jet is experienced when the audio speaker output signal undergoes distortion; accordingly, deviation from the sinusoidal input signal occurs before reaching the speaker's maximum rated power output. Average jet velocities, U_0, of up to 16 m/s and peak velocities, U_P of up to 30 m/s have been reached with the current setup. Working within the operational limits of the synthetic jet the maximum stroke length has been measured to be approximately $L_0/D = 72$ at $80Hz$; this is frequency dependant and reduces with either an increase or decrease in frequency. The speaker's frequency range extends up to $20kHz$ although jet formation does not occur much beyond $940Hz$ due to diminished stroke length; the minimum stroke length for jet formation has been shown in literature to be at $L_0 \approx 3D$.

4.1.3 Position within the Impingement Flow

The impingement surface is instrumented with two thermocouples and two different types of heat flux sensors, one active and the other passive. These sensors are used for point measurement and for this reason relative positioning of the sensors within the impingement flow profile was required. Accurate positioning was achieved by placing both the impingement plate and the synthetic jet assembly on separate carriages. The impingement plate carriage and the synthetic jet assembly travel orthogonally in the x and y directions respectively and both operate using high precision lead screws. The

impingement surface however is traversed through the use of a computer controlled stepper motor which provides a high degree of control and precision. For a nozzle of $5mm$ diameter the travel range in both the x and y-axis is over 40 diameters.

4.1.4 Impingement Surface

Although some modifications have been made, the impingement surface used in this research was originally used in a thesis by O'Donovan [4]. A $5mm$ thick copper plate serves as the impingement surface. The thickness and conductivity of the copper is such that it approximates a uniform wall temperature boundary condition. For a synthetic jet operating at a Reynolds number of $Re = 3000$ there is a maximum variation in the plate temperature of less than $1°C$. A relatively large temperature differential of, on average, over $30°C$ between the cooling airflow and the heated plate minimises errors. The apparatus was designed to be able to heat and maintain the plate temperature at up to, and if required, above $60°C$. Due to buoyancy effects and thermal plumes causing inconsistencies in measurement results, extended test durations of up to 60 seconds per increment have been employed in combination with the implementation of a fine mesh (not pictured) surrounding the plate; this has the function of minimising the effects of both random crossflows and thermal plumes. A thin (approximately $1.1mm$ thick), silicone rubber heater mat was designed and manufactured to specifications by Holroyd Components[1]. To ensure good contact between the heating mat and copper plate so as to optimise heat transfer and ensure uniformity of temperature the mat was attached using a thin, evenly spread layer of silicone glue. Using a hand roller, excess glue was rolled out from between the mat and plate, thereby reducing contact and boundary resistance, subsequently both were compressed until the glue was set. The heating element is rated at a maximum voltage of $240V$ and power of $1500W/m^2$, it has a dimensional area of $425mm \times 550mm$. This rating is more than sufficient to maintain a temperature of $60°C$ while the plate is actively being cooled at what would be considered optimum settings of maximum flow

[1]Holroyd Components Limited, Shirehill Industrial Estate, Saffron Walden, Essex, CB11 3AQ, England, UK (http://www.holroyd-components.co.uk)

rate and axial spacing. A variable voltage DC power supply (max $64V$) controls the level of heating provided by the heater mat.

4.1.5 Jet Design

The heat transfer to an impinging synthetic jet is not only dependent on the dimensionless nozzle to surface spacing, but other factors can play an important role, such as nozzle diameter, length and internal cavity design.

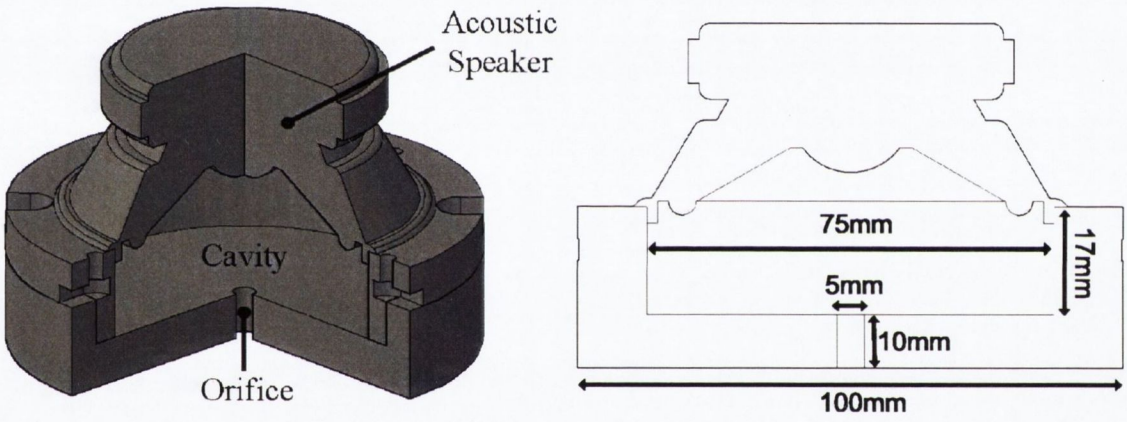

Figure 4.2: AutoCAD rendered image and schematic of synthetic jet assembly

Figure 4.2 shows an accurate AutoCAD rendered image of the synthetic jet assembly and a dimensional schematic. The orifice has a diameter of $D = 5\ mm$ and length of $l_o = 10\ mm$. As this configuration implements a relatively large acoustic speaker and simple orifice geometry it allows for a wide range of operational parameters. The total cavity volume is calculated at $V_c = 101.5\ cm^3$, giving a Helmholtz resonance of $485Hz$. The internal cavity diameter is $D_c = 75\ mm$ and when the volume of the speaker cone is included, the cavity has an effective internal height of $h_c = 26.4\ mm$. The orifice plate has a relatively large diameter of $D_{op} = 100\ mm$ and so provides quite a large degree of confinement, similar to that which might be found in practical applications. Table 4.1 provides a list of these measurements, non-dimensionalised by the orifice diameter D.

Orifice length	Cavity diameter	Cavity height	Orifice plate diameter
l_o/D	D_c/D	h_c/D	D_{op}/D
2	15	5.28	20

Table 4.1: Cavity measurements non-dimensionalised by orifice diameter D

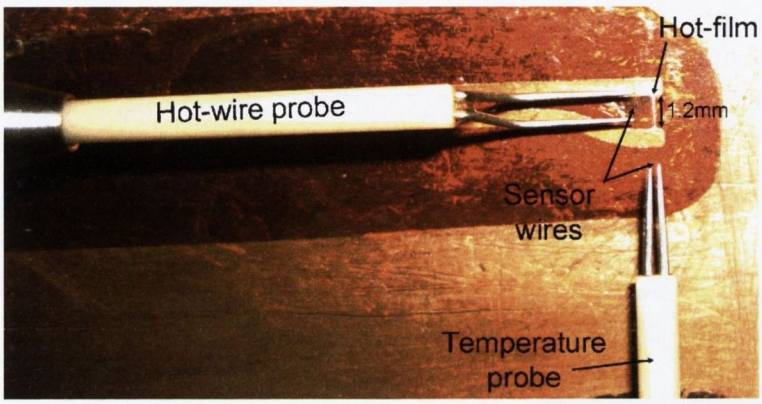

Figure 4.3: Hot-film, hot-wire and temperature probe setup

4.1.6 Simultaneous Measurements

The objective of achieving simultaneous, time-resolved heat flux, boundary layer velocity and local air temperature measurements for a synthetic jet of orifice diameter 5 *mm* proved a challenging one. To acquire useful data it was necessary to have the respective instruments in as close proximity as physically possible, however due to the physical nature of the instruments and their operational requirements a number of concerns must first be taken into consideration. As the instruments are very fragile, contact between themselves or any other object including the impingement surface must be avoided. The elevated operational temperatures of two of the instruments also means significant consideration must be given to avoid any cross-interference. A comprehensive description of the operation and specifications of these instruments are included in sections 5.6, 5.7 and 5.9 respectively.

For simultaneous measurements of all three, the instruments were positioned as seen in figure 4.3. It was decided that this was the optimal arrangement to achieve the desired goals of avoiding cross-interference while maintaining a reasonable proximity between all three. Both the hot-wire and the temperature probe were located 0.3 *mm* above the surface of the plate, and were displaced by 0.6 *mm* and 1.2 *mm*

radially from the centre of the hot-film respectively; the temperature probe was placed at a larger radial distance to avoid concerns that its operation might be affected by the significantly elevated operating temperature of the hot-wire. For all tests in this configuration the plate remained stationary and only stagnation point (nominal) measurements were conducted; consequently the centre of the synthetic jet was positioned and maintained immediately above the centre of the hot-film.

Simultaneous, time-resolved tests to obtain full radial profiles were also conducted using just the combination of the temperature probe and hot-film alone. Tests were performed with the temperature probe operating parallel to the hot-film, offset from the centre of the hot-film by a significantly smaller distance of 0.3 mm in both the axial and radial direction. All tests were conducted at a sample rate of 8192 S/s for a duration of 16 seconds.

Chapter 5

Instrumentation

This investigation is concerned primarily with measuring heat transfer from the heated impingement plate to the impinging synthetic jet. This includes analysing the heat transfer characteristics resulting from variation in the operational parameters of the synthetic jet.

5.1 Speaker Amplifier & Cavity Pressure Measurement

The nature of the synthetic jet means the jet flow is generated by entraining working fluid from its surroundings. Thus, the air temperature is taken to be that of the air expelled from within the jet orifice, and so a thermocouple located within the synthetic jet cavity is used to measure this. A Visaton FR-8 audio speaker is used to drive the synthetic jet and to act as the flexible diaphragm; it has a maximum unloaded deflection of $4mm$ and its specifications can be found in Appendix B. To provide the speaker with a signal of sufficient power the output from the data acquisition system was amplified using a Kemo® 40 Watt power amplifier. This particular synthetic jet assembly was calibrated in accordance with a paper by Persoons and O'Donovan [50] which employs a pressure based estimate of synthetic jet velocity.

Figure 5.1: Synthetic jet assembly with addition of impingement cooling section for acoustic coil.

It was found that under high loads the acoustic speaker coils underwent significant heating which was subsequently conducted through the cone into the jet cavity. This increase in cavity temperature not only impaired the synthetic jet's ability to remove heat, but more significantly resulted in an artificial alteration of the jet's working parameters which could potentially result in incorrect measurements. To remedy this problem an additional section was constructed using a rapid prototyper; this part connects directly to the jet assembly and is pictured in figure 5.1. This new section allowed two air jets impinge either side of the acoustic coil, cooling it and removing the heat directly at the source prior to conduction to the cavity. To prevent jets of air from interfering with normal operation of the synthetic jet and plate boundary layer, a vertical duct (not pictured) was also added to direct the air a sufficient distance away from the jet. Subsequent tests revealed a significant reduction in cavity heating even under heavy loads.

(a) G.R.A.S. 40BP (b) G.R.A.S. 26AC

Figure 5.2: Microphone and Amplifier used to measure cavity pressure.

A system similar to the setup used by Persoons and O'Donovan [50] was implemented to control the frequency and amplitude of the synthetic jet; thereby achieving the desired jet Reynolds number and stroke length. This was done through the measurement of the internal cavity pressure using a 1/4 inch pressure microphone type 40BP and a 1/4 inch preamplifier type 26AC, both supplied by G.R.A.S.[1] and pictured in figure 5.2 (*a*) and (*b*). Power is supplied to the preamplifier through a power module type 12AN, also supplied by G.R.A.S., after which the signal is fed back to the data acquisition system where the measured pressure is then used to estimate the jet Reynolds number (as outlined by Utturkar *et al.* in equation 2.11) and stroke length. Specification sheets for these instruments can be found in Appendix B.

Calibration of the synthetic jet was performed in accordance with the method outlined by Persoons and O'Donovan [50] and the corresponding equation 2.14. For this calibration a hot-wire probe operating in constant temperature anemometer mode was placed $0.5mm$ in front of the orifice exit while the internal cavity pressure was measured using a microphone. A sine wave was supplied to the acoustic speaker using a data acquisition system; this system was also used to record the analogue signals returned from the hot wire and microphone, phase averaging them over 10 periods

[1]G.R.A.S. Sound & Vibration A/S, Skovlytoften 33. DK-2840. Holte, Denmark. (http://www.gras.dk)

achieved an uncertainty level under 5% (on a 95% confidence level). To avoid any adverse effects caused by flow reversal only velocity data recorded in the ejection phase of the jet were used for calibration. As the orifice length is much shorter than the minimum length required for hydraulic development ($l > 200mm$) the measured centreline velocity U_{cl} is assumed to be equal to the area averaged velocity U_0. Data is recorded over a series of cavity pressures ranging from $10Pa$ up to $1000Pa$ and frequencies up to twice that of cavity resonance ($2f_h$). The resulting data were fitted to the least-square linear damping model as outlined by Persoons and O'Donovan [50] using the appropriate fitting parameters of the nonlinear damping coefficient K_p and the added mass coefficient β, which relates to the damping force F_D and the mass of gas in the orifice M_o respectively. These velocity calibrations were later confirmed through the use of PIV.

5.2 Mass Flow Controller

Figure 5.3: Mass flow controller, MKS Instruments 1579A

A continuous supply of air was required to perform initial heat flux calibration using a conventional impinging jet; this air supply was also used to provide cooling to the acoustic coil which drove the synthetic jet. A mass flow controller was employed to

regulate the flow rate of the air supplied for the various applications. An elastomer-sealed, high flow rate mass flow controller model number 1579*A* was supplied by MKS Instruments[2]. The mass flow controller was controlled centrally from the LabView software through the data acquisition system outlined in section 5.10. This controller can provide a range of flow rates from 50 *slm* up to a maximum of 300 *slm*. The accuracy of the system is rated at 1%fsd (full scale deflection) and the certificate of calibration is included in Appendix B.

5.3 T-Type Thermocouples

Four temperature measurements are taken during testing. A fine gauge thermocouple embedded beneath the hot-film sensor is used to monitor the plate temperature as close to the hot-film sensor element as possible. The RdF Micro-Foil® heat flux sensor contains an integrated T-type thermocouple, as the heat flux measurement must be corrected by a calibrated multiplication factor according to the surface temperature; both of these thermocouples measure the surface temperature, T_{surf}. Internal cavity temperature is monitored by a thermocouple located within the synthetic jet cavity itself. This is necessary as the true temperature difference between the impinging synthetic jet and the impingement surface must be measured for accurate heat flux data acquisition. The final thermocouple is kept away from the heated plate and any other heat source so as to measure the ambient temperature in the laboratory, this is required to ensure consistency during and between subsequent tests. All four type-T thermocouples were calibrated simultaneously using a thermostatically controlled water bath and a pre-calibrated high precision Resistance Temperature Detector (RTD) supplied by OMEGA Engineering[3] whose certificate of calibration is included in Appendix B. This instrument has a temperature uncertainty of $0.2°C$ at $100°C$; this constitutes the bias limit for all thermocouples calibrated with the RTD as a reference. Calibration results were input into MATLAB where a third order regression curve was calculated

[2]MKS Instruments, 2 Tech Drive, Suite 201, Andover, MA 01810. (http://www.mksinst.com/)

[3]OMEGA Engineering, INC., One Omega Drive, P.O. Box 4047, Stamford, Connecticut, 06907-0047, USA. (http://www.omega.com)

for each thermocouple. For simplicity each polynomial was applied to the individual thermocouples in the LabVIEW program, these ensured accurate parameters were set and maintained before and during all tests.

Third order polynomials were fitted to all sets of calibration data with their respective graphs plotted from figures 5.4 to 5.7 and corresponding equations displayed beneath them in equations 5.1 to 5.4.

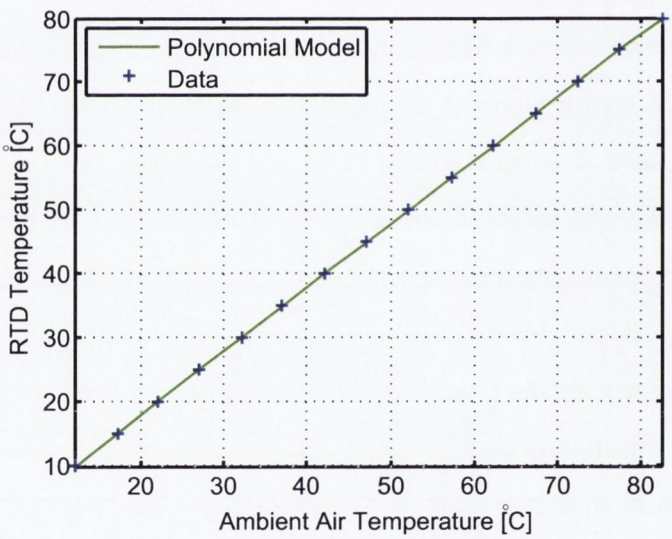

Figure 5.4: Ambient air thermocouple calibration data

$$T_{RTD} = 3.0267e^{-6}{T_{Ambient}}^3 - 0.00063344{T_{Ambient}}^2 + 1.0333T_{Ambient} - 2.5751 \quad (5.1)$$

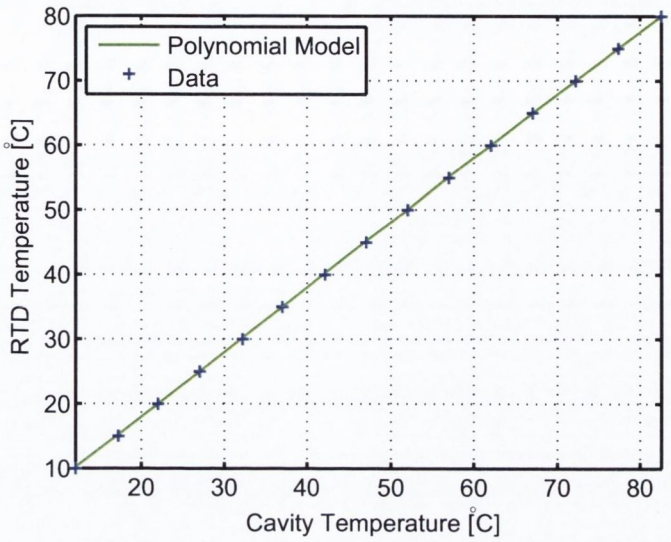

Figure 5.5: Cavity thermocouple calibration data

$$T_{RTD} = -2.2537e^{-6}{T_{Cavity}}^3 + 0.00010438{T_{Cavity}}^2 + 1.0052T_{Cavity} - 2.2603 \quad (5.2)$$

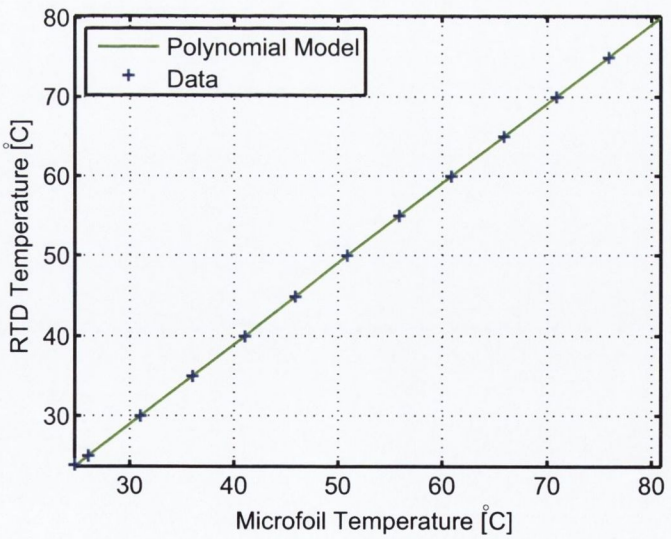

Figure 5.6: Micro-Foil ® thermocouple calibration data

$$T_{RTD} = 7.923e^{-6}{T_{Micro-Foil}}^3 - 3.6471e^{5}{T_{Micro-Foil}}^2 + 0.99702T_{Micro-Foil} - 0.77151 \quad (5.3)$$

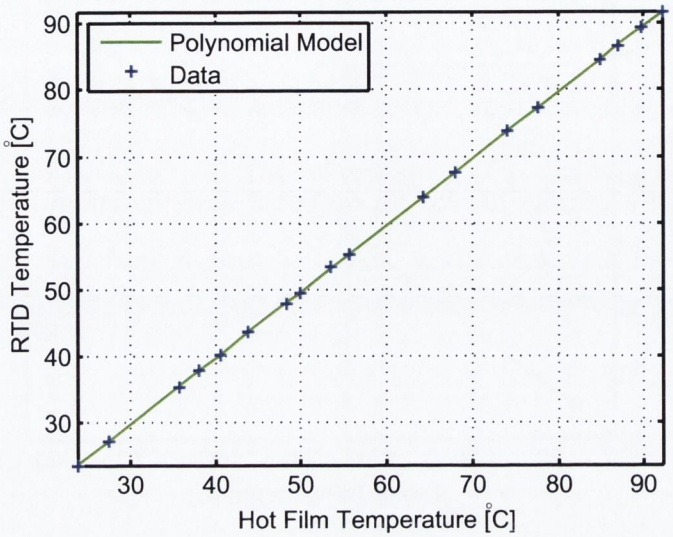

Figure 5.7: Hot-Film thermocouple calibration data

$$T_{RTD} = -2.6346e^{-6}{T_{Micro-Foil}}^3 + 0.00050327{T_{Micro-Foil}}^2 + 0.96842T_{Micro-Foil} + 0.31451 \tag{5.4}$$

The regression fit and precision uncertainties for each thermocouple calibration are presented below in table 5.1

Temperature Measurement	Typical Operating Temperature ($C°$)	Regression Uncertainty (%)	Measurement Uncertainty ($C°$)
Ambient Air	20	0.036	0.107
Cavity Air	30	0.033	0.099
Micro-Foil®	60	0.021	0.070
Hot-Film	60	0.046	0.156

Table 5.1: Uncertainties in calibrated thermocouples at normal operating temperatures.

At a value of less than 0.1% the uncertainty in the regression curve is small, which is also reflected in the magnitude of the measurement uncertainty. Therefore it is omitted in further calculations in this section.

5.4 RdF Micro-Foil® Heat Flux Sensor

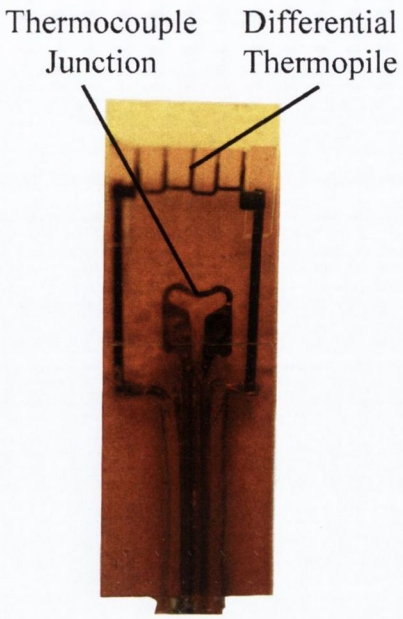

Figure 5.8: Micro-Foil® heat flux sensor model number 27036_1

The Micro-Foil® heat flux sensor shown in figure 5.8 used to measure the local convective heat flux from the impingement surface. The sensor is flush mounted on the surface of the heated plate. The Micro-Foil® contains a differential thermocouple type sensor, which uses a thin foil thermopile bonded to both sides of a known thermal barrier. The thermal barrier is made of Kapton and is used because of its ability to remain stable at a wide range of temperatures. The difference in temperature across the thermal barrier is proportional to the heat flow through the sensor. As such the heat flux through the sensor is determined by the following equation:

$$\ddot{q} = k\frac{\Delta T}{\delta} \tag{5.5}$$

where k is the thermal conductivity of the Kapton barrier, ΔT is the temperature difference across it and δ is its thickness. While a sensor can be implemented with just one differential thermocouple junction, the signal resolution and accuracy can be diminished by the very small voltage returned by the thermocouples. To solve this problem the number of thermocouple junctions can be increased to return a larger

signal, however the drawback is that with an increase in the number of junctions comes an increase in geometric area, as each junction takes up more space. It is for this reason that the thermopile in the Micro-Foil® employs five parallel junctions in close proximity taking up an area of approximately $1mm \times 4mm$ as can be seen in figure 5.8.

This sensor has a relatively slow response time τ of 0.02 seconds for a 62% response to a step function. It is suitable only for time averaged measurements over a number of seconds and for optimum results it is necessary to allow substantial settling time before data acquisition. The following equation can be used to calculate the time constant:

$$\tau = \frac{4(X\delta^2\rho C_p)}{\pi^2 k} \tag{5.6}$$

where X is a factor related to the layer of Kapton between the sensor surface and the thermopile. The sensor output is rated by the manufacturer's own calibration at $93.3nV/(W/m^2)$ (before amplification), however the thermal properties of the Kapton barrier will change depending on what temperature it is operated at. The voltage output from this sensor is proportional to heat flux through the sensor, which in turn is related to the convective heat transfer from the surface. Using an Omega Omni-Amp the voltage from the thermopile is amplified by a factor of 1000; this provides a sufficiently high voltage so that the data acquisition system can achieve a good signal to noise ratio. A single pole thermocouple for the purpose of local surface temperature measurement is also integrated into the sensor $3mm$ from the thermopile. It was necessary to use a heat transfer correlation as a reference for the calibration of the Micro-Foil® sensor. A correlation produced by Shadlesky [138] describes the relationship between the stagnation point heat transfer of an impinging continuous air jet and the axial spacing between the nozzle and impingement surface. The heat transfer was deemed to be constant and independent of the nozzle to impingement surface. Subsequently, several other authors including Liu and Sullivan [15] and O'Donovan [4] have shown this to be untrue. Liu and Sullivan did however go on to prove that for axial distances less than two diameters the convective heat transfer for an impinging

continuous air jet is constant and independent of nozzle height. This relationship is described by the following equation:

$$0.585 = \frac{Nu_{stag}}{Pr^{0.4}Re^{0.5}} \tag{5.7}$$

To apply this correlation the Micro-Foil® heat flux sensor was positioned at the stagnation point of a continuous impinging air jet with contoured nozzle of diameter $13mm$ at an axial spacing of $H = 0.75D$. The voltage output from the heat flux sensor was measured for Reynolds numbers ranging from 430 to 6600 as well as for the zero heat flux condition. Nusselt number was calculated from equation 5.7. Using the temperature differential ΔT measured between the impingement surface and the jet air, equations 5.8 to 5.10 were used to calculate values for surface heat flux.

$$Nu = \frac{hD}{k} \tag{5.8}$$

$$\ddot{q} = h\Delta T \tag{5.9}$$

$$\ddot{q} = \frac{k0.585Pr^{0.4}Re^{0.5}\Delta T}{D} \tag{5.10}$$

The heat flux calculated in equation 5.10 was plotted against Micro-Foil® voltage recorded under experimental conditions required to satisfy equation 5.7. As the mass flow controller and impingement setup reached its lower controllable limit at a Reynolds number of 430, corresponding heat flux data below $770W/m^2$ proved difficult to obtain. The relationship between the heat flux and Micro-Foil® voltage seen in figure 5.9 appears quite linear, but at lower heat flux the relationship tends to deviate significantly. It was found that a fifth order polynomial approximated the data most accurately and so the following regression fit was applied to the data:

$$\ddot{q} = -11882405.71V^5 + 10795504.08V^4 - 3588437.3V^3 + 515245.08V^2 - 16088.12^{+3}V - 47.48 \tag{5.11}$$

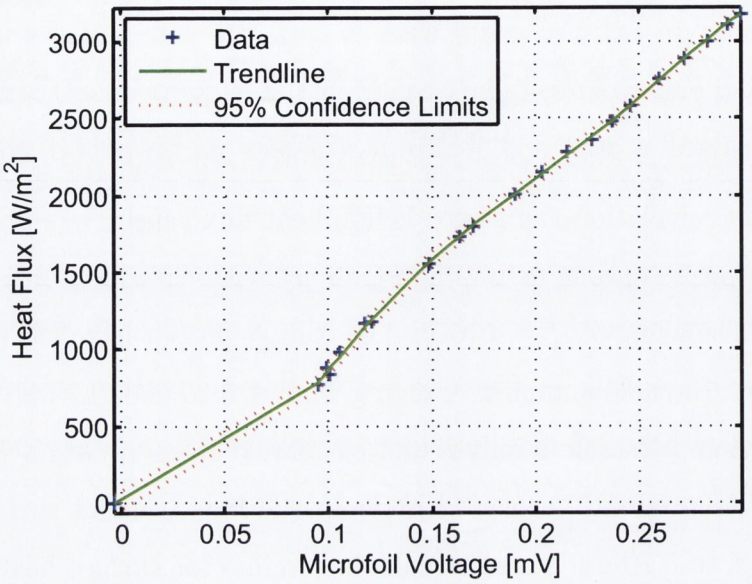

Figure 5.9: Micro-Foil® heat flux calibration data

The calibration data along with a polynomial regression uncertainty is plotted in figure 5.9. The overall slope of the graph $1.11 \times 10^7 \frac{W/m^2}{V}$ is comparable with the calibration certificate which was supplied with the sensor by the manufacturers at $1.07 \times 10^7 \frac{W/M^2}{V}$, presented in Appendix B. Due to the nature of the heat transfer profile a wide range of heat fluxes can be measured throughout a test, as such it would not be appropriate to present just one value of uncertainty in the polynomial regression. Figure 5.10 shows both the precision limit and uncertainty in the regression curve. An expected maximum calculable error of 6% occurs at the lowest heat flux of $770W/m^2$, with a normal range of approximately 1.6-2.9% across the majority of the calibration.

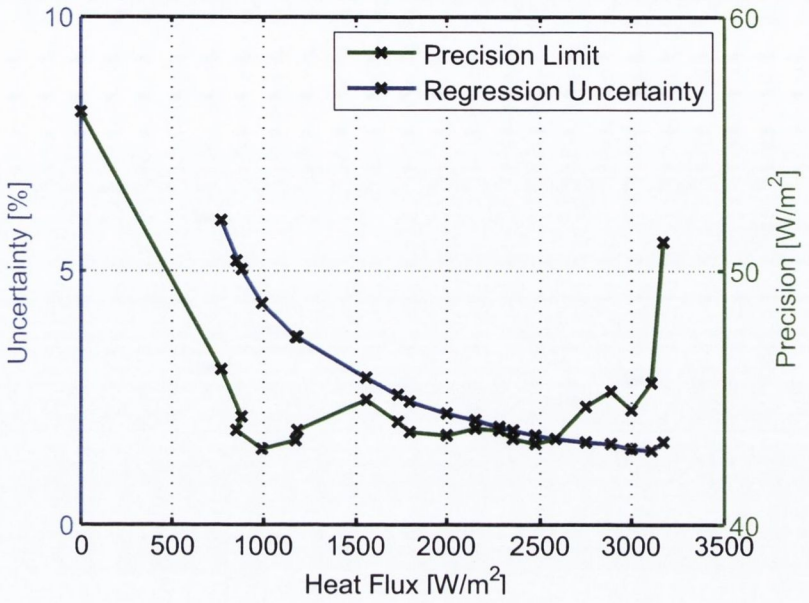

Figure 5.10: Micro-Foil® Regression Uncertainty

5.5 Constant Temperature Anemometry (CTA)

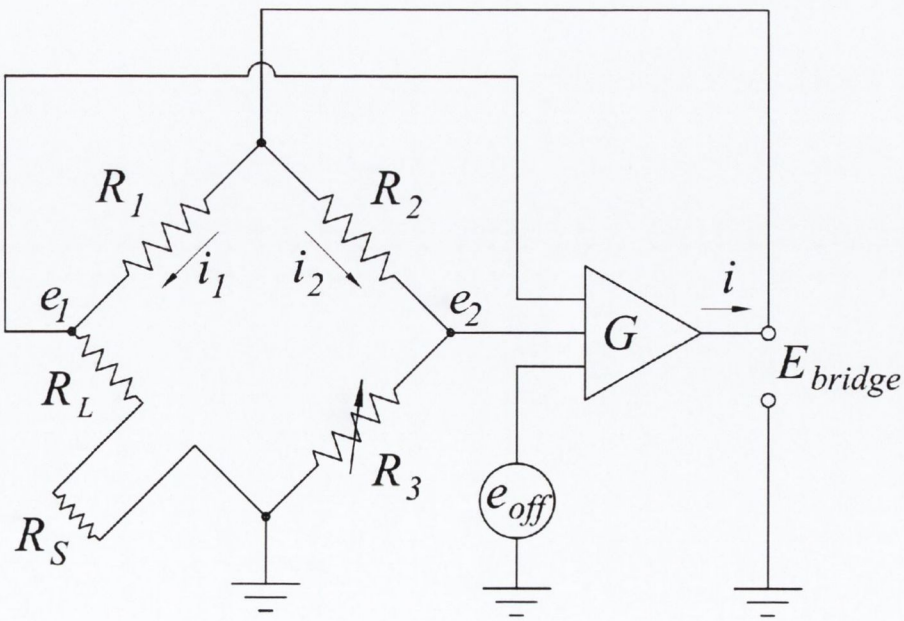

Figure 5.11: Schematic of constant temperature anemometer Wheatstone bridge (CTA) [139]

Figure 5.11 shows a resistive sensor situated in the CTA circuit known as a Wheatstone bridge, where R_S is the active sensor element resistance ($\approx 3\Omega$ for a tungsten wire probe and $\approx 9\Omega$ for a nickel film probe at $20°C$). R_L is the collective resistance of everything between the element and the CTA, generally consisting of prongs, support leads, connectors and cable, where the cable commonly has an inbuilt resistance ($R_L \approx 1.5\Omega$). Heating of the sensor element occurs when the bridge top voltage E_{bridge} is active. The amount of heating is dictated ultimately by the resistances in both arms, $R_1 + R_L + R_S$ which is fixed, and $R_2 + R_3$, where R_3 is the decade resistance which is variable. The current i_1 flowing through the left arm of the bridge can be controlled by choosing a suitable decade resistance; as this flow of current results in the heating of the element a specific overheat can be achieved. While the sensor temperature T_S for hot-wire probes is usually limited to approximately $300°C$, film probes operate at a much lower temperature, especially when used for the purposes of heat flux measurements. To apply the conservation of energy law across the sensor element conduction to the prongs and radiative heat transfer to the surroundings must be neglected:

$$R_S {i_1}^2 = \frac{kNu}{l} A_S (T_S - T_a) \tag{5.12}$$

k is the fluid conductivity, l the sensor characteristic length, A_S the surface area of the sensor exposed to the flow and T_a the ambient temperature. The relationship between sensor resistance R_S and temperature T_S are dictated by the temperature coefficient of resistance and is applied as follows:

$$R_S = R_{S,20}(1 + \alpha_{20}(T_S - 20)) \tag{5.13}$$

$R_{S,20}$ and α_{20} are the sensor resistance and temperature coefficient of resistance (TCR) respectively, both measured at the reference temperature of $20°C$. The TCR is calculated as follows:

$$\alpha_{20} = \frac{R_{S,21} - R_{S,20}}{R_{S,20}} \tag{5.14}$$

An overheat ratio a must be applied to the probe, where a is defined as the ratio

of operating resistance to that at ambient temperature $a = R_S/R_{S,20}$. An overheat ratio of 1.8 is common for wire probes to achieve the previously stated operational temperature of $300°C$.

To convert the measurements for convective heat transfer outlined by the above equations to fluid velocity the empirical relationship known as King's law outlined in Chapter 2 in Bruun [140] must be applied.

$$R_S {i_1}^2 = (T_S - T_a)(A + BU^n) \tag{5.15}$$

A, B and n are correlation parameters with respect to a known velocity U. These parameters are determined during probe calibration.

By looking at the left hand side of equation 5.15 it can be seen that the sensor can be operated in two different modes depending on bridge configuration. Either the sensor resistance R_S (which is equivalent to T_S) can be kept constant to operate as a constant temperature anemometer (CTA), or the current i_1 can be kept constant, operating as a constant current anemometer (CCA). While both methods of operation have their own advantages and disadvantages it has been found that, due to the main limitation of the bandwidth of a CCA system being that of the wire's thermal inertia $\rho_S C_S l D^2$, the CCA method of operation is less suitable for velocity measurements.

To optimise the frequency bandwidth obtainable by a CTA and to minimise the noise it is necessary to ensure the largest possible current (i_1) flows through the probe. Going back to the CTA circuit shown in figure 5.11 it can be seen that to achieve this, the resistance in the passive, right hand side of the Wheatstone bridge (R_2 and R_3) is normally larger than the active, left hand side (R_1, R_L and R_S). This is controlled by what is known as the bridge ratio ($R_2 : R_1$) and has a normal operational ratio of $20 : 1$ for regular wire probe setups, but can be varied to $10 : 1$ ratio for high-power applications, for example film probes in high velocity water flows.

To balance the bridge for the desired overheat and bridge ratio the resistor R_3 is set. This ensures the bridge is in a state of equilibrium, with the voltages e_1 and e_2 being equal. Now that the conditions for left hand side of equation 5.15 have been achieved we turn our attention to the right. It can be seen that this side of the equation

is governed both by the fluid velocity U and the temperature differential $(T_S - T_a)$, however as T_S is held constant, the ambient temperature T_a is in fact the determining factor.

An increase in convective heat flux from the sensor is thus caused in two ways; by either increasing the fluid velocity U, or by decreasing the temperature of that fluid T_a. Either of these events will result in a decrease in the sensor temperature T_S, and consequently its resistance R_S. This change in resistance has the effect of producing an imbalance between e_1 and e_2 and so the voltage differential $e_1 - e_2$ is fed back to the inverting bridge amplifier G which increases the output voltage E_{bridge}. The increase in E_{bridge} at the Wheatstone bridge top junction has a corresponding increase in the current fed to the sensor i_1. In effect there is a greater amount of electrical power going to the sensor resulting in an increase in the sensor temperature; when the temperature returns to a value that puts the bridge resistances back in equilibrium the balance between e_1 and e_2 is restored. In this way the bridge voltage E_{bridge} is correlated to the convective heat transfer from the sensor.

There are a number of additional functions built into the Dantec CTA hardware, such as a signal conditioner which includes both low and high-pass filters and DC-offset and gain control functions. When small fluctuations need to be measured or signal range is poor the signal conditioner provides enhanced resolution and can amplify signal range with the A/D converter. The low-pass filter can also help remove unwanted high frequency noise from the CTA signals and also prevent signal aliasing.

This study employed a Dantec[4] Streamline^{TM}hot-wire anemometer in conjunction with a 90C10 constant temperature anemometer module. The maximum bandwidth for this hardware for an airflow of 30 m/s is approximately 30 kHz rising to over 300 kHz above 100 m/s.

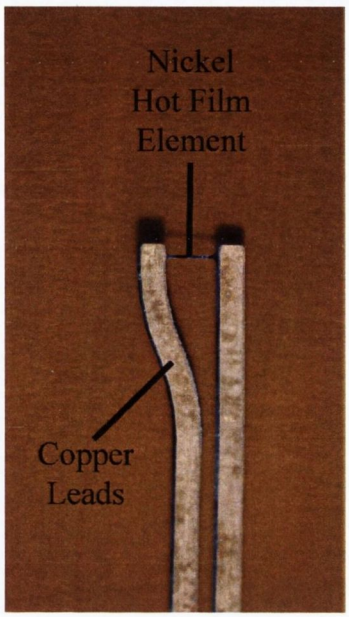

Figure 5.12: Hot-film Sensor

5.6 Senflex Hot-Film Sensor

The hot-film sensor seen in figure 5.12 is capable of time varying or fluctuating heat transfer measurements. This sensor consists of copper leads on a thin ($51\mu m$) Upilex ® C Polyimide film substrate. A nickel sensor element of dimensions $1.2 \times 0.1mm$ has been electron beam deposited onto the Polyimide substrate to a thickness of $\leq 0.2\mu m$. The film is operated by a Constant Temperature Anemometer (CTA) from Dantec Dynamics; this hardware controls the film temperature. As described in the previous section, the CTA is essentially a wheat-stone bridge circuit (figure 5.11) where the hot-film is considered to be one of the resistors in the bridge. It is therefore possible to vary the temperature of the hot-film by varying the resistance values of the other resistors within the bridge. The bridge voltage, or the voltage required to maintain the temperature overheat in the hot-film is used to calculate the heat flux:

$$Q_{diss} = (V_{bridge}^2 - V_0^2)\frac{R_S}{(R_p + R_2)^2} \tag{5.16}$$

[4]Dantec Dynamics, Garonor Way, Royal Portbury, Bristol, BS20 7XE, England, UK. (http://www.dantecdynamics.co.uk)

$$R_p = R_S + R_L \tag{5.17}$$

where Q_{diss} is the electrical power dissipated in the hot-film, V_{bridge} and V_0 are the voltage across the Wheatstone bridge under test conditions and zero flow conditions respectively, R_S , R_p and R_2 are the hot-film element resistance, the resistance of the entire probe arm in the Wheatstone bridge and the top resistance (normally 20Ω) in the Wheatstone bridge respectively. The effective surface area of the hot-film sensor is required for the calibration of the sensor and can be calculated by combining equations 5.16, 5.7 and 5.18:

$$q = hA_{eff}(T_{film} - T_{jet}) \tag{5.18}$$

$$A_{eff} = \frac{R_S(V_{bridge}^2 - V_0^2)D}{0.585(R_p + R_2)^2(T_{film} - T_{jet})kPr^{0.4}Re^{0.5}} \tag{5.19}$$

where A_{eff} is the effective sensor element area when an overheat is active; in air this is normally a number of times larger than the film's physical geometric area. Finally, the effective area can be used to calculate the heat flux:

$$q_{diss} = \frac{Q_{diss}}{A_{eff}} \tag{5.20}$$

Several investigations have used hot-film sensors to perform heat flux measurements such as Baines and Keffer [141], Scholten and Murray [131] and more recently O'Donovan *et al.* [132]. O'Donovan et al. used the hot-film sensor in a similar setup to the one employed in this report for heat transfer measurements in the transitional wall jet region for an impinging continuous air jet. It is necessary that the temperature of the film be greater than that of the surface in order to achieve high sensitivity, this is known as the "sensor overheat".

As the temperature of the hot-film surface can vary during the test from the temperature it had when the value V_0 was measured, and because even a small deviation in temperature difference combined with the small sensor thickness leads to high heat transfer variations, additional conduction through the substrate has to be accounted for. The additional conduction term can be written as:

$$q_{cond} = k_{kapton} \frac{T_{surf} - T_{surf,0}}{\delta} \tag{5.21}$$

where k_{kapton} is the thermal conductivity of the Kapton substrate, T_{surf} and $T_{surf,0}$ are surface temperature under test conditions and zero flow conditions respectively and δ the thickness of the sensor substrate. This is added to the heat flux originating from the dissipation of electric energy to give the convective heat transfer rate:

$$q_{conv} = q_{diss} + q_{cond} \tag{5.22}$$

and so the Nusselt number is then calculated as follows:

$$Nu = \frac{q_{conv} D}{k(T_S - T_\infty)} \tag{5.23}$$

where T_S is the sensor element temperature.

As is evident from equation 5.16 the heat flux from the hot-film sensor is dependent on both operational voltage and sensor resistance. While the voltage V_{bridge} is measured during an experimental test, it is the only quantity in equation 5.16 that varies depending on heat flux Q_{diss}, all other values are either known, fixed quantities, or must be pre-calibrated. The resistance of the sensor element R_S is a quantity which varies linearly with temperature, it must be calibrated so that the decade resistance can be set accurately in order to achieve the desired overheat under test conditions. Calibration was undertaken in situ. A pre-calibrated high precision Resistance Temperature Detector (RTD) was placed securely on the impingement plate as close as possible to the hot-film sensor element. The impingement plate and sensors were heavily insulated with fiberglass insulation making sure to leave no air gaps in order to achieve as uniform a temperature as possible within the insulated envelope. The plate and sensors were incrementally heated from $25°C$ to $82°C$ making sure to leave adequate time for settling. To obtain the most accurate measurements possible, at each step the resistance of the probe arm was measured using the bridge balancing function; returning the exact resistance of the probe arm as experienced by the CTA itself. The recorded calibration data is presented in figure 5.13.

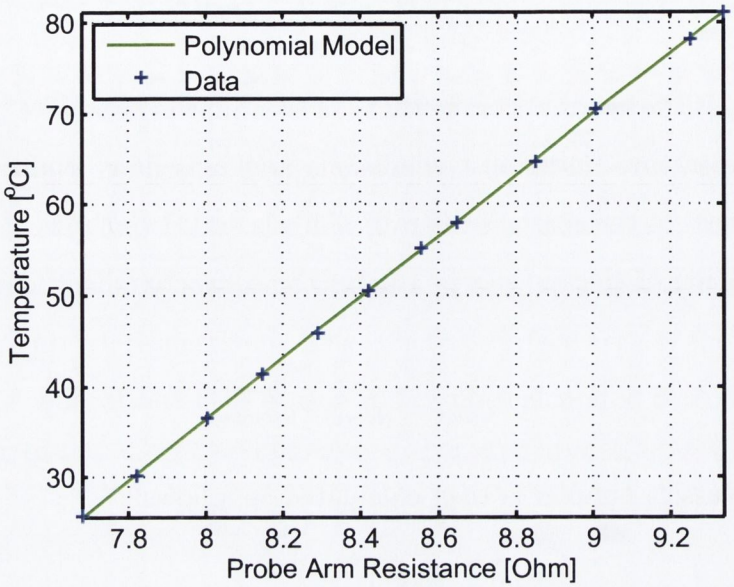

Figure 5.13: Hot-film calibration data

The relationship between the probe arm and the temperature can be seen to be linear; as such a linear fit is applied to the data. Equation 5.24 describes this relationship:

$$R_p = 0.29843T - 6.9137 \tag{5.24}$$

where the probe resistance R_p is comprised of the sensor resistance R_S and the connecting leads resistance R_L as shown in equation 5.17. The resistance of the connecting leads was measured by short circuiting the probe arm close to the sensor element and balancing the bridge once again. The resistance of the leads was measured at $R_L = 0.627\Omega$. The corresponding uncertainty for an operational film temperature of $70°C$ is 0.1% with a precision limit of $0.341°C$.

As the measurement of the heat flux is reliant on the effective surface area of the hot-film (equations 5.19 to 5.23) the experimental uncertainty is calculated from this value. The uncertainty in Nusselt number for a 95% confidence limit was calculated at 21%.

5.7 Hot-wire Probe & Dantec CTA Control

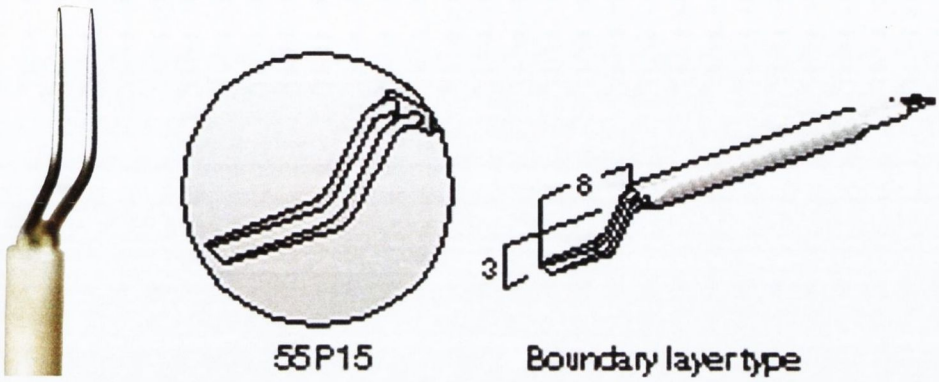

Figure 5.14: Image and dimensions of boundary layer type hot-wire probe 55P15

A number of different types of wire probe's have been used throughout this work. The probe pictured in figure 5.14 was used to acquire velocity data in the boundary layer of the impingement surface. The 55P15 was supplied by Dantec Dynamics and has offset prongs, with a tungsten wire sensor $5\mu m$ in diameter and $1.25mm$ in length orientated perpendicular to the probe axis. This probe is specifically designed to operate within boundary layers as the shape of the prongs permits measurements close to a solid wall without disturbance from the probe body which is positioned out of the boundary layer. The probe axis is mounted parallel to the direction of flow. The measurement principles and signal analysis for these types of wire probes have been described by Bruun [140]; these same principles can be applied to a number of sensors including film sensors, as discussed earlier, and fibre sensors.

5.8 Hot-wire Probe Calibration

As the hot-wire probe was operated in a thermal boundary layer it was necessary to calibrate it for both velocity and temperature. The maximum operating temperature the probe was required to work in was dictated by the operational temperature of the heated surface, which was $60°C$. The minimum was that of the ambient air temperature at approximately $20°C$. The velocity range was dictated by the performance

characteristics of the synthetic jet. At peak performance the jet would be producing a flow velocity of $15m/s$ at the orifice exit, although this was expected to be diminished prior to impingement upon the plate. Once these upper and lower operational limits were identified, the calibration limits were set at a temperature range of $20 - 70°C$ and a velocity range of $0 - 15m/s$.

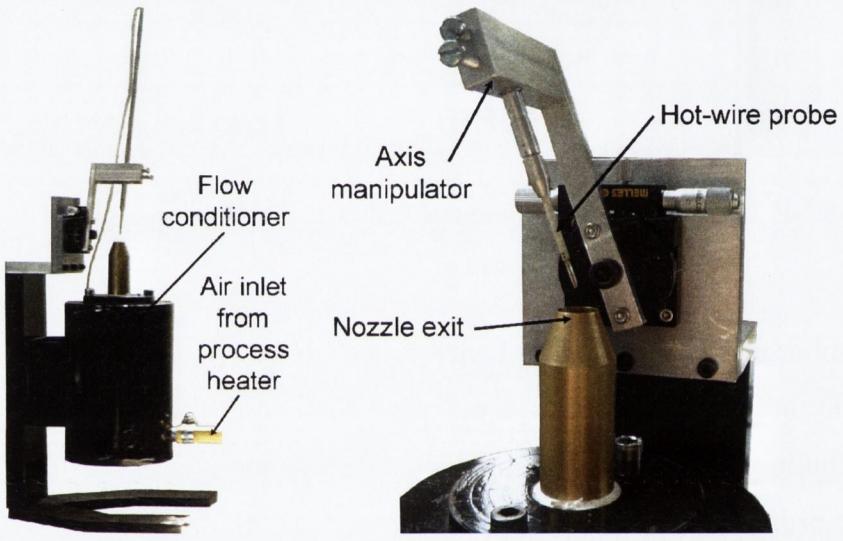

(a) (b)

Figure 5.15: Hot-wire calibration facility

The apparatus shown in figure 5.15 was used to calibrate the hot-wire probe. This apparatus was custom built in-house and consisted of a compressed air line feeding a computer controlled mass flow controller. Prior to entering a flow conditioner (figure 5.15 (a)) the air was heated by an in-line process heater. Inside the body of the flow conditioner is a large chamber which the air initially enters, at the top of the chamber, prior to entering the nozzle, is located a fine scale mesh designed to straighten the flow and break up any large scale structures which remain. The nozzle is approximately five diameters in length with the base of the nozzle being contoured to ensure a smooth flow. This setup ensures a uniform and steady velocity profile is formed at the nozzle exit. As the heated air exits the flow conditioner through the brass nozzle it engulfs the hot-wire held in position by a yaw manipulator, as can be seen in figure 5.15 (b).

The angle of the yaw manipulator can be adjusted depending on what type of probe is being calibrated, but for the type of probe and experimental setup used in this work an angle of 90° to the flow was required. The exit nozzle for the flow conditioner is interchangeable to enable the calibration of different velocity ranges.

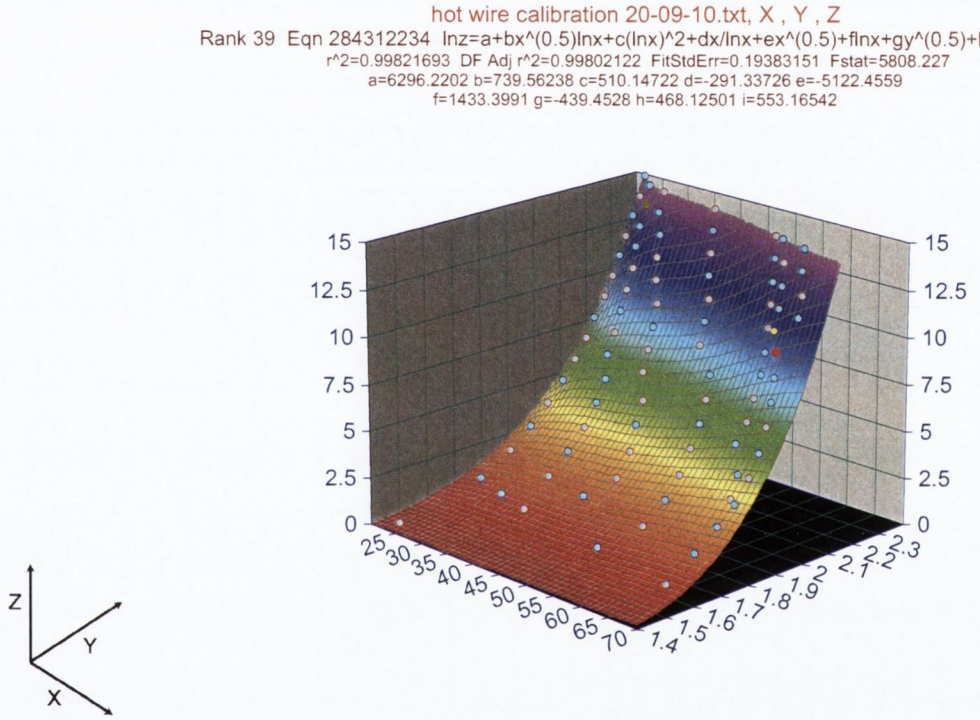

Figure 5.16: Surface fit for hot-wire calibration data. x-axis: temperature $[^oC]$, y-axis: voltage $[V]$, z-axis: velocity $[m/s]$.

Power to the process heater was supplied using an Auto Transformer. A change in air temperature was experienced when either the air flow rate or the power to the process heater was changed; to ensure a stable air temperature was achieved at nozzle exit it was necessary to allow a reasonable amount of time for the system to reach equilibrium. As the mass flow controller was positioned before the process heater it was necessary to correct the velocity calculation for the increase in volume with temperature. This was achieved by continuously measuring the air temperature at the inlet to the mass flow controller and at the nozzle exit using two calibrated thermocouples. The gas law relationship was used to correct for temperature effects:

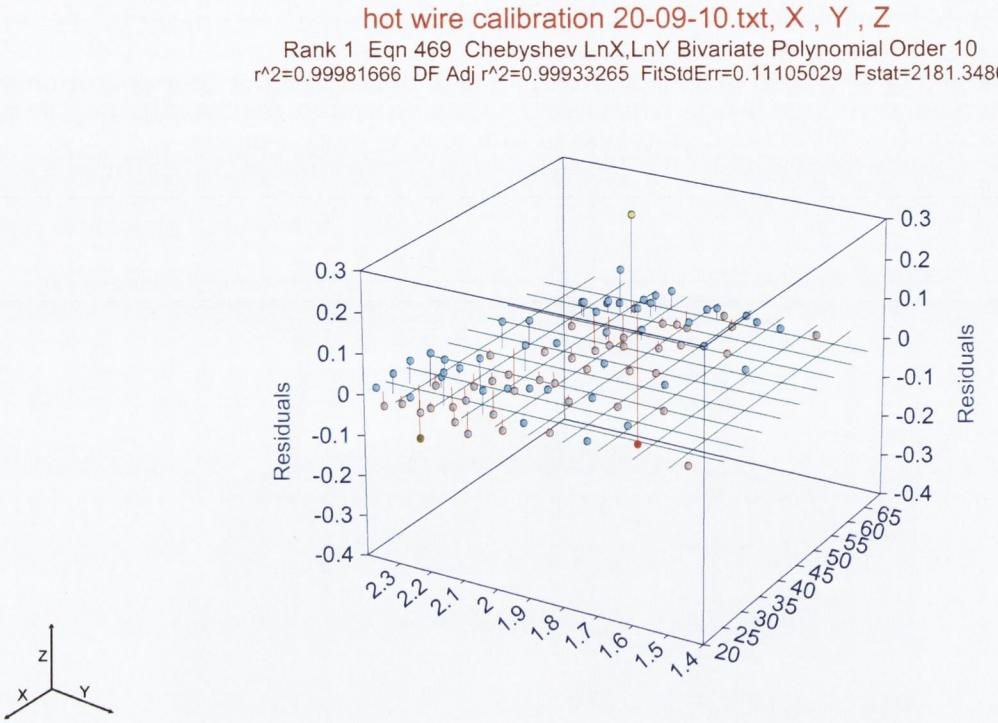

Figure 5.17: Residual error from the hot-wire calibration surface fit. x-axis: temperature [^oC], y-axis: voltage [V], z-axis: velocity [m/s].

$$\frac{P_c V_c}{T_c} = \frac{P_h V_h}{T_h} \tag{5.25}$$

where P, V and T represent pressure, volume and temperature respectively and the subscripts c and h refer to the fluid in its cold and hot state. Temperature is measured in degrees Kelvin. As the pressure at both stages in the system are the same ($P_c = P_h$) and mass flow rate is conserved we can deduce that:

$$U_h = U_c \frac{T_h}{T_c} \tag{5.26}$$

where U relates to flow velocity. With a maximum temperature differential of $50K$ this could account for a velocity correction of over 17%. Calibration results were subsequently put into the software package TableCurve 3D where the best numerical fit was obtained for the data; this is presented in figure 5.16. The residual errors from this curve can be seen in figure 5.17. The fit is quite good across the velocity

and temperature range with a regression uncertainty value of 0.18%. A function in TableCurve 3D enabled the exportation of the three dimensional calibration as a MATLAB function which made subsequent data conversion from the recorded voltages and temperatures into velocities more convenient. It is worth noting that accuracy of the calibration can be influenced by flow oscillations, high turbulence intensity, and flow reversals.

5.9 Temperature Probe & Control Module

The temperature probe is operated upon the same principle as the hotwire outlined above, although in constant current (CCA) mode. The temperature probe is designed for measurement of fast temperature fluctuations in heat transfer studies. The temperature module operates as a resistance thermometer using probes with a fine wire sensor, typical $1\mu m$ in diameter. The output voltage is a linear function of the temperature and can be optimised by offset and gain amplifiers and high-pass or low-pass filters which are integrated into the module. The probe current can be adjusted according to wire type to provide maximum temperature sensitivity without heating the wire. According to section 7.4.3 of Bruun [140] the frequency response for a very thin wire operated in constant current mode at a very low overheat is determined solely by the thermal inertia. The time constant M_t for hot-wire of length l and diameter d is governed by the following equation:

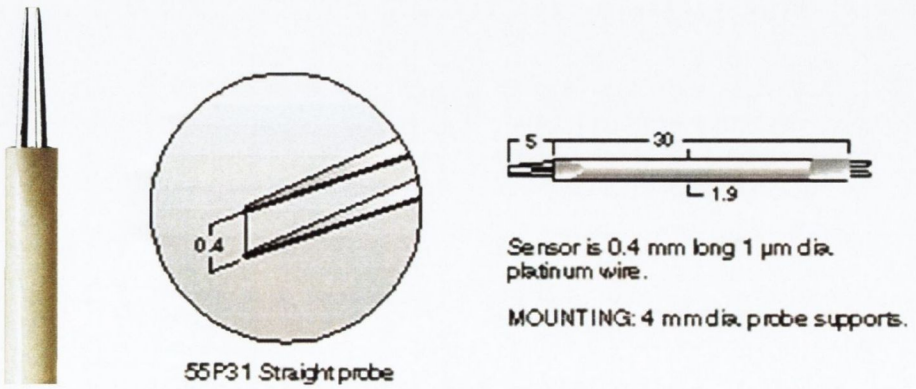

Figure 5.18: Image and dimensions of cold-wire temperature probe type 55P31

$$M_t = \frac{\rho_S c_S (\pi/4) d^2 l}{\alpha_0 R_0 (A + BU^n - I^2)} \tag{5.27}$$

where ρ_S and c_S are sensor density and heat capacity respectively, α_0 and R_0 are the temperature coefficient of resistance and element resistance at zero degrees Celsius and I is the current delivered to the bridge. A, B and n are calibration constants and U the fluid velocity. Using equation 5.28 the relationship for the time constant can be expressed in terms of Nusselt number.

$$Nu = \frac{E_S^2}{R_S \pi l k \Delta T} \tag{5.28}$$

$$M = \frac{\rho_S c_S d^2}{4kNu} \frac{R_S}{R_a} \approx \frac{\rho_S c_S d^2}{4kNu} \tag{5.29}$$

where E_S is the voltage across the sensor wire, k is the thermal conductivity of the sensor wire and R_a and R_S are the active and ambient sensor resistance respectively; although with such a low overheat, ambient and active temperatures are close enough so that $R_S/R_a \approx 1$.

The type of probe employed in this investigation is a Dantec Dynamics Type 55P31 Resistance Thermometer probe which is capable of measuring a 1^oC temperature fluctuation up to $2 - 3kHz$ at approximately $10m/s$. All adjustments are performed manually from the front plate of the control module.

As the resistance of the temperature probes element has a linear relationship with temperature, calibration proved quite straightforward. The probe was placed in a custom made, semi-enclosed Perspex® box along with a calibrated thermocouple. The box was placed on the copper plate seen in figure 4.1 with the open side down and the whole plate was covered with a thick layer of fibreglass insulation. The temperature probe and assembly was incrementally heated using the heating plate, making sure to leave a number of hours between each temperature measurement to allow for settling. While the probe operating temperature varied from ambient temperature

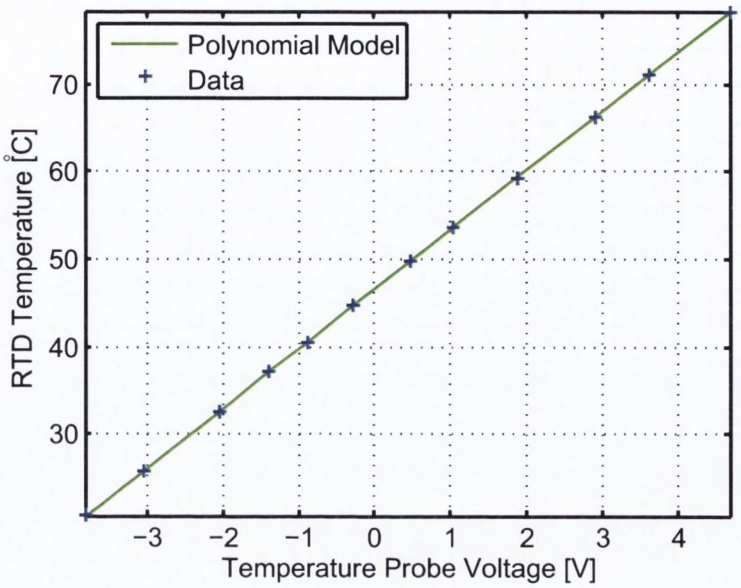

Figure 5.19: Temperature probe calibration data

to plate surface temperature, its average operating temperature when the jet is active is approximately $40°C$. Although calibration data was recorded for temperatures between $20°C$ and $80°C$ the nature of the straight line relationship between temperature and voltage meant this was extendable to the temperature module's maximum voltage range of $+5V$ and $-5V$, giving an effective temperature range of between $12°C$ and $81°C$. A linear regression was fitted to the data with the following equation representing this relationship:

$$T_{tempprobe} = 6.78767 \times V + 46.5585 \tag{5.30}$$

Figure 5.20 shows both the percentage regression uncertainty and the precision limit across the calibrated temperature range.

Based on an average operational temperature of $40°C$ regression uncertainty for the temperature probe is calculated at 0.02% with a precision limit of $0.05C°$.

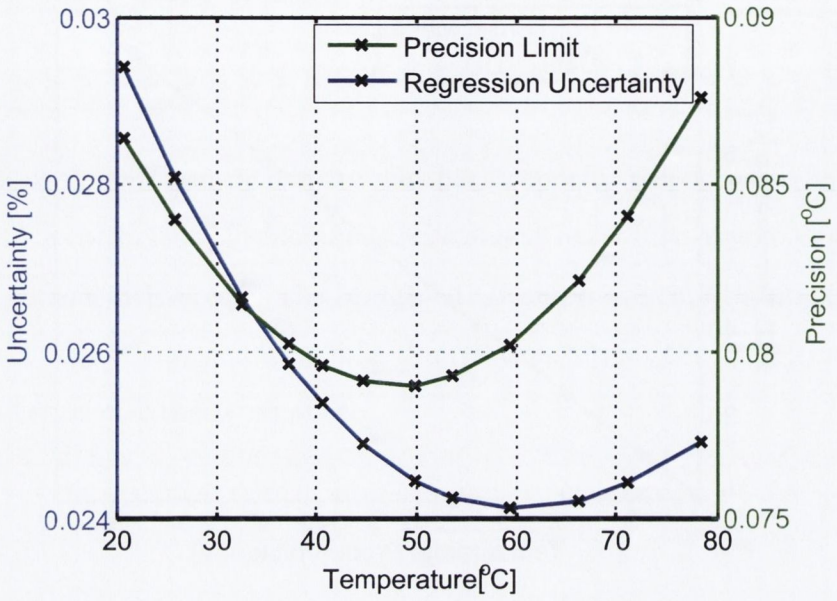

Figure 5.20: Temperature probe regression uncertainty

5.10 Data Acquisition & Processing

Two separate data acquisition (DAQ) boards are used in the experimental setup for the synthetic jet. Both DAQ boards were supplied by National Instruments[5], with the first DAQ, chassis model NI cDAQ-9178 pictured in figure 5.21 (*a*) being used primarily to operate and control the synthetic jet. This chassis employed a number of modules required for the input and output of signals to various instruments. These modules and their specifications are summarised in table 5.2.

All other instrumentation control and data acquisition is performed using a DAQ card NI PCI-6036E and breakout board NI SCB-68 as seen in figure 5.21 (*b*); this

[5]National Instruments Corporation (U.K.) Ltd. Measurement House, Newbury Business Park, London Road, Newbury, Berkshire. RG14 2PS, UK. (http://www.ni.com)

Module	No. of channels	Voltage	Sample rate	Description
NI 9201	8	±10	$500kS/s$	12-bit analog input
NI 9263	4	±10	$100kS/s/channel$	16-bit analog output
NI 9211	4	±0.08	$14S/s$	24-bit thermocouple input

Table 5.2: DAQ module specifications

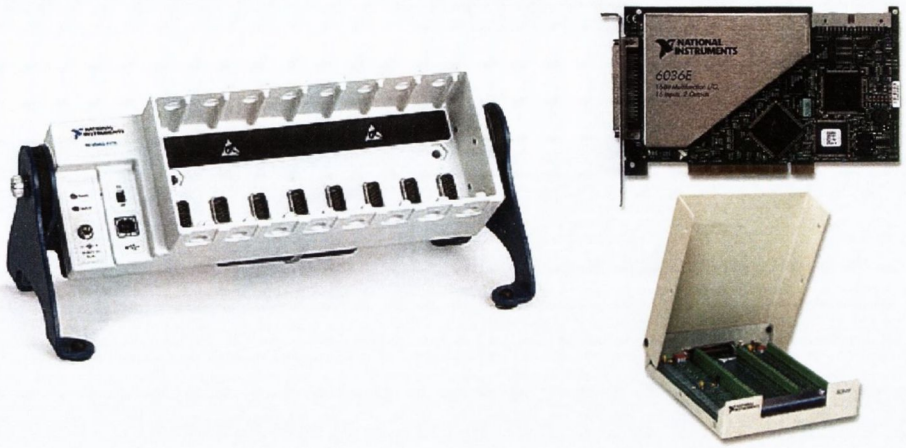

(a) NI cDAQ-9178

(b) NI PCI-6036E and NI SCB-68

Figure 5.21: DAQ modules

board can acquire data at a rate of up to $200kS/s$ and has 16-bit resolution. The board can operate either a maximum of 16 referenced single ended or 8 differential input analogue channels and also has 8 digital I/O channels. All of the sensors provide output voltages, which relate to temperatures, heat flux and velocities. This system is also used to control the stepper motor used to traverse the instrumented plate beneath the jet.

A visual interface (VI) program constructed and operated with the LabVIEW software package was used to view the signals from each sensor in real-time, to record data over an extended period and also to set up and control the various elements of the experimental rig. A number of calibration coefficients are integrated in this program so that accurate readings can be viewed in real-time. LabVIEW drivers for StreamLine have also been implemented to control the operation of the CTA centrally. This software ensures the highest degree of accuracy is obtained during testing with precision control of all the CTA's functions, including the ability to automatically balance the bridge and reset the hot-film overheat to a precise temperature with a change in radial location. This real-time automated interface is instrumental in the setup and execution of an experimental test. Test results are obtained in the form of tab delimited matrices

stored in ASCII formatted text files. These files are subsequently exported, processed and plotted using the numerical software package MATLAB. Custom code has been written in MATLAB in which any further calibrations are applied to the input data and the relevant calculations, processing and plotting of the results is undertaken.

5.11 Particle Image Velocimetry (PIV)

Particle Image Velocimetry (PIV) has been employed extensively in this research to provide flow field visualisation and velocity measurements. The PIV system comprises of a laser system, high speed digital camera, and data acquisition and processing software. In order to perform PIV measurements the area of interest must contain an amount of minute tracer particles known as seeding, these particles enable the illumination of the flow field by the laser; the light reflected by the seeding is then recorded by the camera. The entire PIV system was supplied by LaVision [6].

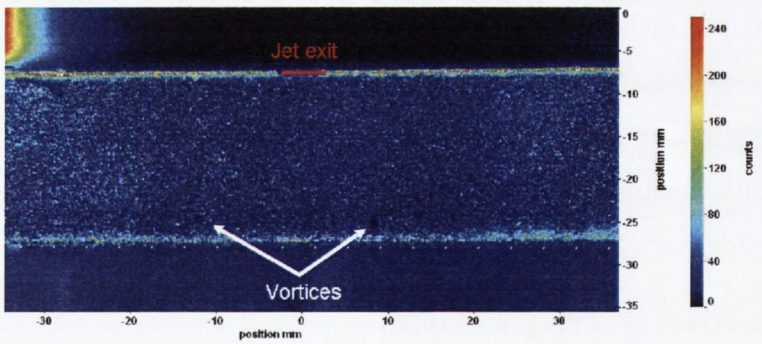

Figure 5.22: Typical PIV image for an impinging synthetic jet, $H/D = 4$, $Re = 3000$, $L_0/D = 6$

The operational principle of PIV is based on tracking the movement of seeding particles which are assumed to follow the flow. By measuring the displacement of particles within an interrogation window between subsequent camera frames of known time separation a correlation relating to the particles velocity is calculated, and hence the fluid velocity can be calculated. Applying these calculations across the whole area

[6]LaVision GmbH, Anna-Vandenhoeck-Ring 19, D-37081 Goettingen, Germany. (http://www.lavision.de/)

between two subsequent frames provides an instantaneous velocity measurement of the entire flow field; this technique can be repeated for a series of frames to provide a time series evolution of the flow velocity.

The laser system employed in this setup includes dual Quantronix Darwin Duo high repetition Nd:YLF lasers (neodymium: yttrium lithium fluoride, $\lambda = 527nm$, $0.1 - 0.3J/s$ at $1000Hz$) employed with a beam combining system fitted within the one laser body; this allows for short duration (in the order of nanoseconds), high frequency (up to $4700Hz$) pulses, with minute time separation ($\Delta t \approx 6\mu s$). The laser beam is directed from the laser head to the measurement plane through the use of a manoeuvrable optical arm. The arm consists of straight aluminium tubing with a number of joints fitted with specialised optics, providing a significant degree of freedom and flexibility. A cylindrical lens located in the head of the arm converts the laser beam into a thin light sheet which can be aligned perpendicular to the jet exit and the impingement surface to form the measurement plane. The light sheet was approximately $1mm$ in thickness across the measurement plane.

The accuracy of PIV is heavily reliant on the suitability of seeding in two key ways; the particles should (i) follow the motion of the flow faithfully and (ii) scatter light from the laser sheet shining across the measurement plane uniformly. Seeding was provided in the form of smoke particles generated by a Pea Soup [7] Colt 4 Portable Smoke Generator. This smoke generator uses an oil based aerosol to produce seeding with a particle size of $0.2 - 0.3\mu m$ mass median diameter; this meets with the requirements outlined above.

A high speed CMOS (Complementary metal-oxide-semiconductor) digital camera (Photron[8] HighSpeedStar 6, $1024x1024$ pixels, 12-bits per pixel, 8GB on-board memory) was used to record images of the flow field containing the illuminated seeding particles; a typical image can be seen in figure 5.22. All PIV images in this study were acquired at a frequency of $1024Hz$. Camera memory constraints meant that 3118 full

[7]Pea Soup Ltd., 3 Thornwood Avenue, Ingleby Barwick. TS17 0RS, UK. (http://www.pea-soup.com)

[8]Photron Europe Limited, The Barn, Bottom Road, West Wycombe, Bucks. HP14 4BS, United Kingdom. (http://www.photron.com)

resolution frames were captured for $H/D = 8$ and $H/D = 12$, while it was possible to incerease this to 4365 frames at $H/D = 4$ due to the ability to reduce the resolution of the camera at the smaller field of view. These operational parameters resulted in acquisition durations of 3.065 seconds and 4.263 seconds respectively. The chosen high frame rate provides excellent time resolved velocity data, enabling the visualisation of the evolution of an entire synthetic jet period at most operational parameters, while the relatively long acquisition duration and large quantity of frames ensured accurate time averaged results, in particular for the region of most interest; this is something that can prove difficult with such a highly periodic and inhomogeneous flow.

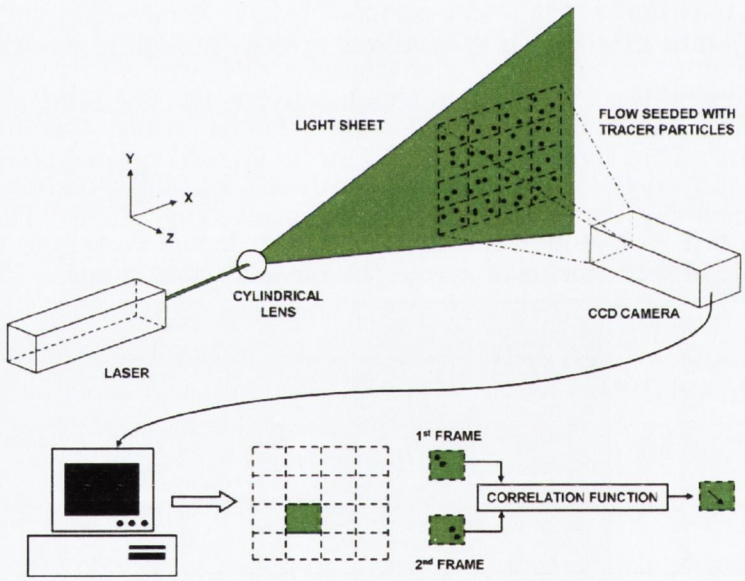

Figure 5.23: PIV schematic [142]

There are two main types of PIV measurement, single exposure PIV and double frame PIV, the latter method being used in this investigation. Single exposure PIV takes single images separated by a specific time interval dictated by the acquisition frequency. Velocity vectors are calculated by measuring particle shift between subsequently acquired frames, with a desirable amount being 5 pixels. While the maximum acquisition frequencies in single exposure PIV systems can be quite good ($< 5000Hz$), acquiring at this rate is only possible for a very short duration because of camera memory constraints, as such this technique is most suited to relatively low velocity flows. Double frame PIV is similar to single exposure PIV in that it also acquires images at

regular intervals dictated by the acquisition frequency. However, while the single exposure technique only takes one image, double frame PIV takes two images separated by a very small time period (in the order of microseconds). The result of this is that the time separation between the two images can be very small, thereby providing a method of obtaining a suitable particle shift in flows of much higher velocity while also maintaining a regular sampling period and long test duration. Disadvantages of this technique include poor velocity calculation in areas of the flow where velocity is particularly low. A PIV measurement technique has recently been developed by Persoons *et al.* [143] which is based on multi pulse separation (MPS) imaging. This technique acquires images with variable pulse separation. Whereas single exposure PIV acquires a sequence of single-frame images, multi pulse separation PIV is more analogous to the double frame technique where frames are acquired at a fixed frame rate. The difference lies in the ability of the MPS technique to acquire double frames with variable pulse separation; thereby increasing the dynamic range of conventional PIV by over an order of magnitude. This result can provide significantly greater accuracy in the measurement of mean flows and turbulence intensity ranges particularly in low velocity regions.

Processing of the raw images was undertaken using LaVision's DaVis 6 software package. Vector calculation involves dividing each image up into a grid of interrogation windows of specific size. Contained in these windows are a number of tracer particles which will be used to calculate the fluid velocity; a minimum of ten particles in each window is desirable. For double frame PIV a correlation function operates on the particle intensities between coincident interrogation windows from the two frames, one vector per window is subsequently produced. The current study calculated vectors using a multi-pass cross-correlation with an interrogation window size decreasing from $64x64$ pixels with a 50% overlap down to $32x32$ with a 75% overlap.

Chapter 6

Analysis Techniques

The literature review presented in this thesis has shown that the synthetic jet flow field is highly complex and can vary greatly depending on operational parameters such as Reynolds number, stroke length, jet spacing and confinement. As such, the resulting flow conditions can result in very different heat transfer effects upon impingement. A number of analysis techniques have been selected and developed which aim to not only reveal aspects of the jet flow, local air temperature and heat transfer mechanisms previously obscured by the highly complex nature of the flow, but also to identify the primary couplings between the mechanisms which drive heat transfer.

While the synthetic jet will always attract comparisons to the continuous jet, there are a number of reasons why analytic techniques commonly used on the continuous jet, while effective in their own right, prove far less useful when implemented on synthetic jets. The fundamentally intermittent nature of the synthetic jet means that many time averaging techniques traditionally used to identify aspects like transitions to turbulence, potential cores and shear layers are rendered ineffective. It is for this reason the following techniques have been selected and implemented in this investigation.

6.1 Proper Orthogonal Decomposition (POD)

The principles and operation of Proper Orthogonal Decomposition (POD) have been explained in section 2.6.2 of the literature review. To date, POD has been a little used technique in the analysis of the synthetic jet. For the purposes of this research,

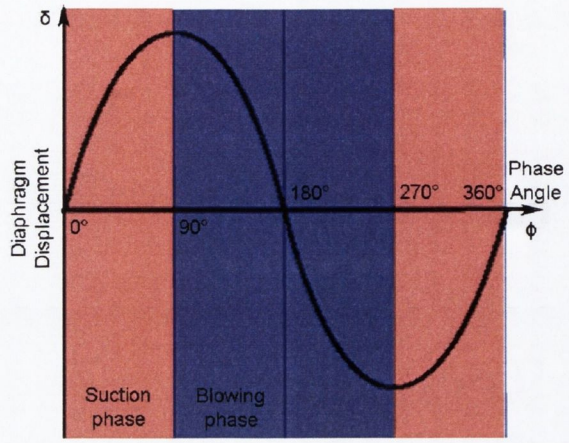

Figure 6.1: Schematic of diaphragm displacement vs. phase angle. Maximum synthetic jet blowing and suction velocities occur at $\varphi = 0^o$ and 180^o respectively.

POD has been implemented in conjunction with high speed PIV so as to decompose the flow field and to isolate the coherent structures from the turbulent flow.

Throughout this chapter instantaneous velocity and vorticity flow fields are presented with a corresponding phase angle φ, this angle refers to the stage at which the oscillating flow through the orifice is captured, as depicted in figure 6.1. The angle of $\varphi = 0^o$ is taken to coincide with the position at which the synthetic jet's diaphragm is in its naturally unloaded state; when the synthetic jet is operating this also corresponds to that of maximum suction velocity. Maximum blowing velocity corresponds to an angle of $\varphi = 180^o$.

Figure 6.2 (a) shows one instantaneous image of the synthetic jet flow field from a PIV time series at a phase angle of $\varphi = 157^o$; once decomposed using POD, the flow field components can be analysed. The red white and blue colour bar represents vorticity with red and blue being in counter clockwise and clockwise rotation respectively. Figure 6.2 (b) shows the percentage energy content captured in each successive mode; a near linear logarithmic relationship between energy content and mode number is clearly visible for this particular decomposed flow field, indicating how effectively this technique can account for significant energy containing flow structures with few modes. The first mode of the jet, shown in figure 6.2 (c), signifies the most energetic mode of operation, with 61.2% of the flow energy captured by this eigenmode. The

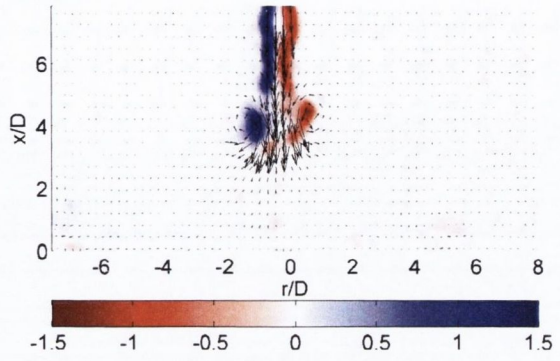

(a) Instantaneous flow field, $\varphi = 157^o$

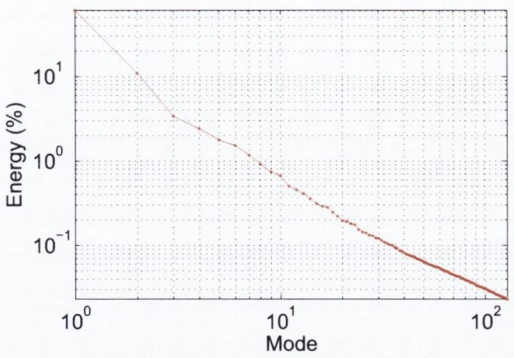

(b) Eigenmode energy

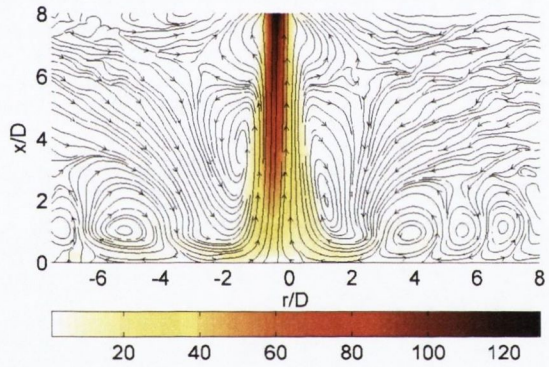

(c) First eigenmode

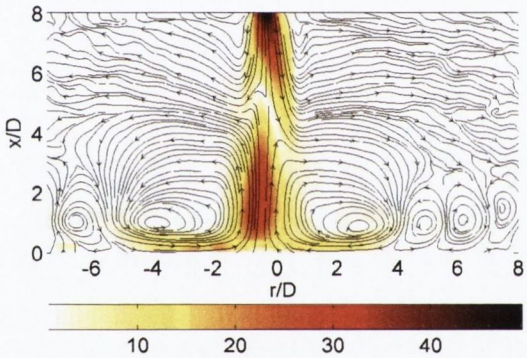

(d) Second eigenmode

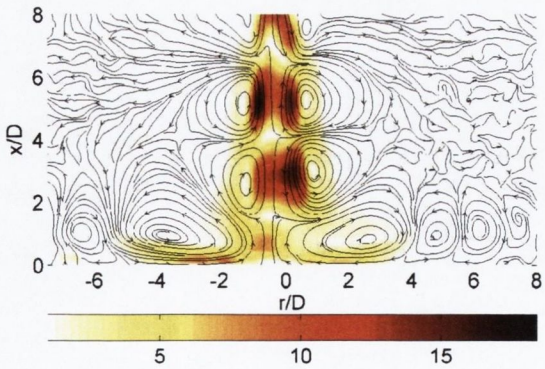

(e) Fourth eigenmode

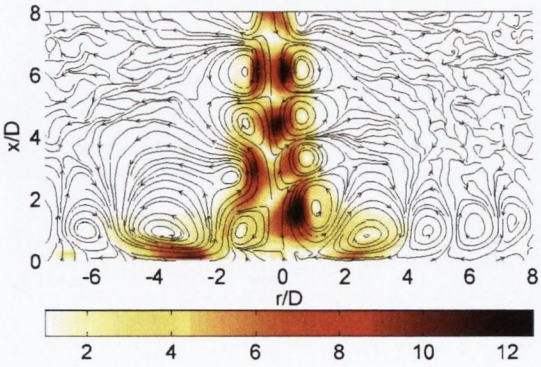

(f) Sixth eigenmode

Figure 6.2: POD decomposition for synthetic jet at $H/D = 8$, $Re = 3000$ and $L_0/D = 32$.

flow field reveals that this mode corresponds to the ejection phase of the jet. The second eigenmode, depicted in figure 6.2 (*d*) accounts for a further 10.9% of the energy within the flow field, this mode can be seen to capture the suction stroke with the vectors at the orifice exit acting in the opposite direction. Figure 6.2 (*e*) shows the fourth eigenmode, this depicts the advection of the primary vortex ring away from the orifice. While only containing 2.4% of the energy, this mode clearly reveals that the coherent vortex is a dominant structure in the flow. Finally, figure 6.2 (*f*) shows the sixth eigenmode. This mode can be seen to still include flow characteristics of the vortex rings but at a significantly reduced energy level. While quite well defined, these vortices only account for 1.5% of the energy content of the flow field, where the sum of all 6 eigenmodes approximate 81.2% of the total energy in the flow field. Further eigenmodes reveal successively smaller and more erratic flows.

6.2 Swirl and Shear

As many of the synthetic jet operational parameters greatly influence the type of flow field formed by the synthetic jet, particularly that of the vortex ring, a method to track the average path and strength of the vortex was developed. An analysis technique outlined by Adrian *et al.* [144] was used to calculate the swirling plus the shear strength of a PIV flow field, it can be calculated as follows:

$$-(E_{xy}.E_{yx} - (E_{xx}.E_{yy})/2 + (E_{xx}^2 + E_{yy}^2)/4) \tag{6.1}$$

and has units of $[s^{-2}]$. E is the strain tensor whose magnitude can be calculated as follows:

$$E_{ij} = \frac{\partial V_i}{\partial j} \text{ where } i \in \{x, y, z\} \;\; j \in \{x, y, z\} \tag{6.2}$$

which is the change (gradient) in the vector component i when going along the j axis.

6.3 Spectral Analysis

In this work the technique of spectral analysis has been applied to a number of simultaneous, time resolved signals including those of heat flux, air temperature and velocity. The primary method of processing and presenting data in spectral form was through the use of the software package MATLAB, which contains a number of functions for such applications; in particular the cross power spectral density (cpsd) function was used. This function estimates the cross power spectral density Pxy of the discrete-time signals x and y using the Welch's averaged, modified periodogram[1] method of spectral estimation. The cross power spectral density can be defined as the distribution of power per unit frequency and is calculated as follows:

$$P_{xy}(\omega) = \sum_{m=-\infty}^{\infty} R_{xy}(m) e^{-j\omega m} \tag{6.3}$$

with the cross correlation sequence being defined as

$$R_{xy}(m) = E\{x_{n+m} {y_n}^*\} = E\{x_n {y_{n-m}}^*\} \tag{6.4}$$

where x_n and y_n are jointly stationary random processes, $-\infty < n < \infty$ and $E\{.\}$ is the expected value operator. All time resolved signals were acquired at a data rate of 8192 S/s for a duration of 16 seconds, the results of this were very large data sets which can prove difficult to analyse. This particular spectral analyser was chosen as it provides a wide range of functionality which can help present results in a more simple and concise form than can be achieved with other more basic spectral analysers. Such functions include control of the fast Fourier transform length which determines the frequencies at which the PSD is estimated and Hamming window size selection which allows control of the number of samples used in each section and, also, the size of the overlap of each window. All spectra produced from hot-film, temperature probe or hot-wire data in this work used an overlap of 0.5 and 32 averages.

The cross correlation equation (6.4), part of the cpsd function, enables the calculation of coherence magnitude between simultaneously acquired signals. When the

[1]The periodogram is an estimate of the spectral density of a signal.

coherence between two signals at a specific frequency is found to be above 0.2 it is generally considered that significant correlation exists; this can prove to be a useful tool when comparing heat transfer data to velocity and air temperature signals.

6.4 Spectral Decomposition

While spectral analysis is by no means a new technique, a new method of interpreting the spectral results was needed to compliment the application of POD. As the objective of POD is to isolate the most energetic aspects of the flow field enabling reconstruction with the most coherent structures it was decided that this must also be the objective for the analysis of the high-frequency, time-resolved data, specifically the velocity, heat flux and local air temperature recordings. As was seen in section 6.1, the primary, and most energetic structures returned through the application of POD to the flow field were clearly functions of the synthetic jet driving frequency, indicated in figure 6.2 (b) and (c) by the capture of the ejection and vortex modes. Consequently, it was determined that to obtain results which enabled comparison to those produced by POD it was necessary to isolate the most powerful spectral frequencies, i.e. the primary synthetic jet driving frequency and its harmonics. This leaves just the more erratic fluctuations present in the flow, which can be attributed to flow evolution and subsequent degradation and can indicate a transition to turbulence. A further step was taken to split the residual frequencies into those above and below the jet driving frequency

The implementation of this technique requires a number of steps to convert data from the raw time series into the three domains, hereafter referred to as the periodic, low and high frequency spectral components. Firstly, the raw data file containing the time-resolved recorded data x, of specific frequency and duration, was imported into MATLAB; an example of this can be seen in figure 6.3 (a). Once imported, these data were converted into the frequency domain, as seen in 6.3 (b), using an inbuilt discrete Fourier transform function $y = fft(x)$, for a vector of length N; this is computed using a fast Fourier transfer (FFT) algorithm:

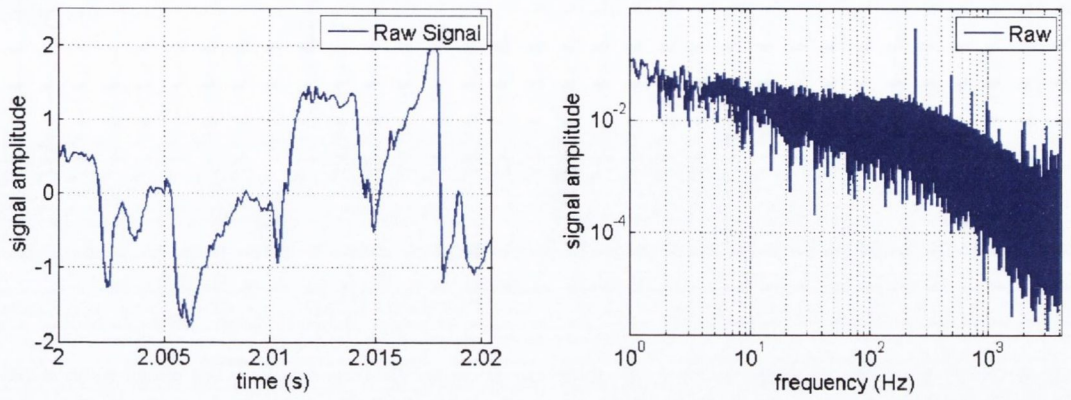

(a) Time-resolved raw signal (b) Raw data displayed in frequency domain

Figure 6.3: Conversion of raw data to frequency domain.

$$X(k) = \sum_{j=1}^{N} x(j)\omega_N^{(j-1)(k-1)} \tag{6.5}$$

where $\omega_N = e^{(-2\pi i)/N}$ and is an Nth root of unity. The resulting frequency spectrum can be seen in figure 6.3 (b).

The second step involves isolating the specific frequencies related to the coherent, high-energy structures in the flow which appear as peaks in the spectrum, some of which are clearly seen in figure 6.3 (b) at the driving frequency ($113Hz$) and its harmonics $n \times 113Hz$. A spectral bandwidth of $1Hz$ above and below the isolated

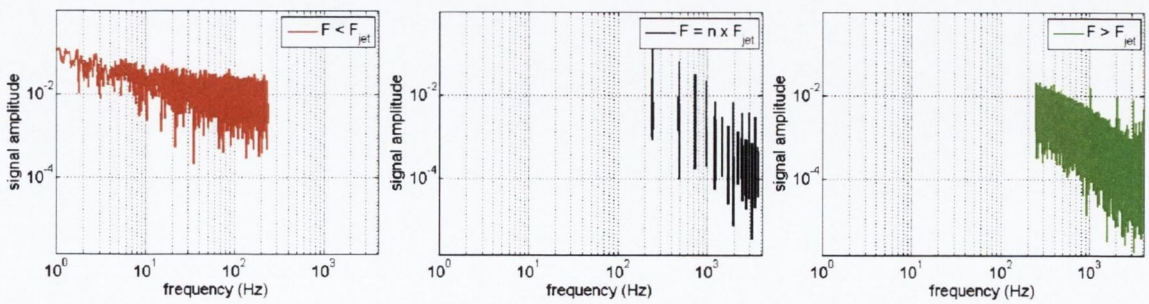

(a) Low frequency domain (b) Periodic domain (c) High frequency domain

Figure 6.4: Frequency isolation and decomposition.

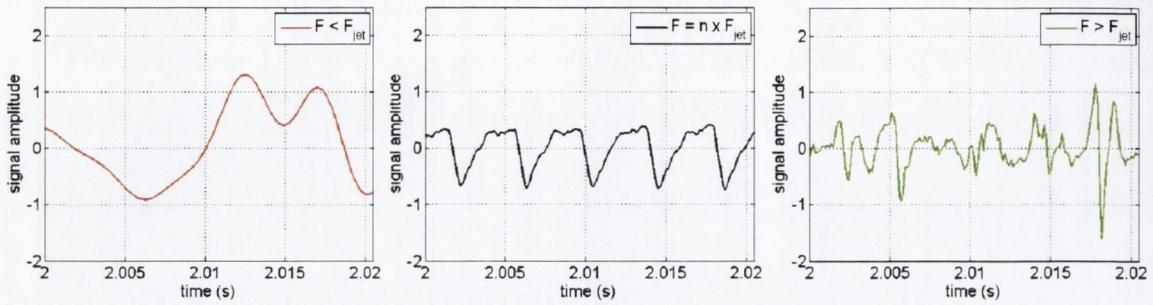

(a) Low frequency signal (b) Periodic signal (c) High frequency signal

Figure 6.5: Reconstructed components of the time resolved signal.

frequencies is also included in the reconstruction of the periodic domain; the result of this isolation can be seen in figure 6.4 (*b*). The remaining spectrum now only contains frequencies which were not generated as a direct result of the periodic ejections of the synthetic jet, moreover they were created by the degradation of the flow from its originally periodic nature. These remaining frequencies are then separated into two further domains, with the first domain lying above the driving frequency of the jet, as seen in figure 6.4 (*c*). These higher energy frequencies are often considered to be indicative of the level of turbulence present in the flow, as energy is dissipated at these smaller scales. The final domain includes the frequencies below the jet driving frequency and can be seen in figure 6.4 (*a*); this domain tends to become more prominent as flow momentum is diminished and lower frequency phenomena dominate in the absence of external excitation.

The final step of the procedure is the reconstruction of the real-time signal by conversion of the respective decomposed spectra back to the time domain. Once again this is done through the use of an inbuilt inverse Fourier transform function $Y = ifft(X)$ in MATLAB. This also employs the reverse of the same FFT algorithm.

$$x(j) = (1/N) \sum_{k=1}^{N} X(k) \omega_N^{-(j-1)(k-1)} \tag{6.6}$$

The reconstructed time-domain signals can be seen in figure 6.5, these correspond to the decomposed spectra presented in figure 6.4. Once the spectrum has been de-

composed into its component parts it is possible to evaluate the level to which the flow is developed. As the periodicity is now decoupled from the general flow, RMS values of each component reflect more accurately the levels of turbulent fluctuation present in the flow; this in turn can enable a more in-depth analysis of the flow development.

As well as presenting fluctuating data in the form of the root mean squared (RMS) of its decomposed components, the RMS of the raw signal is also used. Values for fluctuating Nusselt number Nu', fluctuating velocity V' and fluctuating air temperature T' are presented in this form. These calculations are performed using MATLAB, with the calculation for the RMS of a series x containing n elements being defined as follows:

$$X_{rms} = \left(\frac{1}{n-1} \sum_{i=1}^{n} (x_i - \bar{x})^2 \right)^{\frac{1}{2}} \tag{6.7}$$

where

$$\bar{x} = \frac{1}{n} \sum_{i=1}^{n} x_i \tag{6.8}$$

Chapter 7

Results and Discussion

In this chapter heat transfer and fluid measurement results obtained for an impinging synthetic jet are presented and analysed. Two main flow measurement techniques (PIV and hot-wire anemometry) have been implemented and the results are presented in various forms including instantaneous velocity and vorticity flow field measurements and flow field decomposition using POD which provides information on jet structures and the corresponding mode energy. Local fluid velocity measurements are also presented in conjunction with local surface heat transfer and air temperature measurements. Many of these measurements provide stagnation point data but radial distributions are presented also for simultaneous local surface heat transfer and air temperature. Spectral decomposition and reconstruction is performed on the local measurements to aid with the identification of various flow regimes and transitions. These local measurements are analysed on a time averaged, time resolved basis and also within the frequency spectrum. All Reynolds numbers reported in this work have been calculated using the methid outlined in equation 2.11 unless otherwise stated. It is worth noting that this method of calculation will give a value double that used by authors such as Smith and Glezer [46] calculated in equation 2.9.

There are many parameters which can affect the heat transfer and flow characteristics of an impinging synthetic air jet. These parameters include Reynolds number (Re), non-dimensionalised stroke length (L_0/D), non-dimensionalised nozzle to impingement surface spacing (H/D), orifice geometry and confinement. However,

Re	L_0/D	2	3	4	6	8	12	16	20	24	32	40	48
1000	f (Hz)	160	106.67	80	53.33	40	26.67	20	16	13.33	10	8	6.67
2000	f (Hz)	320	213.33	160	106.67	80	53.33	40	32	26.67	20	16	13.33
3000	f (Hz)	480	320	240	160	120	80	60	48	40	30	24	20

Table 7.1: Approximate synthetic jet operational parameters

the investigations undertaken in this study addresses only the influence of the first three of these parameters. Thus, all tests were performed on a semi-confined synthetic air jet issuing through an orifice of diameter $5mm$ and length $10mm$. Table 7.1 shows the range of Reynolds numbers ($Re = 1000, 2000, 3000$) and dimensionless stroke lengths ($L_0/D = 2, 3, 4, 6, 8, 12, 16, 20, 24, 32, 40, 48$) with the corresponding actuation frequencies which were investigated. The relationship between these parameters is described by equation 7.1. Height above the impingement surface was also varied ($H/D = 2, 3, 4, 6, 8, 10, 12, 16$). This range of parameters covers the various synthetic jet flow regimes, from threshold jet formation at small stroke lengths to a slug flow regime experienced at large stroke lengths and small spacings to a fully developed flow occurring at large orifice to impingement surface separations.

$$f = 0.32\frac{Re}{L_0/D} \tag{7.1}$$

While a range of Reynolds numbers was investigated, particular attention was paid to the Reynolds number of 3000. It was found that where certain trends of interest were present, their dependence on dimensionless stroke length L_0/D and axial spacing H/D was more significant than on Reynolds number. It was decided that a Reynolds number of 3000 was an appropriate operational setting to achieve the desired consistent results. Using the highest Reynolds number in the range helped in overcoming the intermittent, natural buoyancy effects present at the heated impingement surface which can periodically affect levels of heat transfer in a semi-confined setup. It was helpful in achieving a reasonably high level of heat transfer, thereby providing a greater resolution across the range of testing parameters and aiding with the identification of various heat transfer and flow regimes. However, representative results for the Reynolds number of 1000 and 2000 are included for completeness.

As an established flow is required to achieve convective heat transfer, this chapter leads with a comprehensive flow field analysis of the impinging synthetic jet. Firstly, instantaneous flow fields are used to identify individual structures formed at various stroke lengths and how they evolve within the flow field. Time averaged swirl and shear data is used to track the path and strength of the vortex after which volume flux and mean velocity profiles are presented. The final section, addressing the synthetic jet flow field, presents results obtained through Proper Orthogonal Decomposition which depicts the most powerful flow structures and energy containing eigenmodes. The second half of the results section presents heat transfer data corresponding to the flow field data. This section leads with stagnation point heat transfer, local velocity and local fluid temperature data revealing a number of impingement regimes across various stroke lengths. Spectral decomposition is subsequently used on the stagnation point data to further reveal the dominant frequency components involved in each impingement regime. Further stagnation point power and coherence spectra are used to provide correlation data between the heat transfer signal and local fluid velocity and temperature. Radial profiles are reconstructed from the fluctuating Nusselt number and fluid temperature data using the spectral reconstruction methods outlined earlier; these results help reveal the state of the jet upon impingement and how it transitions after impact has occurred.

7.1 Jet Evolution

The two most significant variables in the establishment of an effective flow from a synthetic jet are Reynolds number and stroke length. Before presenting experimental results in the form of heat transfer or flow fields, it is important to understand how changing either of these variables may affect jet formation and subsequent evolution. While Shuster and Smith [48] have shown that Reynolds number can have an effect on the coherence and stability of the vortex once formed, there is no available evidence to suggest that Reynolds number plays a dominant role in the formation and advection of a vortex. In contrast, it has been established that dimensionless stroke length not only plays a key role in jet formation, but also has a significant bearing on flow field

characteristics [145, 20, 48]. It is noteworthy, however, that few authors, with the exception of Cater and Soria [23] and Crittenden and Glezer [25], have investigated the effects of jet formation much beyond $L_0/D = 10$, with neither of these documenting the evolution of an ejection. Some of the most relevant research pertaining to this field of study has been undertaken by Gharib *et al.* [60] where it was established that there exists a universal stroke length $L_0/D \approx 4$, also referred to as formation length, for complete vortex ring formation. Beyond this threshold stroke length the vortex does not increase in size but advects away from the orifice, with subsequent ejected fluid forming a trailing jet following the vortex. Gharib *et al.* presented data primarily for impulsively started jets and a limited number of other velocity programs but none were tested which are directly comparable to the type of velocity program produced by a synthetic jet. Nevertheless, this finding has significant implications for the formation and evolution of the synthetic jet.

Most synthetic jets are formed by applying a voltage in the form of a sinusoidal wave of specific frequency and amplitude across an acoustic speaker, thereby producing both a corresponding deflection in the diaphragm and fluid flow across the jet orifice. As such it is reasonable to consider the velocity program across the orifice of the synthetic jet as that of a sine wave, with adjustments in frequency and amplitude resulting in corresponding changes in Reynolds number and stroke length. For now, however, a constant Reynolds number and hence velocity is assumed. In keeping with the findings of Gharib *et al.* [60] that complete vortex formation occurs at a dimensionless stroke length $L_0/D \approx 4$, we see that figure 7.1 (a) satisfies this requirement; a complete vortex is formed in a single ejection phase of the jet. Significantly, no trailing jet is formed at this stroke length and peak velocity V_{max} occurs half way through vortex formation. Once formed, the vortex convects away from the orifice and the cycle of suction and ejection begins again. Any subsequent increase in stroke from $L_0/D = 4$ will result in the formation of a trailing jet following the vortex; this case is represented by figure 7.1 (b). At this particular stroke length of $L_0/D = 8$ the velocity of the flow continues to accelerate until the vortex is fully formed at $L_0/D = 4$, peak velocity V_{max} now occurs just as vortex formation ends; subsequently ejected fluid forming the trailing jet is ejected at a lower velocity. A further increase in stroke length is represented by figure

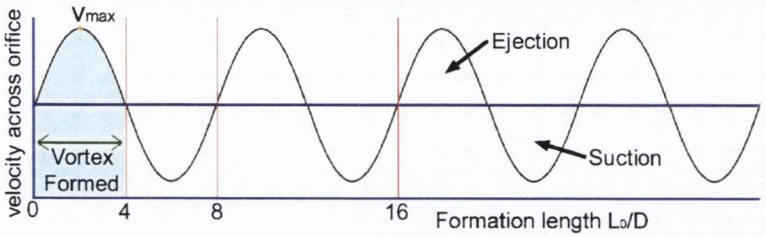

(a) Instantaneous velocity for formation length $L_0/D \leq 4$

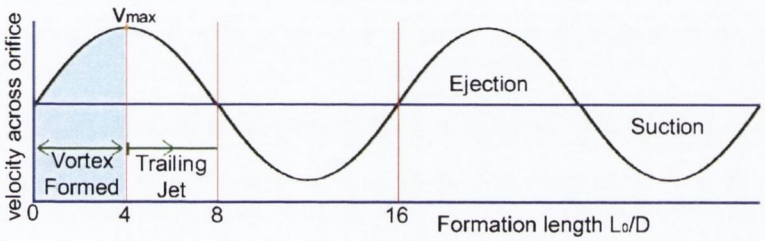

(b) Instantaneous velocity for formation length $4 < L_0/D \leq 8$

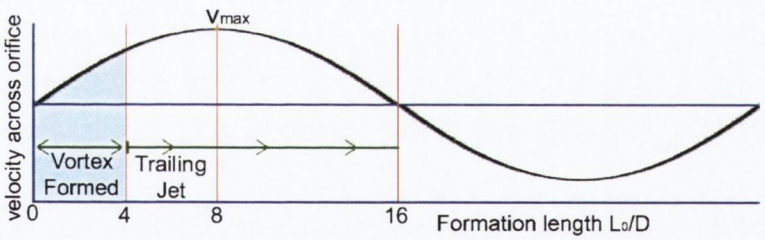

(c) Instantaneous velocity for formation length $L_0/D > 8$

Figure 7.1: Jet formation with increasing formation length (stroke length).

7.1 (*c*). At large stroke lengths it can be seen that vortex formation length occupies only a fraction of the ejection time, with the majority of the fluid ejected forming a trailing jet. Peak velocity can be seen to occur after the vortex has formed, in effect the flow velocity will continue to accelerate into the trailing jet and an inevitable collision between the two will ensue. Gharib *et al.* [60] documented this velocity program up to a dimensionless stroke length $L_0/D = 12$. It was reported that the primary vortex was able to accommodate a temporary increase in circulation, resulting from the impact of the trailing jet, before shedding the excess vorticity, but it was common for total

destruction of the vortex to occur. It is understandable that at dimensionless stroke lengths $L_0/D >> 8$ this may well be characteristic behaviour.

7.1.1 Instantaneous Flow Fields

7.1.1.1 H/D=8

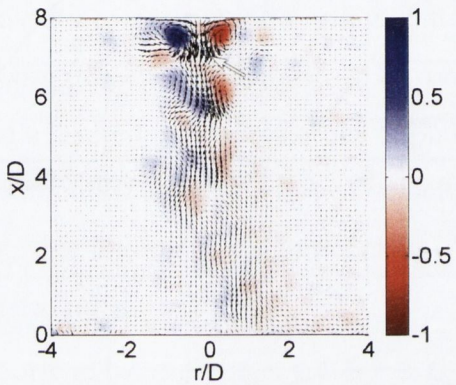

Figure 7.2: Instantaneous flow field; $\varphi = 230^o, H/D = 8, Re = 3000, L_0/D = 3$.

Figure 7.2 presents an instantaneous velocity and vorticity flow field at an orifice to impingement surface spacing of $H = 8D$, Reynolds number of 3000 and dimensionless stroke length $L_0 = 3D$. The phase angle of the jet, φ, relates to what stage in the suction or blowing phase the jet is at and corresponds to figure 6.1, the red, white and blue colour bar represents vorticity with red and blue being in counter clockwise and clockwise rotation respectively. It can be seen in figure 7.2 that a vortex ring begins to form during the ejection stroke immediately in front of the orifice, however none appear in the far field. At this small stroke length there is insufficient time and momentum imparted to the partially formed vortex to allow it fully escape the effects of the subsequent suction stroke associated with the reciprocating nature of a synthetic jet flow. Although no vortex rings associated with classic synthetic jet flow reach the far field there is however a diminished, turbulent net flow established. This flow comes from a small amount of high velocity fluid at the front of the partially formed vortex which is indicated by the arrow; due to the omnidirectional effect of the suction stroke

this fluid reaches a sufficient distance to escape its effect. The flow that is established has diminished momentum and as such at this axial spacing the fluid impinging upon the plate appears to lack periodicity and is of significantly reduced velocity.

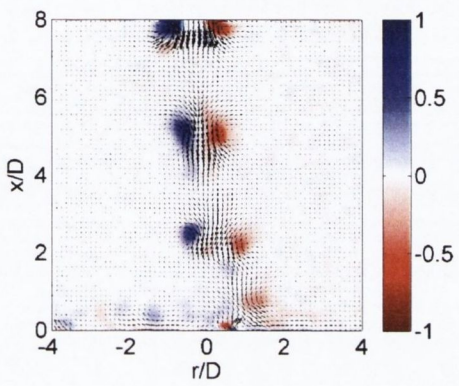

Figure 7.3: Instantaneous flow field depicting velocity vectors and vorticity; $H/D = 8, Re = 3000, L_0/D = 4, \varphi = 230^o$.

Figure 7.3 shows a flow field for an increased stroke length $L_0 = 4D$; this regime is consistent with that reported in figure 7.1 (a). It can be seen that at this stroke length a coherent vortex is formed at the mouth of the orifice and subsequently propagates towards the impingement surface; three discrete vortex rings at increasing axial locations are clearly visible in this flow field. Confirming what was hypothesised in figure 7.1 (a), maximum velocity can be seen to occur inside the vortex ring's core; as the vortex moves farther from the orifice this location naturally moves towards the front of the impinging fluid due to its higher velocity. No visible trailing jet is present following vortex formation at this stroke length. Prior to impingement, at $x/D \approx 2$, the vortices appear to lose coherence due to an accumulation of preceding vortices on the impingement surface. It is evident from the low-level vorticity present immediately above the plate surface that preceding vortex rings neither have the time nor momentum to clear the impingement zone prior to the arrival of the next vortex ring. This results in significant mixing occurring before reaching the plate; no high velocity core associated with the vortex ring is detectable upon impingement.

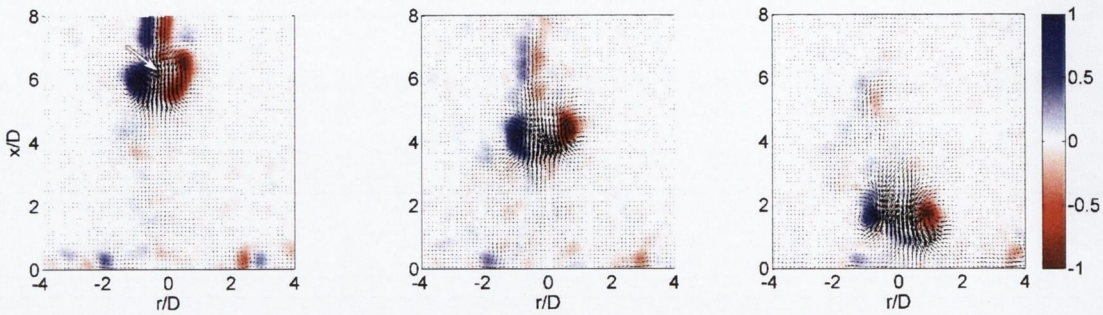

(a) $\varphi = 230^o$ (b) $\varphi = 300^o$ (c) $\varphi = 400^o$

Figure 7.4: Instantaneous flow fields; $H/D = 8, Re = 3000, L_0/D = 8$.

Figure 7.4 shows the progression of the flow field as the stroke length is increased to $L_0 = 8D$ (as represented by figure 7.1 (*b*)). It is immediately apparent that a significantly larger vortex is formed at this larger stroke length. While Gharib *et al.* [60] found that maximum vortex circulation for a similar velocity program was delivered at a stroke length of $L_0 = 4.2D$, these results indicate that a synthetic jet may indeed require a larger stroke length to achieve maximum circulation; time resolved flow field images indicate that at $L_0 = 4D$, a nominal amount of fluid which would otherwise contribute to vortex circulation is reingested into the orifice during the suction stroke. The flow field at $L_0 = 8D$, presented in figure 7.4, is broadly in line what has been proposed by figure 7.1 (*b*). Once the primary vortex has been established in its entirety, the excess fluid ejected at this larger stroke length forms a trailing jet. Figure 7.4 (*a*) indicates that the location of maximum fluid velocity now occurs closer to the rear of the vortex, as shown by the arrow; while not at the immediate interface as indicated by figure 7.1 (*b*), this is because the high velocity fluid originally located at the interface between the vortex ring and the trailing jet is in fact travelling faster than the vortex itself. As the flow progresses to $\varphi = 300^o$, figure 7.4 (*b*), the maximum velocity is now located in the centre of the vortex ring, along with the bulk of the flow; it is noteworthy that the vortex ring has become substantially wider in diameter to accommodate this extra bulk. The trailing jet at this point is far less coherent and appears to undergo a degree of detachment from the primary vortex

and by $\varphi = 400^o$ (figure 7.4 (c)) is virtually non-existent, a phenomenon which has also been documented by Gharib *et al.* [60]. Nevertheless a coherent vortex ring with a significant amount of bulk flow intact can be seen impinging on the surface.

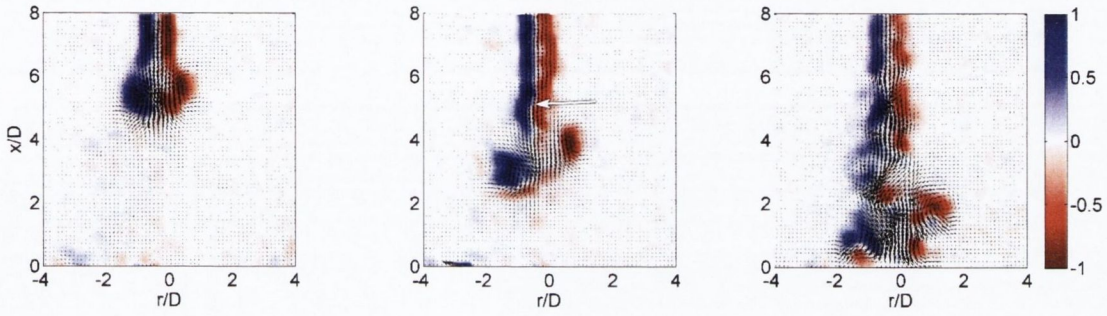

(a) $\varphi = 170^o$ (b) $\varphi = 210^o$ (c) $\varphi = 260^o$

Figure 7.5: Instantaneous flow fields; $H/D = 8, Re = 3000, L_0/D = 16$.

As the stroke length is increased beyond $L_0 = 8D$ to the third and final regime represented in figure 7.1 (c) the flow field changes once again. The stroke length required for vortex formation becomes increasingly smaller in comparison to the amount of fluid injected into the trailing jet. Consequently, peak jet ejection velocity is reached long after the vortex ring is formed. Looking at figure 7.5 (a) it is immediately evident that the vortex formed is on the same scale as that at $L_0 = 8D$, indicating that a universal time scale for vortex formation does exist and has indeed been achieved. At this phase, $\varphi = 170^o$, the vortex is both symmetric and coherent, however the jet has yet to reach peak ejection velocity. Figure 7.5 (b) shows the flow field at $\varphi = 210^o$, when a fluid length of $L_0 = 10.7D$ has been ejected. The arrow indicates the location of peak velocity in the trailing jet at $x/D = 5$, and as the higher velocity fluid impacts upon the vortex ring, as with $L_0 = 8D$, it is forced to spread. In contrast to the vortex behaviour at a smaller stroke length it is unable to accommodate the excess fluid and consequently becomes unstable; figure 7.5 (b) shows that this is initially manifested as a skewed vortex ring. Figure 7.5 (c) shows that with an increase in phase to $\varphi = 260^o$, the vortex ring undergoes a comprehensive destruction, leaving what can only be described as an isolated turbulent fluid ejection to impinge upon the

surface with no detectable vortex ring. This jet can be seen to be significantly wider than an equivalent vortex and trailing jet. The velocity field within this flow appears highly erratic with little obvious remnants of the sinusoidal flow which formed the jet. Figure 7.6 presents a flow field for an even larger stroke length at $L_0 = 32D$.

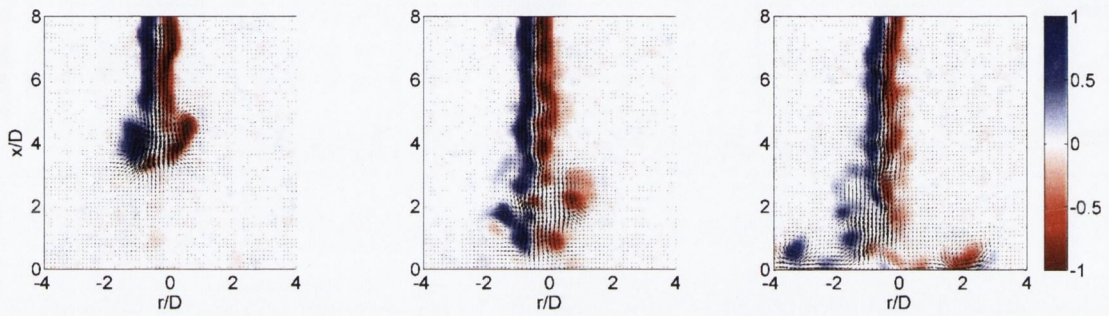

(a) $\varphi = 160^o$ (b) $\varphi = 180^o$ (c) $\varphi = 220^o$

Figure 7.6: Instantaneous flow fields; $H/D = 8, Re = 3000, L_0/D = 32$.

This flow field can be seen to have much in common with that of $L_0 = 16D$ presented in figure 7.5, where a coherent vortex ring with a high degree of circulation is initially formed in the first stages of the ejection at $\varphi = 160^o$. However as the flow develops further at $\varphi = 180^o$, the vortex undergoes destabilisation, resulting in complete destruction before impingement on the surface. While no coherent vortices reach the impingement surface at these parameters, it is worth noting that in figure 7.5 (c) once the mass flux has impacted on the plate surface, vortex rollup is experienced at the periphery of the impact zone resulting in the observable vortices at $r \approx 2.5D$.

While the reported outcomes have been the case for these stroke lengths at this particular spacing of $H = 8D$, it is important to acknowledge that a certain axial distance was required for flow to develop in each of these cases and so a change in axial spacing may provide very different results. As such, other axial spacings will now be considered.

7.1.1.2 H/D=4

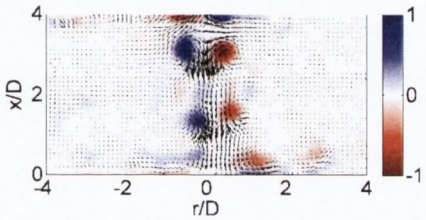

Figure 7.7: Instantaneous flow field; $\varphi = 360^o, H/D = 4, Re = 3000, L_0/D = 3$.

While figure 7.2, $L_0 = 3D$ at $H = 8D$, showed a flow field devoid of impinging vortices, the same stroke length presented in figure 7.7 shows a flow field for an orifice to plate spacing of 4 diameters with a number of small impinging vortices. These vortices travelling towards the plate appear just above the threshold of formation. While before, the vortex rings that were formed appeared unable to escape the effects of the suction phase and subsequently degraded rapidly, now the impingement surface lies within reach of some of the more well formed vortices at this stroke length. It is notable that while the vortex rings themselves appear to lack the level of coherence present at greater stroke lengths there is a sizeable momentum remaining upon impingement. This combination of reduced coherence and increased impingement momentum is seen to result in vigorous mixing and interaction at the plate surface; conditions which can potentially produce high rates of heat transfer.

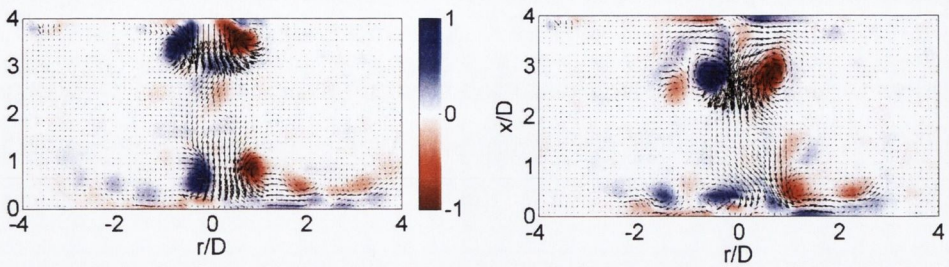

(a) $\varphi = 220^o$ (b) $\varphi = 310^o$

Figure 7.8: Instantaneous flow field; $H/D = 4, Re = 3000, L_0/D = 4$.

Figure 7.8 presents a flow field at an axial spacing of $H = 4D$, with a similar stroke length to that present in figure 7.3. At a stroke length of $L_0 = 4D$ this jet formation regime lies purely in that of vortex formation, represented by figure 7.1 (a). Once again, coherent vortices appear to be formed in front of the orifice and advect away with no detectable trailing jet present. While this behaviour is consistent with that observed at $H = 8D$ in the near field, there are significant differences upon impingement. Figure 7.8 (a) shows that a coherent, if not substantial, core in the centre of the vortex ring is present upon impingement, resulting in high velocity fluid periodically impacting upon the plate; this can be attributed to a greater amount of momentum remaining in the flow as the jet is required to travel a smaller distance prior to impingement at this reduced axial spacing. Consequently, the more coherent impingement has a greater ability to push any remaining fluid from previous impingements out of the way, this includes vortices seen to be lying in the impact zone, a feat that was not possible at smaller stroke lengths or larger axial spacings. Once the fluid ejection has impacted upon the surface, any remaining momentum causes its own vortices to travel radially outwards; a number of tightly packed vortices can be observed above the plate surface at a radial location beyond the impingement zone. Figure 7.8 (b) shows evidence of the suction stroke reingesting fluid from the vortex formed in front of the orifice, thereby reducing the circulation of the vortex at this stroke length from the maximum value of circulation recognised by Gharib *et al.* to occur at $L_0 \approx 4D$. It is for this reason that it is believed that maximum circulation for a synthetic jet is reached at a larger stroke

length than for non-reciprocating flows. A saddle point, or local stagnation point in the flow is also present in front of the orifice in figure 7.8 (*b*).

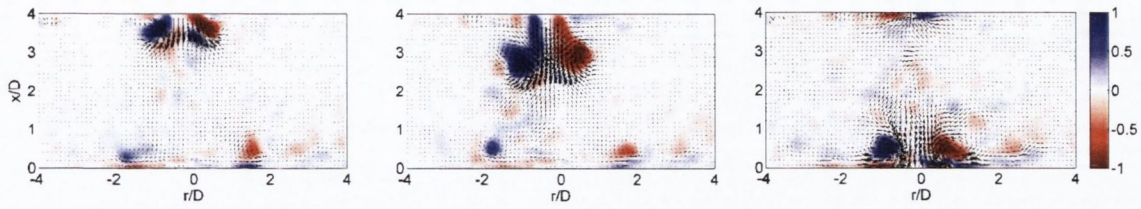

(a) $\varphi = 160^o$ (b) $\varphi = 230^o$ (c) $\varphi = 380^o$

Figure 7.9: Instantaneous flow fields; $H/D = 4, Re = 3000, L_0/D = 6$.

An increase in stroke length to $L_0 = 6D$, presented in figure 7.9, reinforces what has been observed at $L_0 = 4D$. Vortex ring formation once again appears slightly larger, however, while the initial formation of a trailing jet is clearly visible at the orifice in 7.9 (*b*), little or no trailing jet is evident in 7.9 (*c*). Time resolved data reveals that a significant portion of the trailing jet is reingested during the suction stroke. This evidence strongly suggests that synthetic jets may indeed require a larger formation length to achieve maximum vortex circulation than an equivalent impulsively started jet due to their reciprocating cycle. Little momentum is lost as the fluid travels from the orifice to the impingement surface; the fully formed vortex ring and large core can be seen impacting discretely upon the surface at $\varphi = 380^o$. The most notable difference between $L_0 = 6D$ and $L_0 = 4D$ is that while there are a number of vortices present at the plate surface for the shorter stroke length, there is only one set visible at $L_0 = 6D$. The reasons for this are twofold. Firstly, there is a significant increase in core volume between $L_0 = 4D$ and $L_0 = 6D$. Consequently, once the vortex has impacted, the extra fluid in the core has the effect of displacing the vortex radially. Secondly, with the increase in fluid volume per ejection there is simply less space available above the impingement surface for multiple, larger vortices to exist; the evidence for this can be seen in figure 7.9. Upon impact the vortex becomes displaced radially by the fluid from its own core, there is little or no further movement prior to the arrival of the next ejection, as can be seen between $\varphi = 160^o$ and $\varphi = 230^o$. As fluid from the next

ejection stroke approaches the impact zone, figure 7.9 (c) shows that the vortex on the impingement surface becomes further displaced.

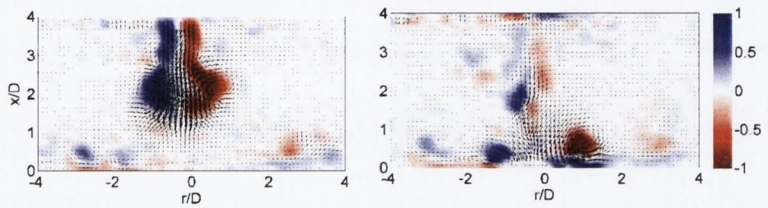

(a) $\varphi = 230^o$ (b) $\varphi = 310^o$

Figure 7.10: Instantaneous flow fields; $H/D = 4, Re = 3000, L_0/D = 8$.

Figure 7.10 shows an increase in stroke length to $L_0 = 8D$ for the smaller jet to plate spacing of $H = 4D$. Although no increase in vortex size is evident, the greater stroke length does contribute to the formation of a trailing jet and a visibly larger core. Rather than impinging as a discrete vortex ring, figure 7.10 (a) indicates that impingement is led by the core flow followed by the vortex ring at a removed axial and radial distance, with maximum velocity being located within the core. Comparing the locations of the vortices remaining from the previous ejection period for different stroke lengths, visible just above the impingement surface in figures 7.10 (a) and 7.9 (b), it is clear to see that they exist at different radial locations. Once impingement occurs, the increased volume of fluid contained in the core and trailing jet at $L_0 = 8D$ forces the vortex to a greater radial distance, where it remains until the next ejection phase displaces it further once again.

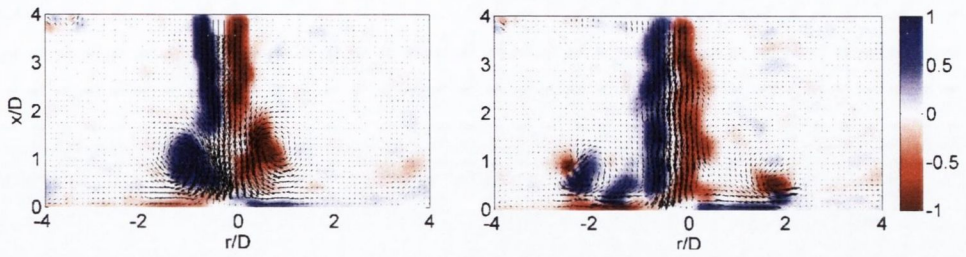

(a) $\varphi = 190^o$ (b) $\varphi = 230^o$

Figure 7.11: Instantaneous flow fields; $H/D = 4, Re = 3000, L_0/D = 16$.

At this low axial spacing any increase in stroke lengths serves only to increase the length of the trailing jet. At $L_0 = 16D$ figure 7.11 shows that while a coherent vortex ring is formed, it plays very much a secondary role in the impingement flow compared to the dominance of the trailing jet. Peak velocity is experienced in the middle of the core which is visibly larger compared to smaller stroke lengths; this can be attributed to an accumulation of high velocity fluid behind the vortex ring. Once again, figure 7.11 (a) shows the impingement to be leading with the core flow rather than a vortex ring. As the high volume, high velocity core fluid impinges on the surface it stagnates and is forced to move radially outwards. Figure 7.11 (b) shows that the vortex ring, which is now visibly unstable, is maintained well above the impingement surface. It is quite evident that at this large stroke length and small axial spacing the flow undergoes little or no development prior to impingement, and with such little interaction and large interval between ejections it can be argued that they should be analysed as independent events.

In contrast to the PIV flow fields presented for $H = 8D$ in figures 7.2 to 7.6, this lower axial spacing allows for a significantly different evolution of the jet. For stroke lengths above $L_0 = 4D$, little or no interaction and mixing was evident prior to or upon impingement. Subsequent increases in stroke length merely accentuated this case by adding to the length of the trailing jet, increasing the duration between impingements and depowering the vortex ring as a flow mechanism.

It was seen that there were a greater number of flow regimes present at $H =$

$8D$. The larger axial spacing allowed for significantly more flow development prior to impingement at both small and large stroke lengths. While at particularly small stroke lengths $L_0 \leq 4D$ a loss of momentum attributed to the smaller vortices resulted in diminished velocity at the plate surface, larger stroke length provided the required momentum for a coherent, higher velocity vortex ring to reach the plate; however a corresponding reduction in mixing was experienced. Subsequent increases in stroke length resulted in a spectacular destruction of the vortex ring prior to impingement, with a wider, more turbulent jet impacting upon the surface.

7.1.1.3 H/D=12

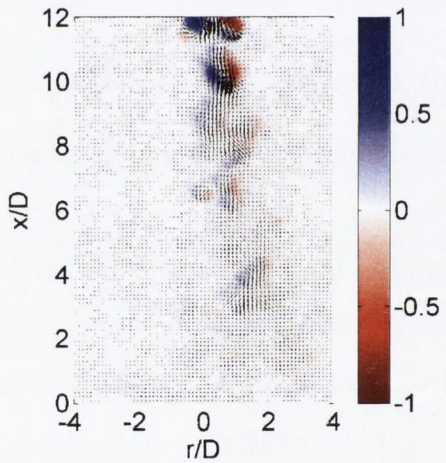

(a) $\varphi = 230^o$

Figure 7.12: Instantaneous flow fields; $H/D = 12, Re = 3000, L_0/D = 3$.

The flow field presented for a stroke length of $L_0 = 3D$ in figure 7.12 for the increased jet to plate spacing of 12 diameters is much like that for the equivalent case at $H = 8D$ in figure 7.2. Similarities include the formation of a vortex ring at the orifice during the ejection phase, the absence of visible vortex rings escaping beyond the near field due to the suction stroke and the formation of a diminished turbulent jet in the far field. The larger axial spacing can be seen to further reduce fluid velocity and momentum upon impingement.

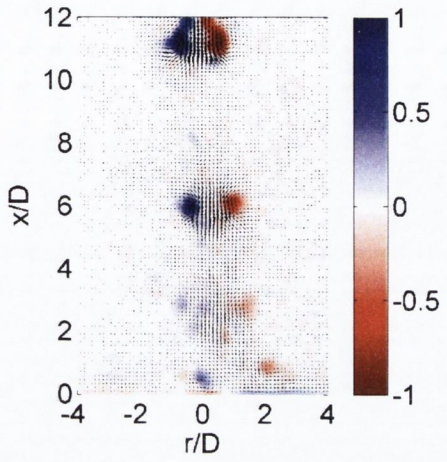

Figure 7.13: Instantaneous flow field; $\varphi = 230^o, H/D = 12, Re = 3000, L_0/D = 6$.

Data presented for a stroke length of $L_0 = 6D$ and axial spacing of $H = 12D$ is shown in figure 7.13. As expected at this stroke length, large coherent vortices are formed with a large core flow. While figure 7.1 (b) would suggest that a notable trailing jet might be present in this case there appears to be only a nominal amount of vorticity trailing the vortex in the middle of the flow field; this gives further weight to the argument that a larger formation length (and hence stroke length) is needed to reach maximum circulation for a synthetic jet. As the vortex ring progresses towards the impingement surface it becomes notably weaker in strength; by $x = 4D$ most of the flow momentum appears to be lost, with an accumulation of weak vortices and diminished flow visible above the impingement surface. It is understandable that an increase in stroke length may provide the vortex with more momentum with which to reach the surface and displace fluid from previous ejections.

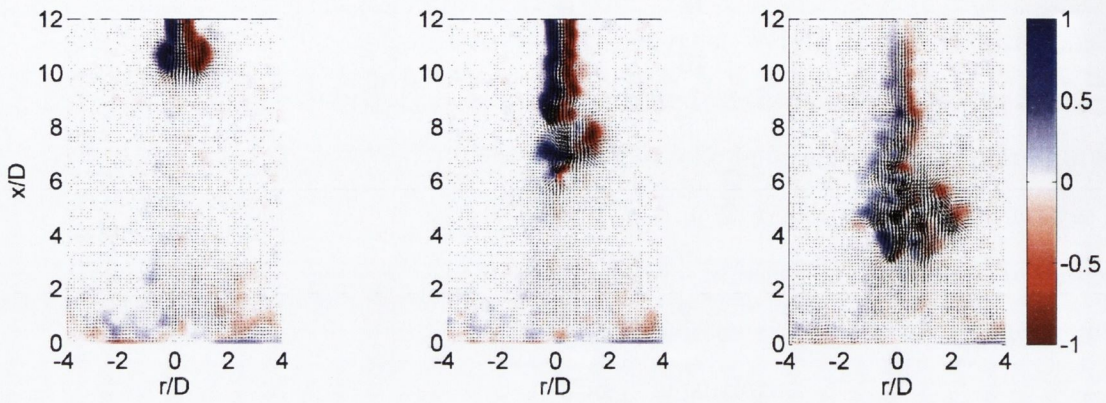

(a) $\varphi = 150^o$ (b) $\varphi = 200^o$ (c) $\varphi = 290^o$

Figure 7.14: Instantaneous flow fields; $H/D = 12, Re = 3000, L_0/D = 18$.

A familiar flow pattern to that seen in figures 7.6 and 7.11 appears once again as the stroke length is increased into the regime where maximum ejection velocity occurs after vortex formation. Figure 7.14 (a) shows the regular formation of a large coherent vortex; as the flow progresses the vortex advects downstream with the trailing jet extending all the way to the orifice. However, figure 7.14 (b) shows that as the higher velocity fluid present in the trailing jet tries to force its way past the vortex two things happen: firstly, an accumulation of fluid occurs at the interface between the trailing jet and vortex ring, skewing the ring and forcing a separation of the two. Secondly, the instability created in the ring by the separation causes the fluid at the very front of the core, leading the vortex ring, to break off forming a secondary vortex and destabilising the entire flow. The result of this destabilisation is depicted in figure 7.14 (c). While the exact method of destruction in which a secondary vortex is formed from the leading flow may not happen consistently, this is down to the erratic nature of the flow at large stroke lengths. What does seem consistent is that destruction always starts with the skewing of the primary vortex, followed by a turbulent dissipation of the remaining fluid ejection. Further increases in stroke length to $L_0 = 32D$, presented in figure 7.15, confirm this assertion. No visible secondary vortex is present, however a skewed primary vortex in the process of destruction can be seen in figure 7.15 (b). Once

destruction has occurred a significant spread in the jet is observed and impingement occurs as a turbulent wave rather than a passing vortex.

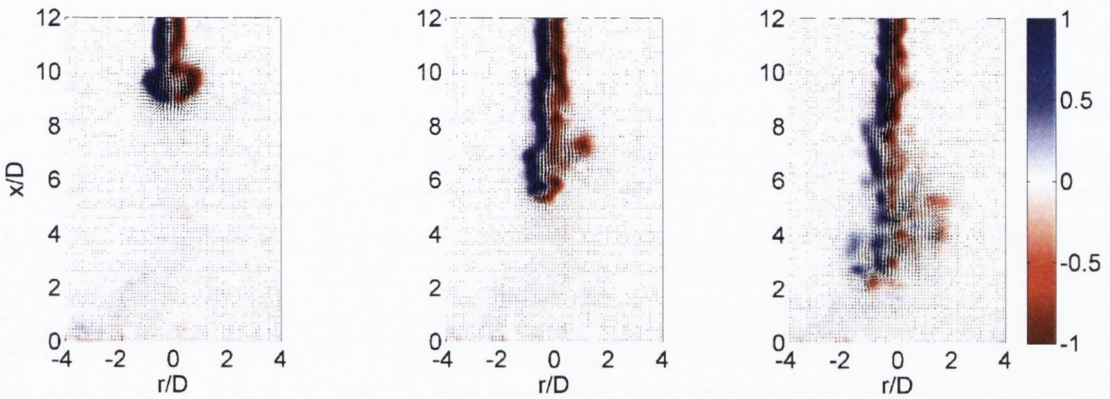

(a) $\varphi = 140^o$ (b) $\varphi = 180^o$ (c) $\varphi = 240^o$

Figure 7.15: Instantaneous flow fields; $H/D = 12, Re = 3000, L_0/D = 32$.

In contrast with results observed at $H = 8D$, once impingement from a flow which has undergone destruction occurs, minimal vortex rollup on the plate surface is visible. The increased axial distance at $H = 12D$ has allowed for a significantly greater amount of viscous dissipation and spreading, resulting in a loss of impact momentum and therefore the ability to perform vortex rollup.

It has been found that the two opposing regimes of small stroke length ($L_0 \leq 4D$), where a highly turbulent jet of diminished momentum is formed, and large stroke length, where the vortex ring undergoes comprehensive destruction prior to impingement in isolation ($L_0 \geq 12D$) are more or less similar at axial spacings of $H = 12D$ and $H = 8D$. However, significant differences have been identified in the intermediate range where an optimum balance can be struck between imparting a sufficient level of momentum to the vortex so that it can reach the impingement surface relatively undiminished, and not imparting so much momentum that the vortices impact in isolation, thereby reducing the turbulence intensity caused by vortex interactions. Each axial spacing will achieve this optimum balance at a different stroke length, with a greater stroke length required at large axial distance. The sole proviso for this condition may

well be that, as the axial separation and stroke length required to impart sufficient momentum to the vortex ring increases, it may encroach on the regime where total vortex destruction occurs, thereby making the optimum condition effectively unachievable. Further results are required to reveal more about these regimes.

7.1.1.4 Findings

This section confirmed some of what has previously been seen in the literature, namely that jet formation at small stroke lengths, $L_0 < 4D$, is significantly diminished as little fluid can escape the suction phase of the jet. What little fluid does escape possesses little momentum with which to impinge upon the surface, regardless of axial spacing. Maximum vortex ring circulation was shown to occur at a stroke length of $4D$, however beyond this value any excess fluid forms a trailing jet behind the vortex ring. While the vortex alone was seen to have a relatively high level of coherence, at large axial distances it possessed insufficient momentum to impact upon the surface undiminished. Larger stroke lengths were seen to provide the vortex with the impulse required to traverse the axial spacing without significant degradation. However, as the maximum ejection velocity starts to occur in the trailing jet at stroke lengths beyond $L_0 = 8D$, a build-up of fluid occurs behind the vortex ring resulting in its ultimate destruction.

7.1.2 Vortex Strength & Path

All synthetic jet cycles begin with the formation of a vortex in front of the orifice. As the presence, strength and path of the vortex is highly dependent on many other aspects of the jet such as the jet formation process, core size, flow coherence upon impact and vortex rollup upon impact it can be used to help identify which flow regime exists at each stroke length and to assess what stage of development the jet is at. Data presented in this section are computed from the same high frequency, time resolved PIV data presented previously. Instantaneous swirl and shear, as outlined in section 6.2, were calculated for the entire data set and subsequently averaged using the same LaVision software as was used for the time resolved flow fields. Magnitude was scaled

by the jet driving frequency, thereby giving the units in the form of $[s^{-1}]$, as such an indication of the average vorticity per cycle is acquired; consequently all data are on the same scale and as such the colour intensity of the vortex paths can be compared directly. Mean swirl and shear data are plotted on top of time averaged velocity streamlines to provide information on mean flow direction and recirculation. Some flow asymmetry is present in the data; while much of it is produced by genuine asymmetries in the flow field there is a certain amount resulting from the relatively short recording time enforced by the high acquisition frequency and dual frame PIV techniques required to obtain high quality instantaneous jet velocities and time resolved data. This testing configuration can result in weak ambient cross flows producing what appear to be noticeable asymmetries in the flow, however, PIV results also show that the regions that these asymmetries regularly exist are in regions of low velocity themselves, and therefore are unlikely to effect a significant level of heat transfer themselves. A number of authors including Shuster and Smith [48], Valiorgue *et al.* [89] and Smith and Glezer [46] have presented data on the evolution of the vortex ring, however only Valiorgue *et al.* documented its behaviour upon impingement but only for an axial spacing of $H = 2D$ and stroke length of $L_0 = 8.7D$.

7.1.2.1 H/D=4

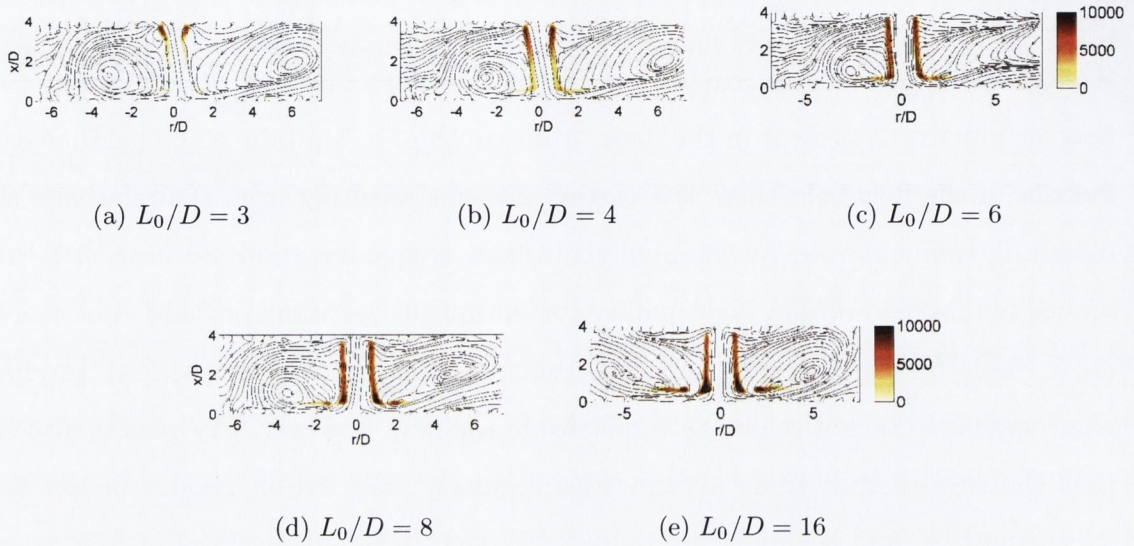

(a) $L_0/D = 3$ (b) $L_0/D = 4$ (c) $L_0/D = 6$

(d) $L_0/D = 8$ (e) $L_0/D = 16$

Figure 7.16: Time averaged swirl and shear, scaled by frequency; $H/D = 4$, $Re = 3000$.

Earlier results have shown that at an axial spacing of $H = 4D$ there is limited room for the jet flow to develop prior to impingement, however the nature of the synthetic jet means that parameters other than Reynolds number can be selected to optimise the flow condition even for such restrictive geometries. Figure 7.16 shows the mean vortex strength and path for a wide range of stroke lengths at $H = 4D$. At the smallest stroke length $L_0 = 3D$, pictured in figure 7.16 (a), while a clear mean flow in the direction of the plate exists, high vorticity doesn't extend beyond the surrounds of the orifice. As was seen in the instantaneous flow fields this is due to reingestion of the vortex during the suction stroke. Shuster and Smith reported upon a similar jet up to a stroke length of $L_0 = 3D$, however they noted that the vortex at this stroke length travelled a distance of $x = 3.3D$ from the orifice, figure 7.16 (a) indicates that little vorticity is present at this axial location as the vortex often fails to escape the effects of the suction phase of the synthetic jet, this finding was confirmed by instantaneous flow field results presented in figure 7.7. An increase in stroke length to $L_0 = 4D$ shows a corresponding increase in vorticity; although the vortex trail extends all the way to the plate, the intensity reduces and the path narrows with axial distance. This indicates

that although a strong vortex ring is initially formed, as it moves down stream vorticity is shed, while the core in the middle of the vortex becomes diminished and consequently contracts. At this separation distance, the stroke lengths of $L_0 = 6D$ and $L_0 = 8D$ prove to be quite similar in behaviour. A strong vortex ring and core is formed at the orifice which travels undiminished to the plate; the vortex path is notably wider than that at $L_0 = 4D$. Valiorgue *et al.* [89] reported that for a stroke length of $L_0 = 8.7D$ and a lower axial spacing of $H = 2D$ the vortex ring impacted upon the surface at approximately $r = 1D$ after which it travelled to a maximum radial distance of $r = 3D$; figure 7.16 (*d*) shows a similar result for the increased axial spacing of $H = 4D$. At a stroke length of $L_0 = 16D$, figure 7.16 (*e*) shows a change in behaviour, most notably the vortex path appears to be discontinuous upon impingement. At this large stroke length, the flow impacts the surface with such force that the vortex ring originally formed at the orifice is destroyed. However, vortex rollup caused by the powerful radial flow resulting from the impact forms a new vortex just above the surface. This appears to be a unique characteristic of flows with large stroke length, as they have both enough energy to destroy their own vortex ring and sufficient momentum to form another subsequent to impingement. It is also noteworthy that at this small axial spacing large recirculation zones exist; while an extended testing duration would be expected to yield symmetric zones, some of the apparent asymmetries are indicative of the relatively strong effects of ambient crossflows especially in the low velocity recirculation zones. The stroke lengths producing large, coherent vortices $L_0 \geq 6D$ can be seen to have stronger recirculation zones with more tightly packed streamlines extending down to the impact zone; this is a direct result of the presence of a vortex in this region over an extended period of time, whether it be part of the original ejection, or formed upon impact. This zone appears much stronger with increasing stroke length.

7.1.2.2 H/D=8

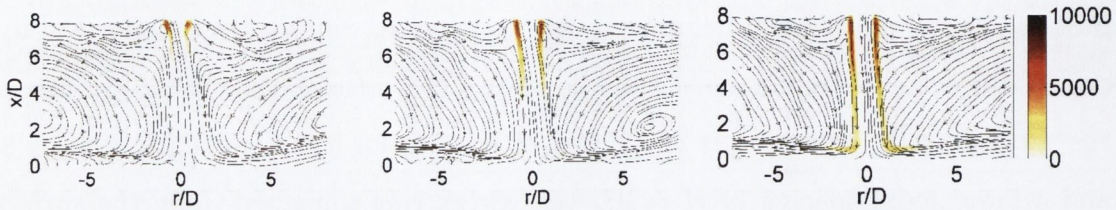

(a) $L_0/D = 3$ (b) $L_0/D = 4$ (c) $L_0/D = 6$

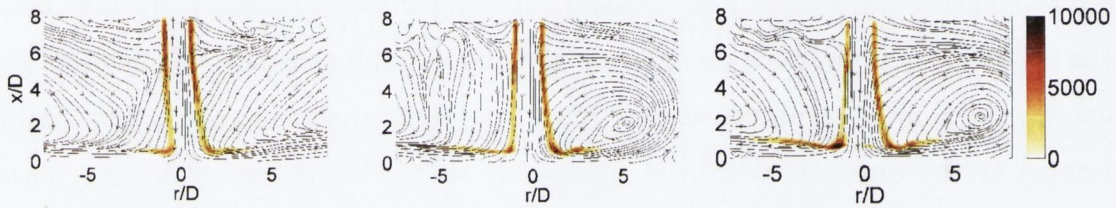

(d) $L_0/D = 8$ (e) $L_0/D = 16$ (f) $L_0/D = 32$

Figure 7.17: Time averaged swirl and shear, scaled by frequency; $H/D = 8$, $Re = 3000$.

Much like the lower axial spacing of $H = 4D$, the stroke length of $L_0 = 3D$, seen in figure 7.17 (a), for a jet height of 8 diameters above the surface shows a near field with a strong vortex presence at the orifice but a far field devoid of vortices. Nevertheless, a mean flow is established that extends to the plate. While the stroke length of $L_0 = 4D$ was sufficient at $H = 4D$ to transport the vortex ring the whole way from the orifice exit to the plate, figure 7.17 (b) shows that at the increased axial spacing of $H = 8D$ the fluid ejection is unable to impart adequate momentum to the flow for the vortex ring to travel the entire distance undiminished. Similarly, this stroke length is characterised by a reduction in intensity and a narrowing of the vortex path with axial distance. A further increase in stroke length to $L_0 = 6D$, figure 7.17 (c), provides the required momentum for the vortex ring to reach the impingement surface at this axial spacing. A greater stroke length of $L_0 = 8D$ merely ensures a more powerful vortex ring impacts upon the surface in a similar flow regime, an increase beyond this point will move to the regime dominated by vortex destruction by the powerful trailing jet.

Figure 7.17 (e) shows that the path of the vortex becomes significantly wider as the encroaching trailing jet forces the vortex ring wider. While there is still a clear vortex path visible, instantaneous images show that this particular case has a tendency for the vortex ring to rotate counter clockwise, with the left hand side of the ring undergoing destruction first. The result of this is that the average vortex strength is visibly weaker on the left hand side of both figures 7.17 (e) and (f). Average vorticity can be seen to increase significantly above the impingement surface once again, as a vortex is formed by rollup of the wall jet subsequent to impact.

7.1.2.3 H/D=12

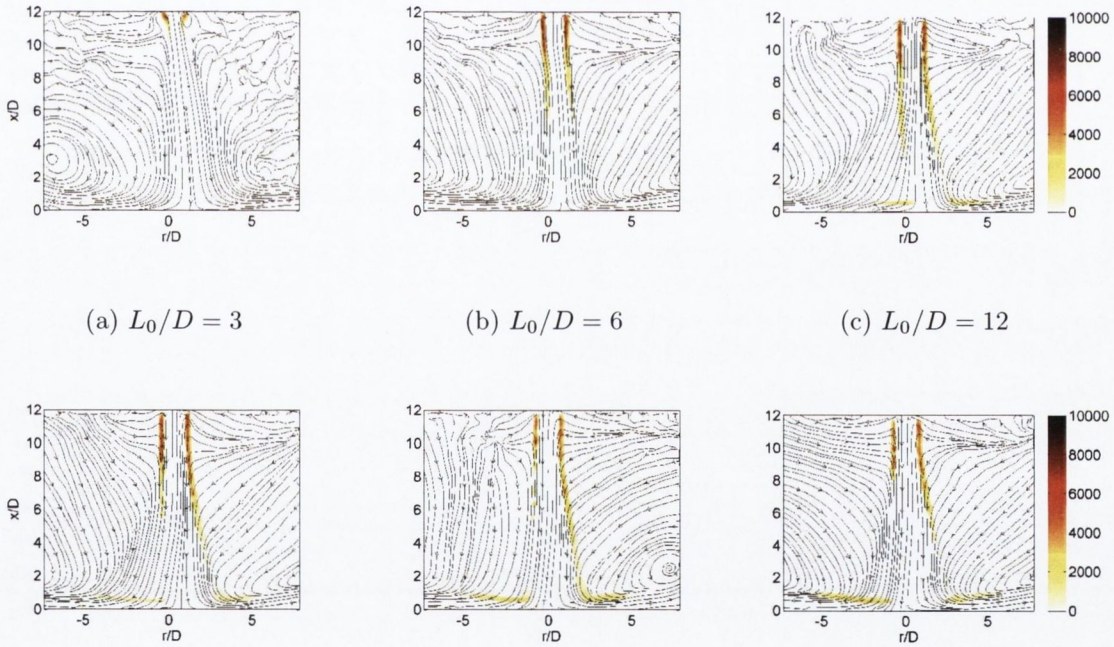

(a) $L_0/D = 3$ (b) $L_0/D = 6$ (c) $L_0/D = 12$

(d) $L_0/D = 18$ (e) $L_0/D = 24$ (f) $L_0/D = 32$

Figure 7.18: Time averaged swirl and shear, scaled by frequency; $H/D = 12$, $Re = 3000$.

The average vortex trails shown in figure 7.18 for an axial spacing of $H = 12D$ initially seem very similar to those seen at $H = 8D$. While the ability of the flow formed at $L_0 = 3D$ to impact upon the plate is further diminished by the increased axial spacing,

this is also the case for the rest of the stroke lengths. In particular, the vortex ring formed in figure 7.18 (*b*) at $L_0 = 6D$ no longer possesses the required momentum to impinge upon the plate undiminished, much like the case for $L_0 = 4D$ at $H = 8D$. It can be inferred that at a stroke length of about $L_0 = 8D$, falling between figures 7.18 (*b*) and (*c*), the jet imparts the required momentum to the vortex ring for impingement upon the plate with adequate impetus and mixing, without imparting so much that destabilisation by the trailing jet occurs. Such destabilisation is evident to a certain extent at $L_0 = 12D$. Larger stroke lengths of $L_0 = 18D, 24D$ and $32D$, seen in figure 7.18 (*d*), (*e*) and (*f*), show a notable weakening of the vortex path as it approaches the plate, this is as a result of vortex ring destruction; vortex path widening is also evident and is seen to be increasing significantly with stroke length. Path widening is indicative of the much stronger build-up of fluid behind the vortex ring with increasing stroke length. Vortex formation at the impingement surface appears stronger with larger stroke length.

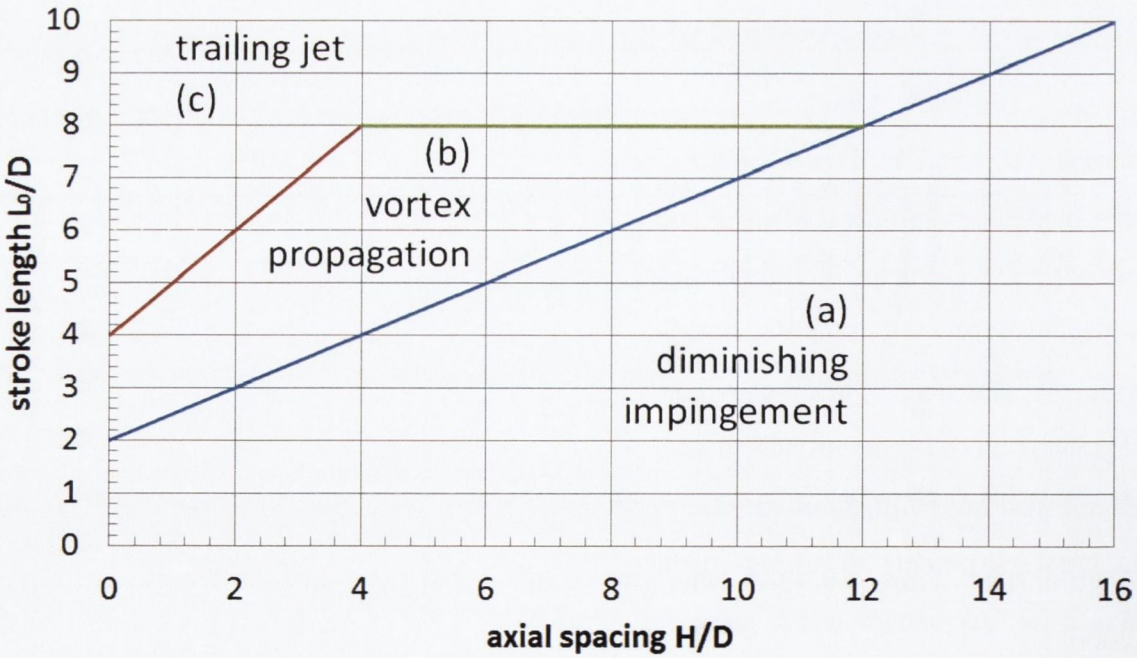

Figure 7.19: A map of the various flow regimes as identified from flow visualisation data.

This flow visualisation data has been used to draw up a flow regime map which is

presented in figure 7.19. Three significant impingement regimes have been identified which depend on stroke length and axial spacing. Regime (a), the flow regime of diminishing impingement is characterised by the formation of a synthetic jet at a stroke below that required to impart sufficient momentum to the flow so as to impinge upon the surface with coherent, periodic motion. Flow produced in this regime experiences a loss of momentum with few significant vortical structures present upon reaching the impingement surface. As the stroke length is increased sufficiently so that the vortex rings possess sufficient impulse to impact upon the impingement surface the flow field enters the vortex propagation regime, bound in figure 7.19 by the blue line and identified as regime (b). The flow field associated with this regime consists of the formation, advection and impingement of vortex rings upon the surface. While this regime does not exist exclusively at stroke lengths which achieve maximum vortex circulation ($L_0 \geq 4D$), those axial spacings below this level lie sufficiently close to the jet exit so that the reciprocating flow experienced at the orifice produces the same periodic impingement effects regardless of flow reingestion. The upper limit to this flow regime can be experienced in two ways, the first is indicated by the red boundary line in figure 7.19 and occurs when the stroke length is so great and the vortex ring so powerful that little development is experienced prior to impingement. Flow fields have revealed that while the vortex ring may indeed be a primary structure, the impinging flow itself is led by the higher velocity fluid contained in the core of the jet pushing its way to the front. Consequently, a significant widening of the vortex ring prior to impingement is experienced along this boundary. The second limit to the vortex propagation regime occurs at a larger axial spacing where there is sufficient distance for the flow to evolve, this regime is highlighted by the green boundary line and represents a constant stroke length of $L_0 = 8D$. Above this stroke length the time at which the maximum fluid ejection velocity occurs moves from within the vortex formation length to that of the trailing jet. Consequently, an accumulation of high velocity fluid is experienced behind the vortex and the flow undergoes a dramatic viscous dissipation. Both of these impingement modes experienced at stroke lengths beyond the vortex propagation regime are dominated by the presence of the trailing jet, and as such this flow regime transitions into regime (c) in figure 7.19. The map

shows that beyond an axial spacing of $H = 12D$ only two flow regimes exist, this result from the diminishing flow regime (a) exceeding the maximum stroke length which limits the vortex propagation regime (b). Beyond this axial spacing no vortex rings are seen to impinge upon the surface intact due to either a loss of momentum prior to impact or destruction by the trailing jet.

Going back to the time averaged swirl and shear results it can be seen that they are in agreement with the flow regime map presented in figure 7.19. The swirl and shear results provided a clearer view on the role the vortex ring plays at various axial spacings, on how it evolves and on the effect that stroke length plays. These flow fields have helped to clarify where certain flow regimes begin and end, each varying with axial spacing. The first regime identified was that in which the intensity of the vortex path was seen to decrease between the orifice and the impingement surface, to the extent that it was unobservable prior to reaching the surface. This indicated that insufficient momentum was imparted to the vortex ring; the jet thereby impacts as a non-periodic flow of diminished momentum. The second regime consisted of a vortex path extending uniformly up to the plate surface, albeit with decreasing intensity. Indicative of a weakly periodic impact, this flow has retained some of its momentum, moreover vigorous mixing between subsequent vortex rings is quite likely in this regime. The third regime identified showed strong vortex paths both leading up to the impingement surface and also traversing radially once impacted. This indicates that the flow is somewhat underdeveloped upon impingement, with sufficient periodic momentum to maintain a coherent vortex ring once impact has occurred. All three of these regimes are highly dependent on jet to surface spacing. The stroke length required to achieve each regime is seen to increase with increasing axial spacing, although a limiting stroke length appears to exist at $L_0 > 8D$ beyond which a new regime dominates. The fourth and final flow regime deviates from all previously documented in that the vortex ring plays very much a secondary role in the evolution of the jet. This regime is dominated by the presence of a powerful trailing jet travelling at a higher velocity than the primary vortex ring. Average swirl and shear results revealed a significant spreading of the jet and widening of the vortex ring with subsequent destruction beyond $L_0 \approx 10D$. While there may not be sufficient axial dis-

tance for this to occur at small axial spacings, destruction occurs upon impingement. Vortex reformation by the rollup of the wall jet once impact has occurred is also a common characteristic of this type of flow; this was observed at all axial spacings and is accentuated at larger stroke lengths.

7.1.2.4 Findings

These vortex strength and path results have confirmed in more detail what we have seen with the instantaneous flow fields. It has been shown that low stroke lengths of $L_0 \leq 3D$ result in very little vorticity escaping the suction stroke, even at the lowest axial spacing of $H = 4D$ there is no evidence of coherent vortex rings reaching the impingement surface. Results also showed that once an advecting vortex ring has been established vortex strength and ring diameter reduces with increasing distance from the orifice exit as momentum and vorticity is lost. Larger stroke lengths were seen to produce wider vortex rings as the core of the ring contained an increasing amount of fluid; at stroke lengths $L_0 \geq 8D$ the higher velocity fluid was in the tail. If the vortex possessed significant momentum upon impact it was seen to travel radially outwards across the plate; it was also noticed that vortex rollup occurred at the plate surface as the fluid impacted, regardless of whether or not the vortex ring remained intact upon impact. The largest axial spacing of $H = 12D$ showed that no stroke length in the range $L_0 \leq 8D$ provided the vortex with the required momentum for the vortex ring to impinge upon the surface before losing momentum and that above a stroke length of $L_0 = 8D$ no vortex ring impinged intact. These results have been used to draw up a map of the various flow regimes upon impingement, which can be seen in figure 7.19. The three flow regimes consist of: (a) a diminished impingement where insufficient momentum has been imparted to the flow to reach the impingement surface undiminished, (b) a flow regime dominated by the formation, advection and impact of fully formed, coherent vortices and (c) a flow dominated by the highly powerful and periodic ejections of the trailing jet, where the ejected fluid impinges upon the surface in isolation with little or no interaction between subsequent ejections.

7.1.3 Volume Flux

The following volume flux data have been computed from a time averaged velocity flow field produced from the time resolved PIV data. For each data point fluid volume flux is calculated as follows:

$$Q(x) = \sum U_x(r, x)\ 2\pi r\ dr \tag{7.2}$$

where x is the axial coordinate and r is the radius which extends outwards to a distance of two diameters from the centre of the jet. This procedure is repeated for the entire axial spacing between the orifice exit and impingement surface to obtain results showing how the jet volume flux evolves in the axial and radial directions. To prevent the strong effects of the suction phase near the orifice from skewing the net volume flux transported towards the plate only streamwise positive axial velocities were used to calculate volume flux in the axial direction.

7.1.3.1 H/D=4

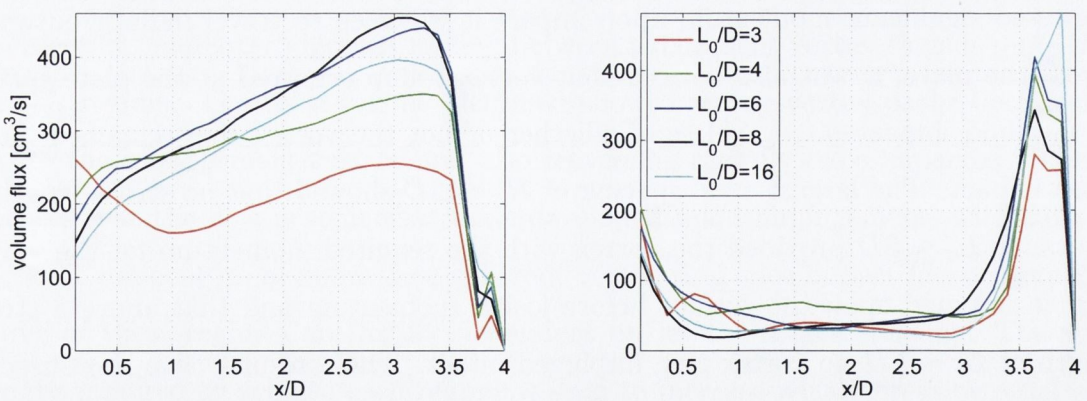

(a) axial flux

(b) radial flux

Figure 7.20: Average volume flux in the axial and radial directions; $r = \pm 2D$, $H = 4D$, $Re = 3000$.

It is immediately obvious from figure 7.20 (a) that although all stroke lengths at a Reynolds number of 3000 start out with a similar volume flux at the orifice, jet evo-

lution can vary greatly with stroke length. In theory, a synthetic jet such as this one ought to produce a net mean flux of $98cm^3/s$ at a Reynolds number of 3000; the significantly larger volumes presented in this section indicate the synthetic jet's impressive ability to entrain further fluid. The general trend present indicates that there is a near linear relationship between volume flux and axial location for the majority of the flow fields. Deviation from this trend is seen to occur once the flow comes into proximity with the impingement surface, at which location a corresponding increase in radial velocity is observed in figure 7.20 (b). While this may be the general trend, it is not the case for all stroke lengths. As was indicated by both vortex path and instantaneous flow fields, vortex ring formation and advection at the smaller stroke length reduces the ability not only of individual vortices to reach the impingement surface, but also for the jet to impact upon the plate with undiminished momentum. Figure 7.20 (a) now reveals that at these operational parameters there is a corresponding reduction in volume flux with axial distance, in particular for the stroke length of $L_0 = 3D$. Significantly, volume flux in both axial and radial directions is almost identical for the two stroke lengths of $L_0 = 6D$ and $8D$, for which vortex circulation is thought to be at its maximum. Also, the greater level of volume flux at $L_0 = 16D$ appears to be primarily achieved in the near field of the jet and then maintained throughout the flow field. At the axial spacing of $4D$, the presence of the plate does not affect the direction of the volume flux until the flow is within one diameter of the surface. An increase in stroke length generally produces a corresponding increase in maximum radial flux experienced at the impingement surface; this has been attributed to greater momentum in the flow upon impact provided by the larger stroke length. The level of radial flux is also indicative of jet spread; prior to the flow entering the impingement affected zone, which lies beyond $x = 3D$, it can be seen that, in general, smaller stroke lengths ($L_0 \leq 6D$) have higher levels of radial flux.

7.1.3.2 H/D=8

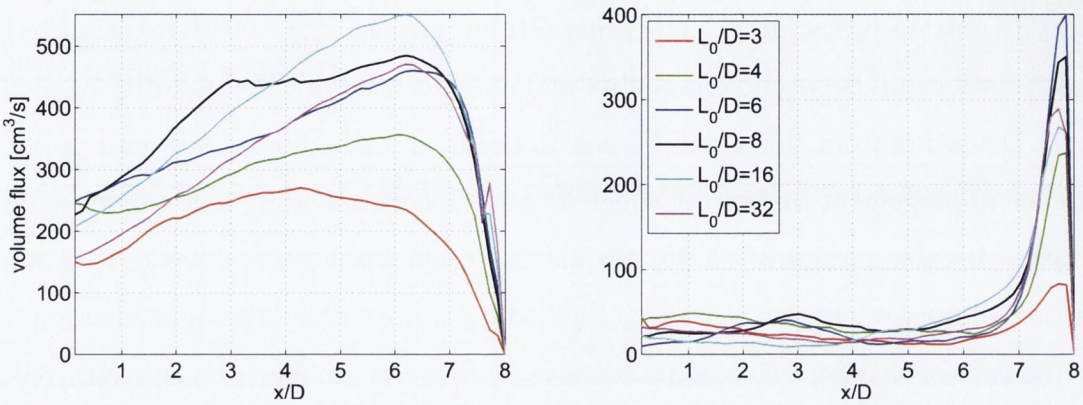

(a) axial flux

(b) radial flux

Figure 7.21: Average volume flux in the axial and radial directions; $r = \pm 2D$, $H = 8D$, $Re = 3000$.

The general trends observed at $H = 4D$ in figure 7.20 also appear to be present at the larger $H = 8D$, in figure 7.21. Once again, the smaller stroke lengths of $L_0 = 3D$ and $4D$ have a much smaller increase in volume flux with axial distance compared to larger stroke lengths; at $L_0 = 3D$ there is in fact a visible decrease in volume flux from $x = 4D$. Peak flux is experienced for a stroke length of $L_0 = 16D$ at $551.5cm^3/s$, occurring at $1.8D$ from the impingement surface. While an increase in volume flux can be attributed to a reduction in confinement and to an increase in the axial distance available for the jet to evolve, the greater spacing also causes the location of maximum axial flux to occur at a greater distance from the impingement surface; momentum is lost with jet evolution, and so the linear increase in volume flux with axial distance cannot be maintained to the same extent as at $H = 4D$. This result is also reflected in the radial volume flux upon impingement where all stroke lengths show a decrease in magnitude compared to the lower jet to plate spacing. Unlike the axial spacing of $H = 4D$, maximum axial volume flux is achieved at a stroke length of $L_0 = 16D$, unusually though, a further increase in stroke length to $L_0 = 32D$ results in a reduction in volume flux back to levels seen at smaller stroke lengths. A possible reason for this

may be because the vortx plays an increasingly minor role as stroke length is increased. As was seen at $H = 4D$, the near field (i.e. close to the jet exit) radial flux for $x < 6D$ appears to be significantly larger for smaller stroke lengths, in particular for stroke lengths that experience significant degradation prior to impingement ($L_0/D = 3, 4$).

7.1.3.3 H/D=12

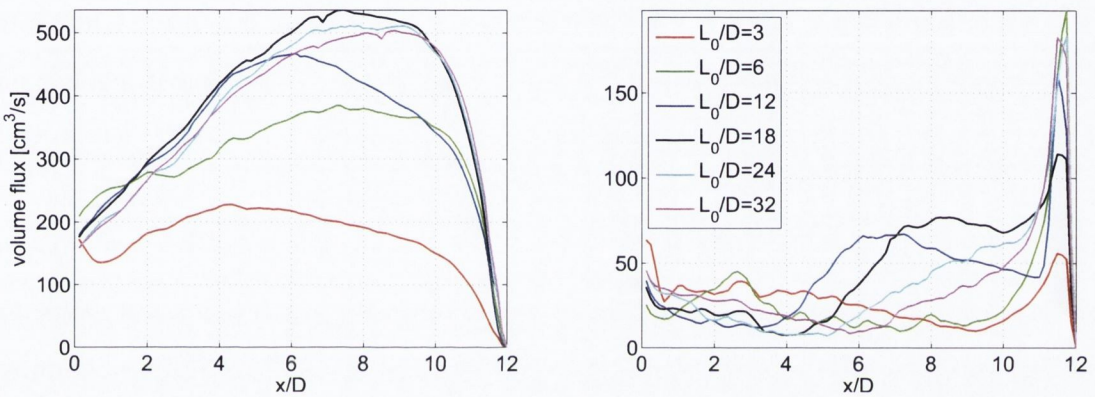

(a) axial flux

(b) radial flux

Figure 7.22: Average volume flux in the axial and radial directions; $r = \pm 2D$, $H = 12D$, $Re = 3000$.

Figure 7.22 shows how volume flux changes with stroke length for the greater axial spacing of $H = 12D$. Most significantly these results show that, at this spacing, no jet in either flow regime below L_0 of $12D$ possesses sufficient momentum to carry it to the impingement surface undiminished, with the smaller stroke lengths ($L_0/D = 3, 6$) showing a noticeable decrease in axial volume flux long before impact. As the flow transitions into the regime dominated by the trailing jet at $L_0 \geq 12D$, the radial volume flux in figure 7.22 (b) shows a trend previously unseen at lower axial spacings. Thus, radial flux is seen to increase significantly beyond $x = 5D$ for a stroke length $L_0 = 18D$; this shows that this location coincides with the destruction of the vortex ring, as seen in instantaneous flow field data (figure 7.14), resulting in a destabilised flow which becomes turbulent and spreads rapidly. The initiation of this jet spreading

is seen to move further downstream with an increase in stroke length; the extended ejection period and the associated increase in momentum provided by the larger stroke length pushes the destroyed vortex ring and its corresponding radial volume flux closer to the impingement surface before spreading has a chance to occur.

These average volume flux data provide quantitative results to compliment the previously presented flow field data. Further evidence has been presented showing the distinct differences in the characteristic flow regimes identified earlier. Data show that a minimum stroke length is required to maintain maximum volume flux right the way up to the impingement surface, however, an increase beyond a threshold stroke length $L_0 \approx 8D$ results in the transition to a substantially different flow regime where vortex ring destruction results in elevated levels of jet spreading prior to impingement. This phenomenon was particularly evident at $H = 12D$. However, the case with $L_0 = 16D$ and $H = 8D$ shows a small yet significant elevation in radial flux at $x = 6D$ (prior to entering the area affected by the impingement surface). It is likely this phenomenon is also present at $H = 8D$ between the stroke lengths $8D < L_0 < 16D$; unfortunately no flow visualisation data have been acquired for this case.

7.1.3.4 Findings

The results in this section have shown that while small stroke lengths $L_0 \leq 3D$ produced diminished axial and radial volume flux larger stroke lengths generally produced a higher axial volume flux while also delaying any effects that the presence of the impingement surface might produce. There was also a corresponding increase in maximum radial flux at the impingement surface at larger stroke lengths while smaller stroke lengths showed greater levels of radial flux prior to impingement. Larger axial spacings were seen to produce a significantly larger volume of axial flux as the increased distance before impingement allowed for greater entrainment. A noticeable bulge in radial flux at larger axial spacings and stroke lengths $L_0 > 8D$ indicated spreading of the jet was occurring; this corresponds well with the location at which the vortex ring undergoes destruction and a viscous dissipation of the flow occurs, as was seen previously in the instantaneous flow fields.

7.1.4 Mean Velocity Profiles

The mean velocity profiles presented in this section were produced from the high speed PIV data; the same velocity information has been presented previously in the form of stream lines in conjunction with vortex path data in section 7.1.2. Mean velocity flow fields were calculated by averaging the entire acquired time series using the DaVis software package, thereby producing a two component vector field with axial and radial components. The results were exported to MATLAB, where profiles across the average velocity field at various axial locations were taken and plotted. Profiles start at $x = 0.5D$ from the orifice with subsequent profiles plotted at steps of $2D$ from the orifice, with the final profile taken at half a diameter from the impingement surface. Profiles extend from the jet centreline $r = 0D$, to a radial location four diameters out, $r = 4D$. Figures plotted show axial velocity (red), radial velocity (blue) and absolute velocity (black) for reference. For ease of comparison subsequent profiles beyond that at the orifice are offset by a fixed velocity.

7.1.4.1 H/D=4

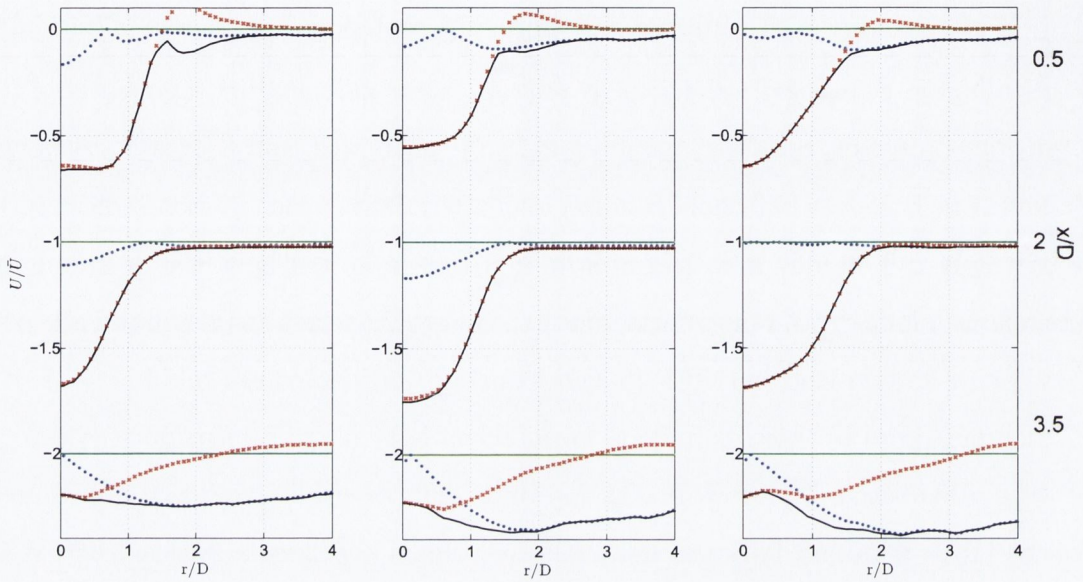

(a) $L_0/D = 3$ (b) $L_0/D = 4$ (c) $L_0/D = 6$

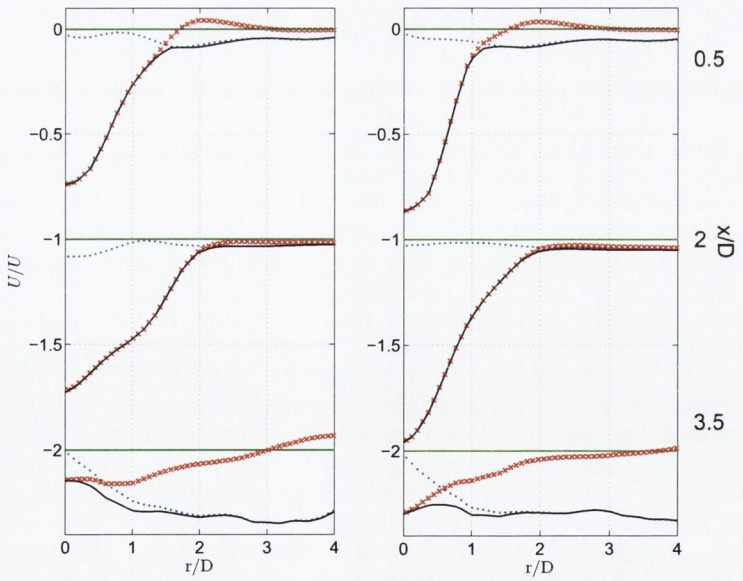

(e) $L_0/D = 8$ (f) $L_0/D = 16$

Figure 7.23: Average absolute (−), axial (×) and radial (•) velocity profiles; $H/D = 4$, $Re = 3000$. Profiles taken at distances of $x/D = 0.5, 2, 3.5$ from the orifice, subsequent profiles offset by $U/\bar{U} = 1$ with corresponding zero velocity also plotted (−).

While mean volume flux data presented in section 7.1.3 provided a good idea of the entrainment, momentum and evolution of the synthetic jet at various stroke lengths and axial spacings, it lacks the detail of local velocity which ultimately dictates local surface heat transfer. Figure 7.23 shows local velocity profiles for $H = 4D$. While initially all stroke lengths look broadly similar, there are small yet significant differences present which can be seen to evolve both with axial distance and change in stroke length. Figure 7.23 (a) presents data for a stroke length of $L_0 = 3D$; at larger axial spacings this small stroke length has been seen to lack momentum and coherence, however at the relatively small spacing of $H = 4D$ this does not appear to be the case. A relatively strong jet is formed in front of the orifice with most of the velocity travelling in the axial direction. As no trailing jet is formed at this stroke length only flow artefacts produced by the intake and ejection phases dominate the flow field which immediately surrounds the orifice. Vortex formation requires the ejected fluid not only to flow in the axial direction but also in the radial direction; for this reason elevated levels of radial flow are experienced about the orifice, especially at stroke lengths which lie primarily in the vortex formation regime. Comparatively few vortices pass at large stroke lengths where ejections are dominated by long trailing jets, consequently low radial velocity near the orifice is observed at these parameters. Similarly, axial velocity can be seen to go negative at $r = 1.5D$; this is attributed to the suction phase of the jet which, unlike the ejection phase, is omnidirectional, resulting in a mean negative velocity to the sides of the orifice. Beyond this, at $r > 1.5D$ local velocity is low and moves primarily in the radial direction; this fluid is moving inwards, towards the orifice, and is indicative of the recirculation eddy present either side of the jet. The axial profile taken at $x = 2D$ shows that no suction effects remain, the vast majority of the flow is positive, axial and undiminished. The final profile taken at $x = 3.5D$, which is half a diameter above the impingement surface, appears dramatically different to the two previous profiles. Where before, the axial and absolute velocities were Gaussian in shape, the absolute velocity profile is now mostly flat, with the axial velocity decreasing almost linearly from the jet centre. As the flow gets closer to the impingement surface, the presence of the surface has an ever increasing effect, the fluid can no longer travel in the axial direction as it impacts upon the surface; it is therefore

forced to turn and flow radially outwards, as indicated by the large increase in radial velocities for all stroke lengths at $x = 3.5D$. The result of this is that as the flow gets progressively closer to the impingement surface, a time averaged stagnation zone is effectively formed at the jet centreline; both axial and radial velocities approach a zero flow in this location. Across the entire range of stroke lengths all velocity profiles at $x = 3.5D$ show that, at this distance above the surface, the stagnation zone has already started to form, axial velocity is significantly reduced and the radial velocity at $r = 0D$ is already zero. Much of the fluid momentum beyond $r = 1D$ has been transferred to the radial direction; it now accounts for the majority of the absolute velocity as it flows outwards parallel to the surface.

As stroke length is progressively increased at $H = 4D$, marginally different trends are evident across the range. At $x = 0.5D$, half a diameter from the orifice, there is a progressive reduction in the centreline radial velocity with increasing stroke length. At $r \approx 1.5D$, likewise there is a reduction in the magnitude of the negative axial velocity; a progressive reduction in the secondary peak in the absolute velocity is observable also with increasing stroke length. This phenomenon is linked to the fact that jet flow at $L_0 = 3D$ is dominated by suction and ejection about the orifice rather than the formation and advection of the fluid structures that are present at larger stroke lengths. Consequently, the jet formed at this stroke length has a stronger tendency to spread radially right from formation. Due to the restricted space available for the jet to develop at $H = 4D$ there is little difference between the respective velocity profiles at $x = 2D$. Data presented at $0.5D$ from the impingement surface show significant changes with increasing stroke length. While all profiles show that the radial velocity stagnates at the jet centreline, the radial velocity magnitude beyond the core is much greater and is maintained at a higher level for longer due to the increased momentum imparted by the larger stroke lengths. The presence of the stagnation zone in the axial velocity also becomes more noticeable at larger stroke lengths.

7.1.4.2 H/D=8

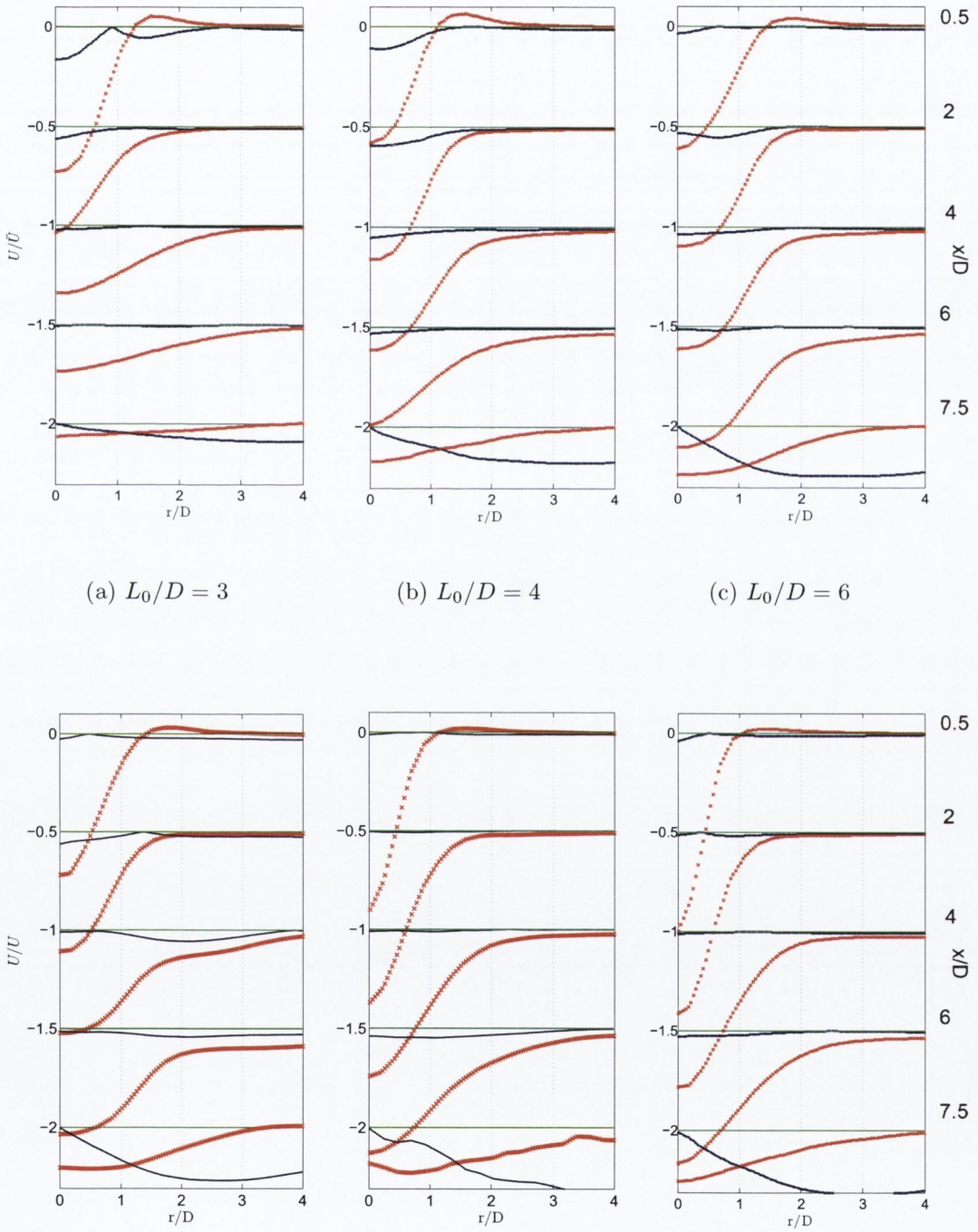

(a) $L_0/D = 3$ (b) $L_0/D = 4$ (c) $L_0/D = 6$

(e) $L_0/D = 8$ (f) $L_0/D = 16$ (g) $L_0/D = 32$

Figure 7.24: Average absolute (−), axial (×) and radial (•) velocity profiles; $H/D = 8$, $Re = 3000$. Profiles taken at distances of $D = 0.5, 2, 4, 6, 7.5$ from the orifice, subsequent profiles offset by $U/\bar{U} = 0.5$ with corresponding zero velocity also plotted (−).

Figure 7.24 presents velocity profiles for the increased axial spacing of $H = 8D$. Substantially more development is present throughout all stroke lengths with visible spreading occurring as the jet proceeds from the orifice to the plate. Similarly, the near field of the jet, $0.5D$ from the orifice, remains relatively unchanged to that seen at $H = 4D$. This is because confinement plays little or no part in the formation of the jet close to the orifice, and as this is where the jet is formed no evolution occurs prior to this point; flow is primarily dominated by structures formed at the various stroke lengths. As was confirmed by figure 7.21 (b), the smaller stroke lengths $L_0 \leq 4D$ experience more jet spreading and a larger reduction in velocity prior to impingement than the corresponding larger stroke lengths. As is evident from the volume flux data presented in figures 7.20 to 7.22 there appears to be a strong link between elevated radial velocity in the near field and subsequent rapid degradation of jet flow, this occurs regardless of the formation of a strong core axial flow; it can be seen in figure 7.24 that as soon as the radial velocity component experiences an increase the core axial velocity experiences a corresponding decrease. This result is unsurprising as any outward radial flux will directly result in a reduction of fluid within the axial core flow which contributes most to the jet's directional momentum. With this in mind, it is noticeable that the flow at large stroke lengths has a relatively small radial velocity component near the orifice and an axial component which is slender and quite large in magnitude; both can be attributed to the presence of a comparatively powerful trailing jet which produces little or no radial flow. It was identified in section 7.1.2 that a stroke length of $L_0 \approx 6D$ was required to impart enough momentum to enable the vortices to reach the impingement surface; this is once again reflected in the centreline impingement velocity, where the absolute and axial stagnation velocities are visibly larger in figure 7.24 (c) than in either (a) or (b). Similar to $H = 4D$, radial velocity across the impingement surface becomes larger with increasing stroke length.

7.1.4.3 H/D=12

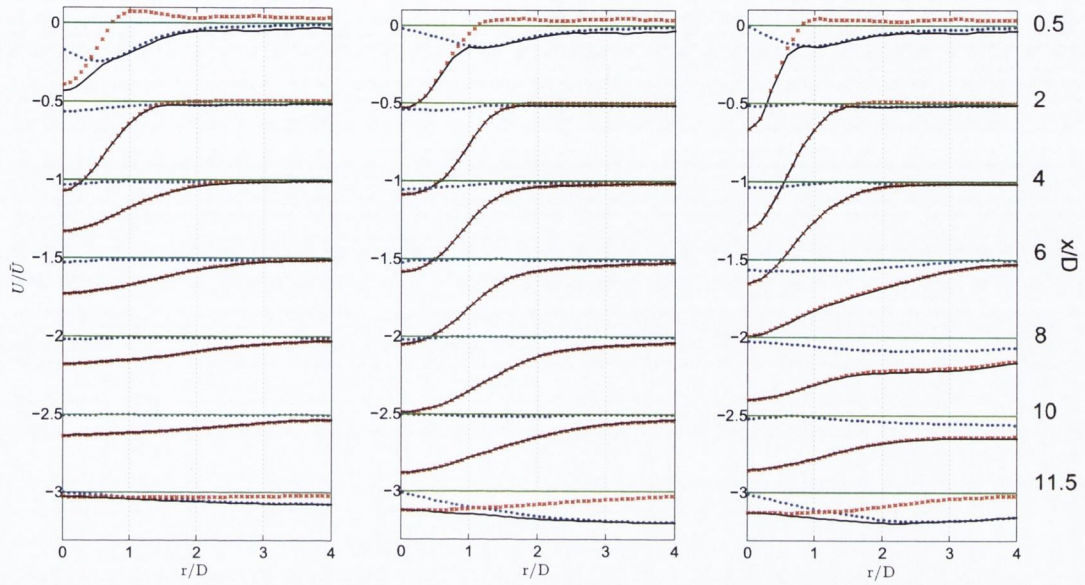

(a) $L_0/D = 3$ (b) $L_0/D = 6$ (c) $L_0/D = 12$

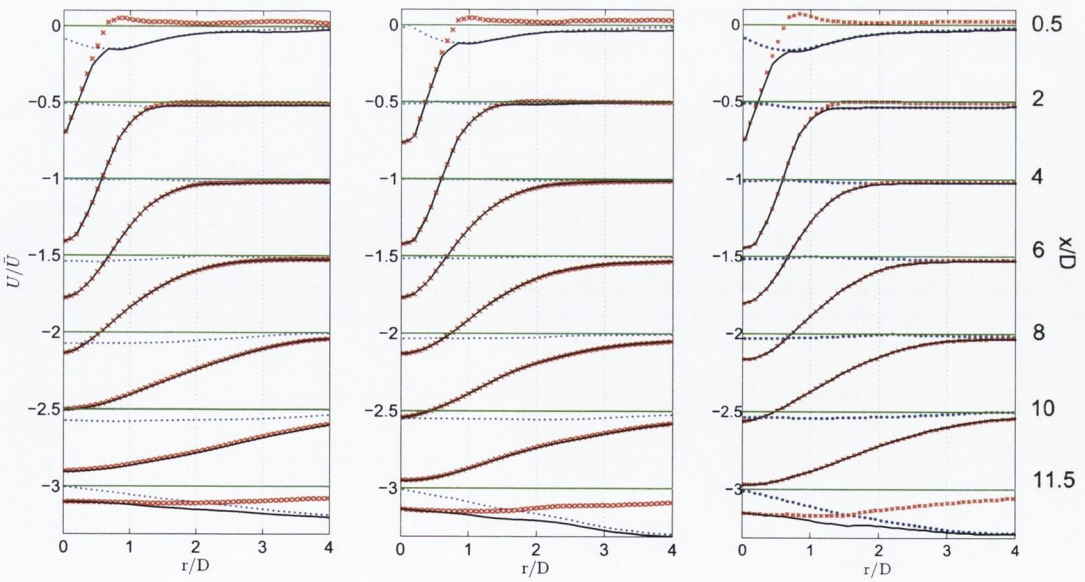

(e) $L_0/D = 18$ (f) $L_0/D = 24$ (g) $L_0/D = 32$

Figure 7.25: Average absolute (−), axial (×) and radial (•) velocity profiles; $H/D = 12$, $Re = 3000$. Profiles taken at distances of $D = 0.5, 2, 4, 6, 8, 10, 11.5$ from the orifice, subsequent profiles offset by $U/\bar{U} = 0.5$ with corresponding zero velocity also plotted (−).

Once again, the near field results presented in figure 7.25 at $H = 12D$ are rather similar to those seen at $H = 4D$ and $H = 8D$ in that the orifice area is dominated by familiar jet formation flows in both the axial and radial directions. All profiles start out as Gaussian in shape and, as with the corresponding lower axial spacings, larger stroke lengths appear to produce narrower centreline axial velocities of greater magnitude. However, due to the greater axial spacing between the orifice and impingement surface all velocity profiles can be seen to degrade to an even greater extent prior to impingement, with that of $L_0 = 3D$ having an almost negligible impact velocity. Shuster and Smith presented similar results ($L_0/D = 1, 2, 3$, $Re_{\bar{U}} = 2500$) for a free synthetic jet, as pictured in figure 7.26.

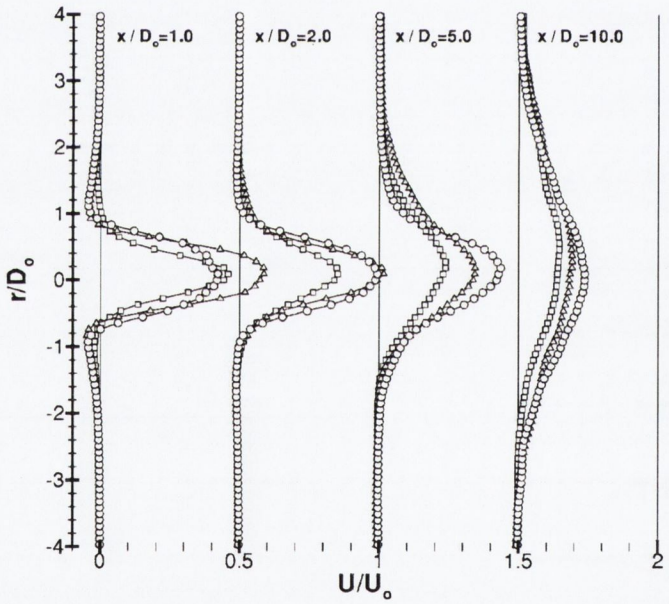

(a) $L_0/D = 3$

Figure 7.26: A comparison of cross-stream profiles of the streamwise velocity for differing values of L_0/D at $Re_{\bar{U}} = 2500$. Profiles for $x/D \geq 2$ have been shifted along the U/U_0 axis by successive increments of 0.5. L_0/D: □ 1; △ 2; ◯ 3 [48].

While some similar trends are visible, such as the effects of the suction stroke close to the orifice in which axial velocity is seen to go negative, the results differ substantially in other ways. Although both sets of data are scaled differently ($U_0 =$

$2\bar{U}$), and figure 7.25 does not present a truly free jet, it is obvious that the jet presented by Shuster and Smith is of substantially higher initial velocity, suffers less degradation with axial distance and appears much more similar to some of the jets formed at larger stroke lengths in figure 7.25. The discrepancy between the results may be attributed to nozzle design, as Shuster and Smith showed that, for their experimental setup, entire vortex rings were able to escape the effects of the suction phase, whereas no significant vortices were identifiable in the flow fields presented earlier in this work (figure 7.12). The increase in jet spreading observed in figure 7.22 (*b*) at $x > 6D$ for $L_0 = 12D$ can clearly be seen in both the radial and axial velocity in figure 7.25 (*c*). Although the overall volume flux was shown not to decrease significantly, this spreading appears to result in a small yet significant decrease in jet centreline velocity compared to both higher and lower stroke lengths. A progressive increase in stroke length can be seen to push the spread to increased axial distances. As was seen at previous axial spacings, larger stroke lengths produce higher radial velocities parallel to the surface upon impingement which are also maintained to greater radial distances.

7.1.4.4 Findings

The results presented in this section showed that flows established at small stroke lengths had a much stronger radial velocity component immediately surrounding the orifice, this is attributed to the strong radial component involved in the vortex formation process which occurs at a much greater frequency at small stroke lengths. For the axial spacings presented, proximity of the impingement surface to the jet exit appeared to have little effect on the flow in the region immediately surrounding the jet exit. All velocity profiles showed evidence of a time averaged stagnation zone forming in the flow as it approached the impingement surface. The results indicated that flows formed at small stroke lengths, $L_0 < 4D$, spread more rapidly in the absence of a coherent vortex ring. In general, axial core flow was seen to be maintained to a greater distance from the jet exit at larger stroke lengths; this also resulted in larger radial flows to greater axial distances upon impingement.

7.1.5 POD Analysis

Proper orthogonal decomposition (POD) applied to particle image velocimetry can be useful in identifying the primary energy containing eigenmodes in complex flows; this is done by identifying where the energy within the flow lies. Depending on operational parameters such as axial spacing and stroke length the synthetic jet's flow field can vary greatly. It is quite common to find that the near field of a synthetic jet is comprised of large velocity fluctuations caused by highly periodic, predictable structures. In contrast, in the far field large velocity fluctuations may still exist, but jet evolution and subsequent mixing may cause them to be quite erratic and turbulent. POD provides a method of isolating these modes within the respective flow fields and evaluating the associated energy levels. The following figures were calculated using the entire time series of each PIV data set, as outlined in section 7.1.1. Processing was done using the DaVis software package and subsequent results were exported to MATLAB in vector file format, after which any further post processing and plotting was performed.

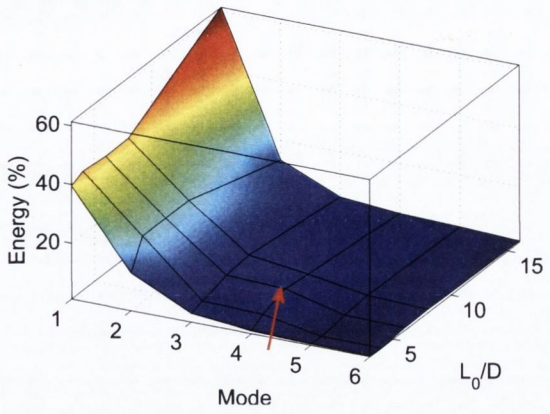

(a) $H/D = 4$

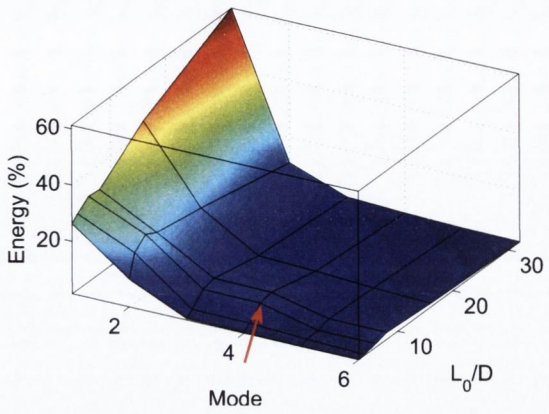

(b) $H/D = 8$

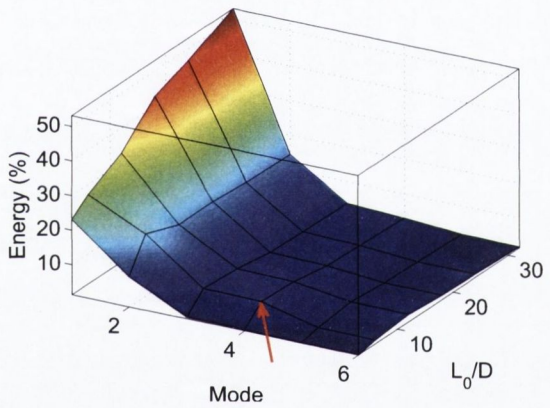

(c) $H/D = 12$

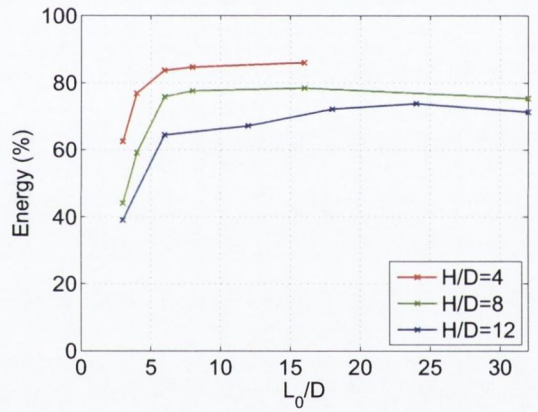

(d) Cumulative energy of first 3 modes

Figure 7.27: POD modal energy content for PIV flow fields; $Re = 3000$.

Figure 7.27 (a) to (c) provides a graphical representation of the energy levels contained in each of the first six eigenmodes for the full range of stroke lengths presented earlier and at axial spacings of $H = 4D, 8D$ and $12D$. As is the nature of POD the first eigenmode always has the largest energy content, with subsequent modes containing progressively less energy; this is the case throughout figure 7.27. The percentage of energy captured by the first few modes at smaller axial spacings is consistently more than that at larger axial spacings, the reasons for this are twofold. Firstly, as the jet develops it deviates from the predictable, structured flow; larger axial spacing allows

for greater development, making it more difficult to approximate with few eigenmodes. Therefore the most powerful modes at larger axial spacings are less likely to account for as much of the jet flow as they would at low spacings. Secondly, with the field of view being significantly reduced at the lower axial spacing the more coherent jet flow now occupies a larger percentage of this field; consequently, less energy is required to represent the (now fewer) low energy flow features (including noise) more commonly found in the remaining flow field not occupied by the jet.

The most striking feature across all axial spacings is that a larger percentage of energy is consistently accounted for by the first mode with increasing stroke length; this is particularly noticeable for large stroke lengths $L_0 \geq 8D$. It has been established that $L_0 \approx 8D$ is the threshold stroke length beyond which the trailing jet becomes the dominant feature in the flow; the evidence of figure 7.27 suggests that this phenomenon is accounted for by the first eigenmode beyond a stroke length of $L_0 \approx 8D$. While this may be the case for large stroke lengths, jets formed at $L_0 < 8D$ have been shown to be primarily dominated by vortex formation and advection, with maximum vortex ring circulation being achieved between $4 \leq L_0 \leq 8D$. This corresponds very well with figures 7.27 (a) and (b) in particular, where the energy contained in the first mode for this range of stroke length appears to remain near constant at about 40% for $H = 4D$ and around 30% for $H = 8D$, indicating that the flow fields operate similar flow regimes. While this regime is clearly evident at $H = 4D$ and $8D$ it may also be present at $H = 12D$, however as only one flow field within this regime has been decomposed at this spacing it remains unconfirmed. Across all axial spacings the stroke length which consistently contains the least amount of energy in the first mode is $L_0 = 3D$. This case does not lie in the trailing jet regime, nor does it have the required stroke length to form a fully coherent vortex ring; not only does the jet formed at $L_0 = 3D$ contain less energy due to its diminished stature, but the energy present is more difficult to account for because of its more erratic, turbulent nature.

Eigenmodes 2, 3 and 4 across all axial spacings present similar trends, as evident from figure 7.27. Energy content at $L_0 = 3D$ again exhibits a low magnitude in line with its erratic nature, while the large energy contribution to the first eigenmode at large stroke lengths, $L_0 \geq 8D$, results in a shift of energy from subsequent modes,

particularly as the power of the vortex ring reduces compared to the dominance of the trailing jet. It is the intermediate stroke lengths $4 \leq L_0 \leq 8D$ that provide a more interesting analysis, with the red arrows in figure 7.27 pointing to eigenmodes which have a consistently larger energy content (small local bulges) compared to the same modes in other flow regimes. Evidently, a greater number of eigenmodes are required to approximate flow fields dominated by vortex formation and advection. Further analysis of the respective eigenmode flow fields will provide a more detailed picture of the energetic flow mechanisms identified thus far at the various axial spacings and stroke lengths.

7.1.5.1 H/D=4

Figure 7.28 depicts the first three most powerful eigenmode flow fields at an axial spacing of $H = 4D$ for progressively increasing stroke length; results correspond to the energy map presented in figure 7.27 (a). While these flow fields confirm much of what has been presented earlier, they also reveal aspects of the synthetic jet which were previously unknown. Some of the velocities (represented by the colour intensities) and flow directions (represented by the stream lines) may at times appear very large, or suggest that the flow is travelling in a direction which is incorrect, but it is important to remember that each eigenmode has a set of eigenvalues spanning the length of the time series, each value corresponds to a particular frame in the series and are all required to reconstruct the flow field in its entirety. An eigenvalue can have a value between $+1$ and -1. For a positive value less than 1 the velocity of the reconstructed eigenmode will be reduced by a proportional amount, whereas in the case of a negative eigenvalue greater than -1 it will also reverse the direction of the flow for that mode. For example: If an eigenmode has a streamwise velocity of 150 m/s at the jet exit and the corresponding blowing and suction phase both reach a maximum value of ± 15 m/s respectively, eigenvalues of $+0.1$ and -0.1 will be required at those times in the corresponding time series to approximate both phases, thereby scaling the eigenmode and reversing the direction of flow for the suction phase.

At a stroke length of $L_0 = 3D$ the first, and most powerful eigenmode by far can be seen to account for flow structures within the immediate vicinity of the orifice; this

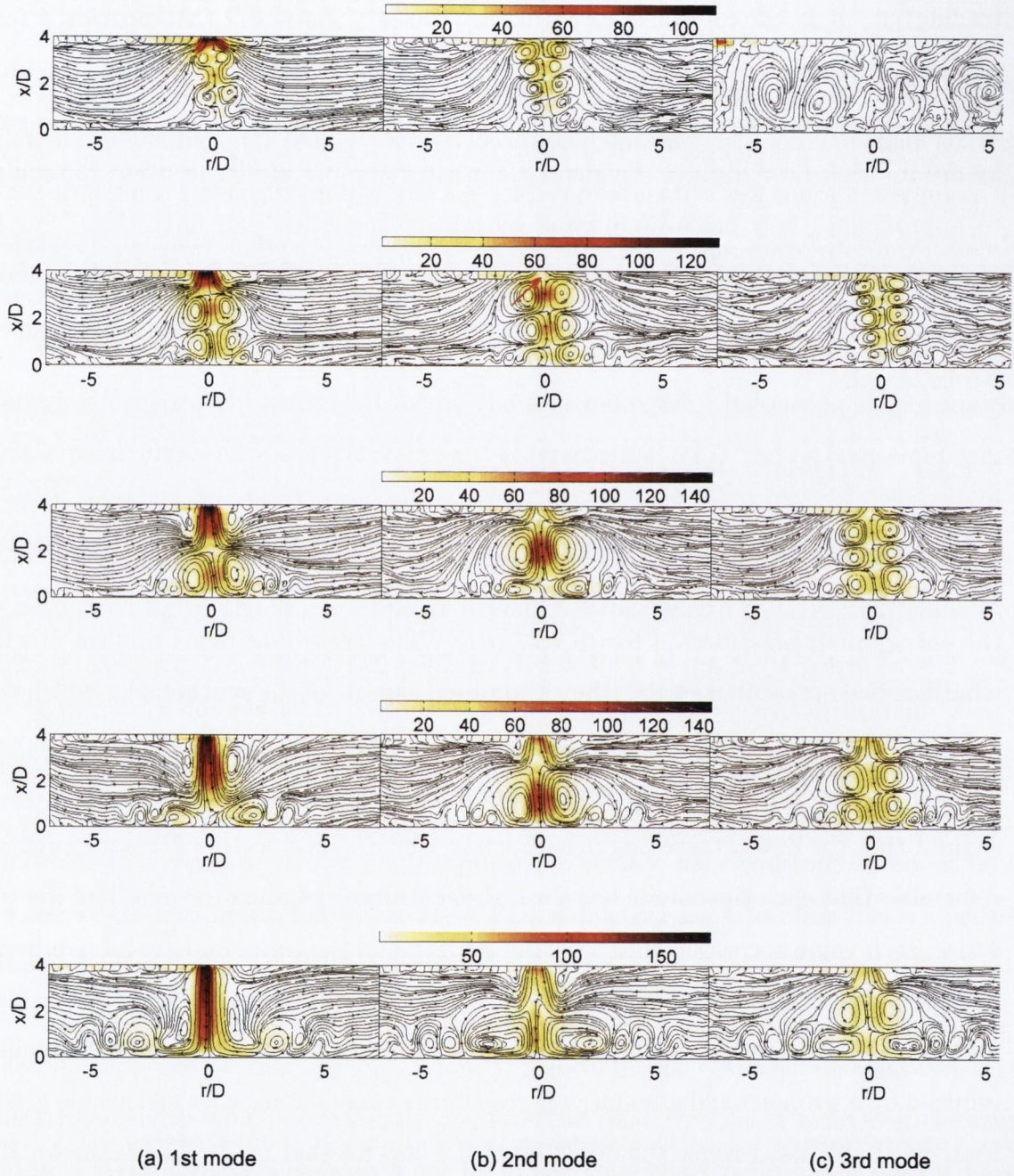

Figure 7.28: First three POD eigenmode flow fields; $Re = 3000$, $H/D = 4$, from top down $L_0/D = 3, 4, 6, 8, 16$.

corresponds to the location where the highly periodic ejection and subsequent reingestion occurs. Few vortices can be seen to escape the near field in this mode, with none present at the impingement surface. The second eigenmode presented shows a

substantial reduction in flow energy as indicated by the reduction in colour intensity. This mode is less concerned with the periodic motion of the jet, but more with vortex propagation. Comparatively weak vortices can be seen extending up to the impingement surface, but no further radially. As the subsequent eigenmode flow field shows no jet characteristics whatsoever it is reasonable to believe that there are no coherent structures, merely a turbulent diminished jet impinges upon the surface at this stroke length. There are two reasons why the third eigenmode contains very little visible flow structure; the main reason is that this mode is primarily accounting for an artefact of reflection in the PIV image which has manifested itself as a vector; this can be seen up in the top left corner of the flow field on the right. The second reason is that because there are so few coherent structures in the flow at this stroke length, many more low energy modes are required to approximate the erratic nature of the flow. As such, any noise manifested as spurious vectors may contain energy on a similar scale to those modes representing the less powerful jet features.

In keeping with the trends presented in figure 7.27 (a), where greater first mode energy levels were seen to correspond with an increase in stroke length, so it is the case in the first eigenmode flow field for $L_0 = 4D$ presented in figure 7.28. Once again the flow energy appears to be concentrated about the jet orifice, indicating that this regime is similarly dominated by the highly periodic suction and ejection stroke. The regime does however differ to a greater extent in the far field, where in all three modes vortex structures appear to extend right the way up to the impingement surface; these results indicate a much stronger impingement dominated by vortex propagation. Small scale vortices present at the impingement surface indicate mixing and a presence of small scale turbulence. It is also worth highlighting at this point that POD also identifies the presence of a stagnation point, or saddle point, in the flow. This point appears immediately in front of the orifice during the suction stroke where there is a location at which the flow is neither travelling towards the orifice due to the suction stroke, nor travelling away from the orifice with the ejected fluid. It has been documented previously by McGuinn *et al.* [67] that the saddle point can be located farther from the orifice with larger stroke length and is also affected by confinement. The saddle point at a stroke length of $L_0 = 4D$ is identified in the second eigenmode by the red

arrow. Similar stagnation points can be identified at other stroke lengths and axial spacings however, depending on dominant flow characteristics, it may not be present in the second eigenmode, as powerful flow characteristics produced by greater stroke lengths can sometimes push it to the third mode.

With further increases in stroke length the first eigenmodes show a progressive transition from a flow field primarily dominated in the near field by the periodic suction-ejection phase of the jet and large vorticular structures in the far field, to one where the periodically ejected fluid alone dominates the entire span between jet exit and impingement zone; this can be seen in figure 7.28 for stroke lengths $L_0 \geq 6D$ and is indicative of a progressive transfer of the primary power mode away from the vortex ring in favour of the trailing jet as it becomes the dominant form of mass transport from orifice to impingement surface. It is also noticeable that in figure 7.28 showing the first eigenmodes for the final two presented stroke lengths ($L_0 = 8D$ and $16D$) no vortices exist directly between the orifice and impact zone. No eigenmodes for stroke lengths greater than $L_0 = 4D$ show the type of small vortices impinging on the stagnation zone which are associated with small scale mixing. However, $L_0 = 6D$ and $8D$ do show similar vortices developing above the surface at a removed radial location, suggesting that interaction may ensue once impingement has occurred. There are substantially fewer small scale structures present in the first three eigenmodes at $L_0 = 16D$ compared to those at lower stroke lengths; this arises as a result of an inadequate amount of space for a jet of this length scale to develop sufficiently. The first eigenmode is seen to mainly account for the strong periodic motion of the jet formation, and as a consequence of the trailing jet, vortex behaviour is not nearly so periodic. As was indicated by the red arrows in figure 7.27, increases in stroke length between $3D \leq L_0 \leq 8D$ contribute to an increase in energy levels at modes $2, 3$ and 4; the corresponding data in figure 7.28 indicate that these modes are predominantly associated with vortex size and strength. Subsequent increases beyond $L_0 = 8D$ have been shown to contribute primarily to energy increases in the first mode, that of the highly periodic trailing jet. These energy increases are manifested in a corresponding increase in modal velocity, as seen in 7.28 for a stroke length of $L_0 = 16D$. The presence of vortex rollup upon impact is also quite obvious at $L_0 = 16D$ with both

the first and second eigenmode showing a powerful flow moving radially outwards at the impingement surface. Above this fluid, mode 1 still depicts a recirculation from the vortex ring moving towards the surface, while mode 2 shows the powerful vortices formed upon impingement travelling in a radial direction. These vortices are maintained at a height above the plate until the powerful impingement flow degrades and forms further vortex structures itself beyond $r \approx 2.5D$, as can be seen across all three eigenmodes.

7.1.5.2 H/D=8

The first three eigenmodes for various stroke lengths at an axial spacing of $H = 8D$ are depicted in figures 7.29 and 7.30. These results correspond to the energy map presented in figure 7.27 (*b*). Much of the behaviour that was observed at the lower axial spacing of $H = 4D$ appears similar to that at $H = 8D$. Once again the first eigenmode appears to be primarily related to the periodic suction and ejection phases of the jet, as is indicated by the high modal velocities in the vicinity of the orifice. For small stroke lengths of $L_0 = 3D, 4D$ and $6D$, as shown in figure 7.29, this mode also accounts for a significant amount of vortex propagation in the far field. However, as was the case at $H = 4D$ the jet formed at a stroke length of $L_0 = 3D$ is largely diminished with few coherent structures which can be easily captured using POD. For the increased axial spacing, all eigenmodes at $L_0 = 4D$ show that the coherent flow structure is dissipated prior to surface impingement, whereas at $L_0 = 6D$ there appears to be sufficient momentum imparted in the first mode to transport the flow to the impingement surface just as small scale vorticular interaction commences. This flow regime matches up with that seen at $H = 4D$ for $L_0 = 4D$, however the increased axial spacing requires a corresponding increase in stroke length to $L_0 = 6D$ to achieve the same flow condition. Further increase in stroke length results in the impingement of larger structures in the stagnation zone with similar smaller vortices developing in the wall jet following impact; this can be seen for all stroke lengths in figure 7.30. As with the lower axial spacing of $H = 4D$ the increase in energy at modes $2, 3$ and 4 for stroke lengths of $L_0 \leq 8D$ corresponds to eigenmodes depicting vortex propagation. At greater stroke lengths of $L_0 = 16D$ and $32D$, presented in figure 7.30, eigenmodes

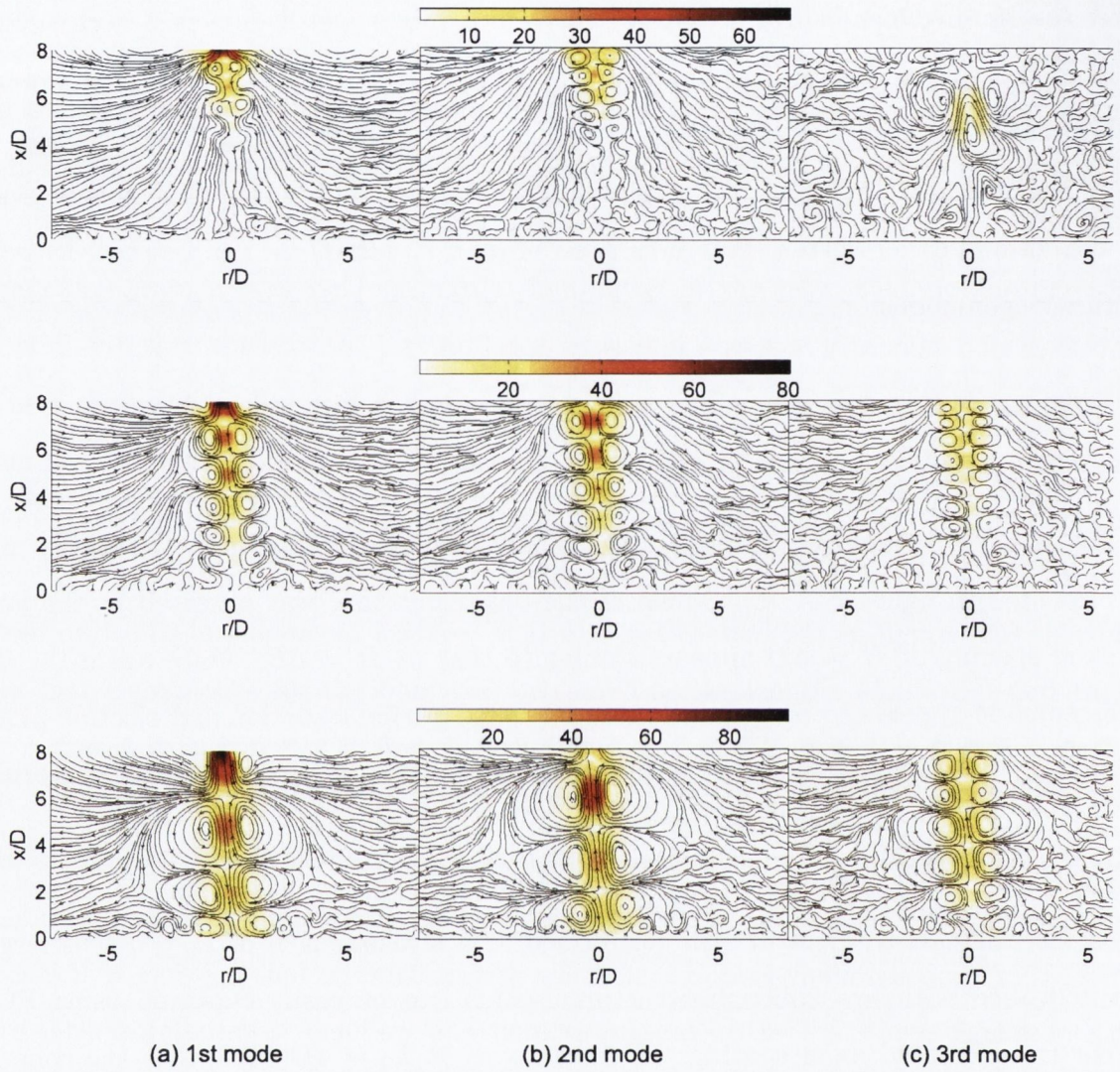

Figure 7.29: First three POD eigenmode flow fields; $Re = 3000$, $H/D = 8$, from top down $L_0/D = 3, 4, 6$.

2 and 3 do also show vortex propagation. However, being at a much larger scale, and with the flow clearly not as developed as at lower stroke lengths, the energy contained in these modes does not contribute to the type of small scale turbulent interactions most desirable for heat transfer. In fact, the energy levels in these vortex containing modes, 2, 3 (and 4 which isn't shown), decrease with increasing stroke length as the vortex becomes an increasingly minor feature either through destruction or through less frequent formation; energy is seen to accumulate in the highly periodic first mode

containing the increasingly more powerful trailing jet. The stroke length of $L_0 = 32D$, seen in figure 7.30, shows strong evidence of vortex rollup upon impingement, particularly in the second eigenmode. While there are no vortices to be seen in the near and intermediate field, two large recirculations are present either side of the impinging fluid at the plate surface. All three eigenmodes indicate that after impingement these structures traverse radially, remain quite large and undergo relatively little degradation; this is particularly evident at larger stroke lengths.

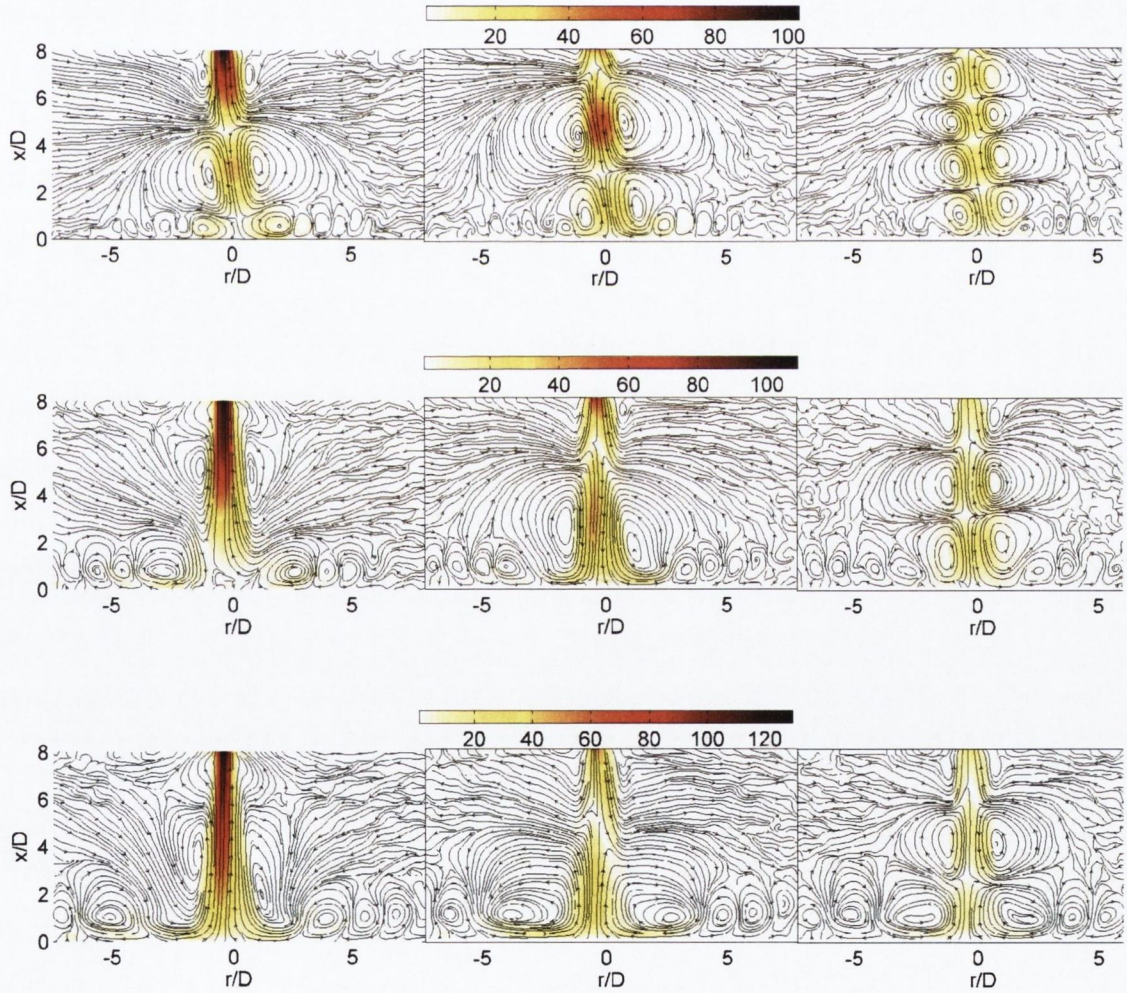

Figure 7.30: First three POD eigenmode flowfields; $Re = 3000$, $H/D = 8$, from top down $L_0/D = 8, 16, 32$.

Figures 7.31 and 7.32 show the first three most powerful eigenmode flow fields for a range of stroke lengths at an axial spacing of $H = 12D$. These results correspond to the first three modes presented in figure 7.27 (c). It can be seen that in the near field, the eigenmodes look much the same as those presented for similar parameters at $H = 8D$. The major differences in flow fields arise as jet development occurs. Once again the first mode approximates the most powerful, highly periodic structures in the flow, which for small stroke length includes the suction and ejection phases, while for large stroke lengths it takes the form of the mass fluid ejection, largely consisting of the trailing jet. At this axial spacing, flow structures at the stroke lengths of $L_0 = 3D$ and $6D$, seen in figure 7.31, appear to dissipate prior to impingement on the surface. Comparing this to the flow fields at $H = 8D$, shown in figure 7.30, a larger stroke length is required to impart sufficient momentum so that a reasonably undiminished flow can impact upon the plate. As $L_0 = 12D$ shows quite large scale structures impinging on the surface in all three eigenmodes, an intermediate stroke length of $L_0 \approx 8D$ is likely to provide small scale interaction at the stagnation zone. This axial spacing may well prove to be the limit of this small scale mixing regime provided by vortex formation, propagation and interaction. Increasing the stroke length much beyond $L_0 = 8D$ has shown that an accumulation of fluid in the higher velocity trailing jet behind the vortex commonly results in its destruction prior to impingement. Also, as a vortex ring is only formed at the beginning of each ejection phase, the reduced frequency of formation means a larger interval between subsequent ejections, thereby making vortex interaction increasingly unlikely.

7.1.5.3 H/D=12

The flow regimes dominated by the trailing jet have been shown to exist beyond $L_0 = 8D$. One of the characteristics observed in this regime in section 7.1.1.3 was a skewing of the vortex ring followed by destruction. This phenomenon has been captured clearly in the eigenmodes for the stroke length of $L_0 = 12D$ in figure 7.31. The far field of mode 1 shows a separation between the ejected fluid and the impinging jet at $x = 6D$; this corresponds to the location of vortex ring destruction, which in turn causes the direction of the impinging flow itself to become skewed and to undergo

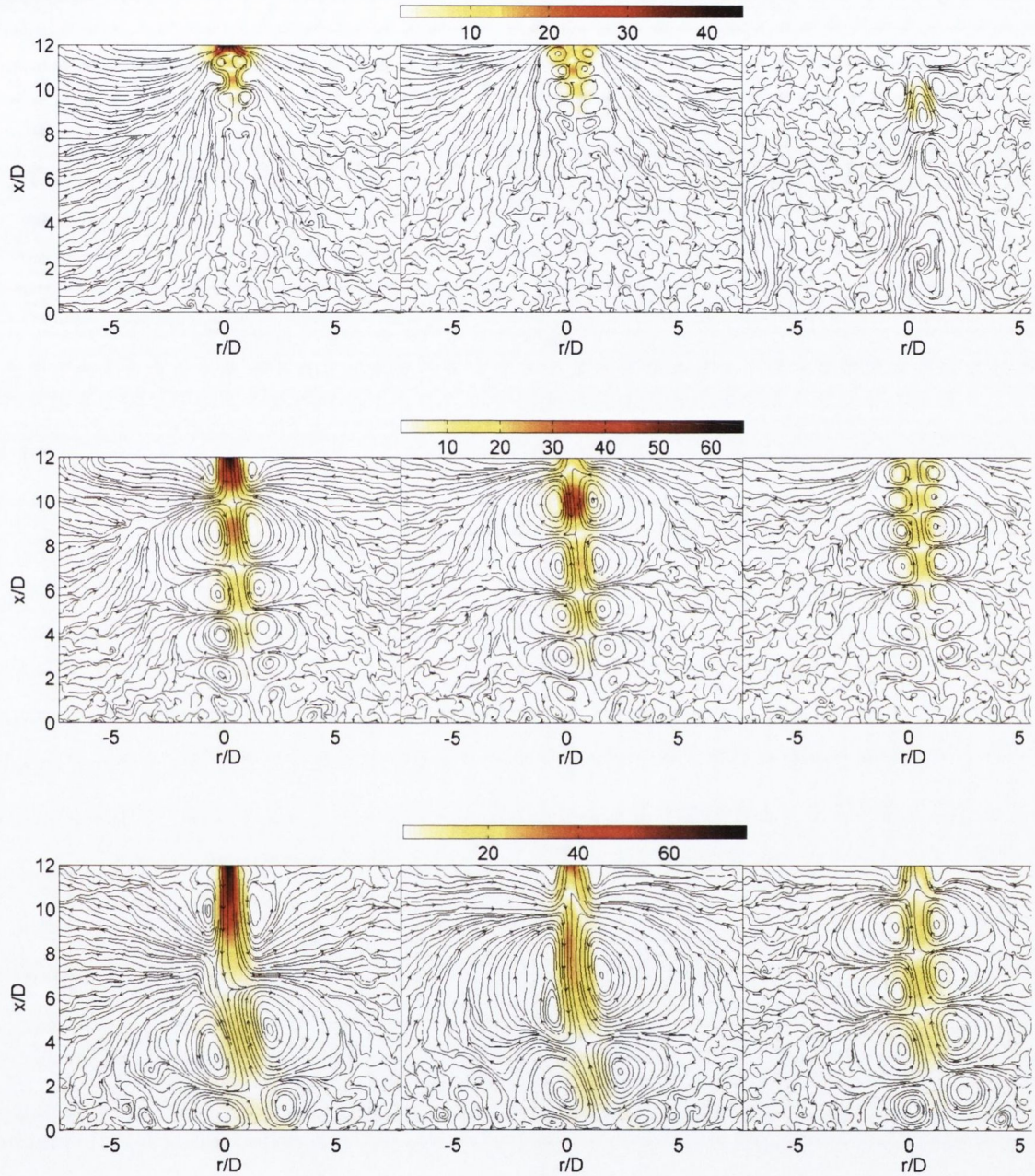

Figure 7.31: First three POD eigenmode flow field; $Re = 3000$, $H/D = 12$, from top down $L_0/D = 3, 6, 12$.

a significant amount of spreading. While at lower axial spacings this stroke length resulted in the impingement of large coherent structures and a substantial trailing

jet, the destruction of the vortex destabilises the entire flow. Even for the largest stroke length ($L_0 = 12D$) in figure 7.31 either side of the impinging flow at the plate surface there appears to be a total lack of flow structures in all three eigenmodes. This indicates that the reduced coherence caused by the vortex destabilisation has resulted in a premature viscous dissipation of the jet; the jet neither has a coherent leading vortex to help it reach the impingement surface, nor does the fluid ejection alone possess enough momentum at this stroke length to arrive by itself.

Figure 7.32 presents eigenmode flow fields which show how this particular flow regime changes further with increasing stroke length. The increased amount of momentum imparted to the flow at $L_0 = 18D$ is now sufficient to allow large structures to impinge directly upon the surface and also for smaller scale turbulent structures to develop after impact. All three first mode flow fields in figure 7.32 indicate that along with the increasing dominance of the trailing jet, the position at which viscous dissipation of the ejected fluid occurs is pushed to a progressively greater axial distance. With an increase in the first mode power containing the trailing jet, the impinging flow becomes more resistive to skewing caused by the destabilising influence of the vortex destruction. The flow continues to undergo a powerful viscous dissipation and spreading, however by $L_0 = 32D$ no obvious asymmetry of the flow is observable. At this axial spacing vortex rollup upon impingement is only seen to be present in the first eigenmode beyond a stroke length of $L_0 \geq 24D$, although there is evidence of rollup present at $L_0 = 18D$ in the less powerful second mode.

The maximum location of the saddle point, measured from the nozzle exit, has been calculated from the POD flow fields and results have been presented in figure 7.33. While the overall data appear quite consistent, that at $H = 4D$ does deviate somewhat compared to that of higher axial spacings. This can be attributed to confinement effects, as documented by McGuinn *et al.* [67]. These data show that the location of the saddle point is primarily dependent on stroke length. Figure 7.33 (*b*) shows that for axial spacings which provide minimal confinement, $H = 8D$ and $12D$, the relationship between the stroke length and the location of the saddle point can be described with a second order polynomial. The data are seen to conform very well to this fit. Using the equation it is possible to extrapolate that the saddle point may reach a maximum

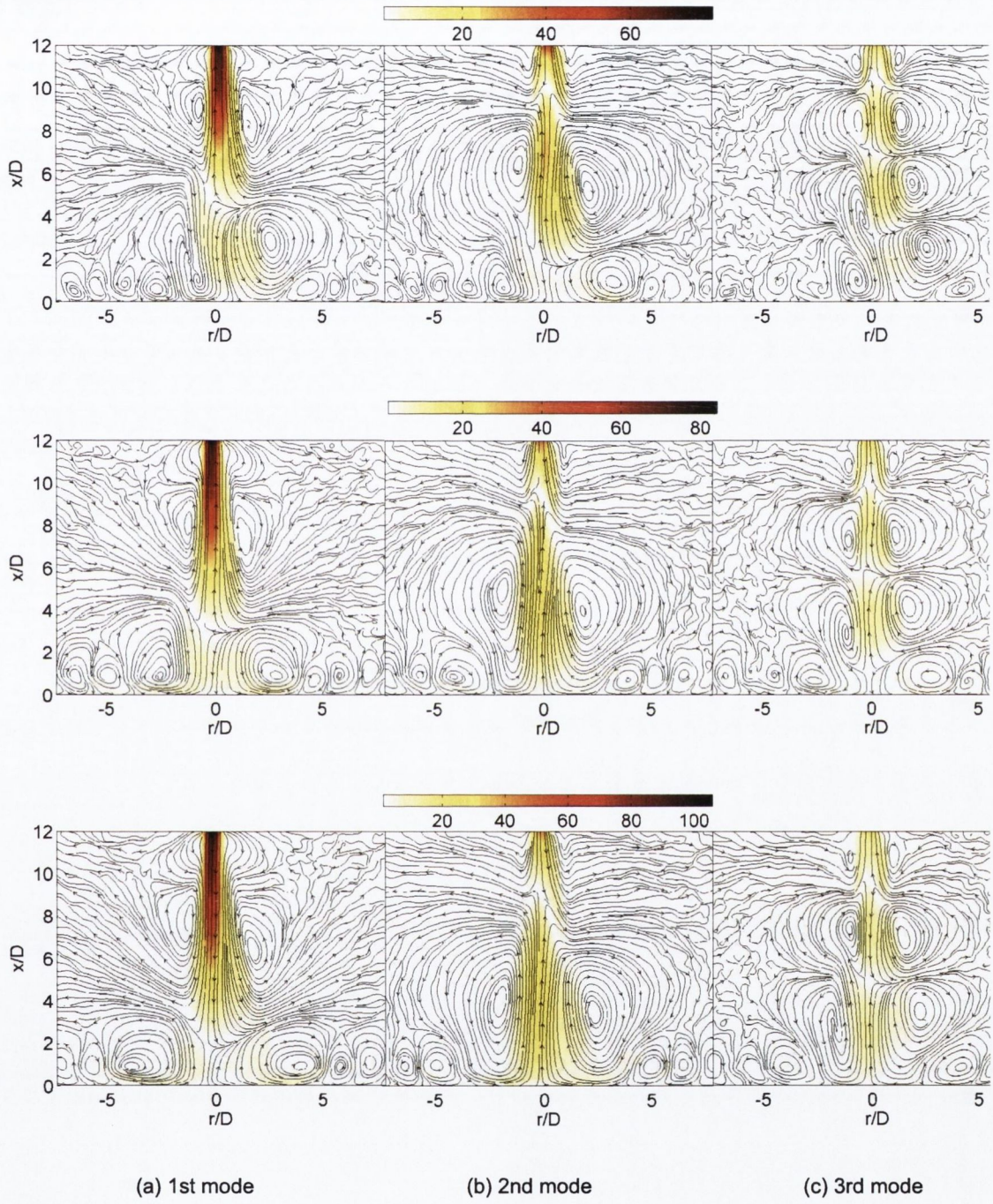

Figure 7.32: First three POD eigenmode flow field; $Re = 3000$, $H/D = 12$, from top down $L_0/D = 18, 24, 32$.

possible distance from the orifice of $x = 2.67D$ at a stroke length $L_0 = 36.7D$.

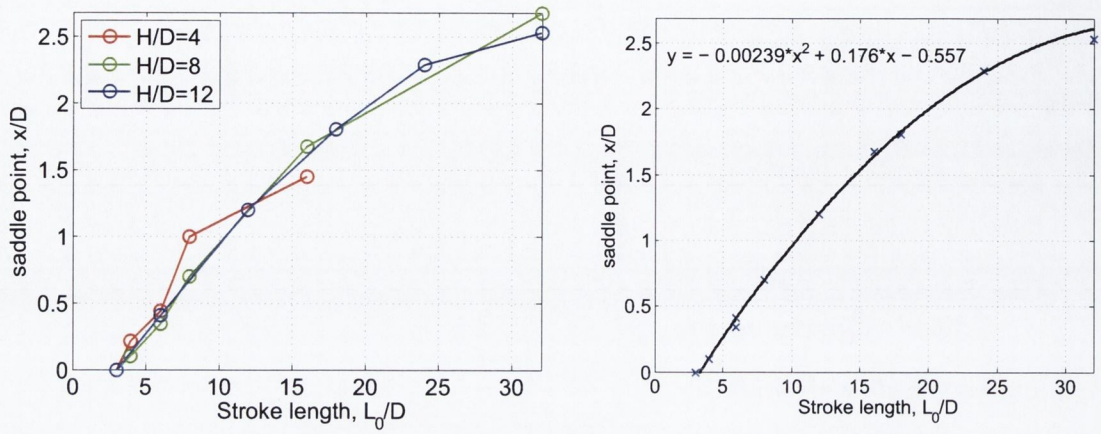

(a) (b)

Figure 7.33: (*a*) Maximum saddle point location calculated from POD flow fields for $H/D = 4, 8$ and 16. (*b*) Polynomial fit applied to data at $H/D = 8$ and 16.

7.1.5.4 Findings

POD flow fields have revealed that for stroke lengths $L_0 \geq 8D$ the first eigenmode captures the relatively large energy of the highly periodic trailing jet, whereas the first eigenmode at smaller stroke lengths primarily contains flow structures concerned with vortex formation and propagation. It was also evident that intermediate stroke lengths, $4D \leq L_0 \leq 8D$, required a greater number of eigenmodes to account for the more complex type of flow produced by vortex formation and advection. Eigenmodes help to provide clarity on the evolution of the flow with varying stroke length; this analysis has also shown what state the flow was in upon impingement. The results are in good accordance with the flow regime map presented in figure 7.19 in that they confirm exactly which combination of stroke length and axial spacing achieve a specific flow and impingement condition. POD has also proved to be a useful tool in identifying the location at which the leading vortex ring undergoes destruction as well as the maximum location of the saddle point.

7.2 Heat Transfer

This section will primarily present local heat transfer data for the full range of dimensionless stroke lengths seen in table 7.1, as well as for a range of axial spacings and, to a lesser extent, Reynolds number. Heat transfer data will be accompanied by local velocity and temperature data to help identify the dominant mechanisms and to relate these back to the flow analysis presented in section 7.1. The majority of the data in this section were acquired using three instruments, namely hot-film, hot-wire and cold-wire temperature probes; these were used for the measurement of heat transfer, velocity and air temperature respectively. Data acquired include stagnation point and radial profile measurements presented in the form of time averaged and time resolved values for raw and spectrally reconstructed data. Frequency spectra of signal power and coherence are also presented.

7.2.1 Stagnation Point Measurements

Simultaneous stagnation point heat transfer, local fluid velocity and air temperature measurements were performed for a wide set of operational parameters including stroke lengths $2D \leq L_0 \leq 32D$ and axial spacing $2D \leq H \leq 16D$ at a Reynolds number of 3000; the post-processed data are presented in figure 7.34. Although tests at each axial spacing were performed at a constant Reynolds number, results show that differing stroke lengths can effect very different levels of heat transfer; it is proposed that this can be attributed to the different flow regimes created by varying stroke length and orifice to plate spacing, as identified in section 7.1. Further analysis of these heat transfer data using the local velocity and temperature measurements helps to reveal the effective mechanisms.

Along with Nusselt number and velocity data, figure 7.34 also presents T^*, a dimensionless temperature which represents the temperature differential between the local impinging air and the surface as a fraction of the total differential between the surface temperature and the jet temperature as measured within the cavity. T^* is calculated as follows:

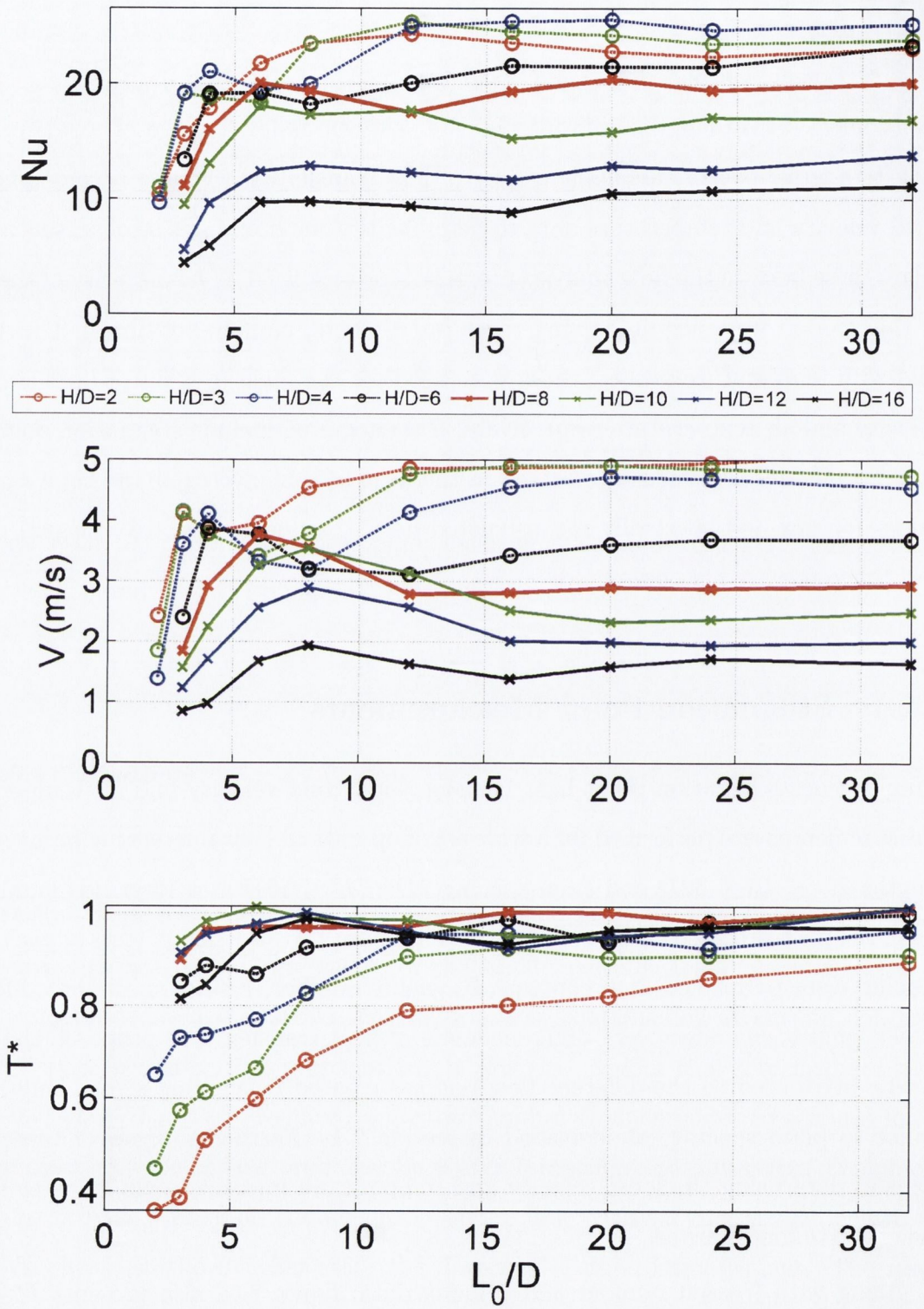

Figure 7.34: Time averaged stagnation point local Nusselt number, velocity and dimensionless air temperature (eqn. 7.3) as a function of stroke length; $Re = 3000$. (vel. & temp. measured at 0.3mm above the surface)

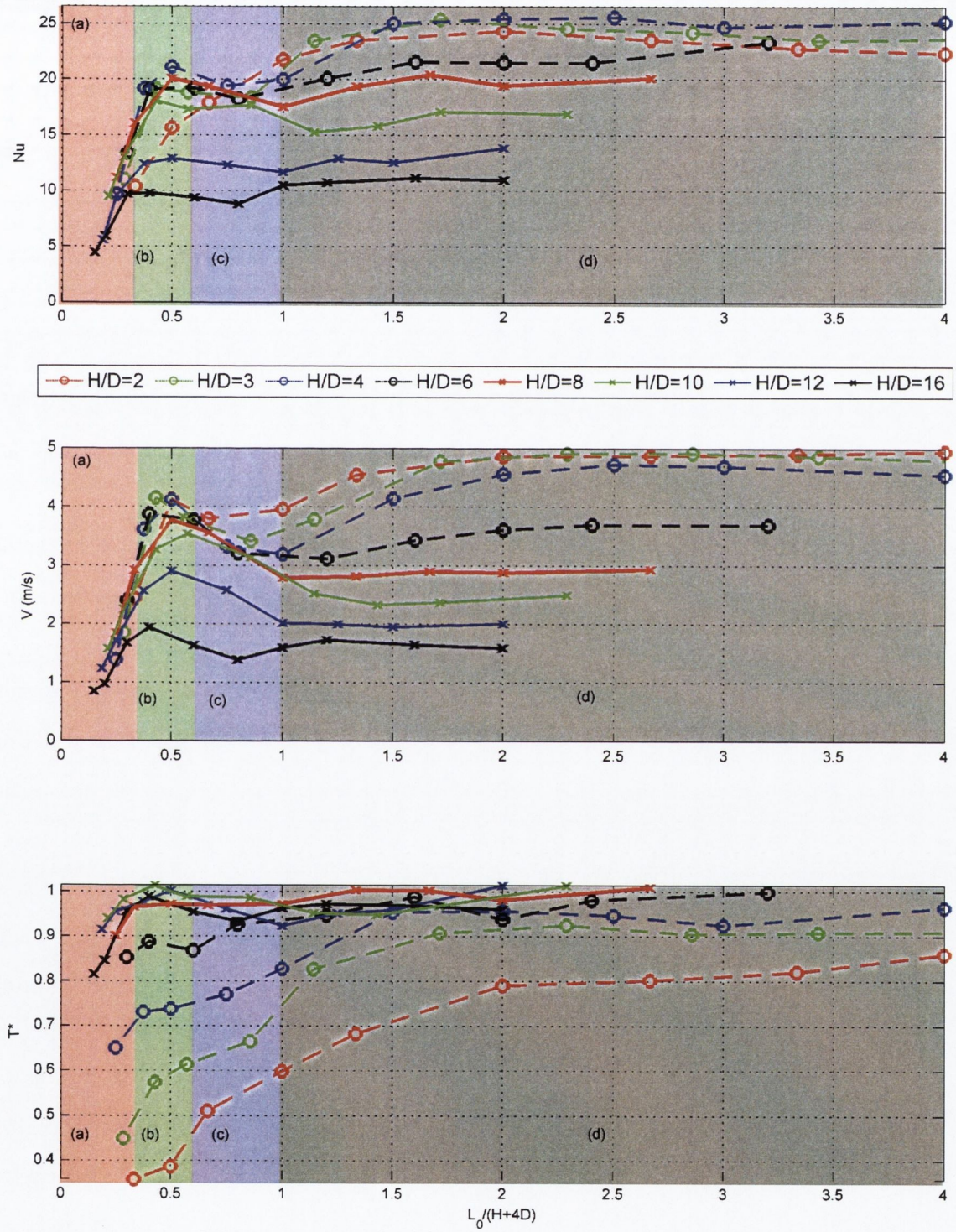

Figure 7.35: Scaled time averaged stagnation point local Nusselt number, velocity and dimensionless air temperature (eqn. 7.3) as a function of stroke length; $Re = 3000$. (vel. & temp. measured at 0.3mm above the surface)

$$T^* = \frac{T_{surf} - T_{air}}{T_{surf} - T_{cav}} \tag{7.3}$$

where T_{surf}, T_{cav} and T_{air} are the surface, internal cavity and local air temperature respectively. A value close to 1 indicates that the average temperature of the impinging air is at a similar level to that of the ejected fluid. A lower value may imply that the jet lacks sufficient momentum to disrupt the thermal boundary layer, or, as we will see in later sections, it may be the case that the air has become thermally saturated with heat from the surface; this result is likely to produce a corresponding reduction in the magnitude of the temperature fluctuation.

Although difficult to determine from figure 7.34, the Nusselt number, velocity and temperature data show strong trends across all three sets of data. When the same data are re-scaled with the stroke length L_0, nondimensionalised by the axial spacing H plus a constant $4D$, as seen in figure 7.35, the various regimes become more apparent.

The first regime, identified in red as zone (a), exists for $L_0/(H + 4D) \leq 0.3$ and represents a synthetic jet flow field of diminished momentum; such instantaneous flow fields have been presented in figures 7.2 and 7.12. Insufficient impulse is imparted to the jet to enable it to travel the required axial spacing and impact upon the plate with significant momentum; in general this may either be caused by a diminished jet being formed at a stroke length below the threshold corresponding to maximum vortex circulation (small dimensionless stroke length, L_0/D), or it may be that the axial spacing is simply too large for the jet to travel without a significant loss of momentum (high axial spacing, H/D). The resulting low impingement velocity is unable to cause significant disruption of the thermal boundary layer thereby causing a noticeable elevation in local air temperature; both of these factors (low velocity and high air temperature) give rise to a reduced heat transfer coefficient.

The second regime, identified in green as zone (b), shows a notable local maximum in heat transfer and velocity and a moderate suppression in air temperature (with a corresponding local maximum in T^*) across most axial spacings for $0.3 \leq L_0/(H + 4D) \leq 0.7$. Across all data sets there appears to be a local maximum at

$L_0/(H + 4D) \approx 0.5$. Consequently, it is possible to use this scaling relationship to calculate a dimensionless stroke length that will optimise these values for any axial spacing. This can be done as follows:

$$\left(\frac{L_0}{D}\right)_{opt} = \frac{H}{2D} + 2 \tag{7.4}$$

The exception to this trend appears to occur in the heat transfer data for $H = 2D$, where there is no local maximum; heat transfer is seen to decline uniformly with decreasing stroke length, a finding that is in agreement with those of Valiorgue *et al.* [89]. This result contrasts with the corresponding velocity data which does conform to equation 7.4, albeit to a lesser extent than at the larger axial spacings. It is thought that this apparent deviation in trend is due to the merging of the respective regimes. Thus, with decreasing axial spacing the corresponding stroke length for which regime (*b*) exists grows smaller, the stroke length is eventually pushed below the threshold for jet formation and therefore is no longer apparent, leaving the trend present at $H = 2D$.

Many flow fields presented for regime (*b*) were found to contain vortex rings of high coherence, consistently at stroke lengths of $4D \leq L_0 \leq 8D$, propagating between the jet orifice and impingement surface, however, reduced axial spacings of $H \leq 4D$ are also seen to extend this pattern to smaller stroke lengths. Flow fields reflecting these results were observed in figures 7.3, 7.4, 7.7, 7.8 and 7.13.

The original jet formation proposal which was outlined using figure 7.1 suggested that maximum vortex circulation would be achieved at $L_0 \approx 4D$, beyond which an increase in stroke length would merely contribute to extending the length of the trailing jet. However, as the synthetic jet ejection phase conforms to a sinusoidal velocity program, the location at which the maximum velocity occurs can play a defining role in the evolution of the flow field. As the stroke length increases beyond $L_0 = 8D$, maximum ejection velocity is inevitably experienced during the ejection of the trailing jet, resulting in vortex disruption, and thereby changing the nature of the flow regime. So far, this evidence corresponds remarkably well with figure 7.35. In this regime, (*b*), some axial spacings experience a maximum in local velocity and

heat transfer at stroke lengths below $L_0 = 8D$; it is clear from figure 7.34 that the axial spacing of $H = 12D$ becomes the upper limit at which maximum velocity is achieved in this regime. There are two reasons why a reduction from the peak is experienced, one being determined by jet development, the other by the nature of jet formation. Firstly, it is desirable to have fully formed vortices impinge as frequently as possible upon the surface. Krueger *et al.* [63] showed that the impulse associated with vortex ring formation was much larger than for the associated trailing jet, therefore the corresponding operational parameter that optimises both frequency and formation requirements occurs at $L_0 \approx 4D$. It can be seen from the velocity data presented in figure 7.34 that this is indeed the location where maximum velocity is experienced for many of the axial spacings; however, deviation occurs with increased nozzle to plate separation. As the separation is increased the vortex requires more impulse to maintain its momentum to the impingement surface; extra momentum is provided to the flow by increasing the length of the trailing jet, with the consequence of a decrease in frequency; consequently peak impingement velocity is experienced at a greater stroke length. Although in theory a continual increase in stroke length with axial distance should maintain this relationship, this is found not to be the case. Beyond $L_0 = 8D$ the fact that the fluid in the trailing jet is now travelling at a higher velocity than that in the vortex ring produces a significant change in the flow evolution, particularly at greater axial spacings. Vortex tracking data presented in section 7.1.2 showed that as the stroke length exceeds $L_0 = 8D$ a widening of the jet occurs, especially at larger axial spacings, as this was linked to the faster moving trailing jet impacting upon the vortex ring with a subsequent accumulation occurring. The consequence of an increase in jet width and no increase in the volume of ejected fluid is that the axial length of the ejection is effectively reduced. This reduction in length combined with no real increase in peak velocity results in a reduction in the mean fluid velocity at the impingement surface, this can be seen in figure 7.35 as regime (c). The reduction in velocity is less evident at smaller axial spacings as there is insufficient distance for the flow to widen prior to impingement. There is a corresponding small decrease in local heat transfer with the reduction in mean velocity, while a subtle change in trend is evident for fluid temperature at this regime.

The final regime (d) is represented in grey in figure 7.35. At $L_0/(H+4D) \geq 1$ this regime is simply dominated by the powerful discharge of the ejected fluid, and in particular by the trailing jet. Flow fields across all axial spacings revealed that as the primary vortex becomes a less prominent feature in the flow field little interaction between subsequent ejections occurs. At lower axial spacings of $H \leq 6D$ (dashed lines) impingement leads with the fluid from the trailing jet as the vortex ring gets pushed to the side; the restricted space between orifice and plate means little spreading occurs and consequently average velocity is maintained at a relatively high level. While larger spacings of $H \geq 6D$ provide increased distance for the flow to evolve, it has been shown that complete destruction of the vortex ring commonly occurs in this regime; subsequent viscous dissipation results in a spreading of the jet and a reduction in mean impingement velocity.

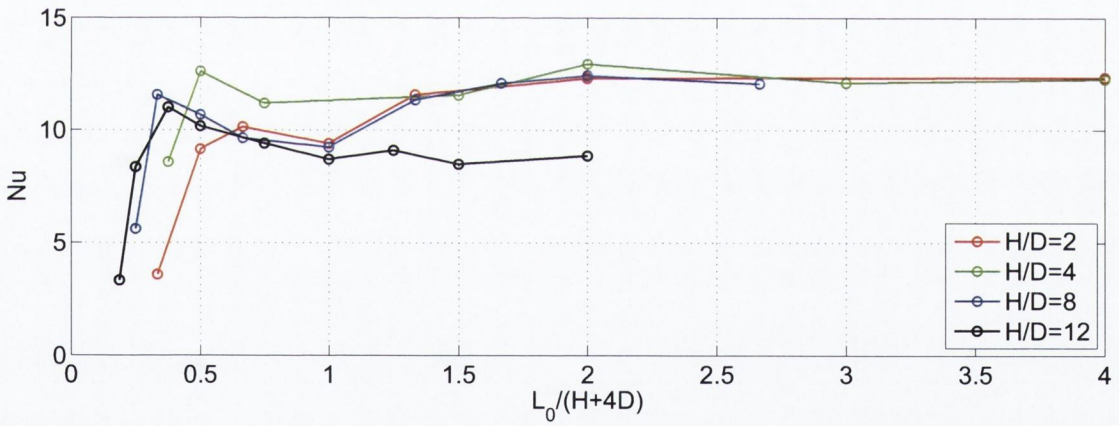

Figure 7.36: Stagnation point Nusselt number; $Re = 1000$

Similar stagnation point heat transfer data are presented in figures 7.36 and 7.37 for Reynolds numbers of $Re = 1000$ and 2000. As is expected, the Nusselt number experiences a decrease with a corresponding reduction in Reynolds number. However, the results show that very similar heat transfer trends to those at the Reynolds number of 3000 are present across all stroke lengths and axial spacings. These findings confirm that the existence of these impingement regimes is independent of Reynolds number within this range and and is largely associated with the stroke length which is the primary influence on the formation, advection and evolution of the vortex ring, trailing

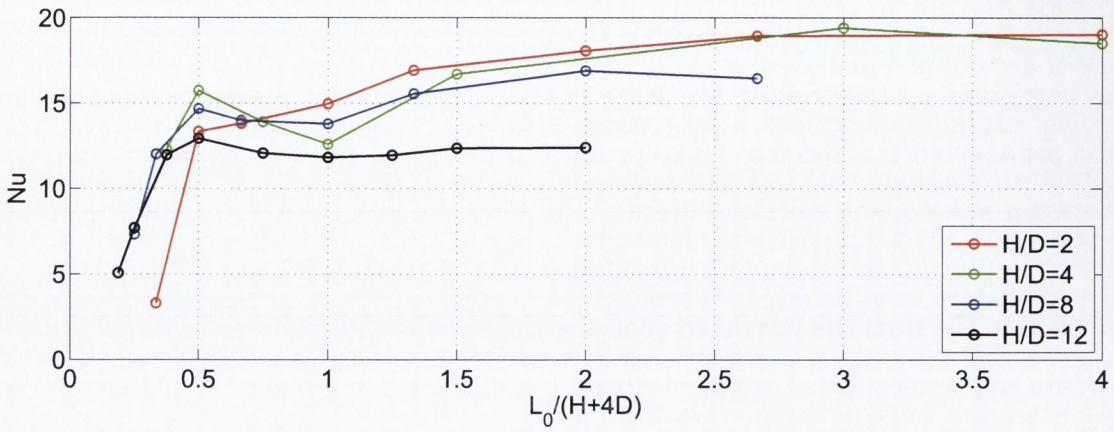

Figure 7.37: Stagnation point Nusselt number; $Re = 2000$

jet and related flow features.

Across all parameter ranges the axial spacing which shows the maximal overall stagnation Nusselt number is $H = 4D$. However, figure 7.35 shows that this is not reflected in the corresponding velocity data where lower axial spacings consistently produce higher mean velocities, indicating that it is not solely impingement velocity that dictates the level of heat transfer. Temperature data reveal that it may be the higher average impinging air temperatures (high T^*) experienced below $H = 4D$ which reduces the heat transfer coefficient for small jet to plate spacings. The increase in air temperature at these low axial spacings may be caused by the high degree of confinement, which restricts the entrainment of cooler ambient air into the flow. Average jet impingement velocities are seen to drop off quite rapidly beyond $H = 4D$; flow fields and volume flux data in section 7.1 revealed that this results from the spreading of the jet as it evolves as well as from a loss in momentum as the ejected fluid traverses the axial spacing. Both of these factors may have significant implications for heat transfer profiles.

Heat transfer data at low axial spacings ($H = 2D$) is in good agreement with the findings of Valiorgue *et al.* [89] who fitted a linear curve to a region below $L_0/H = 2.5$, which experiences a sudden decrease in heat transfer. This was identified as a region operating below the threshold of jet formation. However, the analytical derivation by Holman *et al.* [20] suggests that no synthetic jet is formed below the critical stroke

Regime	Non-dimensionalised spacing	Characterising feature	Description
(*a*)	$L_0/(H+4D) < 0.3$	Diminished momentum.	Reduced impinging flow due to small L_0/D or large H/D produces low Nu, vel. and high local air temp.
(*b*)	$0.3 \leq L_0/(H+4D) < 0.7$	Vortex propagation	High momentum vortices with maximum circulation produce local max. in Nu, vel. and low local air temp.
(*c*)	$0.7 \leq L_0/(H+4D) < 1$	Jet spread	Spreading of the jet reduces local velocity resulting in a drop in Nu and higher average air temp.
(*d*)	$L_0/(H+4D) \geq 1$	Trailing jet	Impingements dominated by powerful trailing jet maintain high velocities, Nu and low air temp.

Table 7.2: Stagnation point regimes identified from figure 7.35 for local Nusselt number, velocity and dimensionless temperature T^* (equ. 7.3).

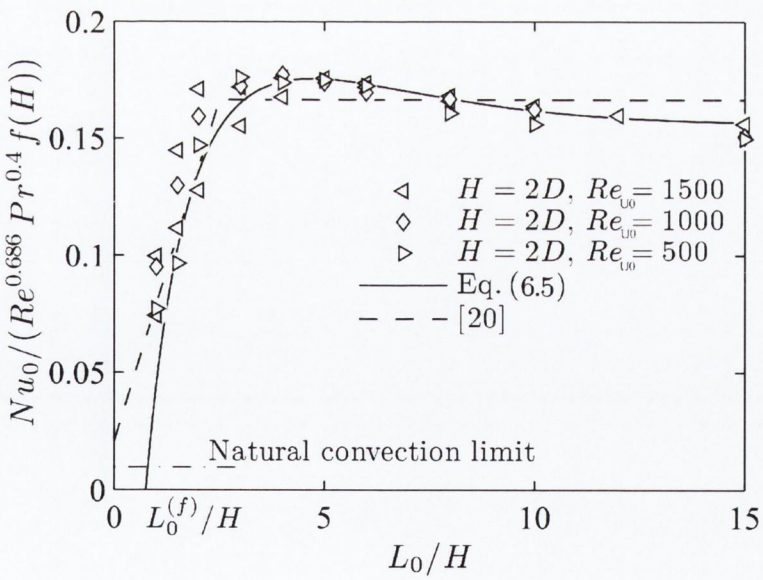

Figure 7.38: Dependence of stagnation Nusselt number $Nu_0/(Re^m Pr^n f(H))$ on stroke length L_0/H (for $H = 2D$, $500 \leq Re_{U_0} \leq 1500$) compared to correlation by Valiorgue *et al.* [89]

length of $L_0/D = 0.16\pi \approx 0.5$. Below this formation threshold, no fluid escapes the suction phase which follows. The heat transfer performance will tend towards the natural convection regime in the absence of any jet formation, it therefore follows that a formation threshold stroke length should be fitted to the correlation outlined by Persoons *et al.* [90] in equation 2.23:

$$\begin{aligned} &Nu_0 = 0.156 Re_{U_0}^{0.686} Pr^{0.4} f(H) g(L_0) \qquad (R^2 = 0.96) \\ &\text{with } g(L_0) = 1 - e^{-\frac{L_0 - L_0^{(f)}}{0.75H}} + 0.244 \left(\frac{L_0 - L_0^{(f)}}{1.8H} \right)^2 e^{-\frac{L_0 - L_0^{(f)}}{1.8H}} \\ &\text{and } L_0^{(f)} = 1.5D \qquad (H = 2D) \end{aligned} \tag{7.5}$$

This correlation has been applied to the stagnation point data and is presented in figure 7.38, with the solid line corresponding to equation 7.5. While the formation threshold parameter $L_0^{(f)}$ exceeds the theoretical value of $0.5D$, which was put forward by Holman *et al.*, it does provide the best fit to the experimental data. The function $g(L_0) = 0$ for $L_0 = L_0^{(f)}$ and tends to unity for $L_0 \to \infty$.

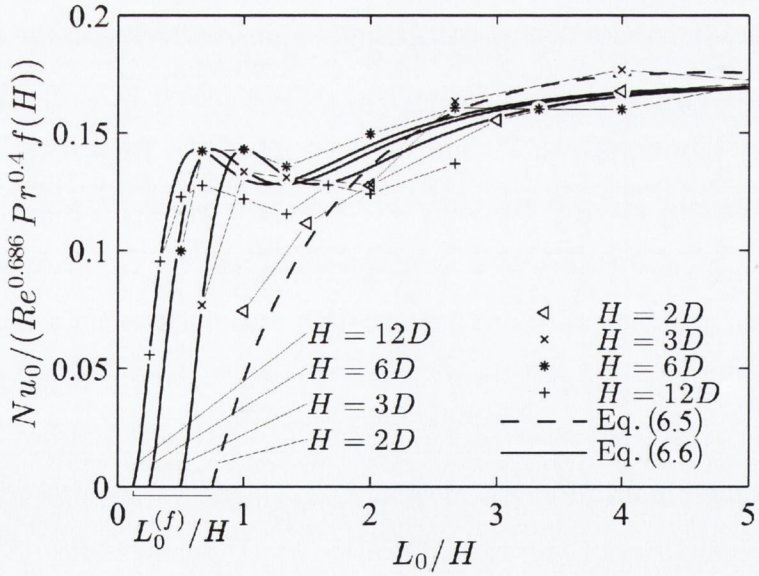

Figure 7.39: Dependence of stagnation Nusselt number $Nu_0/(Re_{U_0}^m Pr^n f(H))$ on stroke length L_0/H (for $3D \leq H \leq 12D$, $Re_{U_0} = 1500$)

Figure 7.39 presents the stagnation point heat transfer results for a wider range of axial spacings ($3D \leq H \leq 12D$) at a Reynolds number of 3000. Compared to figure

7.5, the diminishing heat transfer at low stroke lengths is still evident and shows the same formation threshold at $L_0 = 1.5D$, however the correlation, as represented by the dashed line, does not prove to be as good a fit at these larger axial spacings. Fitting this data at higher jet to surface spacings to the original correlation (equation 2.23) gives the following equation:

$$\begin{aligned} &Nu_0 = 0.171 Re_{U_0}^{0.686} Pr^{0.4} f(H) g(L_0) \qquad (R^2 = 0.822) \\ &\text{with } g(L_0) = 1 - e^{-\frac{L_0 - L_0^{(f)}}{1.01H}} + 0.906 \left(\frac{L_0 - L_0^{(f)}}{0.187H} \right)^2 e^{-\frac{L_0 - L_0^{(f)}}{0.187H}} \\ &\text{and } L_0^{(f)} = 1.5D \qquad (3 \leq H/D \leq 12) \end{aligned} \tag{7.6}$$

which corresponds to the solid line in figure 7.39.

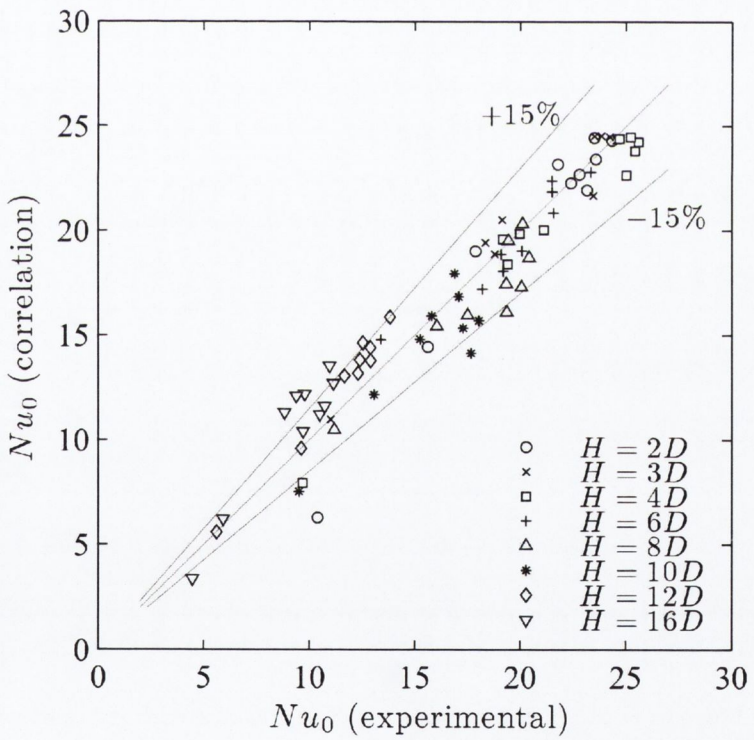

Figure 7.40: Agreement of stagnation Nusselt number Nu_0 between experimental data and correlation eqns. 7.5 and 7.6 for the entire investigated parameter range ($500 \leq Re_{U_0} \leq 2500$, $2 \leq H/D \leq 16$, $2 \leq L_0/D \leq 40$)

Over 85% of the data in the entire parameter range can be matched by the combined correlations equations (7.5 and 7.6) to within ±15% as shown by figure 7.40.

7.2.1.1 Findings

The results in this section have shown that differing stroke length for the a single Reynolds number can achieve very different levels of heat transfer. When time averaged stagnation point Nusselt number, velocity and fluid temperature data were scaled by $L_0/(H + 4D)$ (figure 7.35) it was seen that four heat transfer regimes were clearly identifiable. These regimes were:

(*a*) $L_0/(H + 4D) \leq 0.3$. This corresponds to an impingement of diminished momentum, where insufficient impulse has been imparted to the jet upon formation to provide it with sufficient momentum to impinge upon the surface undiminished.

(*b*) $0.3 \leq L_(0)/(H + 4D) \leq 0.7$. This is a region where a local maximum in heat transfer and fluid velocity and a suppression in fluid temperature was observed; these were shown to commonly correspond to flow regimes containing vortex rings of high coherence.

(*c*) $0.7 \leq L_(0)/(H + 4D) \leq 1$. In this regime the jet undergoes spreading due to compacting of the impingement zone caused by the longer stroke length; this results in a reduction in impinging fluid velocity with a corresponding fall in surface heat transfer and an increase in fluid temperature.

(*d*) $L_(0)/(H + 4D) \geq 1$. This final regime is dominated by the powerful trailing jet as impingements occur in isolation. With the stroke length being so large in comparison to the axial spacing little opportunity is available for spreading of the jet to occur prior to impingement, consequently suppressed fluid temperatures and higher levels of fluid velocity and heat transfer were observed. Further stagnation point heat transfer measurements were presented to confirm that these trends were also present at Reynolds numbers of 1000 and 2000.

7.2.2 Spectral Decomposition

Section 7.2.2 outlined the method of spectral decomposition employed in the analysis of the simultaneously acquired, time resolved measurements of heat flux, velocity and temperature signals at the impingement surface. The following section will present both decomposed and reconstructed data in various forms such as power spectra and

time averaged frequency components for radial profiles as well as for stagnation point measurements.

To obtain the following figures the raw time resolved signals were converted into the frequency domain where the driving frequency and all harmonics were separated off. The remaining spectrum was split into two frequency bands; above and below the synthetic jet actuation frequency. All three spectral components, periodic, high and low frequency, were then converted back to the time domain where the root mean square of the fluctuating component of each signal was calculated; this value is representative of both the state of evolution of the jet and also the amount of energy contained in each component. This procedure was repeated for each data point in the series. The upper section of each figure presents mean fluctuating data at each stroke length, while the lower section presents the magnitude of the periodic, high and low frequency components expressed as a percentage of the magnitude of the raw signal. A detailed explanation of the methods used are outlined in section 6.4. While Nu' and V' are simply the root mean square of the fluctuating value for the local Nusselt number and velocity respectively, fluid temperature fluctuation is nondimensionalised by the temperature differential between the heated surface and the jet air temperature:

$$T^{*\prime} = \frac{T'}{T_{surf} - T_{cav}} \tag{7.7}$$

Figure 7.41 shows reconstructed periodic, high and low frequency data for an axial spacing of $H = 2D$, Reynolds number of 3000 and stroke lengths between $2 \leq L_0 \leq 32D$. It is immediately evident from the magnitude of the periodic frequency component across all sets of data that at this very small axial spacing the impingement zone is dominated by a highly underdeveloped periodic flow. An exception to this is seen to occur at $L_0 = 2D$ where no jet is formed; energy within the flow is particularly low and consequently, the fluctuating magnitude of the raw signal is significantly reduced, no significant periodicity is experienced and low frequency phenomena account for a large majority of the fluctuation. Fluctuations in heat transfer and velocity, in particular, are seen to get larger with increasing stroke length, while

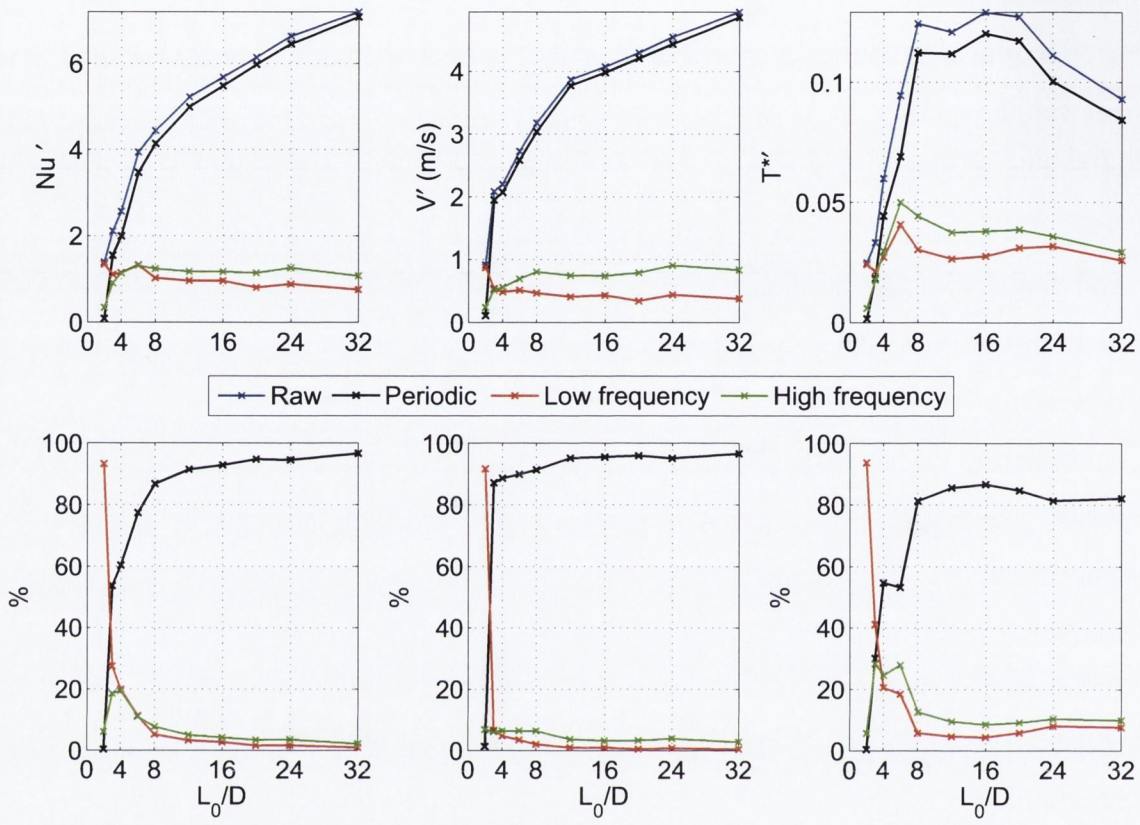

Figure 7.41: Stagnation point fluctuating Nusselt number, velocity and temperature as a function of dimensionless stroke length; $Re = 3000, H/D = 2$

temperature fluctuations appear to reach a maximum at $L_0 = 8D$. This is in contrast with data in figure 7.34 where both average velocity and Nusselt number are seen to level off and remain relatively constant beyond $L_0 = 6D$, and while the average local fluid temperature is seen to experience a moderate yet continual decrease (as indicated by increasing T^*), figure 7.41 shows that a decline in the corresponding fluctuating values are experienced up to $L_0 = 16D$. Considering the continual decrease in local average fluid temperature, the reduction in temperature fluctuations may be attributed to the jet's ability to prevent the thermal boundary layer from reforming to the same extent between impingements, thereby suppressing the higher temperatures which would otherwise increase both the average and fluctuating fluid temperatures; similar results have been reported by McGuinn *et al.* [146]. It is significant to note

that as the highly periodic regime becomes established, both the level of high and low frequency components of the jet are suppressed but continue to account for a surprisingly constant proportion of the total fluctuation, regardless of stroke length.

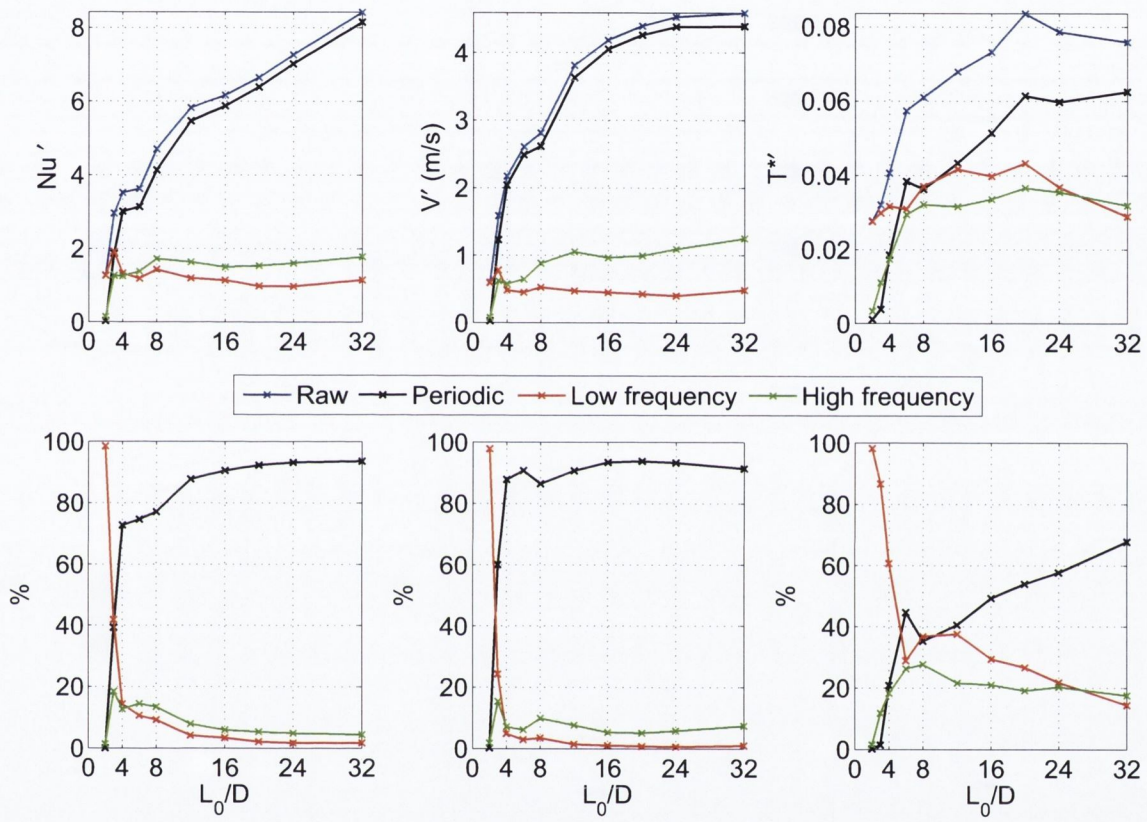

Figure 7.42: Stagnation point fluctuating Nusselt number, velocity and temperature as a function of dimensionless stroke length; $Re = 3000, H/D = 3$

Although marginally reduced, the dominance of the periodic fluctuating component in the heat transfer and velocity data at an axial spacing of $H = 3D$ (figure 7.42) shows little change from that seen at $H = 2D$. It is noticeable however that the corresponding temperature data have undergone a sizeable reduction in periodicity; both high and low frequency components now account for a much larger proportion of the total temperature fluctuation. Such a disproportionate shift between the respective signals indicates that as the jet evolves with axial distance the mixing of fluid that takes place has a much more rapid effect on the redistribution of temperature within

the jet than on velocity fluctuations. Fluctuations in velocity and Nusselt number at this small axial spacing are already beginning to show the existence of the various flow regimes at low stroke lengths. A familiar change in slope corresponding to the various heat transfer regimes identified previously in figure 7.35 is clearly visible for both sets of data, particularly below $L_0 = 8D$. This appears to be consistently a region where the high frequency component of the spectrum accounts for more elevated proportion of the total fluctuation than it does at larger stroke lengths.

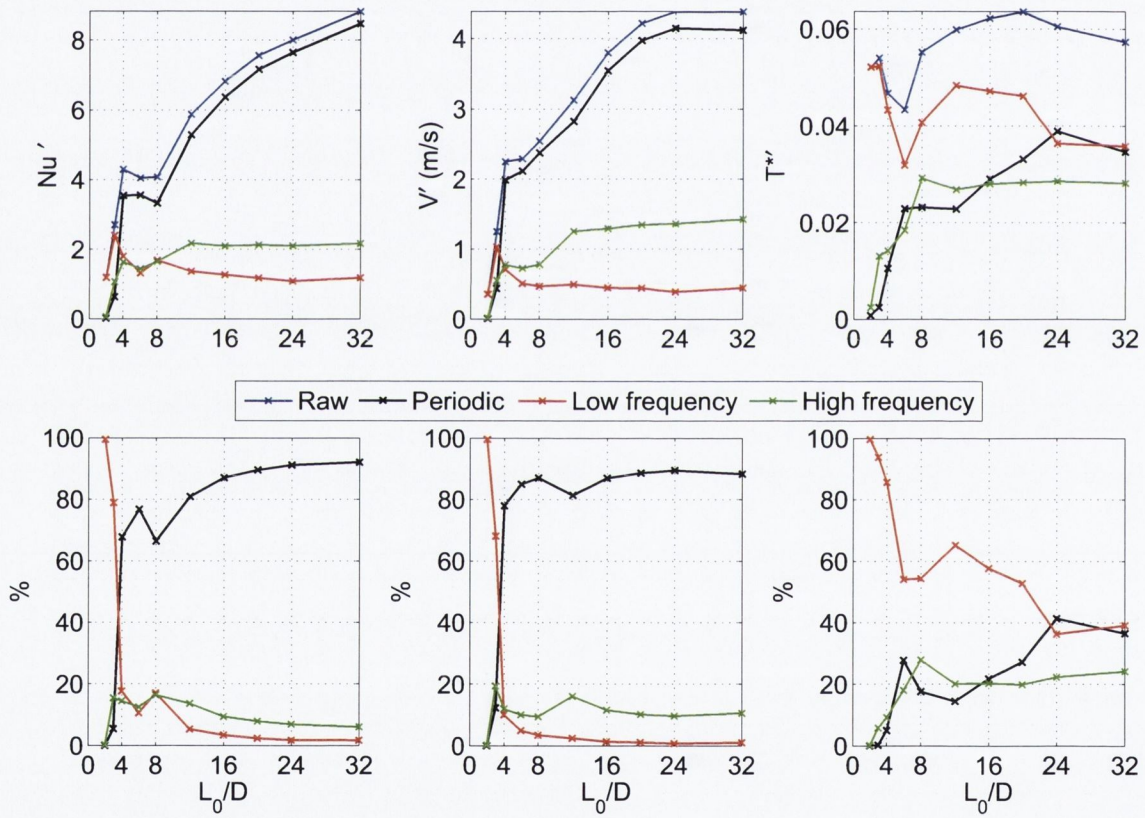

Figure 7.43: Stagnation point fluctuating Nusselt number, velocity and temperature as a function of dimensionless stroke length; $Re = 3000, H/D = 4$

Figure 7.43 shows that a further increase in axial spacing to $H = 4D$ produces a small decrease in the periodic spectral component of the velocity and heat transfer signals while the increase in low frequency component of the temperature fluctuation appears to have been solely at the expense of the periodic component. The most

noticeable behavioural change at the greater axial spacing is the larger temperature fluctuation at small stroke lengths. This fluctuation is seen to be comprised almost completely of low frequency spectral components, thereby confirming the diminished nature of the jet. The fluctuations in the raw signal of the dimensionless temperature are seen to subside temporarily as the stroke length is increased to $L_0 = 6D$, the low frequency components being supressed by a shift in power from the low energy, low frequency domain to the higher energy, periodic and high frequency domains which are associated with a more powerful flow. A subsequent increase in raw signal fluctuation occurs once again, however this time it is due to the increasingly periodic nature of the jet associated with larger stroke lengths.

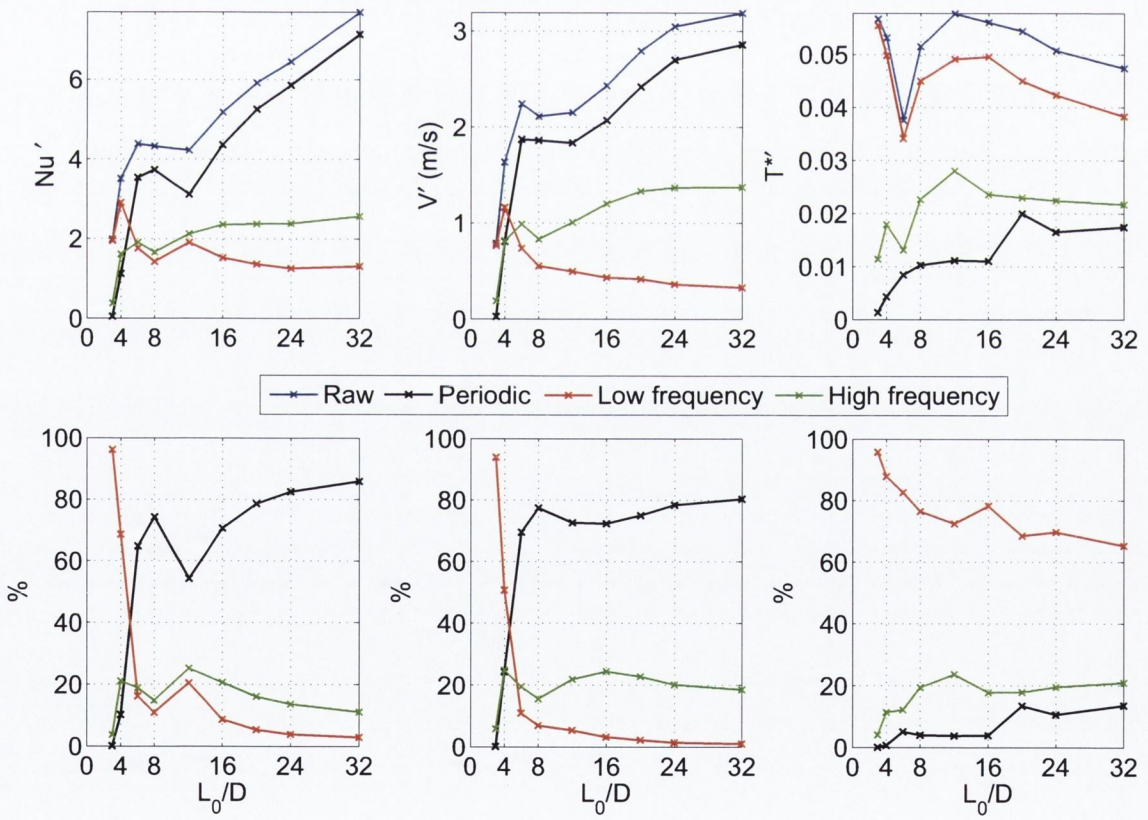

Figure 7.44: Stagnation point fluctuating Nusselt number, velocity and temperature as a function of dimensionless stroke length; $Re = 3000, H/D = 6$

The data presented in figure 7.44 for $H = 6D$ show a continuation in the trends

from those observed at lower axial spacings. The proportion of velocity and heat transfer fluctuation accounted for by the periodic frequency component has been further reduced in favour of both low and high frequencies, indicating additional jet development; this is especially true of stroke lengths between $4D \leq L_0 \leq 16D$ which are seen now to account for up to 25% of the raw fluctuation magnitude for both Nusselt number and velocity signals. The high frequency component of the temperature fluctuation continues to account for a relatively constant 18% of the total fluctuating magnitude, while the periodic component continues to degrade further most of the total fluctuation across the range of stroke lengths is accounted for by frequencies below that of jet actuation.

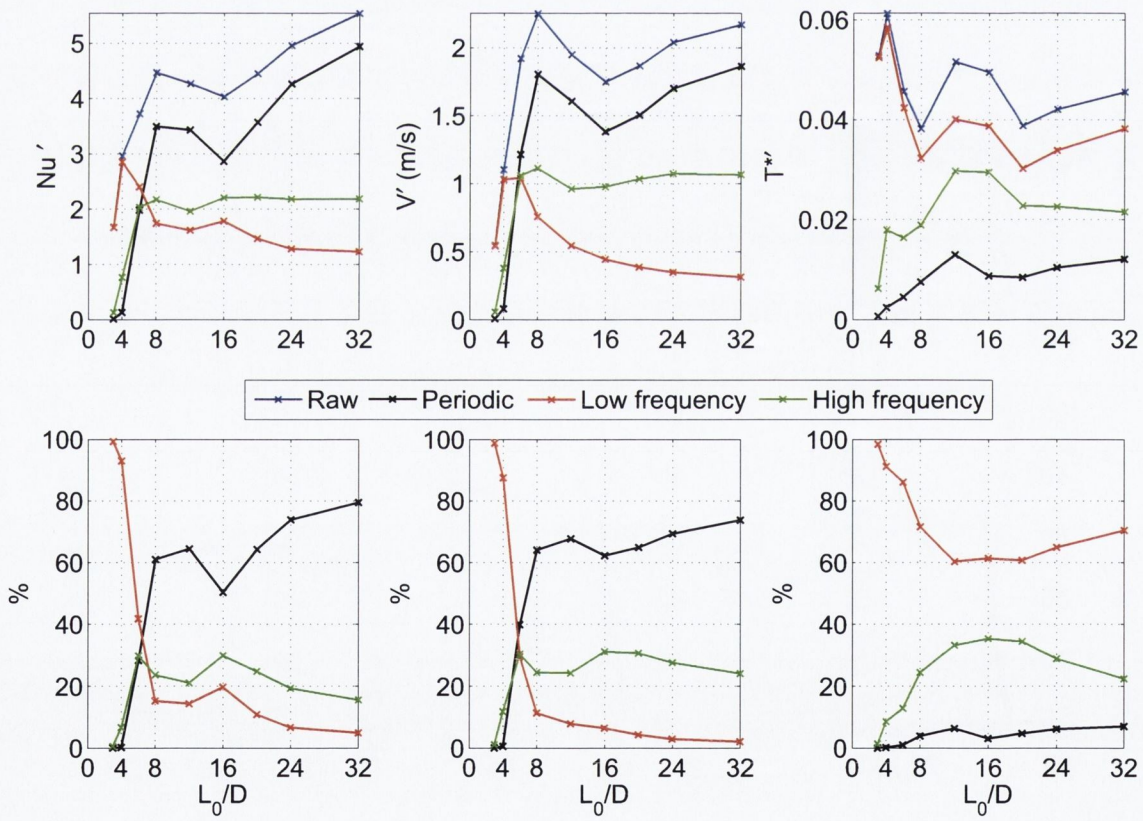

Figure 7.45: Stagnation point fluctuating Nusselt number, velocity and temperature as a function of dimensionless stroke length; $Re = 3000, H/D = 8$

Axial spacings of $H = 8D$ and $10D$ presented in figures 7.45 and 7.46 show a

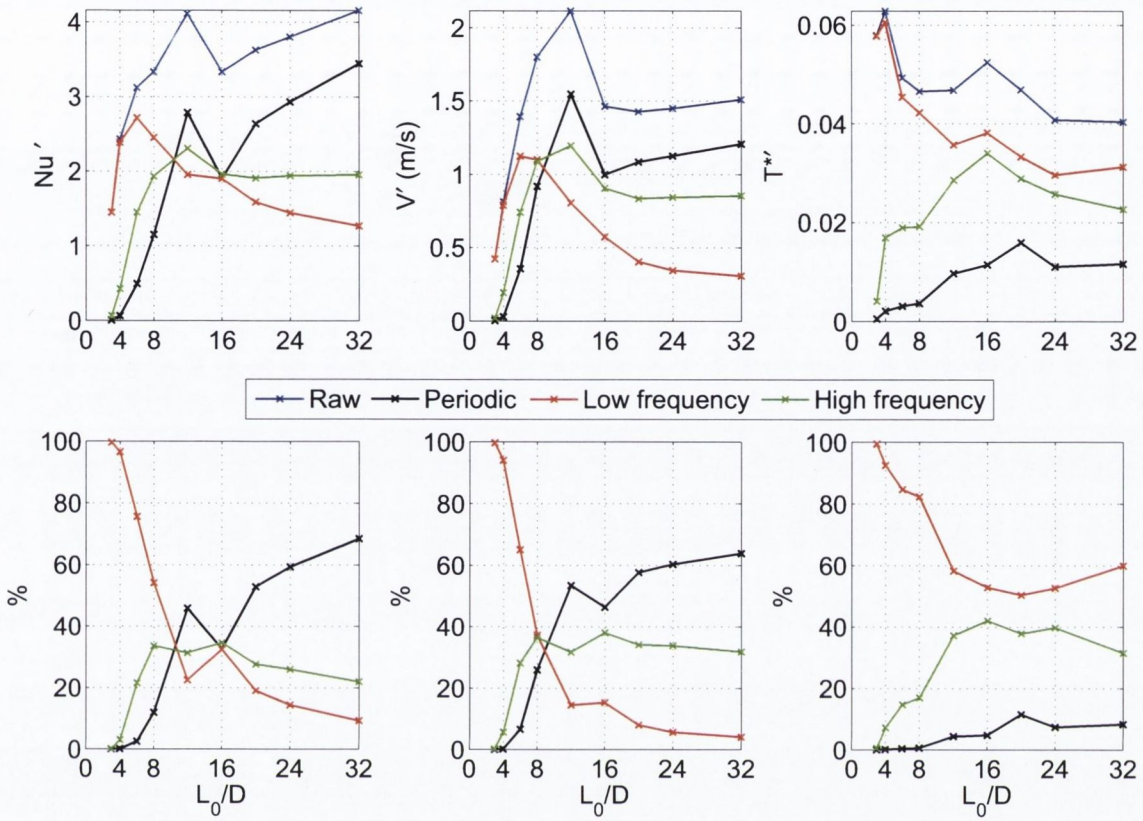

Figure 7.46: Stagnation point fluctuating Nusselt number, velocity and temperature as a function of dimensionless stroke length; $Re = 3000, H/D = 10$

continual increase in the low frequency component of velocity and heat transfer at the expense of periodic oscillations. The high frequency component has consistently accounted for approximately 50% of the total fluctuating magnitude for stroke lengths above $L_0 = 4D$ and for $H \geq 4D$. In keeping with Kolmogorov's power law, jet energy is known to dissipate by cascading to increasingly higher frequencies; the upper limit which the high frequency spectrum appears to have reached indicates a level of saturation has occurred beyond which these frequencies cannot accommodate any further increase in power. As the energy contained within the flow is dissipated at the higher frequencies, and therefore smaller scales, energy is cascaded down from the more powerful periodic components, it is only when all energy transferred to these higher frequencies is dissipated that the low frequency domain dominates.

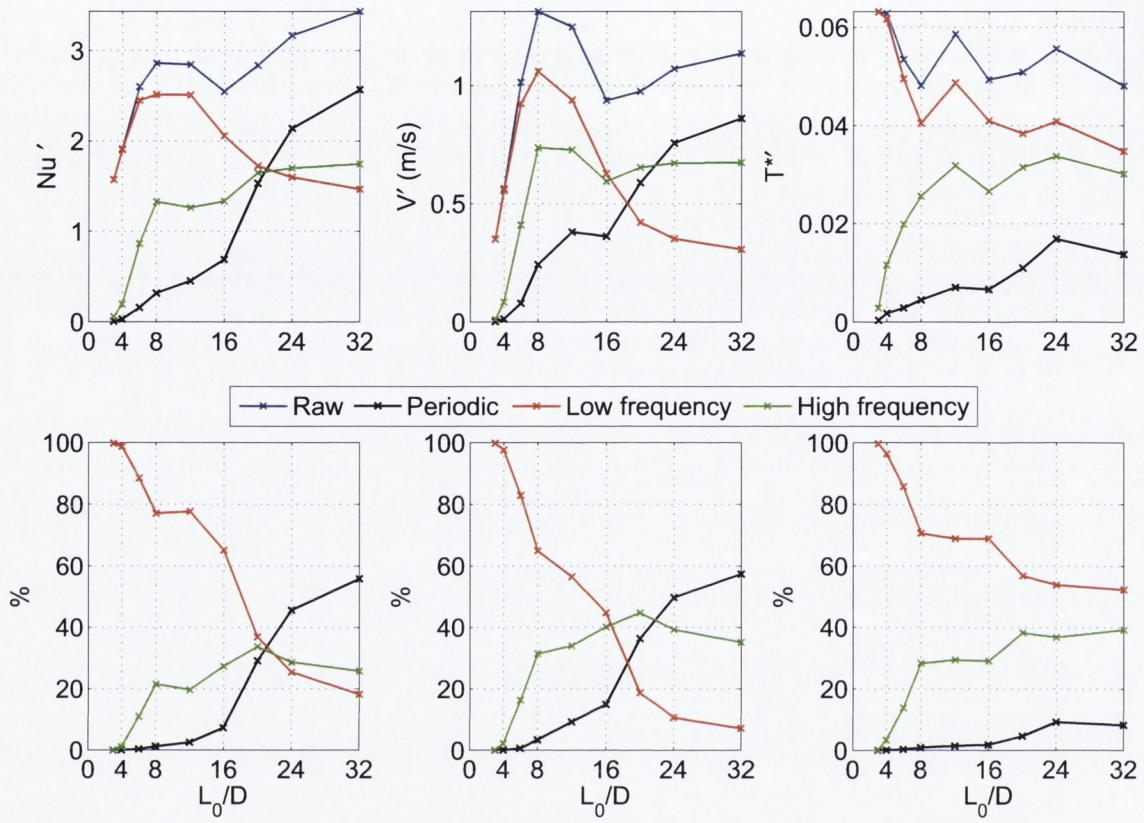

Figure 7.47: Stagnation point fluctuating Nusselt number, velocity and temperature as a function of dimensionless stroke length; $Re = 3000, H/D = 12$

Figure 7.47 and 7.48 show that it is only at axial spacings of $H = 12D$ and beyond that significant deviation from the previous trends occurs. Firstly however, it is notable that there has been little change in the balance of frequency components since $H \approx 10D$. While the sizeable presence of high frequency and periodic components do indeed reflect the nature of the flow, the fact that there is little variation beyond a certain axial distance suggests that temperature fluctuation is not so much related to energy content, as to the extent of flow development and its ability to disrupt the thermal boundary layer. At these increased axial spacings both heat transfer and velocity data show a significant reduction in the periodic frequency component at $L_0 \leq 8D$, corresponding to heat transfer regime (b), the vortex propagating regime (table 7.2). At these axial spacings the vortex alone no longer has sufficient momentum to reach

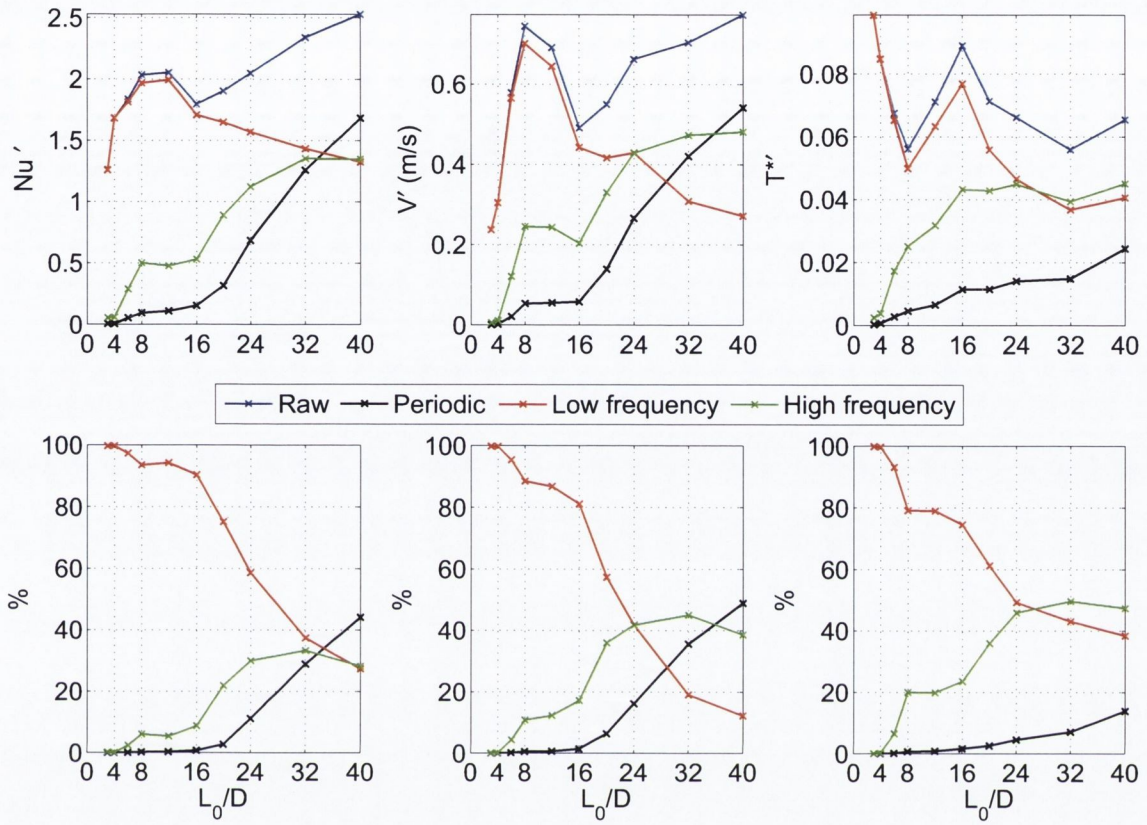

Figure 7.48: Stagnation point fluctuating Nusselt number, velocity and temperature as a function of dimensionless stroke length; $Re = 3000, H/D = 16$

the impingement surface. At $H = 10D$ total fluctuations are still quite large with vortex breakdown and interaction occurring just prior to impingement, energy is still being dissipated in the high frequency domain, while data for $H = 16D$ presented in figure 7.48 shows that this has changed significantly. The reduction in the high frequency component for $L_0 \leq 16D$, combined with minimal periodicity, indicates that not only all periodic energy has been dissipated prior to impingement, but also that any remaining energy is rapidly declining in the high frequency domain. It is therefore desirable to achieve a jet which upon impingement is fully developed yet not diminished; this can be identified by a stroke length which shows a reduction in the periodic fluctuating component, yet still contains a high frequency component which is fully saturated. From figures 7.46 and 7.47, the stroke lengths required to achieve

this fully developed impinging flow with undiminished, cascading, turbulent structures desirable for heat transfer for $H = 10D$ and $12D$ are $L_0 \approx 8D$ and $10D$ respectively. Further analysis of the individual signals and detailed frequency spectra will give a better insight into the type of evolution the jet undergoes at each stroke length and axial spacing. For other axial spacings below $H = 12D$ the stroke lengths required to achieve this transitional regime between periodic and high frequency domains matches up remarkably well with the blue boundary line in figure 7.19 representing the transition between diminishing impingement and vortex propagation. This relationship does not appear to hold at greater axial distances where regime (c) where the trailing jet is dominant.

7.2.2.1 Findings

Spectral decomposition performed on the fluctuating stagnation point heat transfer, fluid velocity and fluid temperature data showed that, in general, larger stroke lengths produced fluctuations dominated by the highly periodic synthetic jet actuation frequency, indicating a highly underdeveloped flow. While also containing a large quantity of high frequency fluctuations, smaller stroke lengths were seen to contain a much higher proportion of low frequency fluctuations; this indicated that they had undergone a much greater amount of development prior to impingement. Diminished flows which underwent significant degradation prior to impingement presented themselves as containing negligible periodic fluctuations and very high proportions of low frequency, low power fluctuations. While small axial spacings commonly resulted in an underdeveloped, highly periodic impingement, the increased opportunity for development presented by large axial spacings often resulted in an overdeveloped impingement dominated by low frequency phenomena. These results also showed that an identical level of mixing has a much greater effect on the temperature spectrum than on the corresponding velocity or heat transfer spectra. This can be attributed to the fact that the fluctuations in the fluid temperature undergo more of a redistribution where they ultimately reach homogeneity, compared to the velocity and heat transfer signals which experienced a dissipation.

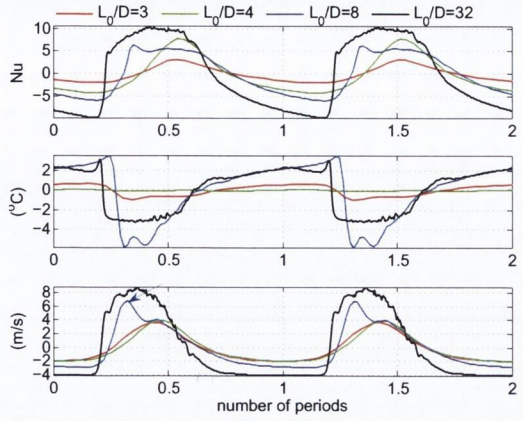

(a) $H/D = 2$

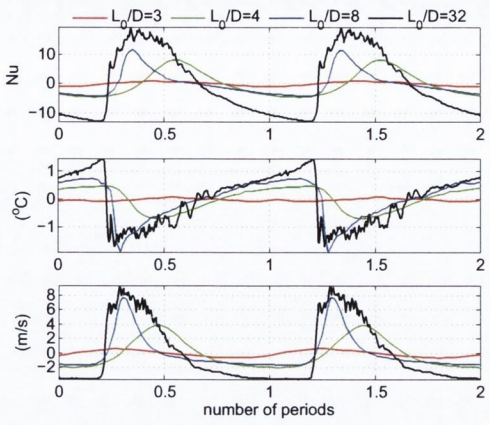

(b) $H/D = 4$

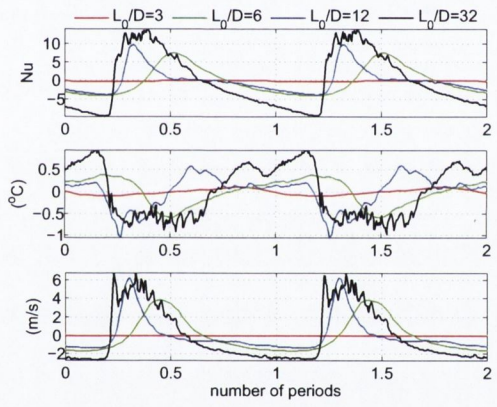

(c) $H/D = 6$

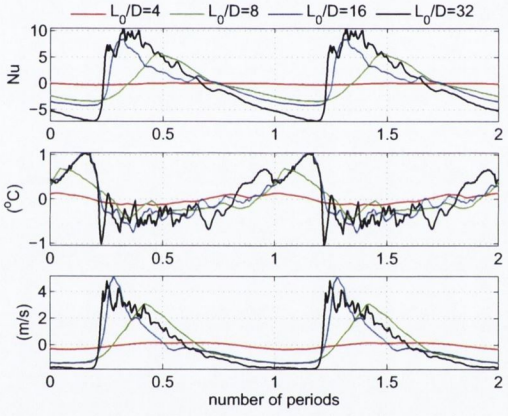

(d) $H/D = 8$

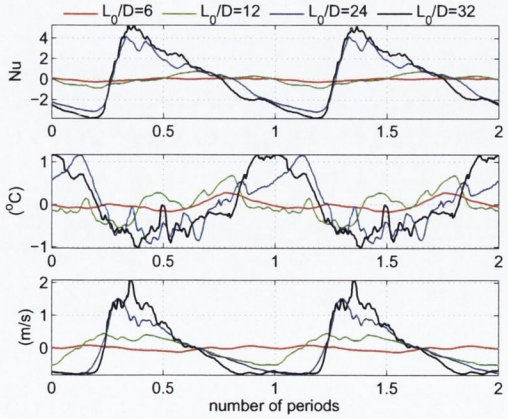

(e) $H/D = 12$

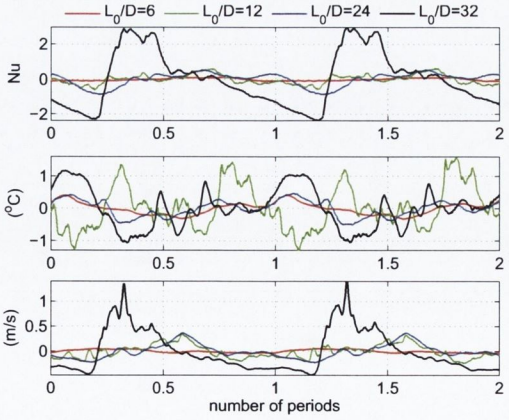

(f) $H/D = 16$

Figure 7.49: Reconstructed periodic time resolved data, $Re = 3000$

7.2.3 Spectral Reconstruction

Figure 7.49 shows two periods of the time resolved local heat transfer, fluid temperature and velocity signals reconstructed with only the periodic frequency components of the signal; all data are aligned so as the fluid impingement is synchronised. As the signals are only reconstructed using the jet harmonics, the value at 0 Hz (steady state) is not included. The results therefore appear as if the mean of the signal has been subtracted and consequently fluctuate about 0. As expected, all stroke lengths at small axial spacing of $H = 2D$ show relatively strong periodic components, although with increasing stroke length the leading edge of the heat transfer and velocity signals and the trailing edge of the temperature signal shows a significant deviation from the sinusoidal mode of diaphragm actuation; these sharp edges are more analogous to square waves as should be revealed by further spectral analysis. The uniformity and magnitude of the fluctuations as well as the location of peak velocity indicates the highly underdeveloped nature of the flow. Velocity data at $L_0 = 8D$ show that there is a local primary peak leading a broader sinusoidal wave, as indicated by the blue arrow. Instantaneous flow field images in section 7.1.1 revealed that this peak is attributed to the leading vortex impinging on the plate followed by the lower velocity fluid contained in the trailing jet. This is not evident at $L_0 \leq 4D$ as no trailing jet is formed at this smaller stroke length, nor can it be seen for the larger stroke length of $L_0 = 16D$ as maximum velocity is now experienced a significant distance into the formation of the trailing jet.

Axial spacings of $H = 4D$ and $6D$ presented in figures 7.49 (b) and (c) show how the periodic components of the respective signals evolve at larger impingement distances. Although somewhat chaotic, the temperature signal is seen to maintain a definite periodic form in phase with the corresponding heat transfer and velocity signals; however the heat transfer signal does not appear to reflect any of the more random fluctuations present in the fluid temperature signal. The same cannot be said for the time resolved velocity signal which bears much resemblance to the heat transfer signal. It is also noticeable how the behaviour of the temperature signal for stroke lengths $L_0 > 8D$ rapidly deviates from the classically sinusoidal form with

such a small increase in axial spacing. This evidence suggests that either the physical scale of the temperature fluctuations is far below that of the corresponding velocity fluctuations, or the level to which fluid temperature affects heat transfer is significantly less at these higher frequencies; full spectral comparisons will perhaps shed more light on this curious trait. Both figures show that periodic components for $L_0 = 3D$ appear to be largely non-existent above $H = 4D$, while velocity and heat transfer signals recorded at $L_0 = 8D$ now only exhibit what appears to be the primary peak associated with the impinging vortex, as the power of the trailing jet falls off.

Where previously a stroke length of $L_0 = 8D$ was sufficient to ensure the flow impinges upon the surface with a sharp increase in velocity and heat transfer, figure 7.49 (d) reveals that at $H = 8D$ it now effects more of a conventional periodic profile which is inherently less powerful. Corresponding decomposed data for $H = 8D$ and $L_0 = 8D$ in figure 7.45 contradicts this statement somewhat, showing that the fluctuating magnitude of the raw signal remains undiminished, as does the high frequency component; this evidence indicates a shift away from a powerful yet undeveloped impinging flow towards one dominated by more random high frequency fluctuations. Figures 7.49 (b) and (c) show a similar trend for stroke lengths of $L_0 = 4D$ and $6D$ respectively suggesting that this is consistent with the heat transfer regime (b); there is sufficient impulse provided at this stroke length to ensure the jet does not impinge undiminished, yet not so much as to cause it to be underdeveloped. Across all axial spacings, $H \leq 8D$, the point of maximum velocity for the stroke length of $L_0 = 32D$ can be seen to move progressively closer to the front of the impingement; this is due to the accelerating nature of the trailing jet caused by the maximum ejection velocity occurring during its formation. Larger axial spacing allows the location of maximum velocity to progress closer to the forefront of the impinging fluid, this trend will continue as long as the flow can remain coherent.

Figures 7.49 (e) and (f) move the jet beyond the axial spacing for which the flow regime dominated by propagating vortices possesses enough momentum to reach the impingement surface undiminished; this is reflected in the very low levels of periodic fluctuations present at $L_0 \leq 12D$. What is particularly noteworthy is that while fluctuating velocity and heat transfer have suffered a reduction in magnitude, the same

cannot be said for the temperature signal which has in fact become far more variable. This indicates that much of the fluctuations in temperature may be attributable to broadband random fluctuations across the entire spectrum rather than being specific to the jet driving frequency and its harmonics. At $H = 16D$ the only stroke length which can maintain a reasonably periodic form prior to impingement is seen to be $L_0 = 32D$, while at $H = 12D$ this is extended down to $L_0 = 24D$.

7.2.4 Stagnation Point Power and Coherence Spectra

This section will present the simultaneous stagnation point heat transfer, velocity and temperature measurements in the form of power and coherence frequency spectra. Coherence data are calculated between the heat transfer signal and the respective velocity and temperature signals, with coherence values of above 0.2 considered to indicate significant correlation. The Kolmogorov spectrum having a slope of $-5/3$ is also displayed in each figure to more easily identify turbulent flows. Three jet operational parameters are chosen at each axial spacing which span the respective flow regimes presented in figure 7.19, these include the diminished impingement, vortex propagation (stroke lengths selected at the blue boundary line) and the underdeveloped periodic flow commonly produced in the trailing jet regime.

The first thing to understand prior to analysing the current spectral data is how different waveforms affect the resultant spectrum.

Artificial sine and square waves have been generated at $80Hz$ using MATLAB with the same sampling frequency and duration as the time resolved local measurements analysed in this work. To make the signals somewhat more comparable to realistic data random noise has also been generated and introduced to both signals after which each were converted to the frequency spectrum. Identical noise was added to both signals whose respective time resolved signals and power spectra are presented in figure 7.50.

While the difference between the two time resolved signals is quite straight forward and obvious to see, it is only when it is converted to the frequency domain that the interpretation becomes somewhat more complicated as significant differences occur. The sine wave is simply represented in the frequency domain as a single powerful spike at

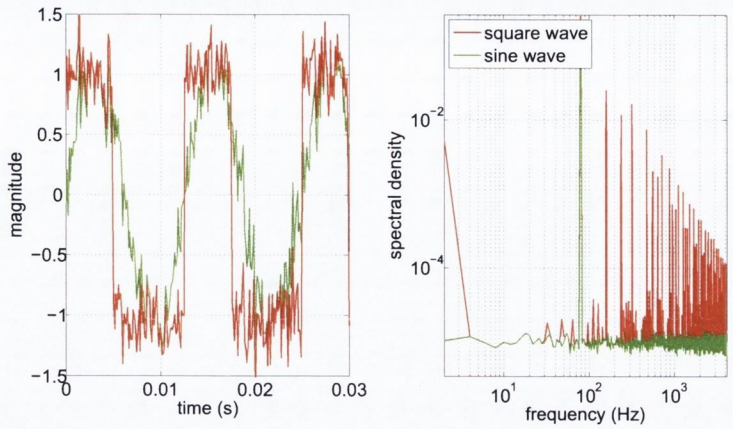

Figure 7.50: Time resolved and power spectra plots of sine and square waves generated at $f = 80\ Hz$ with random noise added.

the generation frequency, which in this case is $80Hz$. While the frequency spectrum for the square wave also shows a similar spike at the generation frequency the remainder of the spectrum appears vastly different. Harmonics of the generation frequency are seen to be present with decreasing magnitude throughout the remainder of the spectrum. These harmonics are attributed to the sharp leading and trailing edges present in the square wave; as either edge becomes more prominent higher harmonics are required to approximate it. Depending on severity, sharp increases in highly periodic signals such as those which have been shown to be present in underdeveloped synthetic jet flows will also produce similar spectra with harmonics; these frequencies produced by the sharp edge contain quite large amounts of energy which is subsequently dissipated by cascading to higher frequencies before becoming a more developed flow. As such, it is important to remember the origin of these harmonics and what implications their presence have for the state of the flow.

7.2.4.1 H/D=2

Stagnation point spectral data for an axial spacing of $H = 2D$ and stroke lengths of $L_0 = 2D, 4D$ and $8D$ are presented in figure 7.51. At such a small orifice to surface spacing there is very little opportunity for jet development to occur; this is reflected in the power spectra. While all three stroke lengths show a noticeable power spike in

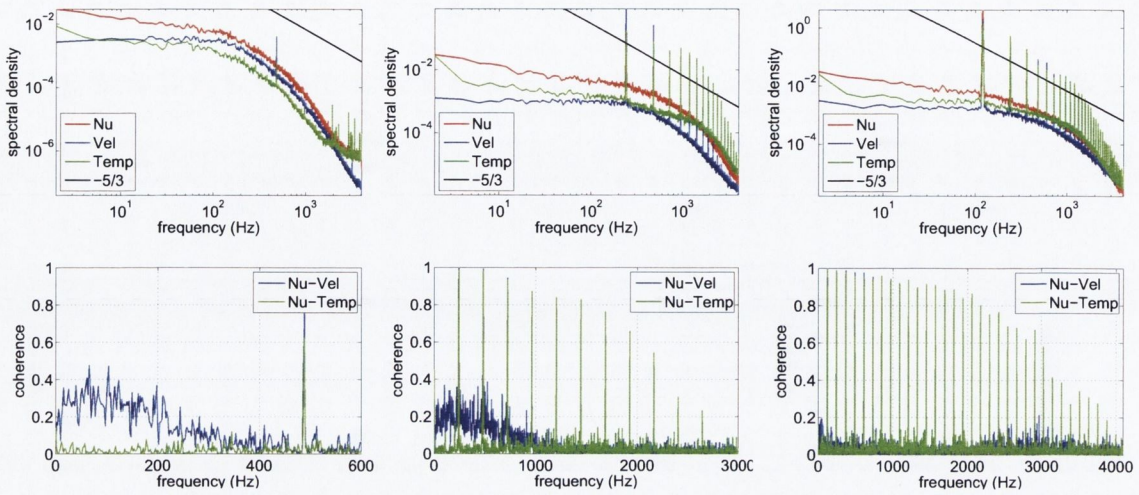

(a) $L_0/D = 2$, $f = 480\ Hz$ (b) $L_0/D = 4$, $f = 240\ Hz$ (c) $L_0/D = 8$, $f = 120\ Hz$

Figure 7.51: Power and coherence spectra of Nusselt number, velocity and temperature $Re = 3000, H/D = 2$

all signals at their respective actuation frequencies, $L_0 = 2D$ is the only one that does not contain any at greater harmonics. Figure 7.51 (a) shows that the power of the fundamental harmonics $(480\ Hz)$ are all smaller in magnitude than much of the lower frequency fluctuations and a rapid drop-off in power at frequencies above $480Hz$ is also seen to occur, thereby deviating from the $-5/3$ regime. It is possible to argue that these traits are indicative of a highly developed flow, however previous flow field evidence suggests that at $L_0 = 2D$ it may be more attributable to an under formed jet, as this is far below the stroke length of maximum vortex circulation experienced at $L_0 \geq 4D$. At $L_0 = 4D$ and $8D$, both primary driving frequency and subsequent harmonics show fluctuations far greater than are present at lower frequencies, reflecting the highly periodic, underdeveloped nature of both jets as was highlighted by the reconstructed periodic frequency components in figure 7.49.

Plotted below the power spectra in figure 7.51 are the corresponding coherence spectra showing the correlation magnitude of the heat transfer signal versus both the velocity and temperature signals. All three stroke lengths show strong correlation between the pairs of signals at the actuation frequency in particular, and at higher

harmonics for $L_0 = 4D$ and $8D$. Apart from at actuation and harmonic frequencies no significant coherence between heat transfer and temperature signals is shown. However, both $L_0 = 2D$ and $4D$ show reasonable correlation between local Nusselt number and velocity at broadband low frequencies while at $L_0 = 8D$ this appears to be supressed. This increase in relatively low frequency coherence may be associated with jet development as some of the power from the periodic harmonics is dissipated through other frequencies. The fact that the coherence between the temperature and heat transfer signal does not show similar trends suggests that rather than power dissipation by energy transfer to other frequencies as is occurring in the velocity spectrum, the temperature fluctuations undergo more of a redistribution.

7.2.4.2 H/D=4

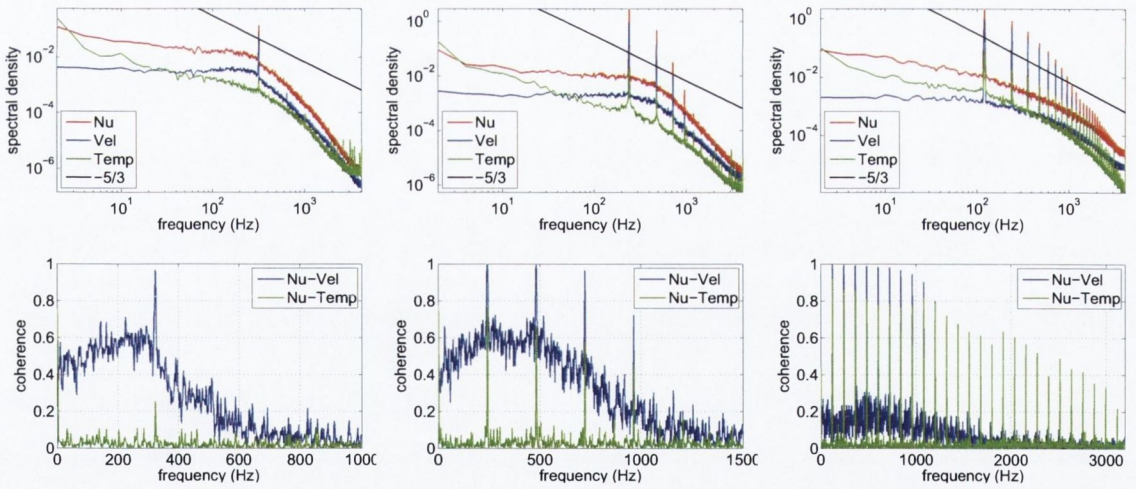

(a) $L_0/D = 3$, $f = 320\ Hz$ (b) $L_0/D = 4$, $f = 240\ Hz$ (c) $L_0/D = 8$, $f = 120\ Hz$

Figure 7.52: Power and coherence spectra of Nusselt number, velocity and temperature $Re = 3000, H/D = 4$

Three similar regimes at the larger axial spacing of $H = 4D$ are presented in figure 7.52. While still below the threshold for maximum vortex circulation, a larger stroke length of $L_0 = 3D$ now achieves the diminished impingement regime containing few periodic, coherent structures. As with figure 7.51 (a) only the fundamental harmonic

of 320 Hz is present and a large drop-off in power is evident at the higher frequencies. This finding is in good agreement with the POD flow fields presented earlier in section 7.1.5 which concluded that at this stroke length and axial spacing few coherent structures were seen to impinge upon the surface. The velocity-Nusselt number coherence spectrum in figure 7.52 (a) shows broadband low frequency correlation, particularly at frequencies below that of actuation. This indicates that these are the frequencies of fluid motion at which thermal dissipation is occurring. In contrast, the temperature-Nusselt number coherence spectrum shows little significant correlation apart from the actuation frequency (320 Hz) and also increasingly at very low frequencies $f \leq 1\ Hz$. While at the larger stroke length of $L_0 = 4D$ in figure 7.52 (b) the presence of a number of well-defined harmonics across all signals suggests a highly periodic flow, compared to the same stroke length at $H = 2D$ the magnitude and number of harmonics is significantly reduced indicating a substantially more developed flow. This is confirmed by the higher broadband correlation present in the velocity - heat transfer coherence spectrum.

Comparing the slope of the temperature spectrum to that of the velocity and Nusselt number spectra in figure 7.52 (b), they are seen to be significantly different, particularly in the lower frequency domain. The entire temperature spectrum approximates a $-5/3$ slope which is associated with Kolmogorov's power law of turbulence; this suggests that the temperature spectrum undergoes a much more rapid transition to chaotic fluctuation than the corresponding velocity signal. As the jet develops fluid mixing occurs; the kinetic energy of the flow represented by the velocity power spectrum is transferred down the frequency spectrum, and ultimately this energy is dissipated at increasingly smaller scales, i.e. higher frequencies. In contrast, the fluid temperature power spectrum does not represent the kinetic energy contained within the flow; unlike velocity, temperature gets redistributed rather than dissipated, therefore the spectrum is more representative of the inhomogeneity of the local fluid temperature within the flow. Accordingly, the evolution of the fluid temperature spectrum merely requires redistribution rather than the type of dissipation to smaller scales experienced by the velocity spectrum. Consequently, an identical amount of mixing in the flow can effect a more dramatic change in the temperature spectrum compared to the corresponding

velocity spectrum. The fact that the Nusselt number spectrum so closely resembles the velocity rather than the temperature spectrum, and also that velocity and heat flux show a far greater coherence across a broad range of frequencies, suggests that heat transfer to a synthetic jet is primarily driven by the fluid velocity and its respective flow structures. There is of course substantial evidence to suggest that average fluid temperature does play a significant role in heat transfer, but these findings suggest that local temperature fluctuations are secondary to velocity fluctuations.

The stroke length of $L_0 = 8D$ in figure 7.52 (c) shows many harmonics across all signals; suggesting a highly underdeveloped, periodic flow. Comparing this to the same stroke length at the smaller axial spacing of $H = 2D$ in figure 7.51 (c) shows a reduction in harmonic magnitude and a small yet significant increase in broadband coherence between Nusselt number and velocity signals. Once again this suggests a further development in flow with increased axial spacing.

7.2.4.3 H/D=6 and 8

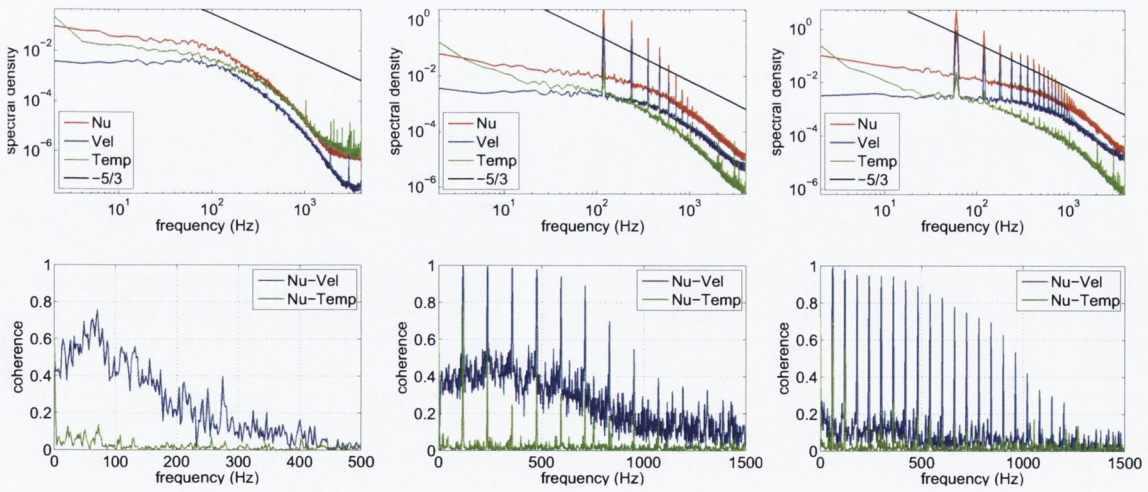

(a) $L_0/D = 3$, $f = 320\ Hz$ (b) $L_0/D = 8$, $f = 120\ Hz$ (c) $L_0/D = 16$, $f = 60\ Hz$

Figure 7.53: Power and coherence spectra of Nusselt number, velocity and temperature $Re = 3000, H/D = 6$

Figures 7.53 and 7.54 both show spectra at diminished, intermediate and highly

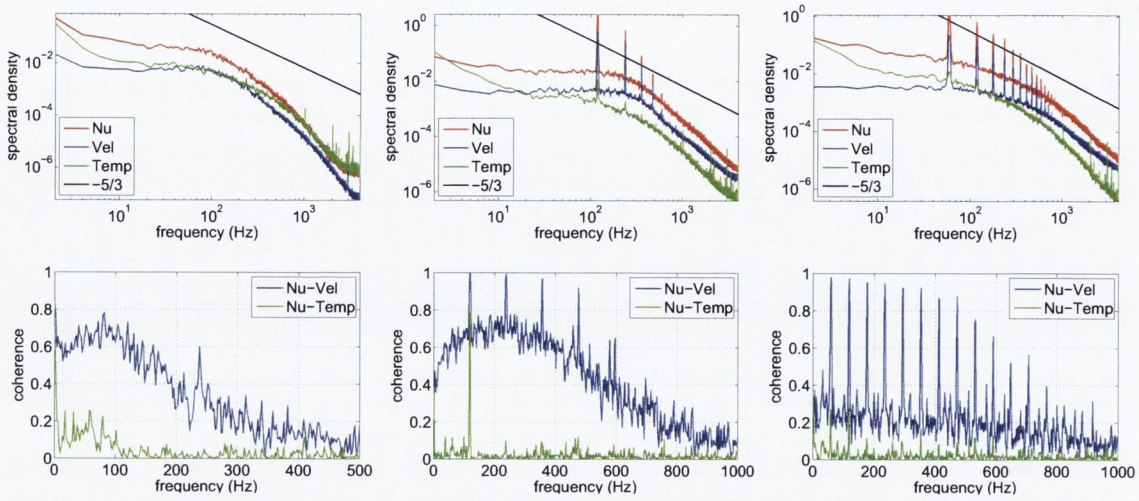

(a) $L_0/D = 4$, $f = 240\ Hz$ (b) $L_0/D = 8$, $f = 120\ Hz$ (c) $L_0/D = 16$, $f = 60\ Hz$

Figure 7.54: Power and coherence spectra of Nusselt number, velocity and temperature $Re = 3000, H/D = 8$

periodic impingement regimes for increased axial spacings of $H = 6D$ and $8D$. While the two later regimes can be represented by the same stroke lengths, the magnitudes of the harmonics are seen to attenuate with the increased distance available for development, as was seen at lower axial spacings. Where before (figure 7.8) a stroke length of $L_0 \approx 4D$ was shown to form vortices approaching maximum circulation and produce a flow field dominated by propagating vortices right the way to the impingement surface, all spectra in figure 7.54 (a) for the same stroke length now resemble those seen in the diminished regime, as has been present for the stroke length $L_0 = 3D$ (figure 7.53 (c)). While a significant broadband coherence between Nusselt number and velocity is still present, compared to $L_0 = 8D$ the bandwidth has narrowed substantially from $900Hz$ down to the lower energy containing frequency of $300Hz$. Figures 7.53 (c) and 7.54 (c) both show high levels of coherence at the actuation harmonics but low levels in between, indicating once again that the flow is highly under developed and heat transfer is dictated by the powerful periodic motions of the flow as little fluctuation at other frequencies has developed.

7.2.4.4 H/D=12 and 16

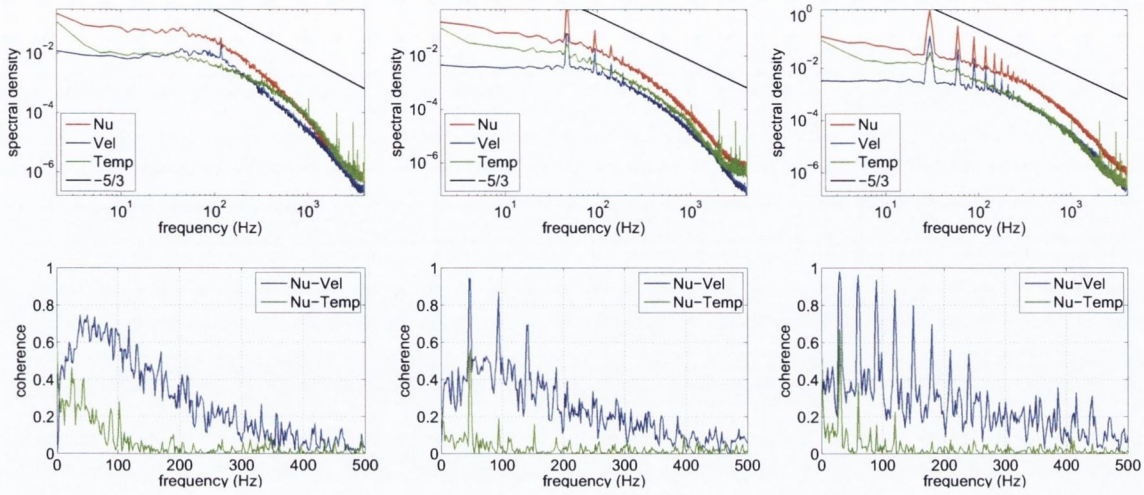

(a) $L_0/D = 8$, $f = 120\ Hz$ (b) $L_0/D = 20$, $f = 48\ Hz$ (c) $L_0/D = 32$, $f = 30\ Hz$

Figure 7.55: Power and coherence spectra of Nusselt number, velocity and temperature $Re = 3000, H/D = 12$

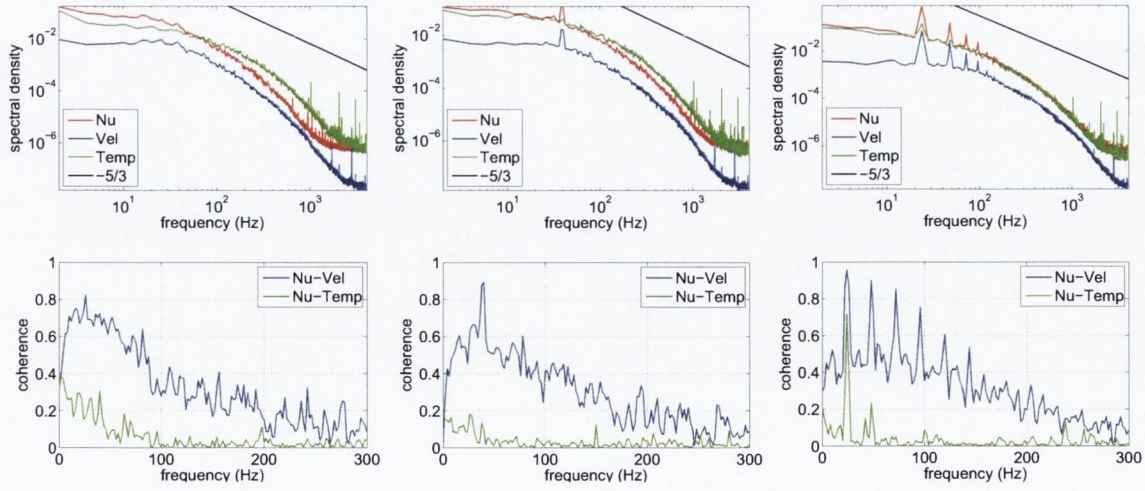

(a) $L_0/D = 8$, $f = 120\ Hz$ (b) $L_0/D = 24$, $f = 40\ Hz$ (c) $L_0/D = 40$, $f = 24\ Hz$

Figure 7.56: Power and coherence spectra of Nusselt number, velocity and temperature $Re = 3000, H/D = 16$

An increase in axial spacing to the upper test limits of $H = 12D$ and $16D$ is presented in figures 7.55 and 7.56. Significantly, at these large axial spacings not even the largest stroke lengths show spectra containing the same number of harmonics as seen at smaller axial spacings. Although average velocity, dimensionless temperature and heat transfer data, presented earlier in figure 7.34 for a stroke length of $L_0 = 8D$, show local maxima, the corresponding spectra in figure 7.55 (a) and 7.56 (a) appear almost devoid of notable definition at any frequency. Although a stroke length of $L_0 = 8D$ was shown to achieve maximum vortex circulation and provide the most impulse so as to reach the impingement surface undiminished, these data confirm the limit of this vortex propagation regime. Although elevated velocity is maintained, fluid motion within the jet is now not occurring at the actuation frequency as the jet is fully developed. It is worth noting that at frequencies $f \leq 50Hz$ a measureable increase in coherence between the temperature and heat transfer signals occurs. This may be attributed to an increase in the power of the lower frequency phenomena in combination with a lower velocity jet; as these structures pass at a lower velocity there is a corresponding increase in the time duration for heat transfer to occur from the heated surface to the fluid. This evidence suggests that for the temperature spectra it is the lowest frequency phenomenon which have the greatest effect, starting at steady state ($0\ Hz$), and increasing from there. The converse of this is true for fluid velocity, as the faster the fluid passes the greater the effect on total heat transfer. Consequently, small scale structures formed from high velocity, energetic flows effect a significant level of heat transfer, as is reflected in the coherence data.

Maximum stroke length spectra for both large axial spacings (figures 7.55 and 7.56) show a significant deviation from what has customarily been seen in the trailing jet regime (flow regime (c) and heat transfer regime (d)). With such a significantly reduced number of harmonics present neither set of spectra can be said to be as highly dominated by the periodic impingements as has been seen at lower axial spacings. Coherence data confirm that although the periodic flow is still a powerful mode of heat transfer, the primary mode appears to lie with the broadband velocity fluctuations as has previously been the case with the other two regimes. It can be concluded that a limit exists beyond $H = 12D$ where jet development results in a type of flow which

deviates significantly from that at formation; consequently, heat transfer is primarily driven by frequencies generated by the evolution of the jet rather than those associated with the periodic jet motion.

7.2.4.5 Findings

Stagnation point power and coherence spectra have been used to provide further information about the mechanisms driving heat transfer in the synthetic jet. The heat transfer signal consistently showed significantly higher correlation to the fluid velocity signal than to the fluid temperature signal; this was particularly evident at the actuation frequency and its harmonics. Broadband correlation between the velocity and heat transfer signal was seen to increase with jet development. Correlation between heat transfer and fluid temperature only experienced an increase at lower frequencies, particularly when jet flow had degraded significantly. These results indicate that while fluid temperature does play a significant role in heat transfer, it is primarily driven by the fluid motion. Frequency spectra have also been used to provide further insight into the state of jet development upon impingement with changing stroke length and axial spacing. The results showed that as the jet developed energy was progressively transferred from the actuation frequency and its harmonics to other frequencies, ultimately being dissipated at higher frequencies. Significantly, it was found that the state of development could be controlled for a particular axial spacing by changing the stroke length of the jet.

7.3 Radial Decomposition

7.3.1 Re=3000

This section decomposes time series data acquired across entire heat transfer profiles, separates out the periodic, high frequency and low frequency fluctuating temperature and Nusselt number components and reconstructs them in the form of time averaged radial profiles. Frequency and coherence spectra of the Nusselt number and temperature signals are provided at locations of $r = 0D, 2D$, and $4D$, this data provides a

good indication of what the dominant mode of flow is across the radial profile.

7.3.1.1 H/D=2

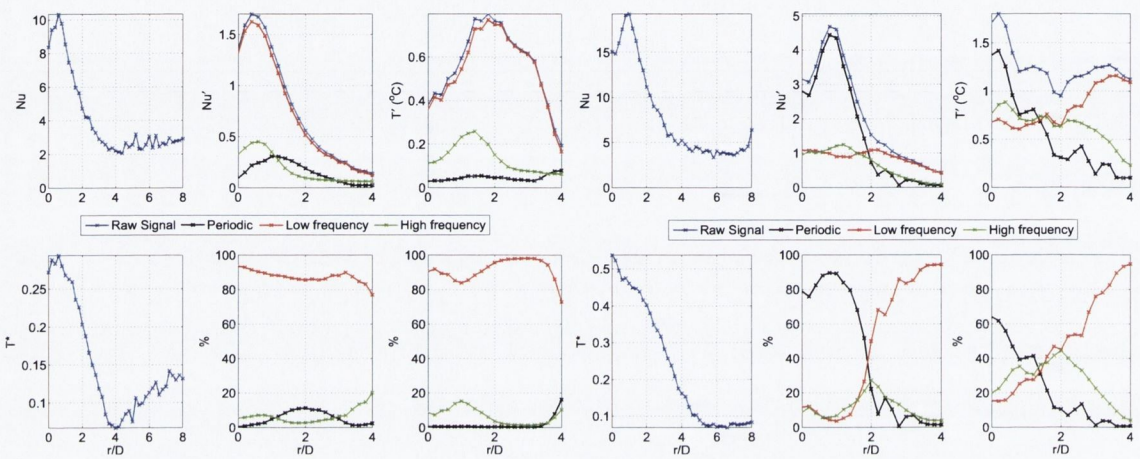

(a) $L_0/D = 2$, $f = 480\ Hz$

(b) $L_0/D = 4$, $f = 240\ Hz$

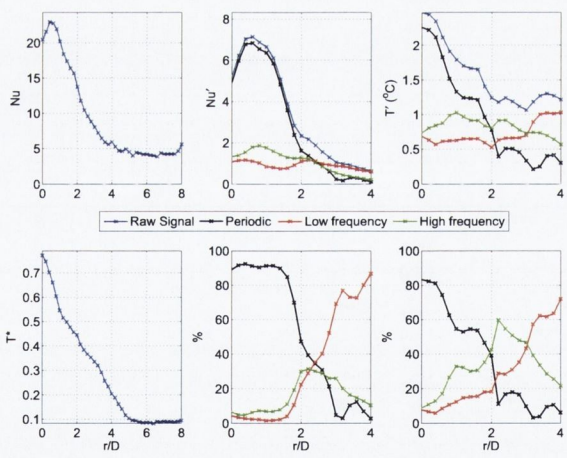

(c) $L_0/D = 8$, $f = 120\ Hz$

Figure 7.57: Radial profiles of average and fluctuating Nusselt number and dimensionless air temperature T^* (eqn. 7.3) decomposed into high, periodic and low frequency components, $Re = 3000$, $H/D = 2$, $L_0/D = 2, 4, 8$

Figure 7.57 shows radial profile data for the smallest axial spacing tested of $H = 2D$; this is also the spacing at which confinement has the greatest effect. Across all

stroke lengths average and fluctuating Nusselt number shows a local minimum at the centre of impingement, this feature has previously been observed in continuous jets and has been attributed to a time averaged stagnation in local velocity at this point. The effects of this are consistently seen at small axial spacings where the flow is highly underdeveloped, it was also evident upon impingement in the mean velocity profiles presented in section 7.1.4. Significantly, a similar local minimum is not experienced in any of the average or fluctuating temperature profiles. This is because contact with the heated surface or mixing of the flow with warmer fluid is required to effect an increase in fluid temperature; however there is no opportunity for either of these events to occur prior to the fluid impinging at the centre of the flow. Even with a velocity approaching zero flow any minimal exchange of fluid within this zone will easily maintain a low temperature as the only other source of heat is conduction from the surface. The effect of high confinement is also present across all sets of data, this is recognisable by the very low rates of heat transfer and saturated local fluid temperatures beyond $r = 4D$.

Although it has been documented that jet formation is severely impaired at a stroke length of $L_0 = 2D$ it can be seen from figure 7.57 (a) that at this small axial spacing surprisingly large levels of heat transfer can be effected. This result is impressive considering the dimensionless temperature only achieves a local reduction of $T^* \approx 0.3$. The Nusselt number and temperature signals are seen to be composed almost exclusively of low frequency fluctuations as few periodic structures escape the suction phase of the jet. Fluctuations in temperature are seen to be quite low at the centre of impingement after which they experience an increase in fluctuation with further radial distance before decreasing rapidly once again. This behaviour can be explained quite simply: there is little temperature variance in the fluid as a constant stream of fluid containing very few periodic motions impinges upon the surface, thereby producing the low levels of fluctuation. After impact heat is transferred from the surface to the fluid as it travels radially outwards, thereby producing the relatively large fluctuation in temperature experienced at $r = 2D$. Beyond this point a rapid drop in fluctuation is experienced as thermal saturation of the fluid occurs and flow momentum is also lost; this corresponds to a noticeable change in slope in the fluctuating Nusselt number data at a similar location.

The periodic component of the fluctuating signals plays a much more substantial role for the larger stroke lengths of $L_0 = 4D$ and $8D$, as seen in figures 7.57 (b) and (c). It is noticeable that up to $r = 2D$ both high and low frequency components are suppressed by the highly periodic motion of the jet, indicating a highly underdeveloped impingement. There is sufficient time between fluid impacts for the local fluid to recover its elevated temperature within the thermal boundary layer, hence the local minimum in fluctuations that was seen at $L_0 = 2D$ and associated with a constant stream of fluid impinging, now becomes a local maximum at greater, more periodic stroke lengths. Beyond $r = 2D$ fluctuations in heat transfer drop rapidly as does the periodic component of the signal. Energy from the powerful periodic domain is dissipated by cascading down to other frequencies, thus causing an increase in their fluctuation percentage. A maximum in all high frequency components for both stroke lengths is experienced at $r = 2D$, beyond which all signals become increasingly dominated by low power, low frequency components, commonly associated with regions containing weak convective flows.

Power and coherence spectra corresponding to data in figure 7.57 are presented in figure 7.58. The heat transfer power spectrum for a stroke length of $L_0 = 2D$ and radial location of $r = 0D$ show that fluctuations across the whole range of frequencies are strong in magnitude; this indicates that a highly developed jet impinges upon the surface at this location. While the temperature spectrum appears similar in shape, fluctuations across it are comparatively small in magnitude, consequently coherence between the two signals is low apart from at the driving frequency. The lack of a large periodic component in either power spectrum indicates that the jet is in rapid decline; by $r = 2D$ all fluctuations in Nusselt number have been significantly reduced, especially those lying above the actuation frequency. The temperature spectrum at this radial location has experienced a broadband increase in magnitude as fluctuations increase with heat being transferred from the surface to the air. There is a corresponding increase in correlation between the two signals below $500Hz$; an increase in contact time between the local fluid and the surface is experienced with the inevitable decrease in fluid velocity. The final set of spectra presented for $r = 4D$ exhibit a significant reduction in magnitude across all frequencies. The only significant fluctu-

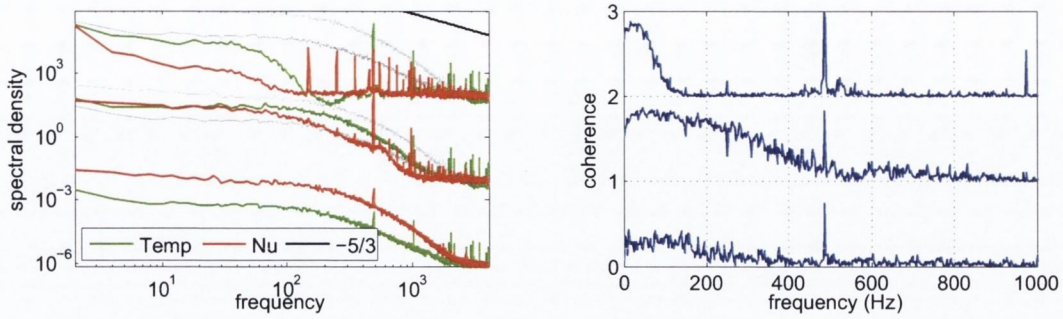

(a) $L_0/D = 2$, $f = 480\ Hz$

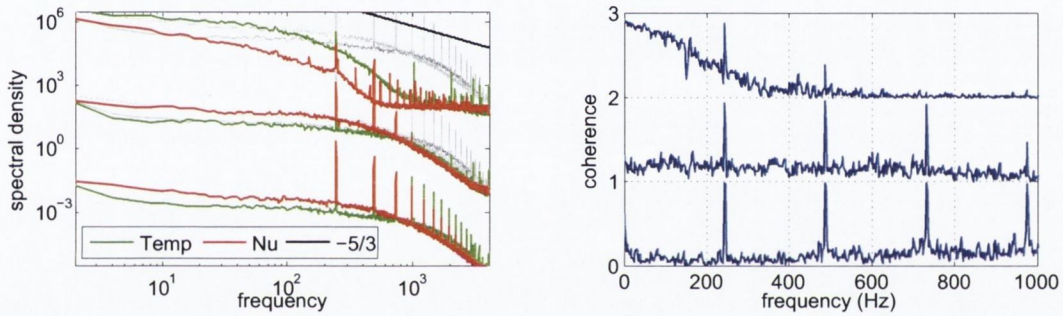

(b) $L_0/D = 4$, $f = 240\ Hz$

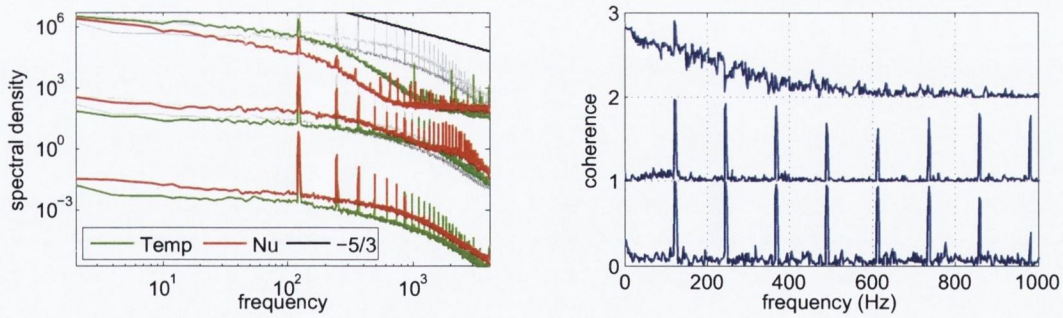

(c) $L_0/D = 8$, $f = 120\ Hz$

Figure 7.58: $Re = 3000$, $H/D = 2$, $r/D = 0, 2, 4$. Power spectra of Nusselt number and air temperature at increasing radial locations are offset by three decades, spectra at $r/D = 0$ are plotted in grey for comparison. Coherence spectra at increasing radial locations are offset by a value of 1.

ations remaining are seen to exist at frequencies below $100Hz$; it is no coincidence that a substantial increase in correlation between the two signals occurs at the same frequencies. This evidence suggests that local fluid temperature has a significantly greater effect on heat transfer in low velocity, diminished flows dominated by low frequency phenomena rather than in the types of high velocity flows dominated by high frequency phenomena. As the Nusselt number drops and fluctuation magnitudes shift to the low frequency domain there appear to be spikes remaining in the heat transfer spectrum at $r = 4D$. Electrical noise which is normally well below the level of detection becomes evident under these conditions and is manifested as peaks from $150Hz$ at intervals of $100Hz$. The fact that these spikes become visible is in fact a strong indication of what little power remains in the spectrum at this location.

The power spectra for $L_0 = 4D$ and $8D$ presented in figures 7.58 (b) and (c) respectively show a strong presence of harmonics of the actuation frequency for radial locations $r = 0D$ and $2D$, however those at $L_0 = 8D$ appear stronger. As most of the fluctuating magnitude for $r \leq 2D$ lies in the periodic domain any reduction in fluctuation occurs at these frequencies; little change is seen in the high or low frequency domain. The corresponding coherence spectra show little correlation between signals at these radial locations indicating that heat transfer is still primarily driven by fluid velocity rather than temperature fluctuations. An increase in correlation is seen below $300Hz$ for both stroke lengths at $r = 4D$, while the corresponding power spectra show a significant increase in the magnitude of low frequency temperature fluctuations. A drop in magnitude across the periodic and high frequency domain indicates that at this radial location the flow momentum is significantly diminished and the sort of low frequency, low power phenomena which operate in the temperature domain dominate.

7.3.1.2 H/D=4

At the increased axial spacing of $H = 4D$ and at $L_0 = 2D$, figure 7.59 (a) has much in common with the trends seen at $H = 2D$ in figure 7.57 (a), in that the impinging heat transfer and temperature fluctuations are almost entirely composed of low frequency phenomena. Now, however, this effect seems to be amplified as the jet loses even more momentum prior to impact. While a similar average Nusselt number is realised,

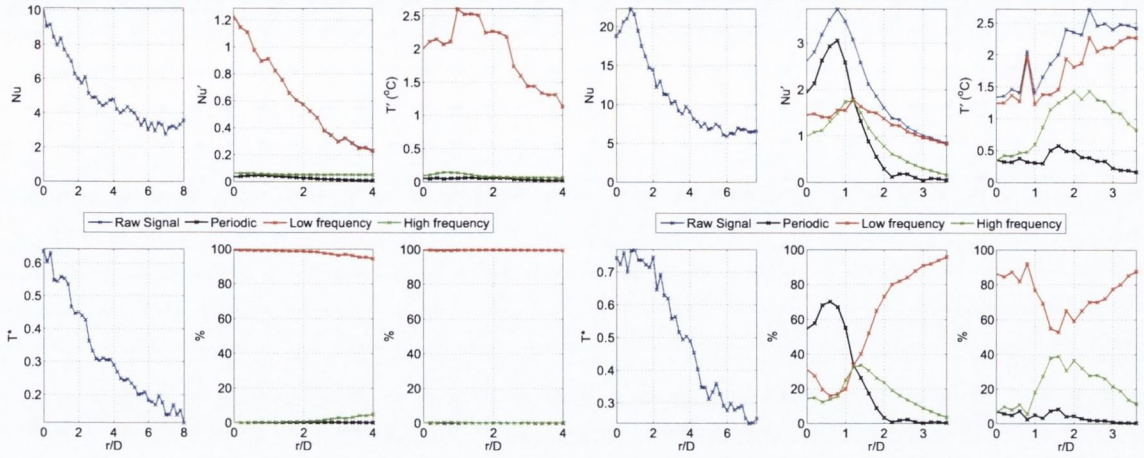

(a) $L_0/D = 2$, $f = 480\ Hz$

(b) $L_0/D = 4$, $f = 240\ Hz$

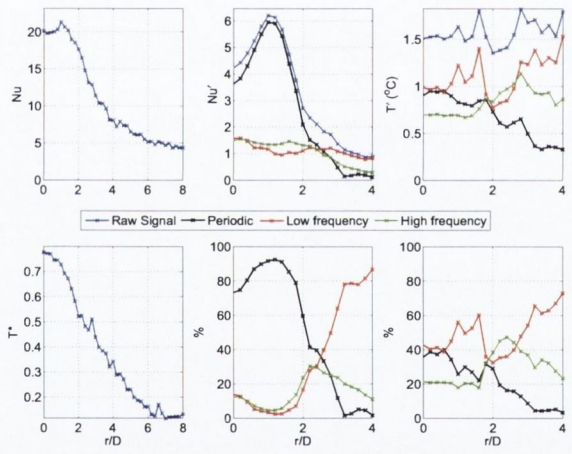

(c) $L_0/D = 8$, $f = 120\ Hz$

Figure 7.59: Radial profiles of average and fluctuating Nusselt number and dimensionless air temperature T^* (eqn. 7.3) decomposed into high, periodic and low frequency components, $Re = 3000$, $H/D = 4$, $L_0/D = 2, 4, 8$

the decrease in confinement means that saturation in the local air temperature does not occur to the same extent; consequently the Nusselt number is not as low as at large radial distances. Both the mean Nusselt number and dimensionless temperature profiles are broader, as increased jet development occurs before impingement and the lateral flow is not as confined after impact. As with the lower axial spacing of $H = 2D$,

average and fluctuating heat transfer profiles at stroke lengths of $L_0 = 4D$ and $8D$ show local minima caused by a stagnation in flow velocity to be present. The dominance of periodic fluctuation in the heat transfer signal previously seen at the stroke length of $L_0 = 4D$ has been significantly reduced. The local maximum in the fractional high frequency component now occurs closer to the centre of impingement; this indicates that the jet has reached the same level of development at a closer radial distance. However, the same data for the stroke length of $L_0 = 8D$ does not appear to be much changed between the two axial spacings. The reason for this may be that there is insufficient space at both axial spacings to allow the flow produced at this stroke length to undergo any form of development prior to impingement.

Power and coherence spectra for the axial spacing of $H = 4D$ and a stroke length of $L_0 = 2D$ presented in 7.60 (a) show no unexpected changes to those experienced at $H = 2D$. As the flow suffers further degradation prior to impingement all high frequency phenomena experience a significant loss in magnitude. The increase in coherence between the signals at low frequencies reflects the dominance of these types of phenomena in both temperature and Nusselt number spectra and at all radial locations. Although the presence of periodic components at the actuation frequency and its harmonics, reported earlier for $H = 2D$ and seen in figure 7.58, do not appear reduced at the stroke length of $L_0 = 8D$ as seen in figure 7.60 (c), the same cannot be said for $L_0 = 4D$ (figure 7.60 (b)). Significant deviation of the flow away from the highly periodic form evident at the lower jet to plate spacings has occurred due to increased development prior to impingement. The periodic components of both spectra are almost negligible at a radial distance of $r = 2D$ as the jet transitions earlier to a diminished flow operating in the low frequency domain. All coherence data at $L_0 = 4D$ shows an elevated level of correlation beyond $r = 2D$ as the jet transitions away from the periodic domain, as is evident from figure 7.59 (b). The same level of electrical noise as was seen at lower axial spacings is not evident across any of the Nusselt number spectra at this axial spacing as the heat transfer is not suppressed by the confinement to the same extent as it was at the lower axial spacing of $H = 2D$.

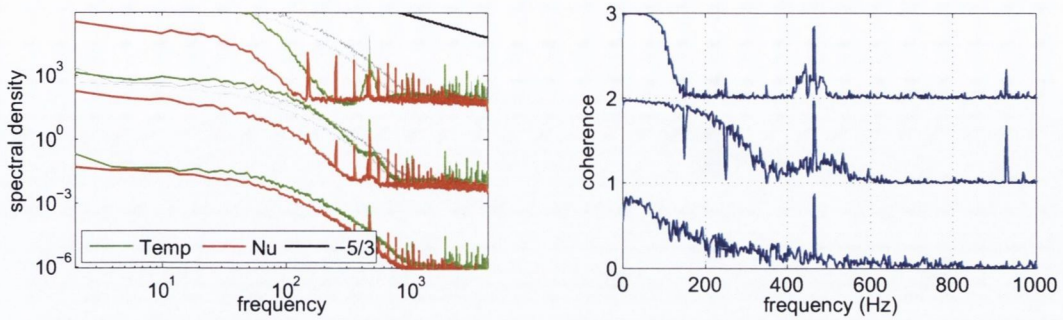

(a) $L_0/D = 2$, $f = 480\ Hz$

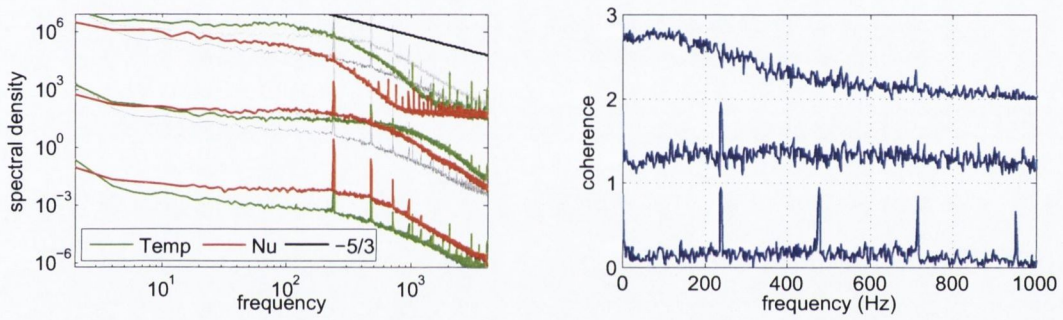

(b) $L_0/D = 4$, $f = 240\ Hz$

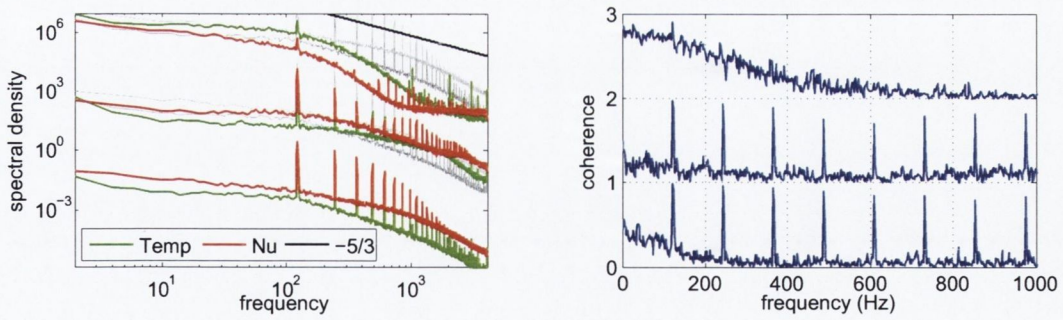

(c) $L_0/D = 8$, $f = 120\ Hz$

Figure 7.60: $Re = 3000$, $H/D = 4$, $r/D = 0, 2, 4$. Power spectra of Nusselt number and air temperature at increasing radial locations are offset by three decades, spectra at $r/D = 0$ are plotted in grey for comparison. Coherence spectra at increasing radial locations are offset by a value of 1.

7.3.1.3 H/D=8

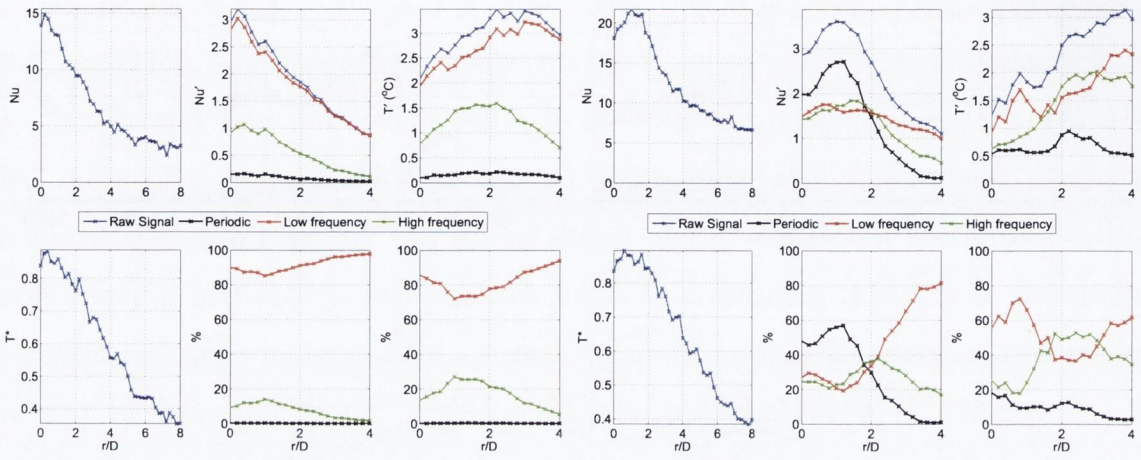

(a) $L_0/D = 4$, $f = 240\ Hz$ (b) $L_0/D = 8$, $f = 120\ Hz$

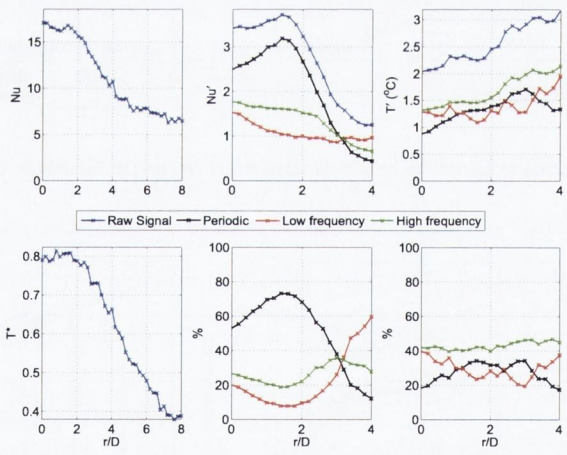

(c) $L_0/D = 16$, $f = 60\ Hz$

Figure 7.61: Radial profiles of average and fluctuating Nusselt number and dimensionless air temperature T^* (eqn. 7.3) decomposed into high, periodic and low frequency components, $Re = 3000$, $H/D = 8$, $L_0/D = 4, 8, 16$

Increasing the axial spacing once again to $H = 8D$, presented in figure 7.61, shows trends similar to those which have been observed with POD and time averaged swirl and shear flow field data in figures 7.29, 7.30 and 7.17. These flow fields indicated that while no coherent vortex structures impinged upon the surface at $L_0 = 4D$, at

$L_0 = 8D$ the flow imparted sufficient momentum to the vortex ring to allow relatively periodic impacts to occur. This assertion is confirmed by the decomposed fluctuating heat transfer profiles in figure 7.61 where little periodicity is experienced at $L_0 = 4D$. Even though the majority of the fluctuating heat transfer signal at $L_0 = 4D$ is composed of low frequency fluctuations, a measureable high frequency component exists throughout. The presence of this high frequency contributor suggests a turbulent flow has been established prior to impingement. However, with virtually no power remaining in the periodic domain, the flow may have lost a substantial amount of its momentum thereby impairing its ability to remove heat from the surface; this is confirmed when heat transfer profiles at this axial spacing are compared.

Heat transfer data for a stroke length of $L_0 = 8D$ presented in figure 7.61 (*b*) show a local minimum at the jet centre, indicating that a time averaged stagnation in the flow velocity exists at this point. Although the presence of a strong high frequency component in the fluctuating heat transfer signal suggests that the impinging flow is adequately developed it is also clear that substantial periodic components remain. These features are characteristic of the type of impinging flow which has good level of development prior to impact, but has not suffered the loss of periodicity and momentum associated with a jet which is overdeveloped. Consequently, a high level of time-averaged heat transfer is observed at the stagnation point and maintained to a good radial distance; low frequency Nusselt number components do not dominate until well beyond $r = 2D$.

Although data presented in figure 7.61 (*c*) for a stroke length of $L_0 = 16D$ look broadly similar to those presented at $L_0 = 8D$, there are subtle yet significant differences. What appears to be a somewhat similar local stagnation point dip is present for the fluctuating Nusselt number data for both stroke lengths, however that observed at $L_0 = 16D$ is substantially flatter and wider. This difference in trend can be attributed to the vastly different flow structure present. As was revealed by flow field analysis in section 7.1.1.1, this stroke length of $L_0 = 16D$ lies beyond the propagating vortex regime (which extends up to $L_0 = 8D$) and is situated in the regime dominated by the impingement of the trailing jet where vortex destruction often occurs prior to impact. While the local minimum is now broader, this can be attributed to the widening of the

impinging flow caused by the peak ejection velocity occurring in the trailing jet. This effect is confirmed by the fact that the extent of the periodic component experiences a corresponding increase. While this larger stroke length does not produce the same maximum level of local heat transfer, the fact that the dominance of the low frequency fluctuating Nusselt number component is extended to a greater radial distance means that once impingement has occurred, the flow maintains a level of coherence for longer; this assertion was also identified by flow field analysis.

The corresponding power and coherence spectra for these data are presented in figure 7.62. Unsurprisingly, at the axial spacing of $H = 8D$ all power spectra show harmonics of the actuation frequency with significantly reduced power and number, with no periodic components whatsoever visible at the stroke length of $L_0 = 4D$ which presents a relatively featureless spectrum. While the stroke length of $L_0 = 8D$, which lies at the limit of the vortex propagation regime, still shows moderately powerful periodic components, decomposed stagnation point data previously presented in section 7.2.2 suggests that this will not be the case beyond $H \approx 10D$, at which point the spectra will begin to resemble those of $L_0 = 4D$ as the periodic components degrade further.

Even though all power spectra show an overall increase in the spectral power of the temperature signal as the radial location is increased from $r = 0D$ to $2D$, there is no corresponding change in the heat transfer spectra. In fact, while it is common for the low frequency component of the temperature signal to experience an increase in fluctuating magnitude with increasing radial distance, the same cannot be said for the heat transfer signal. Results have shown that the low frequency component of the heat transfer signal consistently experiences a reduction in fluctuating magnitude with increasing radial distance; this is not the case for the high frequency component. Depending on flow condition, (i.e. if the jet is underdeveloped prior to impingement) the high frequency component often shows increases to local maximums with radial distance. What is also noteworthy is that these increases in high frequency components very often coincide with a reduction in magnitude of the periodic signal, and experience a similar decline themselves soon after. Such events are particularly evident in flow regimes which are underdeveloped prior to impingement (heat transfer

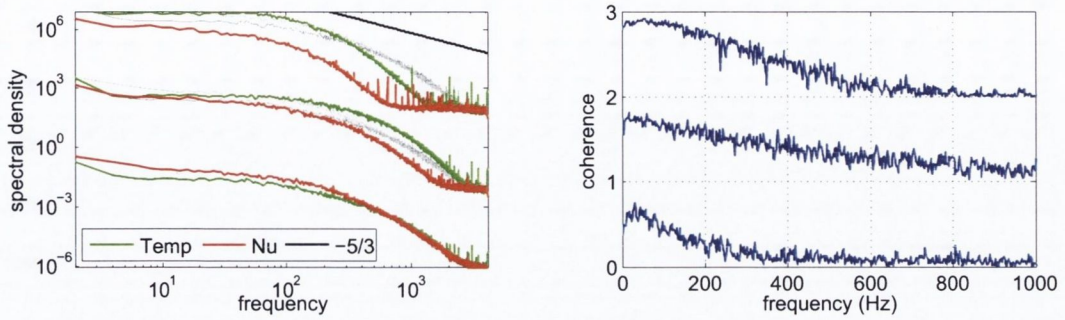

(a) $L_0/D = 4$, $f = 240\ Hz$

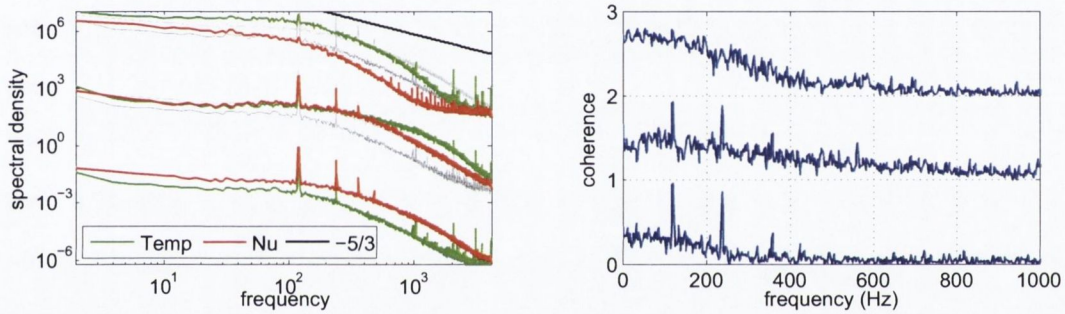

(b) $L_0/D = 8$, $f = 120\ Hz$

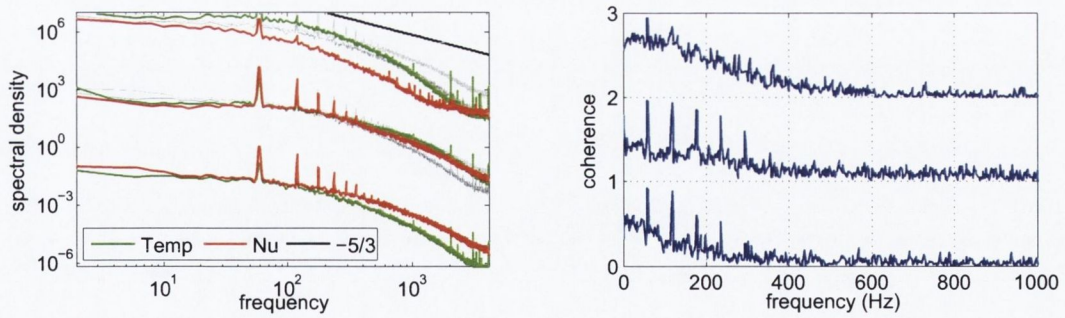

(c) $L_0/D = 16$, $f = 60\ Hz$

Figure 7.62: $Re = 3000$, $H/D = 8$, $r/D = 0, 2, 4$. Power spectra of Nusselt number and air temperature at increasing radial locations are offset by three decades, spectra at $r/D = 0$ are plotted in grey for comparison. Coherence spectra at increasing radial locations are offset by a value of 1.

regime (d)). A similar phenomenon is commonly seen in impinging continuous jets at low axial spacings as a transition to turbulence is experienced in the wall jet. While this phenomenon has not previously been reported in the synthetic jet, it is perhaps because the corresponding turbulent fluctuations have been masked by the natural periodic fluctuations of the synthetic jet itself. In accordance with Kolmogorov's power law, energy contained in the powerful periodic flow is transferred to increasingly higher frequencies at which it is dissipated; this continues until the level of energy supplied by the periodic mode can no longer be sustained. Consequently, the high frequency domain only experiences a major reduction in power after the energy being supplied from the periodic domain is almost exhausted. Once the high frequency component has dissipated all available energy, only the low frequency, low power components remain.

These results are particularly evident in a number of figures, namely (b) and (c) of figures 7.57, 7.59 and 7.61 where, with increasing radial distance, the proportion of the total fluctuation accounted for by the periodic component experiences a rapid decrease significantly earlier than the high frequency component. These regimes were specifically chosen as they presented moderately developed and underdeveloped impingement regimes respectively, while (a) was chosen as a regime which tended to be overdeveloped and somewhat diminished. The fact that these heat transfer data are in good agreement with Kolmogorov's law, a law which specifically relates to fluctuations in fluid velocity with jet development, further reinforces the fact that heat transfer in synthetic jets, and perhaps all turbulent flows, is driven primarily by the fluid velocity and its fluctuations. However, correlation data which have been presented also indicate that local fluid temperature fluctuations do play an important role once the jet has degraded sufficiently and the powerful turbulent fluctuations have subsided. While none of the data presented in figure 7.62 show the types of extremely high low frequency coherence seen at smaller axial spacings, the overall levels of correlation are significantly higher for a much broader range of frequencies, right from the centre of impingement. While other axial spacings showed a suppression in coherence for larger stroke lengths this is not the case at $H = 8D$; with a distance of 8 diameters to traverse before impingement an inevitable amount of jet development occurs and powerful, low

frequency flow structures are formed across all flow regimes, as is reflected in the elevated coherence values. When comparison of coherence spectra between $L_0 = 8D$ and $16D$ is performed it is notable that correlation levels tend to be somewhat larger at $L_0 = 16D$. Flow field results revealed that this may be due to the turbulent dissipation of the flow preceded by the destruction of the leading vortex. Such a viscous destruction produces a far wider range of fluctuations across the frequency spectrum than is experienced with the gradual degradation of the flow experienced at stroke lengths below $L_0 = 8D$, thereby explaining the differences between the two coherence spectra.

7.3.1.4 H/D=16

Nusselt number and dimensionless temperature data presented in figure 7.63 show that all impingement regimes change dramatically, as the axial spacing is increased beyond a state of flow evolution that may be able to maintain coherent impacts. All values of time-averaged dimensionless temperature (T^*) are seen to be quite high across all stroke lengths, indicating a good disruption of the thermal boundary layer. Both average Nusselt number and dimensionless temperature profiles are also seen to be substantially broader and relatively featureless at this axial spacing, although the heat transfer has experienced a reduction in magnitude. The vortex propagation regime known to exist at $L_0 \leq 8D$ now presents an insignificant amount of periodicity in the decomposed fluctuating heat transfer signal, indicating that a state of complete flow development is achieved prior to impingement. Although stroke lengths of $L_0 = 24D$ and $48D$ do show an increase in the amount of periodicity present, unlike what has commonly been present at lower axial spacings no definitive transitions or degradations in any of the frequency components with an increase in radial location are evident. This occurrence is not unexpected, as both of these stroke lengths have been shown to produce flow regimes dominated by the trailing jet which undergoes a dramatic destruction resulting in a significant amount of mixing and spreading prior to impingement. Any turbulent transition within each individual ejection has already occurred and the flow energy is spread out over a larger impingement area. The fact that a greater level of periodicity is experienced at a stroke length of $L_0 = 48D$ is

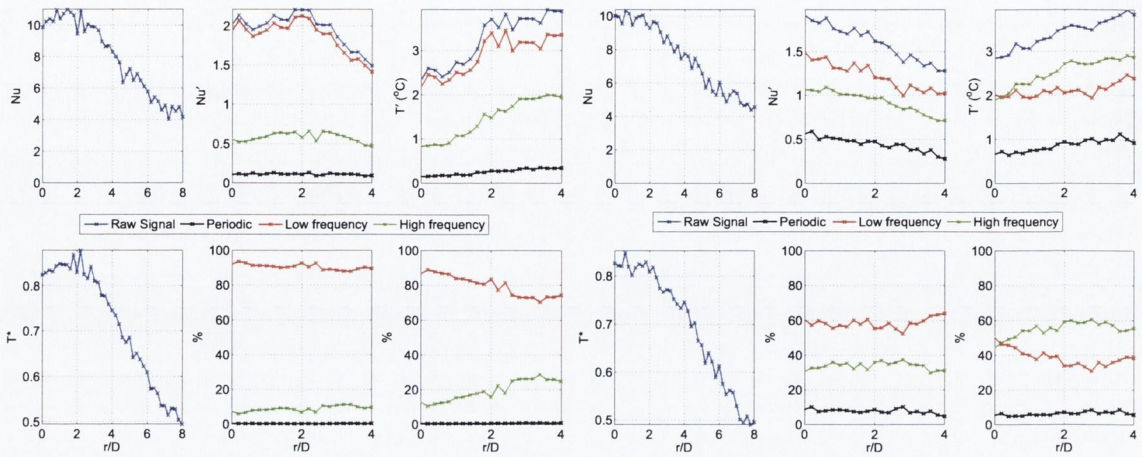

(a) $L_0/D = 8$, $f = 12\ Hz$

(b) $L_0/D = 24$, $f = 40\ Hz$

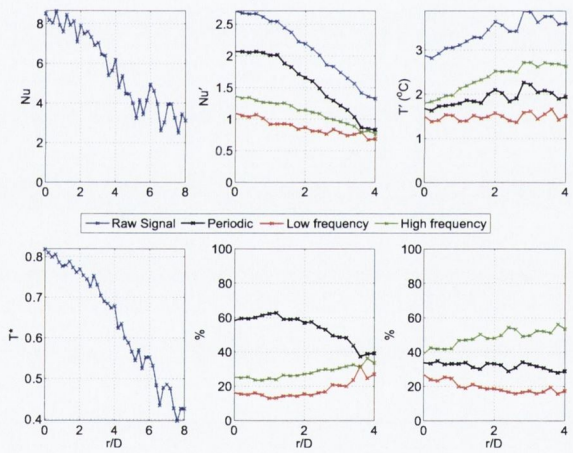

(c) $L_0/D = 48$, $f = 20\ Hz$

Figure 7.63: Radial profiles of average and fluctuating Nusselt number and dimensionless air temperature T^* (eqn. 7.3) decomposed into high, periodic and low frequency components, $Re = 3000$, $H/D = 16$, $L_0/D = 8, 24, 48$

indicative of how discrete each fluid impingement has become.

Frequency spectra for the corresponding parameters presented in figure 7.64 confirm much of this. In general, all spectra describe a broadly similar type of energy distribution, albeit there being a number of harmonics of the actuation frequency present at the larger stroke lengths only. No spectra show any major change in magni-

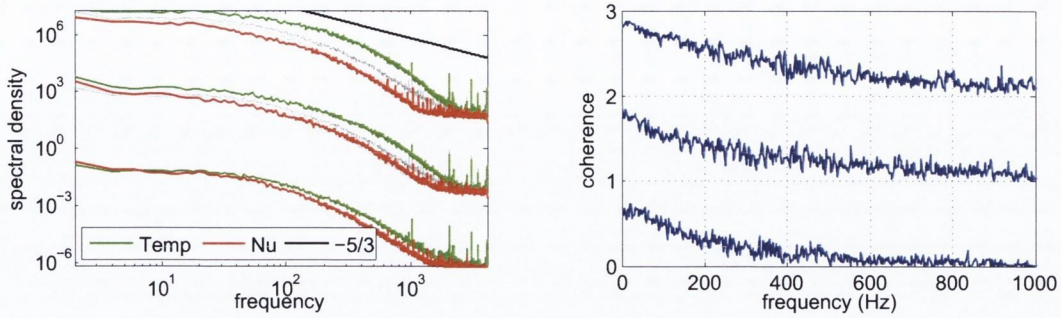

(a) $L_0/D = 8$, $f = 120\ Hz$

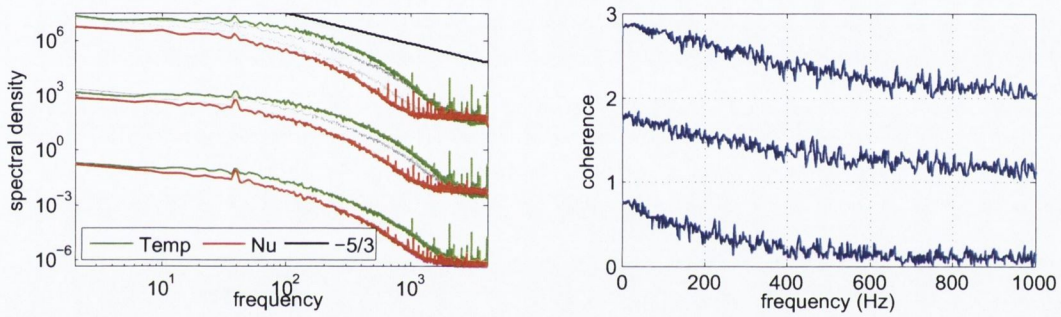

(b) $L_0/D = 24$, $f = 40\ Hz$

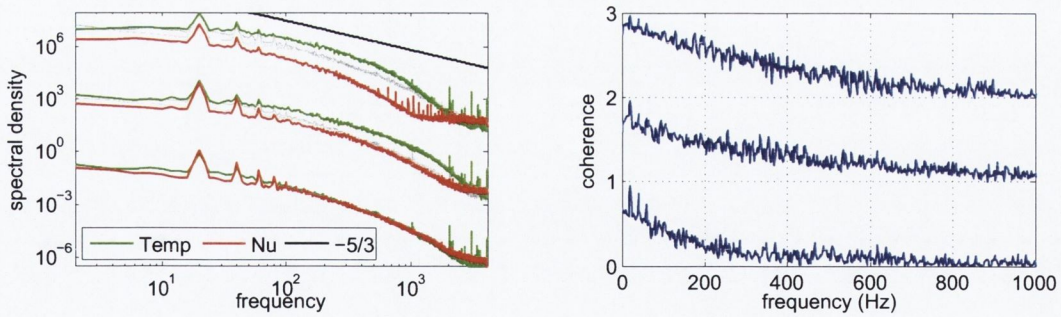

(c) $L_0/D = 48$, $f = 20\ Hz$

Figure 7.64: $Re = 3000$, $H/D = 16$, $r/D = 0, 2, 4$. Power spectra of Nusselt number and air temperature at increasing radial locations are offset by three decades, spectra at $r/D = 0$ are plotted in grey for comparison. Coherence spectra at increasing radial locations are offset by a value of 1.

tude or shape from one stroke length or radial location to the next, and all coherence data present comparable correlation magnitudes at similar frequencies. The reason for these trends is that all flows are highly developed before impact. Even though interactions between fluid ejected from subsequent phases may occur prior to impingement at a stroke length of $L_0 = 8D$, compared to the viscous dissipation of the isolated impingement at the larger stroke lengths, the spectra indicate a similar flow regime exists in which much of the interactions and heat transfer occurs in the low frequency domain developed prior to impingement.

7.3.1.5 Findings

Decomposed radial profiles were used to analyse both the state of jet development upon impingement and how it evolved thereafter. Results showed that while flows which were moderately developed upon impingement produced relatively high levels of heat transfer at the stagnation point, heat transfer dropped off quite rapidly at greater radial distances from the stagnation point. Underdeveloped flows, such as those generally produced at large stroke lengths, were seen also to produce good stagnation point heat transfer; however, as significant momentum was still retained upon impact, the impinging fluid was much more capable of travelling radially outwards once impingement had occurred. Subsequently, rapid development was experienced and elevated heat transfer was maintained to a larger radial distance. Data showing levels of correlation between the heat flux and local fluid temperature reinforced what had been previously observed for the stagnation point measurements; for all impingements which had undergone significant development and degradation prior to impingement increased levels of low frequency correlation between the signals were seen. Even for flows which were underdeveloped upon impingement increasing radial distance showed increasingly elevated levels of low frequency correlation; this was attributed to the further development of the jet.

7.3.2 Effect of Reynolds number on radial decomposition

7.3.2.1 H/D=2, Re=1000

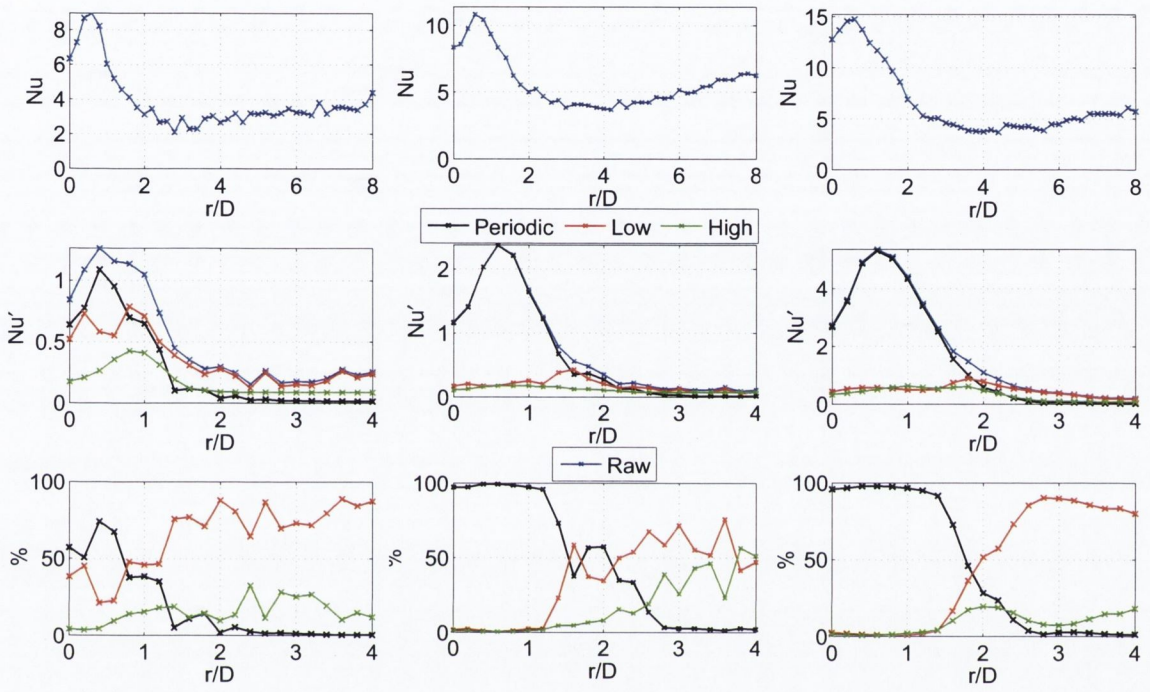

(a) $L_0/D = 3$, $f = 107\ Hz$ (b) $L_0/D = 4$, $f = 80\ Hz$ (c) $L_0/D = 8$, $f = 40\ Hz$

Figure 7.65: Radial profiles of average and fluctuating Nusselt number decomposed into high, periodic and low frequency components; $Re = 1000$, $H/D = 2$, $L_0/D = 3, 4, 8$

Figure 7.65 shows time averaged and fluctuating local heat transfer at a Reynolds number of 1000 and axial spacing of $H = 2D$. The stagnation point heat transfer data presented in figures 7.36 and 7.37 alluded to the existence of similar flow evolution and impinging heat transfer regimes across a wider range of Reynolds numbers and figure 7.65 suggests that this consistency in the result at different Reynolds numbers may be extended to complete radial profiles. Many of the features that were present in figure 7.57 for a Reynolds number of 3000 are also visible here, such as local minimum at the jet centre for mean and fluctuating heat transfer, as well as a high level of periodicity extending not much farther than $r = 2D$. This periodicity drops off significantly for

the stroke length of $L_0 = 3D$ but is very strong at the stroke length of $L_0 \geq 4D$. In these cases, the impingements are dominated by highly periodic impacts which account for an even larger proportion of the total fluctuation at the lower Reynolds number. It is significant that the high frequency component, by and large, accounts for a smaller proportion of the overall fluctuation at the lower Reynolds number. This can be explained by the fact that there is a reduced amount of energy to be dissipated at the lower flow velocities, and less shear between the stationary and moving fluid produces less turbulent fluctuation.

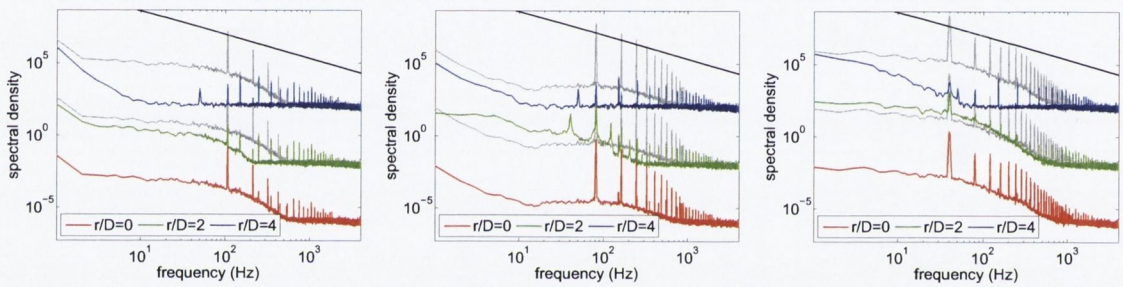

(a) $L_0/D = 3$, $f = 170\ Hz$ (b) $L_0/D = 4$, $f = 80\ Hz$ (c) $L_0/D = 8$, $f = 40\ Hz$

Figure 7.66: $Re = 1000$, $H/D = 2$, $L_0/D = 3, 4, 8$, $r/D = 0, 2, 4$; Nusselt number power spectra, subsequent radial locations are offset by three decades, with spectra at $r/D = 0$ plotted in grey for comparison.

Spectral analysis of the heat transfer data for $Re = 1000$ at $H = 2D$ presented in figure 7.66 shows that, like $Re = 3000$, the high degree of confinement results in little jet development prior to impingement as indicated by the suppression of all frequencies other than those associated with actuation. The exception to this, once again, occurs where the jet is under formed at the smallest stroke length $L_0 = 3D$; in this case all fluctuations are seen to drop off rapidly with increasing radial distance. This is in contrast to $L_0 = 4D$ and $8D$, for which no increase in periodic fluctuation is experienced but energy can be seen to be transferred to other frequencies. As with all data presented at this axial spacing little evidence of coherent flow structures remain in the heat transfer data at $r = 4D$ for all stroke lengths; the highly confined

conditions have ensured jet evolution is impeded and heat transfer therefore becomes highly limited at extended radial distances. Larger stroke lengths appear to have a greater ability to reduce this confinement effect as larger fluctuations can be observed in the power spectra at $r = 2D$ and $L_0 = 8D$; this corresponds to instantaneous flow field results previously presented which showed that the presence of a trailing jet enables the vortices be pushed to a greater radial distance after impact. A phenomenon which was previously unseen in any other data is present in figure 7.66 (b) where at a radial location of $r = 2D$ a sub-harmonic of the driving frequency is present at 40 Hz. This sub-harmonic was not evident at $Re = 3000$ and is found to only occur at a stroke length of $L_0 \approx 4D$; this sub-harmonic has been found to be most prominent at $r = 1.4D$ for an axial spacing of $H = 2D$. As this is only seen to occur in the flow regime dominated solely by the propagation of vortices it is reasonable to infer that this sub-harmonic may be produced by the interaction of these vortices upon impingement.

7.3.2.2 H/D=2, Re=2000

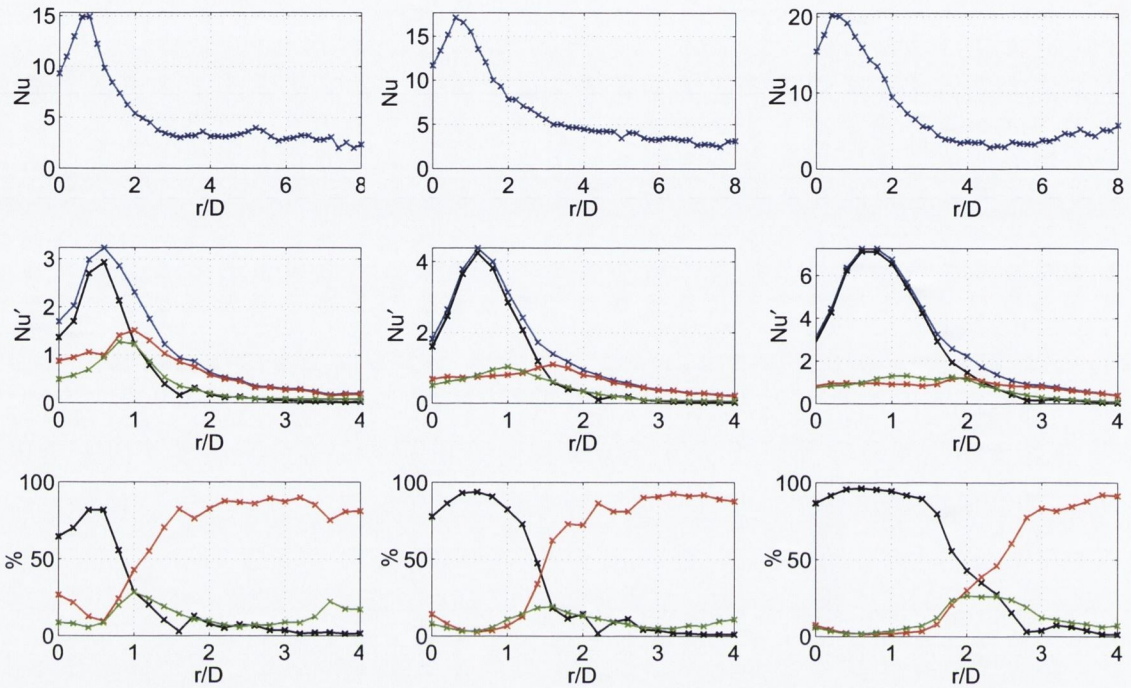

(a) $L_0/D = 3$, $f = 213\ Hz$ (b) $L_0/D = 4$, $f = 160\ Hz$ (c) $L_0/D = 8$, $f = 80\ Hz$

Figure 7.67: Radial profiles of average and fluctuating Nusselt number decomposed into high, periodic and low frequency components; $Re = 2000$, $H/D = 2$, $L_0/D = 3, 4, 8$

Increasing the Reynolds number to 2000, presented in figure 7.67, shows little difference in trends to data presented at other Reynolds numbers, beyond a change in the heat transfer magnitudes. Levels of periodicity for equivalent stroke lengths appear less than those seen at $Re = 1000$ but greater than at $Re = 3000$, while the high frequency component experiences the opposite effect. These results show that an increase in the high frequency fluctuating component is associated with an increase in the synthetic jet Reynolds number. As the flow energy is ultimately dissipated at the small scales associated with these higher frequencies this indicates that, just like conventional continuous jets, greater Reynolds numbers encourage the presence of the higher frequency fluctuations associated with more turbulent flows.

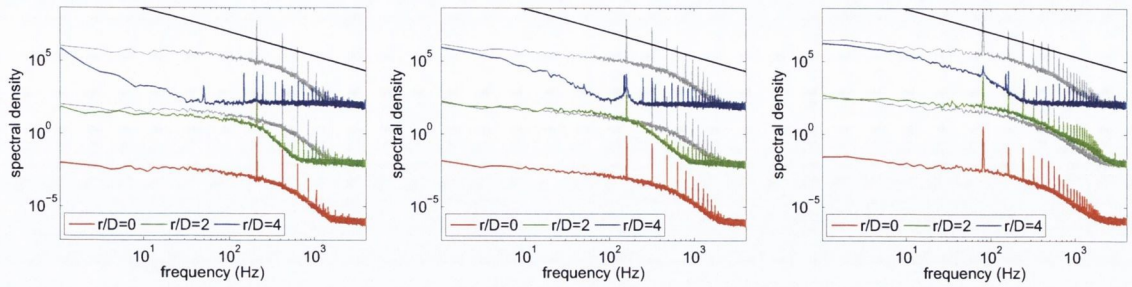

(a) $L_0/D = 3$, $f = 213\ Hz$ (b) $L_0/D = 4$, $f = 160\ Hz$ (c) $L_0/D = 8$, $f = 80\ Hz$

Figure 7.68: $Re = 2000$, $H/D = 2$, $L_0/D = 3, 4, 8$, $r/D = 0, 2, 4$; Nusselt number power spectra, subsequent radial locations are offset by three decades, with spectra at $r/D = 0$ plotted in grey for comparison.

Power spectra for Reynolds number of 2000 and $H = 2D$ presented in figure 7.68 show that increasing the Reynolds number from 1000 to 2000 results in slightly more power remaining in all spectra at $r = 4D$, owing to the increase in kinetic energy initially imparted to the flow. Similar sub-harmonics to those seen at $Re = 1000$ and $L_0 = 4D$ are not evident in the heat transfer spectra, indicating that this phenomenon is manifested solely at the lower Reynolds numbers required for the formation of more laminar vortex rings. Although the stroke length of $L_0 = 3D$ and radial distance of $r = 4D$ (figure 7.68 (a)) shows a spike in the spectrum at a frequency below the actuation frequency, this occurs at 50 Hz and can be attributed to the presence of electrical noise, the absence of any other heat transfer phenomena at similar frequencies have resulted in its emergence. Similar electrical noise present at harmonics of 50 Hz have been previously noted.

7.3.2.3 H/D=8, Re=1000

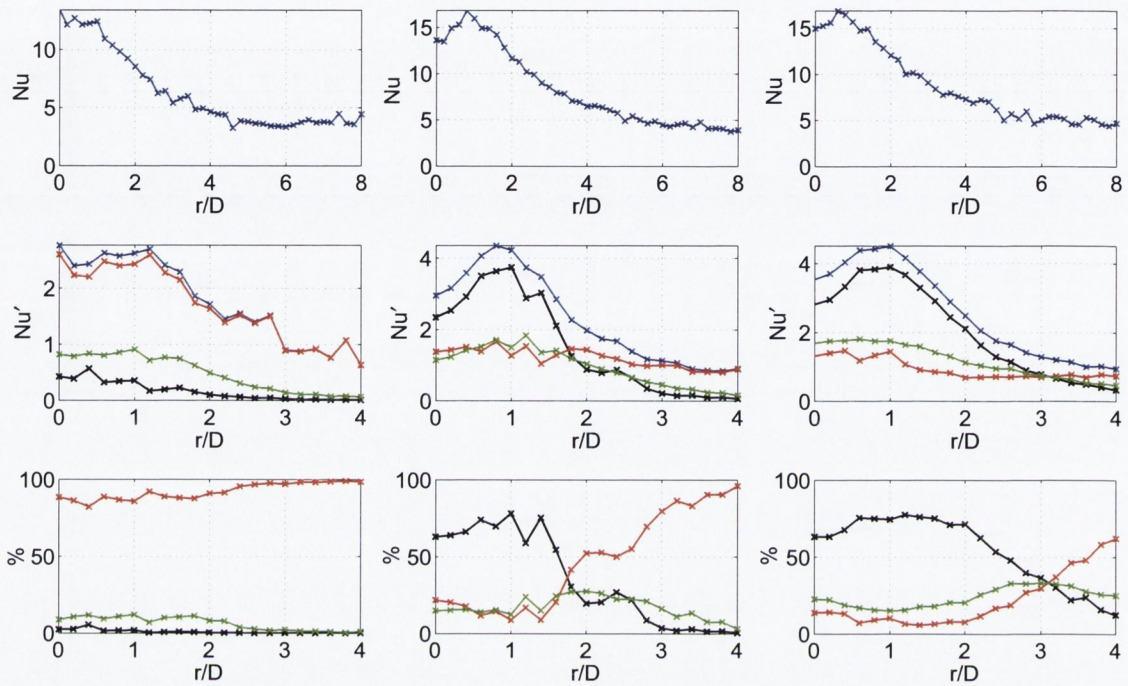

(a) $L_0/D = 4$, $f = 160\ Hz$ (b) $L_0/D = 8$, $f = 80\ Hz$ (c) $L_0/D = 16$, $f = 40\ Hz$

Figure 7.69: Radial profiles of average and fluctuating Nusselt number decomposed into high, periodic and low frequency components; $Re = 1000$, $H/D = 8$, $L_0/D = 4, 8, 16$

Decomposed radial profiles for a synthetic jet of $Re = 1000$ acquired at the greater axial spacing of $H = 8D$ are presented in figure 7.69. Comparing these profiles to data presented for $Re = 3000$ in figure 7.59 highlights the effect that Reynolds number has, not only on heat transfer, but also (indirectly) on the preceding flow. Fluid ejections produced at greater Reynolds numbers contain a much greater quantity of periodic energy; however a significantly greater level of the total fluctuation is also accounted for by the high frequency fluctuating component. It is thought that the increased presence of these high frequency components contributes to the degradation of the periodic nature of the jet; (at the Reynolds number of 3000) this is reflected in the increased level of periodicity in heat transfer experienced across the range of stroke

lengths at the lower Reynolds number of 1000.

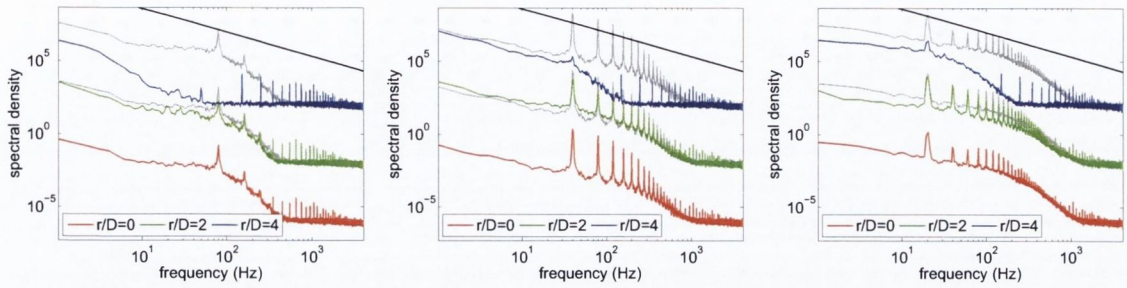

(a) $L_0/D = 4$, $f = 80\ Hz$ (b) $L_0/D = 8$, $f = 40\ Hz$ (c) $L_0/D = 16$, $f = 20\ Hz$

Figure 7.70: $Re = 1000$, $H/D = 8$, $L_0/D = 4, 8, 16$, $r/D = 0, 2, 4$; Nusselt number power spectra, subsequent radial locations are offset by three decades, with spectra at $r/D = 0$ plotted in grey for comparison.

Spectra for the corresponding Reynolds number, axial spacing and stroke lengths are presented in figure 7.70. Compared to corresponding spectra at the higher Reynolds number of 3000, seen in figure 7.62, the actuation frequency and harmonics appear to dominate the impingement regime to a much larger extent, indicating that the flow has undergone significantly less development prior to impingement. It is notable that while harmonics of the actuation frequency are more prominent at $Re = 1000$ they do not appear to transfer their energy to the high frequency domain to the same extent as the more turbulent jet of $Re = 3000$; as such the higher frequencies can be seen to contain little fluctuating energy. While difficult to identify, at $L_0 = 4D$ and $r = 2D$ there exists some evidence of the sub-harmonic phenomenon previously seen at the same parameters for $H = 2D$. While these sub harmonics (starting at 40 Hz) are significantly smaller, due to the greater level of development at the increased axial spacing, it can be seen that between the harmonics of the driving frequency (80, 160, 240 Hz and so on) small elevations associated with the sub-harmonic are present (120, 200 Hz etc.). At this axial spacing these sub-harmonics were found to be strongest at $r = 2.6D$, in comparison to $r = 1.4D$ at $H = 2D$.

7.3.2.4 H/D=8, Re=2000

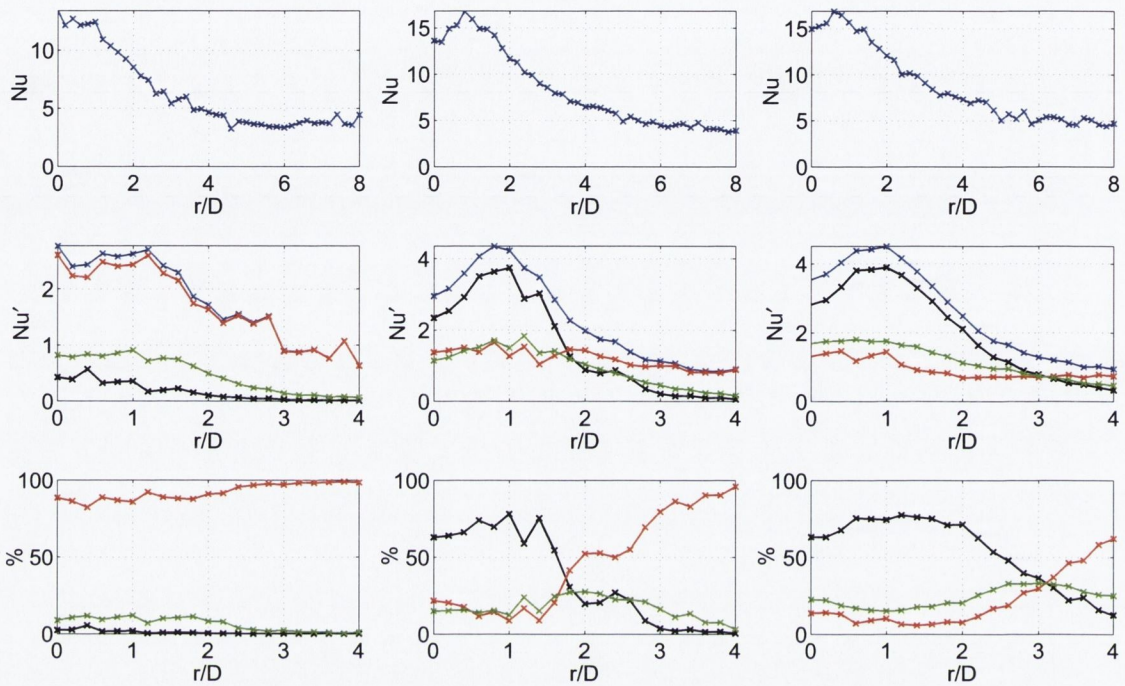

(a) $L_0/D = 4$, $f = 160\ Hz$ (b) $L_0/D = 8$, $f = 80\ Hz$ (c) $L_0/D = 16$, $f = 40\ Hz$

Figure 7.71: Radial profiles of average and fluctuating Nusselt number decomposed into high, periodic and low frequency components; $Re = 2000$, $H/D = 8$, $L_0/D = 4, 8, 16$

Figure 7.71 shows that while the impingement regimes at different Reynolds numbers appear more or less similar with stroke length, the proportion of the total fluctuation accounted for by the periodic component for $Re = 2000$ is less than that experienced at $Re = 1000$ and greater than that at $Re = 3000$. Comparing data for $Re = 2000$ and $H = 8D$ (figure 7.72) to identical data at the lower Reynolds number of 1000 (figure 7.70) confirms that a larger amount of high frequency fluctuation is experienced at larger Reynolds numbers and stroke lengths, the increased amount of energy contained in the flows must be dissipated by cascading to higher frequencies. Further spectral data for the Reynolds number of 2000 at axial spacings of $H = 4D$ and $12D$ are included in Appendix A.

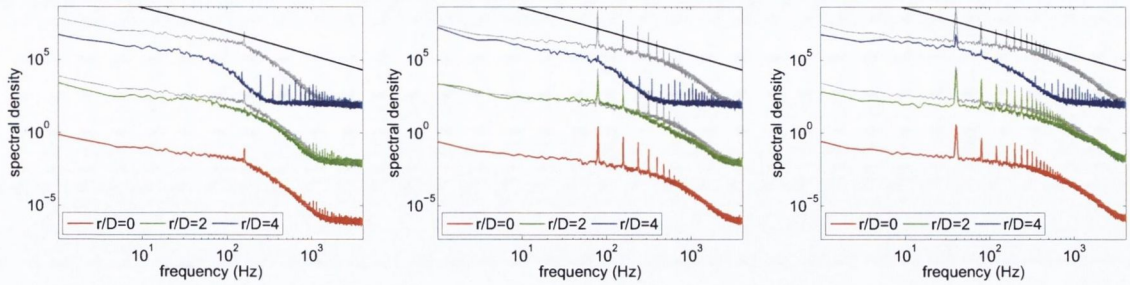

(a) $L_0/D = 4$, $f = 160\ Hz$ (b) $L_0/D = 8$, $f = 80\ Hz$ (c) $L_0/D = 16$, $f = 40\ Hz$

Figure 7.72: $Re = 2000$, $H/D = 8$, $L_0/D = 4, 8, 16$, $r/D = 0, 2, 4$; Nusselt number power spectra, subsequent radial locations are offset by three decades, with spectra at $r/D = 0$ plotted in grey for comparison.

7.3.2.5 Findings

The decomposition of lower Reynolds number flows revealed that the trends seen at $Re = 3000$ also hold at these parameters. The most notable difference at lower Reynolds numbers is that the periodic component of the fluctuating signal is consistently maintained to a much greater level while high frequency fluctuations are reduced. It has been concluded that as there is a lower amount of energy contained in the flow at the lower velocities there is less to be transferred to and dissipated at other frequencies. It was also shown that the reduction in Reynolds number not only reduced the jet's overall ability to remove heat from the surface but it also impaired the jet's ability to travel radially once impact occurred, thereby reducing further the level of heat transfer achieved.

7.4 Summary

Flow field data have been presented in this chapter and used to identify a number of different flow regimes for the Reynolds number of 3000, stroke lengths ranging from $3D \leq L_0 \leq 32D$ and axial spacings of $H = 4D, 8D$ and $12D$. Corresponding local Nusselt number, velocity and fluid temperature data have been presented so as to

identify the primary drivers and mechanisms for heat transfer for each regime. Further data supporting and validating the existence of these regimes at lower Reynolds numbers have also been presented.

Instantaneous flow visualisation results confirmed what had previously been shown by Gharib *et al.* [60], namely that the initial fluid ejection continued to form a vortex ring in front of the orifice until the maximum vortex circulation was achieved at a stroke length of approximately $L_0 \approx 4D$. Once the vortex reaches this maximum circulation it advects away from the orifice with any additionally ejected fluid merely contributing to the formation of a trailing jet. With varying stroke length these flow features can play very different roles in the flow field and in influencing heat transfer from the impingement surface with which they are associated. The impingement regimes (figure 7.19) which were identified are as follows:

- A flow of diminished impingement has been identified where fluid lacking the periodic motion associated with the formation of a synthetic jet impacts upon the plate, often at a reduced velocity. This impingement regime may be produced in one of two ways. Firstly, small stroke lengths of $L_0 \leq 3D$, result in the partial formation of a vortex at the orifice; this vortex possesses inadequate momentum to fully escape the effects of the subsequent suction stroke. Although a mean net flow is established it lacks coherence and cannot effect the same volume flux; it therefore rapidly degrades to a flow dominated by low frequency phenomena. The second circumstance which may result in a flow of diminished impingement is when, although the vortex may have achieved maximum circulation upon formation, insufficient impulse may be imparted to it to ensure it traverses the axial distance without a loss of momentum. This case is especially prevalent at larger axial spacings, $H > 6D$. This type of impingement corresponds to the region (a) in the flow regime map in figure 7.19.

- The second flow regime to be identified is where vortices which are fully formed at a stroke length $L_0 \geq 4D$ dominate the flow field and impinge upon the surface undiminished. This regime only exists when the stroke length is large enough to enable the vortex to escape the effects of the suction stroke, but it must also be small enough so that maximum ejection velocity occurs during vortex formation, i.e. $4D \leq L_0 \leq 8D$. Results showed that this regime no longer exists beyond $H = 10D$ as no vortex can

maintain coherence or momentum to this axial spacing. This type of impingement corresponds to the region (*b*) in the flow regime map in figure 7.19.

• The third and final flow regime identified was that dominated by the trailing jet. At a stroke length $L_0 > 8D$ the majority of the ejected fluid goes into the formation of the trailing jet rather than the leading vortex. In contrast to the impact of subsequent vortices at low axial spacings, the fluid impingement is overwhelmingly lead by the prolonged ejection of fluid from the trailing jet. Greater axial spacings allows for further development of the flow, as an accumulation of the higher velocity fluid at the interface between the leading vortex and trailing jet. A subsequent skewing of the vortex and the following flow is common before complete vortex destruction, viscous dissipation and spreading of the fluid ejection occurs. The consequential spreading results in a lower average impingement velocity being experienced. No significant coherent structures impinge for this flow regime although, once impingement has occurred, vortex rollup on the surface is common. This type of impingement corresponds to the region (*c*) in the flow regime map in figure 7.19.

Results showing the stagnation point heat transfer, velocity and temperature data for various axial spacings, presented in figure 7.35, identified impingement regimes broadly corresponding to the flow regimes identified. The local maximum in heat transfer (regime (*b*)) which was discovered to be consistently present in the vortex propagation regime was attributed to a combination of factors, it was concluded that it was favourable to have vortices impinging upon the surface as frequently as possible. At low axial spacings the limit to this frequency was found to be dictated by the minimum stroke length required for jet formation, beyond which a diminished impingement occurred. At larger axial spacings it was concluded that a decrease in frequency, and therefore an increase in stroke length, is required to impart sufficient momentum to the leading vortex to enable it travel the greater distance to the surface with least possible degradation while still maintaining the maximum rate of impingement. Consequently, the data were scaled by a combination of the stroke length, axial spacing and a diameter, $L_0/(H + 4D)$, and the stroke length at which the local maximum in heat transfer occurs could be calculated using the following equation:

$$\left(\frac{L_0}{D}\right)_{opt} = \frac{H}{2D} + 2 \tag{7.8}$$

A stroke length of $L_0 = 8D$ was shown to be the limit of the vortex propagation regime, thus equation 7.8 identifies the axial spacing of $H = 12D$, beyond which no coherent impinging vortices are experienced. This result was confirmed both by POD flow field data and also by spectral decomposition, where it was seen that at $H \geq 12D$ significant reduction in the periodicity of the flow produced at stroke lengths of $L_0 \leq 8D$ is experienced. Further stagnation point Nusselt number data confirmed these regimes to exist across a range of Reynolds numbers from 1000 to 3000.

Results showing coherence and power spectra indicated that, in terms of heat transfer behaviour, fluid velocity plays a much more prominent role for the impinging synthetic jet than local fluid temperature. For an undiminished flow both Nusselt number and velocity spectra resembled each other to a much greater extent than the corresponding temperature spectrum; higher levels of coherence were also experienced to significantly larger frequencies, indicating heat transfer was primarily being driven by fluid motion rather than local temperature. However, an increase in correlation between temperature and heat transfer was experienced under conditions where lower velocities were experienced due to degradation in the flow. At these lower velocities the local fluid was in contact with the heated surface for an increased duration and thereby had a greater opportunity to influence heat transfer. Although the correlation between the temperature and heat transfer signals did not appear as strong at higher velocities, it was seen that the average fluid temperature still had influence on heat transfer.

Results revealed that there is no single optimum operational parameter for all axial spacings. Although highly underdeveloped, small axial spacings and larger stroke lengths ($L_0 > 8D$) effect equal or higher rates of local heat transfer compared to smaller stroke lengths; this is thought to be due to the high impinging velocities. Similar stroke lengths at larger spacings provide room for the jet to develop prior to impingement. As maximum ejection velocity occurs during the formation of the trailing jet an accumulation of fluid is experienced at the interface with the vortex;

destruction of the vortex and a subsequent viscous dissipation of the fluid ejection commonly ensues, with a corresponding spreading of the jet occurring. A decrease in impingement velocity and in heat transfer at the stagnation point thus occurs. For stroke lengths of $L_0 \leq 8D$ at large axial spacings maximum velocity is present during the formation of the vortex, therefore spreading is not experienced and stagnation point impinging velocity and Nusselt number remains undiminished. The results suggested that although some of the smaller stroke lengths at the larger axial spacings were capable of maintaining a greater stagnation point heat transfer, the rates of heat transfer at increased radial distance were frequently less than those of larger stroke lengths due to an inability to maintain a similar level of momentum and volume flux up to impingement.

Spectrally decomposed radial profiles revealed that less high frequency fluctuations were produced at low Reynolds numbers where the energy content of the flow was reduced. As a consequence, the periodic fluctuating component of the heat transfer signal accounted for a much larger proportion of the fluctuation at low Reynolds numbers; this is indicative of a more laminar, coherent flow produced at the orifice and the subsequent development of a less turbulent jet flow prior to impingement. Power spectra of the various data revealed a previously unseen phenomenon occurring at low Reynolds numbers and at $L_0 = 4D$ where a sub-harmonic of the jet frequency is manifested in the heat transfer signal; it is proposed that this sub-harmonic is attributed to the interaction of the individual coherent vortices. This phenomenon is more evident at lower axial spacings but has been detected at jet to surface distances of up to $H = 8D$.

Chapter 8

Conclusions

8.1 Conclusions

An extensive investigation has been undertaken into the heat transfer processes associated with impinging synthetic jets and the evolution of the respective flow fields from which they are produced. In particular, this includes documentation of the role that dimensionless stroke length plays in the formation and evolution of the jet flow which ultimately dictates the impinging heat transfer regime.

A comprehensive literature review identified that the mechanisms involved in heat transfer to the impinging synthetic jet were poorly understood. Evaluation of the limited information available regarding heat transfer to the impinging synthetic jet proved difficult due to the inconsistent use of standardised, universal parameters, particularly those which dictated the formation and evolution of the jet. No literature has been published documenting the role that local air temperature plays in heat transfer to the impinging synthetic air jet. An experimental rig was designed and built specifically for the purposes of undertaking further research into the synthetic jet flow field and heat transfer. The resulting apparatus is capable of exercising accurate control of each synthetic jet operational parameter, including jet Reynolds number, stroke length and axial spacing. The acquisition of simultaneous local heat flux, velocity and air temperature measurements with high temporal resolution is also possible as is high speed flow field visualisation through the use of PIV. Results presented include the docu-

mentation of the variance in flow field evolution for a Reynolds number of $Re = 3000$, stroke lengths between $L_0 = 3D$ and $32D$ and axial spacings of $H = 4D, 8D$ and $12D$. Three flow regimes were identified:

(i) Flow field data confirmed that the minimum dimensionless stroke length required to achieve maximum vortex circulation was $L_0/D = 4$. Below this level a smaller vortex was seen to initially form in front of the orifice, however, much of this is reingested in the suction phase therefore producing a diminished flow field lacking coherent structures.

(ii) Vortices formed at a stroke length of $L_0 = 4D$ to $8D$ produce a flow field consisting of the formation and advection of fully formed vortices with high momentum and coherence. Fluid ejections larger than $L_0 > 4D$ were seen cause a widening of the vortex ring, due to the increased quantity of fluid in the core, and also to contribute to the formation of a trailing jet behind the leading vortex. This flow regime was seen to be dominated by vortex propagation.

(iii) As the stroke length was increased beyond $L_0 = 8D$, the maximum fluid ejection velocity now occurring in the trailing jet resulted in the accumulation of the higher velocity fluid at the interface between the trailing jet and the leading vortex ring. This accumulation resulted in a skewing and subsequent sudden destruction of the leading vortex ring, followed by a viscous dissipation of the entire fluid ejection. As this flow field was largely dominated by the fluid ejected after vortex formation it has been labelled the trailing jet regime.

Due to the highly intermittent nature of the synthetic jet flow it was necessary to develop custom software code which allowed for the decomposition of the resulting data into its periodic, high frequency and low frequency spectral components, before reconstruction back to the time domain. This analytic technique was developed to compliment the implementation of proper orthogonal decomposition with the flow field data which aided in the identification of the powerful jet flow structures and operational modes.

Local average and fluctuating heat transfer, velocity and temperature data was used to identify four separate impingement regimes. While these are broadly in line with the flow regimes identified, nozzle to plate spacing does dictate the extent to

which the jet evolves prior to impingement.

(i) A reduced level of heat transfer produced by a diminished impingement is experienced where insufficient impulse has been imparted to the ejected fluid to provide it with the required momentum to impinge upon the surface undiminished.

(ii) The second heat transfer regime identified was that where sufficient impulse is provided to the fluid so a high impinging velocity can be maintained as far as the surface. Sufficient development has occurred so as the type of small scale turbulence desirable for heat transfer from a solid surface is present upon impingement.

(iii) Stagnation point heat transfer and impinging velocity experiences a decrease in magnitude with an increase in stroke length, this is caused by the spreading of the jet with no increase in volume flux. Impingements are periodic and underdeveloped.

(iv) The final heat transfer regime sees an increase in velocity and heat transfer once again as impingements occur in isolation and become dominated by the trailing jet. The flow is highly periodic and underdeveloped upon impingement, with much development occurring in the wall jet.

Stagnation point Nusselt number correlations were developed for axial spacings ranging from $2 \leq H/D \leq 16$, Reynolds numbers $1000 - 3000$ and stroke lengths from $2 \leq L_0/D \leq 40$.

Power and coherence spectra revealed that the heat flux and velocity signals resembled each other to a much greater extent than the corresponding temperature spectrum. Greater levels of coherence between velocity and heat transfer signals indicates that heat transfer is primarily driven by fluid motion. An increase in the correlation between the temperature and heat flux signals at low velocities suggest that an increase in contact duration provides a greater opportunity for the fluid to affect heat transfer. While correlation between the signals at higher velocities is poor, average heat transfer and temperature data suggest that the average fluid temperature still plays an important role.

These results indicate that, in contrast to a continuous jet, a high degree of variability in the effective length of the potential core is achievable for a synthetic jet by simply changing the dimensionless stroke length at which it is formed. Consequently, at the same Reynolds number various flow regimes and corresponding heat transfer

regimes can be achieved and potentially optimised for the one geometric arrangement. The presentation of further local heat transfer results confirmed that these findings also hold for lower Reynolds numbers including $Re = 1000$ and 2000.

8.2 Further Work

A more detailed parametric study could be undertaken by varying stroke length and Reynolds number throughout the vortex propagation regime. Further investigation into the phenomenon driving the sudden destruction of the vortex ring may reveal much about the conditions required to maintain vortex coherence beyond a stroke length $L_0 = 8D$. To this end, various synthetic jet duty cycles and velocity programs could also be tested to optimise the impulse imparted to the ejected fluid and also to minimise the effect of the reingestion stroke at small stroke lengths. Such data could be used to enhance heat transfer by extending the axial distance to which the synthetic jet is capable of effectively operating, and also to improve it at more moderate separations.

As heat transfer to the synthetic jet can suffer as a result of high confinement conditions, it would be interesting to test angled nozzle geometries designed to encourage crossflow. Multiple orifices could also be implemented in a similar fashion encouraging flow interaction prior to impingement which has the potential to promote a higher level of fluid mixing and turbulence.

Various other phenomena below the scale of the vortex are present during the formation of the synthetic jet, many of which have a reliance on Reynolds number. High resolution PIV could be used to perform additional fluid measurements immediately at the orifice exit to identify the presence and effect of such phenomena.

Bibliography

[1] L. Gomes, W. Crowther, and N. Wood. Towards a practical synthetic jet actuator for industrial scale flow control applications. In *IUTAM Symposium on Flow Control and MEMS*, volume 7 of *IUTAM Book series*, pages 111–118. Springer Netherlands, 2008.

[2] A. K. Chaniotis, D. Poulikakos, and Y. Ventikos. Dual pulsating or steady slot jet cooling of a constant heat flux surface. *Journal of Heat Transfer*, 125:575 – 587, 2003.

[3] W. Z. Black, A. Glezer, and J. G. Hartley. Heat transfer modules for cooling electronics packages. In *International Symposium on Advanced Packaging Materials*, pages 209 – 215, Braselton, GA , USA, 1998.

[4] T. S. O'Donovan. *Fluctuating fluid flow and heat transfer of an impinging air jet.* PhD thesis, Trinity College, 2005.

[5] D. Lytle and B. W. Webb. Air jet impingement heat transfer at low nozzle-plate spacings. *International Journal of Heat and Mass Transfer*, 37(12):1687–1697, 1994.

[6] D. S. Kercher, J. B. Lee, O. Brand, M. G. Allen, and A. Glezer. Microjet cooling devices for thermal management of electronics. *IEEE Transactions on Components and Packaging Technologies*, 26(2):359 – 367, 2003.

[7] R. M. Farrelly, T. A. McGuinn, T. Persoons, and D. B. Murray. A heat transfer comparison between a synthetic jet and a steady jet at low Reynolds numbers. In

ASME International Mechanical Engineering Congress and Exposition, Boston, Massachusetts, USA, 2009. ASME.

[8] A. A. Pavlova and M. Amitay. Electronic cooling using synthetic jet impingement. *Journal of Heat Transfer*, 128:897–908, 2006.

[9] A. Glezer and M. Amitay. Synthetic jets. *Annual Review of Fluid Mechanics*, 34:503–536, 2002.

[10] A. Bar-Cohen. Computer-related thermal packaging at the millennial divide. *Electronics Cooling Magazine*, 6(1), 1 January 2000.

[11] J. S. Campbell, W. Z. Black, A. Glezer, and J. G. Hartley. Thermal management of a laptop computer with synthetic air microjets. In *Intersociety Conference on Thermal Phenomena*, Seattle, WA , USA, 1998.

[12] R. Mahalingam and A. Glezer. Design and thermal characteristics of a synthetic jet ejector heat sink. *Journal of Electronic Packaging*, 127:172–177, 2005.

[13] Z. Travnicek and V. Tesar. Annular synthetic jet used for impinging flow mass-transfer. *International Journal of Heat and Mass Transfer*, 46:32913297, 2003.

[14] R. J. Gardon and J. C. Akfirat. The role of turbulence in determining the heat transfer characteristics of impinging jets. *International Journal of Heat and Mass Transfer*, 8:1261 – 1272, 1965.

[15] T. Liu and J. P. Sullivan. Heat transfer and flow structures in an excited circular impinging jet. *International Journal of Heat and Mass Transfer*, 39(17):3695–3706, 1996.

[16] F. S. Sherman. *Viscous Flow*, volume 1 of *Mechanical Engineering Series*. McGraw-Hill, Singapore, 1990.

[17] H. J. Hussein, S.P. Capp, and W.K. George. Velocity measurements in a high-Reynolds-number, momentum-conserving, axisymmetric, turbulent jet. *Journal of Fluid Mechanics*, 258:31–75, 1994.

[18] N. R. Panchapakesan and J. L. Lumley. Turbulence measurements in axisymmetric jets of air and helium. part 1. air jet. *Journal of Fluid Mechanics*, 246:197–223, 1993.

[19] U. Ingard and S. Labate. Acoustic generation of circulation currents and jet effects. *The Journal of the Acoustical Society of America*, 22(1):87–87, 1950.

[20] R. Holman, Y. Utturkar, R. Mittal, B. L. Smith, and L. Cattafesta. Formation criterion for synthetic jets. *American Institute of Aeronautics and Astronautics*, 43(10):2110–2117, 2005.

[21] B. L. Smith and G. W. Swift. Synthetic jets at large Reynolds number and comparison to continuous jets. *American Institute of Aeronautics and Astronautics*, 3030, 2001.

[22] B. L. Smith and G. W. Swift. A comparison between synthetic jets and continuous jets. *Experiments in Fluids*, 34:467–472, 2003.

[23] J. E. Cater and J. Soria. The evolution of round zero-net-mass-flux jets. *Journal of Fluid Mechanics*, 472:167–200, 2002.

[24] J. L. Xu, J. Sha, C. F. Lin, and K. Y. Zhang. PIV experimental research of instantaneous flow characteristics of circular orifice synthetic jets. *Journal of Hydrodynamics*, 19(4):453–458, 2007.

[25] T. Crittenden and A. Glezer. A high-speed, compressible synthetic jet. *Physics of Fluids*, 18:1–18, 2006.

[26] G. M. Di Cicca and G. Iuso. On the near field of an axisymmetric synthetic jet. *Fluid Dynamics Research*, 39:673–693, 2007.

[27] K. E. Wu and K. S. Breuer. Dynamics of synthetic jet actuator arrays for flow control. *American Institute of Aeronautics and Astronautics*, 2003.

[28] M. B. Gillespie, W. Z. Black, C. Rinehart, and A. Glezer. Local convective heat transfer from a constant heat flux flat plate cooled by synthetic air jets. *Journal of Heat Transfer*, 128:990–1000, 2006.

[29] B. L. Smith and A. Glezer. Jet vectoring using synthetic jets. *Journal of Fluid Mechanics*, 458:1–34, 2002.

[30] S. G. Mallinson, J. A. Reizes, G. Hong, and P. S. Westbury. Analysis of hot-wire anemometry data obtained in a synthetic jet flow. *Experimental Thermal and Fluid Science*, 28:265272, 2004.

[31] A. A. Pavlova, K. Otani, and M. Amitay. Active control of sprays using a single synthetic jet actuator. *International Journal of Heat and Fluid Flow*, 29:131–148, 2008.

[32] L. D. Gomes, W. J. Crowther, and N. J. Wood. Towards a practical piezoceramic diaphragm based synthetic jet actuator for high subsonic applications - effect of chamber and orifice depth on actuator peak velocity. In *3rd AIAA Flow Control Conference*, pages 1–17, San Francisco, California, USA, 2006.

[33] M. Arik. An investigation into feasibility of impingement heat transfer and acoustic abatement of meso scale synthetic jets. *Applied Thermal Engineering*, 27:1483–1494, 2007.

[34] T. A. McGuinn, T. S. O'Donovan, and D. B. Murray. Heat transfer measurements of impinging synthetic air jet. In *ASME-JSME Thermal Engineering Summer Heat Transfer Conference*, Vancouver, British Columbia, Canada, 2007.

[35] T. J. Cox and P. D'Antonio. Acoustic absorbers and diffusers: theory, design and application. Spon Press:London, 2004.

[36] U. Ingard and H. Ising. Acoustic nonlinearity of an orifice. *The Journal of the Acoustical Society of America*, 42(1):6–17, 1967.

[37] M. Chaudhari, G. Verma, B. Puranik, and A. Agrawal. Frequency response of a synthetic jet cavity. *Experimental Thermal and Fluid Science*, 33:439–448, 2009.

[38] Q. Gallas, R. Holman, T. Nishida, B. Carroll, M. Sheplak, and L. Cattafesta. Lumped element modelling of piezoelectric-driven synthetic jet actuators. *American Institute of Aeronautics and Astronautics*, 41(2):240–247, 2003.

[39] Q. Gallas, G. Wang, M. Papila, M. Sheplak, and L. Cattafesta. Optimization of synthetic jet actuators. In *41st Aerospace Sciences Meeting and Exhibit*, volume 0635, Reno, NV, USA, 2003.

[40] M. Papila, M. Sheplak, and L. N. Cattafesta III. Optimization of clamped circular piezoelectric composite actuators. *Sensors and Actuators A: Physical*, 147(1):310–323, 2008.

[41] D. C. McCormick. Boundary layer separation control with directed synthetic jets. *American Institute of Aeronautics and Astronautics*, 2000-0159, 2000.

[42] J. Kordik, P. Safarik, and Z. Travnicek. Parametric study of the resonance frequency of synthetic jet actuators. In *Developments in machinery Design and Control*, Nowogrd, Poland, 2008.

[43] Z. Travnicek, P. Dancova, J. Kordik, T. Vit, and M. Pavelka. Heat and mass transfer caused by a laminar channel flow equipped with a synthetic jet array. In *14th International Heat Transfer Conference*, Washington, DC, USA, 2010.

[44] M. Chaudhari, B. Puranik, and A. Agrawal. Effect of orifice shape in synthetic jet based impingement cooling. *Experimental Thermal and Fluid Science*, 34(2):246–256, 2010.

[45] M. Gordon and J. Soria. PIV measurements of a zero-net-mass-flux jet in cross flow. *Experiments in Fluids*, 33:863–872, 2002.

[46] B. L. Smith and A. Glezer. The formation and evolution of synthetic jets. *Physics of Fluids*, 10(9):2281–2297, 1998.

[47] C. Nae. Numerical simulation of a synthetic jet actuator. In *22nd Congress of International Council of the Aeronautical Sciences*, volume 2403, Harrogate, UK, 2000.

[48] J. M. Shuster and D. R. Smith. Experimental study of the formation and scaling of a round synthetic jet. *Physics of Fluids*, 19(045109), 2007.

[49] Y. Utturkar, R. Holman, R. Mittal, B. Carroll, M. Sheplak, and L. Cattafesta. A jet formation criterion for synthetic jet actuators. In *41st Aerospace Sciences Meeting and Exhibit*, volume 0636, Reno, NV, 2003. AIAA.

[50] T. Persoons and T. S. O'Donovan. A pressure-based estimate of synthetic jet velocity. *Physics of Fluids*, 19(128104), 2007.

[51] D. K. L. Wu and M. A. Leschziner. Large-eddy simulations of circular synthetic jets in quiescent surroundings and in turbulent cross-flow. *International Journal of Heat and Fluid Flow*, 30:421–434, 2009.

[52] G. Le Song and M. Prudhomme. Prediction of coherent vortices in an impinging jet. *International Journal of Heat and Fluid Flow*, 28:11251135, 2007.

[53] H. Ha Minh. Order and disorder in turbulent flows: Their impact on turbulence modelling. In *Osborne Reynolds Centenary Symposium*, UMIST, Manchester, UK, 1994.

[54] C. Nae. Unsteady flow control using synthetic jet actuators. *American Institute of Aeronautics and Astronautics*, 2403, 2000.

[55] Q. Gallas, R. Holman, R. Raju, R. Mittal, M. Sheplak, and L. Cattafesta. Low dimensional modeling of zero-net mass-flux actuators. In *2nd AIAA Flow Control Conference*, volume 2413, Portland, OR, USA, 2004. AIAA.

[56] R. B. Kotapati, R. Mittal, and L. N. Cattafesta III. Numerical study of a transitional synthetic jet in quiescent external flow. *Journal of Fluid Mechanics*, 581:287–321, 2007.

[57] R. D. James, J. W. Jacobs, and A. Glezer. A round turbulent jet produced by an oscillating diaphragm. *Physics of Fluids*, 8(9):2484–2495, 1996.

[58] R. Mittal, P. Rampunggoon, and H. S. Udaykumar. Interaction of a synthetic jet with a flat plate boundary layer. *American Institute of Aeronautics and Astronautics*, 2773, 2001.

[59] A. J. Ward-Smith. Critical flowmetering: The characteristics of cylindrical nozzles with sharp upstream edges. *International Journal of Heat and Fluid Flow*, 1(3):123–132, 1979.

[60] M. Gharib, E. Rambod, and K. Shariff. A universal time scale for vortex ring formation. *Journal of Fluid Mechanics*, 360(-1):121–140, 1998.

[61] M. O. Muller, L. P. Bernal, P. K. Miska, P. D. Washabaugh, T. K. Chou, B. A. Parviz, C. Zhang, and K. Najafi. Flow structure and performance of axisymmetric synthetic jets. In *39th Aerospace Sciences Meeting and Exhibit*, volume 1008, Reno, NV, USA, 2001. AIAA.

[62] M. Rosenfeld, E. Rambod, and M. Gharib. Circulation and formation number of laminar vortex rings. *Journal of Fluid Mechanics*, 376(-1):297–318, 1998.

[63] P. S. Krueger and M. Gharib. The significance of vortex ring formation to the impulse and thrust of a starting jet. *Physics of Fluids*, 15(5):1271–1281, 2003.

[64] M. Shusser, M. Rosenfeld, J. O. Dabiri, P.l S. Krueger, and M. Gharib. Effect of time-dependent piston velocity program on vortex ring formation in a piston/cylinder arrangement the significance of vortex ring formation to the impulse and thrust of a starting jet. *Physics of Fluids*, 18(033601), 2006.

[65] L. E. Fraenkel. Examples of steady vortex rings of small cross-section in an ideal fluid. *Journal of Fluid Mechanics*, 51(01):119–135, 1972.

[66] R. Q. Shan and J. J. Wang. Experimental studies of the influence of parameters on axisymmetric synthetic jets. *Sensors and Actuators A: Physical*, 157(1):107–112, 2010.

[67] T. A. McGuinn, T. Persoons, P. Valiorgue, T. S. O'Donovan, and D. B. Murray. Heat transfer measurements of an impinging synthetic air jet with constant stroke length. In *5th European Thermal-Sciences Conference*, Eindhoven, the Netherlands, 2008.

[68] B. L. Smith and A. Glezer. Vectoring and small-scale motions effected in free shear flows using synthetic jet actuators. *American Institute of Aeronautics and Astronautics*, 0213, 1997.

[69] A. Agrawal and G. Verma. Similarity analysis of planar and axisymmetric turbulent synthetic jets. *International Journal of Heat and Mass Transfer*, 51(25-26):6194–6198, 2008.

[70] C. Nae. Active flow control over a circular cylinder. *22nd Congress of International Council of the Aeronautical Sciences*, 2000.

[71] M. Jabbal and S. Zhong. The near wall effect of synthetic jets in a boundary layer. *International Journal of Heat and Fluid Flow*, 29:119–130, 2007.

[72] A. Crook, W. J. Crowther, and N. J. Wood. A parametric study of a sja in a crossflow. In *22nd International Congress of Aeronautical Sciences*, Harrogate, UK, 2000. ICAS.

[73] C. Lee, G. Hong, and S. G. Mallinson. A piezoelectrically actuated micro synthetic jet for active flow control. *Sensors and Actuators*, A 108:168–174, 2003.

[74] T. Ozawa, S.l Lesbros, and G. Hong. Les of synthetic jets in boundary layer with laminar separation caused by adverse pressure gradient. *Computers and Fluids*, 39(5):845–858, 2010.

[75] J. P. Bonnet, W. L. Siauw, S. Bourgois, and J. Tensi. Influence of a synthetic jet excitation on the development of a turbulent mixing layer. *International Journal of Heat and Fluid Flow*, 29:957966, 2008.

[76] B. Han, R. J. Goldstein, and H. G. Choi. Energy separation in shear layers. *International Journal of Heat and Mass Transfer*, 45:47–55, 2002.

[77] B. Han and R. J. Goldstein. Instantaneous energy separation in a free jet. part i. flow measurement and visualization. *International Journal of Heat and Mass Transfer*, 46:39753981, 2003.

[78] B. Han and R. J. Goldstein. Instantaneous energy separation in a free jet - part ii. total temperature measurement. *International Journal of Heat and Mass Transfer*, 46:39833990, 2003.

[79] W. E. Carscallen, T. C. Currie, S. I. Hogg, and J. P. Gostelow. Measurement and computation of energy separation in the vortical wake flow of a turbine nozzle cascade. *Journal of Turbomachinery*, 121(4):703–708, 1999.

[80] S. H. Gunther, F. Binns, D. M. Carmean, and J. C. Hall. Managing the impact of increasing microprocessor power consumption. *Intel Technology Journal*, Q1, 2001.

[81] I. Mudawar. Assessment of high-heat-flux thermal management schemes. *Components and Packaging Technologies, IEEE Transactions on*, 24(2):122–141, 2001.

[82] G. E. Moore. Progress in digital integrated electronics. *International Electron Devices Meeting*, 1975.

[83] J. Citarella. The cooling challenge ahead. http://www.overclockers.com/cpu-die-size-cost-and-function(06 Jan 2011), 2010.

[84] International Roadmap Committee. International technology roadmap for semiconductors 2010 update. Technical report, 31 December 2010.

[85] International Roadmap Committee. International technology roadmap for semiconductors 2007 edition. Technical report, 31 December 2007.

[86] M. Li and S. Zhong. Heat transfer and flow characteristics of impinging synthetic jets. In *9th UK National Heat Transfer Conference*, Manchester, UK, 2005.

[87] S. Ashforth-Frost and K. Jambunathan. Effect of nozzle geometry and semi confinement on the potential core of a turbulent axisymmetric free jet. *International Communications in Heat and Mass Transfer*, 23(2):155–162, 1996.

[88] M. Chaudhari, B. Puranik, and A. Agrawal. Heat transfer characteristics of synthetic jet impingement cooling. *International Journal of Heat and Mass Transfer*, 53:1057–1069, 2010.

[89] P. Valiorgue, T. Persoons, T. A. McGuinn, and D. B. Murray. Heat transfer mechanisms in an impinging synthetic jet for a small jet-to-surface spacing. *Experimental Thermal and Fluid Science*, 33:597–603, 2009.

[90] T. Persoons, T. A. McGuinn, and D.B. Murray. A general correlation for the stagnation point nusselt number of an axisymmetric impinging synthetic jet. *International Journal of Heat and Mass Transfer*, 54(17-18):3900–3908, 2011.

[91] Z. Travnicek, A. I. Fedorchenko, and A. B. Wang. Enhancement of synthetic jets by means of an integrated valve-less pump, part i. design of the actuator. *Sensors and Actuators*, A 120:232240, 2004.

[92] T. A. McGuinn, T. Persoons, T. S. O'Donovan, and D. B. Murray. Surface heat transfer from an impinging synthetic air jet. In *10th UK National Heat Transfer Conference*, Edinburgh, Scotland, 2007.

[93] S. Corrisin. *Extended applications of the hotwire anemometer. Investigations of the flow in round, turbulent jets.* Ph.d., California Institute of Technology, 1947.

[94] S. A. Torkelsson. New type of resistance thermometer for accurate temperature measurements in high gradient thermal boundary layers. *Journal of Physics E: Scientific Instruments*, 13:549–552, 1980.

[95] P. Burattini and L. Djenidi. Velocity and passive scalar characteristics in a round jet with grids at the nozzle exit. *Flow, Turbulence and Combustion*, 72:199218, 2004.

[96] S. Drobniak, J. W. Elsner, and E.-S. A. El-Kassem. The relationship between coherent structures and heat transfer processes. *Experiments in Fluids*, 24:225–2373, 1998.

[97] D. K. Heist and I. P. Castro. Combined laser-doppler and cold wire anemometry for turbulent heat flux measurement. *Experiments in Fluids*, 24(5):375–381, 1998.

[98] H. A. Rydholm. An experimental investigation of the velocity and temperature fields of cold jets injected into a hot crossflow. In *41st International Gas Turbine and Aeroengine Congress and Exhibition*, volume 120, Birmingham, UK, 1996.

[99] M. B. Jovanovic, H. C. Lange, and A. A. van Steenhoven. Effect of hole imperfection on adiabatic film cooling effectiveness. *International Journal of Heat and Fluid Flow*, 29:377–386, 2008.

[100] Z. Travnicek, V. Tesar, and A. B. Wang. Enhancement of synthetic jets by means of an integrated valve-less pump, part ii. numerical and experimental studies. *Sensors and Actuators*, A 125:50–58, 2005.

[101] R. Mahalingam, N. Rumigny, and A. Glezer. Thermal management using synthetic jet ejectors. *IEEE Transactions on Components and Packaging Technologies*, 27(3):439–444, 2004.

[102] R. Mahalingam. Modelling of synthetic jet ejectors for electronics cooling. In *23rd IEEE SEMI-THERM Symposium*, Fairmont Hotel, San Jose, CA, USA, 2007.

[103] N. Beratlis and M. K. Smith. Optimization of synthetic jet cooling for microelectronics applications. In *19th IEEE SEMI-THERM Symposium*, pages 66–73, 2003.

[104] D. Gerty, D. W. Gerlach, Y. K. Joshi, and A. Glezer. Development of a prototype thermal management solution by interleaved solid spreaders and synthetic jets. In *Therminic*, Budapest, Hungary, 2007. EDA Publishing.

[105] Y. Wang, G. Yuan, Y. K. Yoon, M. G. Allen, and S. A. Bidstrup. Optimization of synthetic jet fluidic structures in printed wiring boards. *Journal of Electronic Packaging*, 128:353–359, 2006.

[106] Y. Wang, G. Yuan, Y. K. Yoon, M. G. Allen, and S. A. Bidstrup. Large eddy simulation (LES) for synthetic jet thermal management. *International Journal of Heat and Mass Transfer*, 49:21732179, 2006.

[107] B. D. Ritchie, D. R. Mujumdar, and J. M. Seitzman. Mixing in coaxial jets using synthetic jet actuators. *American Institute of Aeronautics and Astronautics*, 0404, 2000.

[108] W. M. Hartmann. *Signals, Sound, and Sensation.* Modern Acoustics and Signal Processing. AIP Press, New York, 1997.

[109] J. Cooley and J. Tukey. An algorithm for the machine computation of the complex fourier series. *Mathematics of Computation*, 19:297–301, 1965.

[110] V. Tesar and J. Kordik. Spectral analysis of a synthetic jet. *Sensors and Actuators A: Physical*, In Press - Corrected Proof, 2011.

[111] Y. Scholten and D. B. Murray. Heat transfer and velocity fluctuations in a staggered tube array. *International Journal of Heat and Fluid Flow*, 19:233–244, 1997.

[112] T. S. O'Donovan and D. B. Murray. Fluctuating fluid fow and heat transfer of an obliquely impinging air jet. *International Journal of Heat and Mass Transfer*, 51:6169–6179, 2008.

[113] J. H. Citriniti and W. K. George. Reconstruction of the global velocity field in the axisymmetric mixing layer utilizing the proper orthogonal decomposition. *Journal of Fluid Mechanics*, 418:137–166, 2000.

[114] G. Addington, J. Hall, and J. Myatt. Reduced order modelling applied to reactive flow control. In *AIAA Atmospheric Flight Mechanics Conference and Exhibit*, Monterey, CA, USA, 2002.

[115] O. K. Rediniotis, J. Ko, and A. J. Kurdila. Reduced order nonlinear navier-stokes models for synthetic jets. *Journal of Fluids Engineering*, 124:433–443, 2002.

[116] N. K. Yamaleev and M. H. Carpenter. A reduced-order model for efficient simulation of synthetic jet actuators. *NASA, Technical Report*, TM-2003-212664, 2003.

[117] S. V. Gordeyev and F. O. Thomas. Coherent structure in the turbulent planar jet. part 1. extraction of proper orthogonal decomposition eigenmodes and their self-similarity. *Journal of Fluid Mechanics*, 414(-1):145–194, 2000.

[118] B. Weitao, Y. Sugii, K. Okamoto, and H. Madarame. Time-resolved proper orthogonal decomposition of the near-field flow of a round jet measured by dynamic particle image velocimetry. *Measurement Science and Technology*, 14(8):L1–L5, 2003.

[119] S. Bernero and H. E. Fiedler. Application of particle image velocimetry and proper orthogonal decomposition to the study of a jet in a counterflow. *Experiments in Fluids*, 29(0):S274–S281, 2000.

[120] S. S. Papell. Influence of thermal boundary conditions on heat transfer from a cylinder in crossflow. Technical report, NASA Lewis Research Center, August 1981.

[121] B. M. Tchavdarov. Two-dimensional vortex dynamics of inviscid-viscous interaction at turbulent slot-jet impingement. *International Journal of Heat and Fluid Flow*, 18(3):316–327, 1997.

[122] M. Arik, Y. Utturkar, and M. Gursoy. Interaction of synthetic jet cooling performance with gravity and buoyancy driven flows. In *ASME InterPACK '07*, Vancouver, British Columbia, Canada, 2007.

[123] M. R. Anderson and J. W. Baughn. Liquid-crystal thermography, illumination spectral effects, part 1 - experiments. *Journal of Heat Transfer*, 127:581–587, 2005.

[124] M. R. Anderson and J. W. Baughn. Thermochromic liquid crystal thermography, illumination spectral effects, part 2 - theory. *Journal of Heat Transfer*, 127:588–597, 2005.

[125] S.W. Chang, S. F. Chiou, and S.F. Chang. Heat transfer of impinging jet array over concave-dimpled surface with applications to cooling of electronic chipsets. *Experimental Thermal and Fluid Science*, 31:625–640, 2007.

[126] P. R. Souza Mendes. The naphthalene sublimation technique. *Experimental Thermal and Fluid Science*, 4(5):510–523, 1991.

[127] R. J. Goldstein and H. H. Cho. A review of mass transfer measurements using naphthalene sublimation. *Experimental Thermal and Fluid Science*, 10(4):416–434, 1995.

[128] E. M. Sparrow and B. J. Lovell. Heat transfer characteristics of an obliquely impinging circular jet. *Journal of Heat Transfer*, 102(2):202–209, 1980.

[129] R. J. Goldstein and J. R. Taylor. Mass transfer in the neighbourhood of jets entering a crossflow. *Journal of Heat Transfer*, 104(4):715–721, 1982.

[130] J. Ward and M. Mahmood. Heat transfer from a turbulent, swirling, impinging jet. In *7th International Conference*, volume 3 of *Fluid Mechanics and Heat Transfer*, pages 401–407, Munich, West Germany, 1982. Hemisphere Publishing Corp.

[131] Y. Scholten and D. B. Murray. Measurement of convective heat transfer using hot film sensors correction for sensor overheat. *Journal of Heat Transfer*, 118(4):982–984, 1996.

[132] T. S. O'Donovan and D. B. Murray. Jet impingement heat transfer part ii: A temporal investigation of heat transfer and local fluid velocities. *International Journal of Heat and Mass Transfer*, 50:33023314, 2006.

[133] T. S. O'Donovan and D. B. Murray. Jet impingement heat transfer - part i: Mean and root-mean-square heat transfer and velocity distributions. *International Journal of Heat and Mass Transfer*, 50:32913301, 2006.

[134] C. Yao, F. J. Chen, D. Neuhart, and J. Harris. Synthetic jet flow field database for cfd validation. In *2nd AIAA Flow Control Conference*, volume 2218, Portland, Oregon, USA, 2004. AIAA.

[135] R. Mahalingam, S. Heffington, L. Jones, and M. Schwickert. Newisys server processor cooling augmentation using synthetic jet ejectors. IEEE, 2006.

[136] J. L. Gilarranz, L. W. Traub, and O. K. Rediniotis. A new class of synthetic jet actuators - part i design, fabrication and bench top characterization. *Journal of Fluids Engineering*, 127:367–376, 2005.

[137] J. L. Gilarranz, L. W. Traub, and O. K. Rediniotis. A new class of synthetic jet actuators - part ii: Application to flow separation control. *Journal of Fluids Engineering*, 127:377–387, 2005.

[138] P. S. Shadlesky. Stagnation point heat transfer for jet impingement to a plane surface. *AIAA Journal*, 21(8):1214–1215, 1983.

[139] T. Persoons. *Experimental flow dynamics in automotive exhaust systems with close-coupled catalysts.* PhD thesis, Katholieke Universiteit Leuven, 2006.

[140] H. H. Bruun. *Hot-Wire Anemometry - Principles and Signal Analysis.* Oxford University Press, Department of Mechanical and Manufacturing Engineering, University of Bradford, 1995.

[141] W. D. Baines and J. F. Keffer. Shear stress and heat transfer at a stagnation point. *International Journal of Heat and Mass Transfer*, 19:21–26, 1976.

[142] S.M. O'Shaughnessy. *Bubble induced Marangoni convection.* PhD thesis, The University of Dublin, Trinity College, Dublin, Ireland, 2011.

[143] T. Persoons, T. A. McGuinn, and D.B. Murray. High dynamic range whole-field turbulence measurements in impinging synthetic jets for heat transfer applications. In *15th International Symposium on Applications of Laser Techniques to Fluid Mechanics*, Lisbon, Portugal, 2010.

[144] R. J. Adrian, K. T. Christensen, and Z.C. Liu. Analysis and interpretation of instantaneous turbulent velocity fields. *Experiments in Fluids*, 29(3):275–290, 2000.

[145] A. Glezer. The formation of vortex rings. *Physics of Fluids*, 31(12):3532–3542, 1988.

[146] T. A. McGuinn, T. Persoons, T. S. O'Donovan, and D. B. Murray. Heat transfer and air temperature measurements of an impinging synthetic air jet. In *Turbulence, Heat and Mass Transfer 6*, Rome, Italy, 2009. Begell House, Inc.

Appendix A

Appendix

A.1 Additional Figures

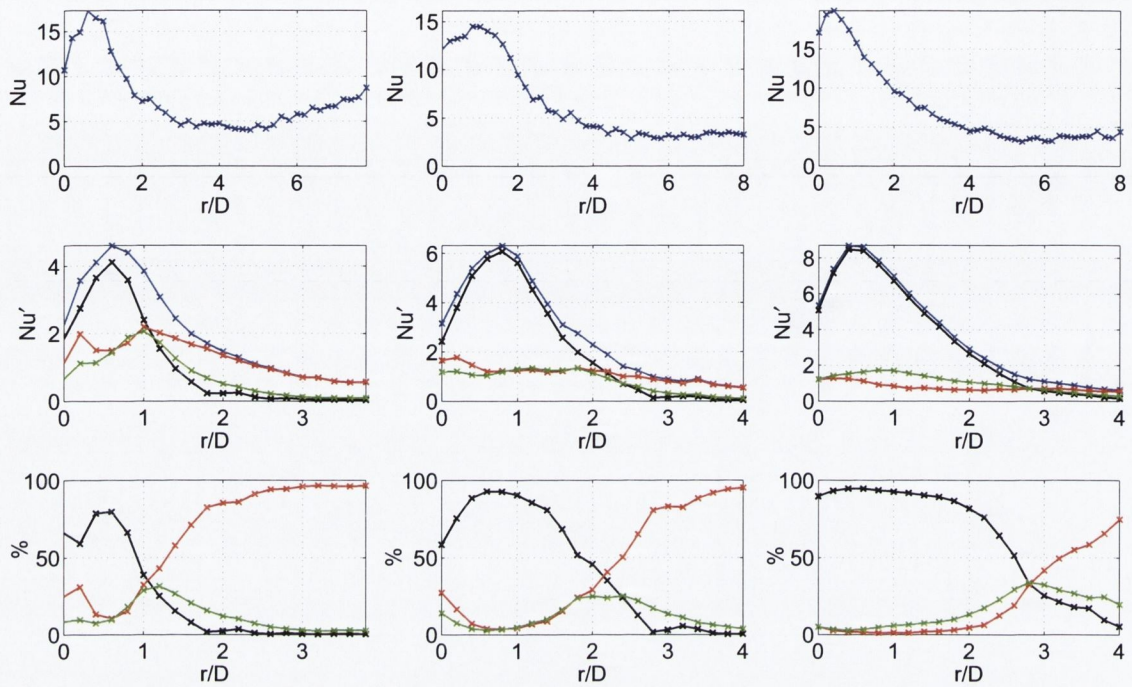

(a) $L_0/D = 4$, $f = 160\ Hz$ (b) $L_0/D = 8$, $f = 80\ Hz$ (c) $L_0/D = 16$, $f = 40\ Hz$

Figure A.1: Radial profiles of average and fluctuating Nusselt number decomposed into high, periodic and low frequency components; $Re = 2000$, $H/D = 4$, $L_0/D = 4, 8, 16$

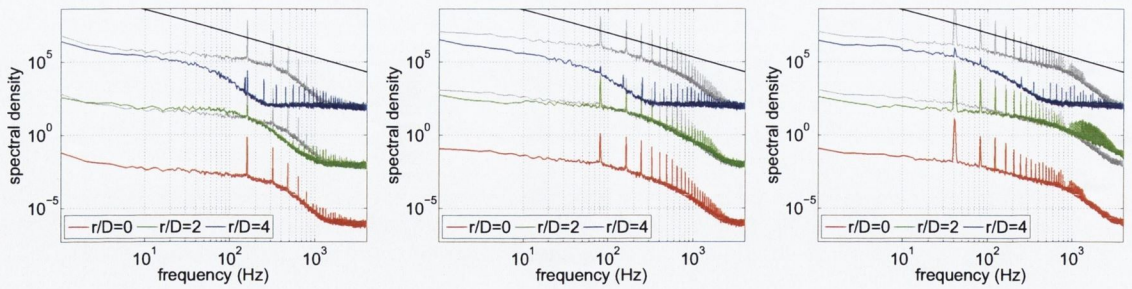

(a) $L_0/D = 4$, $f = 160\ Hz$ (b) $L_0/D = 8$, $f = 80\ Hz$ (c) $L_0/D = 16$, $f = 40\ Hz$

Figure A.2: $Re = 2000$, $H/D = 4$, $L_0/D = 4, 8, 16$, $r/D = 0, 2, 4$; Nusselt number power spectra, subsequent radial locations are offset by three decades, with spectra at $r/D = 0$ plotted in grey for comparison.

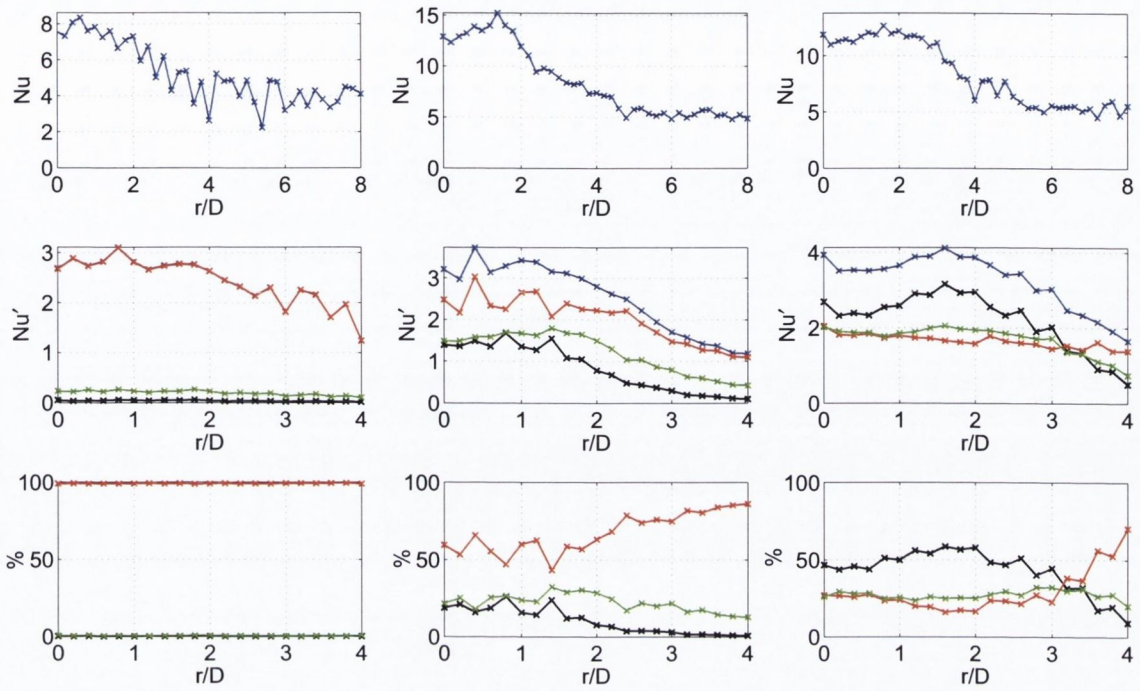

(a) $L_0/D = 4$, $f = 160\ Hz$ (b) $L_0/D = 8$, $f = 80\ Hz$ (c) $L_0/D = 16$, $f = 40\ Hz$

Figure A.3: Radial profiles of average and fluctuating Nusselt number decomposed into high, periodic and low frequency components; $Re = 2000$, $H/D = 12$, $L_0/D = 4, 8, 16$

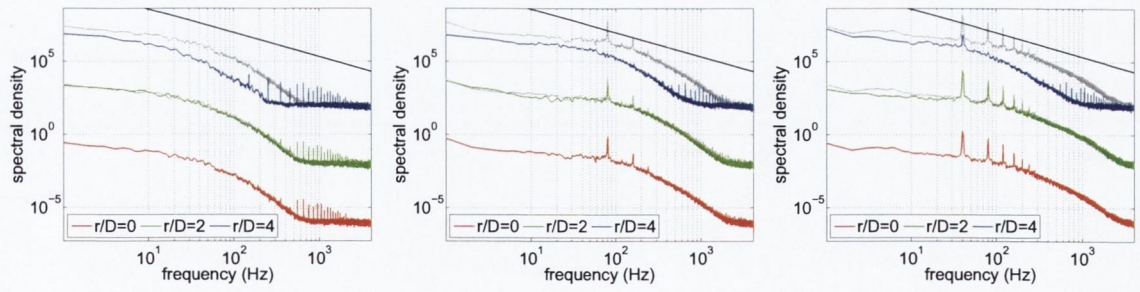

(a) $L_0/D = 4$, $f = 160\ Hz$ (b) $L_0/D = 8$, $f = 80\ Hz$ (c) $L_0/D = 16$, $f = 40\ Hz$

Figure A.4: $Re = 2000$, $H/D = 12$, $L_0/D = 4, 8, 16$, $r/D = 0, 2, 4$; Nusselt number power spectra, subsequent radial locations are offset by three decades, with spectra at $r/D = 0$ plotted in grey for comparison.

A.2 Instrument Specification & Calibration Documentation

VISATON FR-8 8 OHM

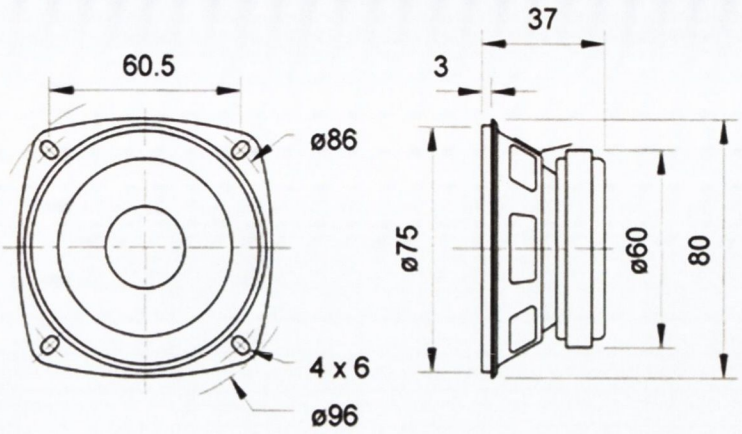

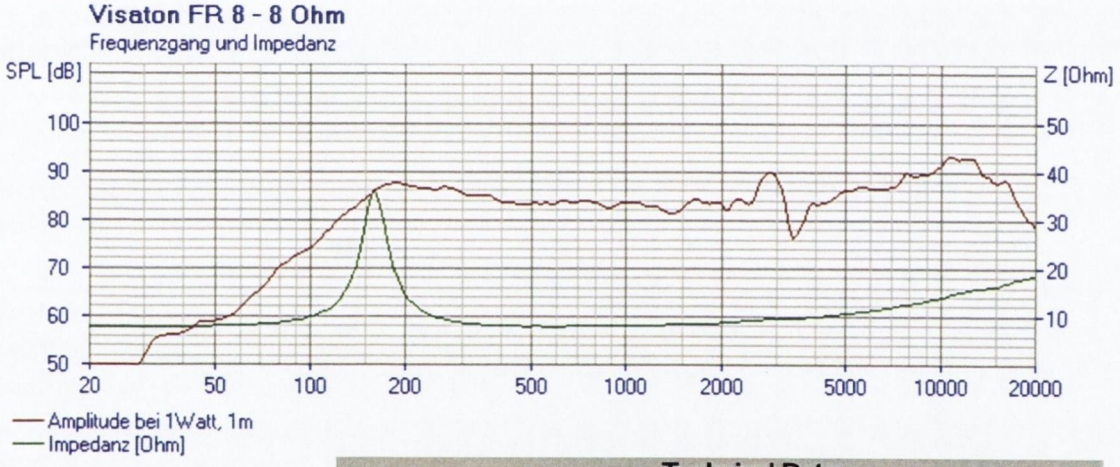

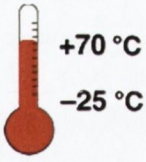

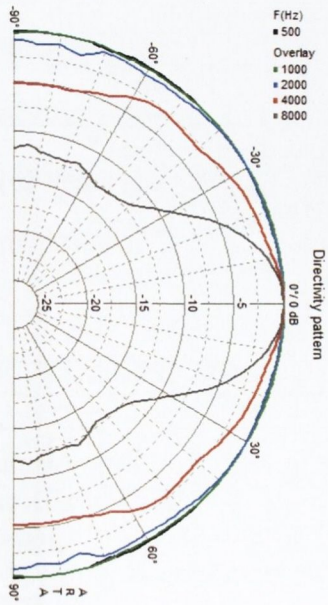

Technical Data:	
Rated power	10 W
Maximum power	15 W
Nominal impedance Z	8 Ohm
Frequency response	130–20000 Hz
Mean sound pressure level	86 dB (1 W/1 m)
Opening angle (-6 dB)	180°/4000 Hz
Excursion limit	+/–2 mm
Resonance frequency fs	150 Hz
Magnetic induction	1,4 T
Magnetic flux	200 µ Wb
Height of front pole-plate	3 mm
Voice coil diameter	15 mm
Height of winding	5 mm
Cutout diameter	75 mm
Net weight	0,24 kg
D.C. resistance Rdc	7,4 Ohm
Mechanical Q factor Qms	5,3
Electrical Q factor Qes	1,38
Total Q factor Qts	1,09
Equivalent volume Vas	0,7 l
Effective piston area Sd	30 cm²
Dynamically moved mass Mms	1,7 g
Force factor Bxl	2,5 Tm
Inductance of the voice coil L	0,6 mH
Temperature range	–25 ... 70 °C

¼-inch Pressure Microphone Type 40BP

Product Data and Specifications

Typical applications

- ***Sound pressure measurements***
- ***High frequency measurements***
- ***High level pressure measurements***

The G.R.A.S. Microphone Type 40BP is a ¼-inch precision condenser microphone for general purpose acoustic measurements, e.g. in couplers and at boundaries. It is an externally polarized pressure microphone with a large dynamic range and a wide frequency response.

As a pressure microphone, the Type 40BP measures the sound pressure at the location of its diaphragm. It has a flat pressure-frequency response over its entire working frequency range (see Fig. 2).

In an open sound field, a pressure microphone will also include the disturbing effects of its presence in the sound field. These are minimal for most of its frequency range because of its small dimensions (see Fig. 1 inset). At higher frequencies, the effects of reflections and diffractions must be accounted for. Generally, they lead to an increase in the measured sound pressure and corrections have to be made. Fig. 3 shows what these corrections are in a free field for various angles of incidence.

G.R.A.S. ¼-inch preamplifiers (see data sheet for Types 26AA, 26AB, 26AC and 26AL) are also available for use with the Type 40BP. The mounting thread (5.7 mm - 60 UNS-2) is compatible with other available makes of similar microphone preamplifiers.

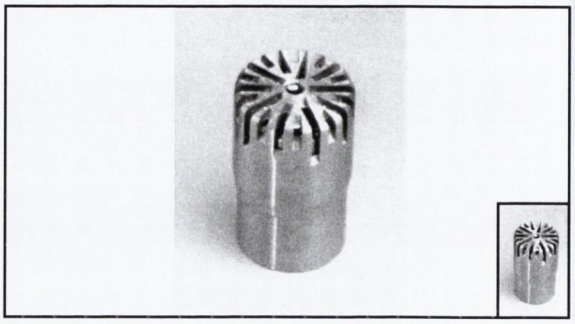

Fig. 1 ¼-inch Pressure Microphone Type 40BP (inset shows true size)

All G.R.A.S. microphones comply with the specifications of IEC 1094: *Measurement Microphones, Part 4: Specifications for working standard microphones*.

Non-corrosive, stainless materials are used in manufacturing these microphones to enable them to withstand rough handling and corrosive environments.

All G.R.A.S. microphones are guaranteed for 5 years and are individually checked and calibrated before leaving the factory. An individual calibration chart is supplied with each microphone.

Specifications

Frequency response:	
4 Hz - 70 kHz	±2.0 dB
10 Hz - 25 kHz	±1.0 dB
Nominal sensitivity:	1.6 mV/Pa
Polarization voltage:	200 V
Upper limit (3 % distortion):	174 dB re. 20 µ Pa
Microphone thermal noise:	31 dBA re. 20 µ Pa
Capacitance:	7 pF

...continued overleaf

Ver 06 Aug 2010

G.R.A.S.
Sound & Vibration

Skovlytoften 33
2840 Holte, Denmark
Tel +45 45 66 40 46 Fax +45 45 66 40 47
e-mail: gras@gras.dk www.gras.dk

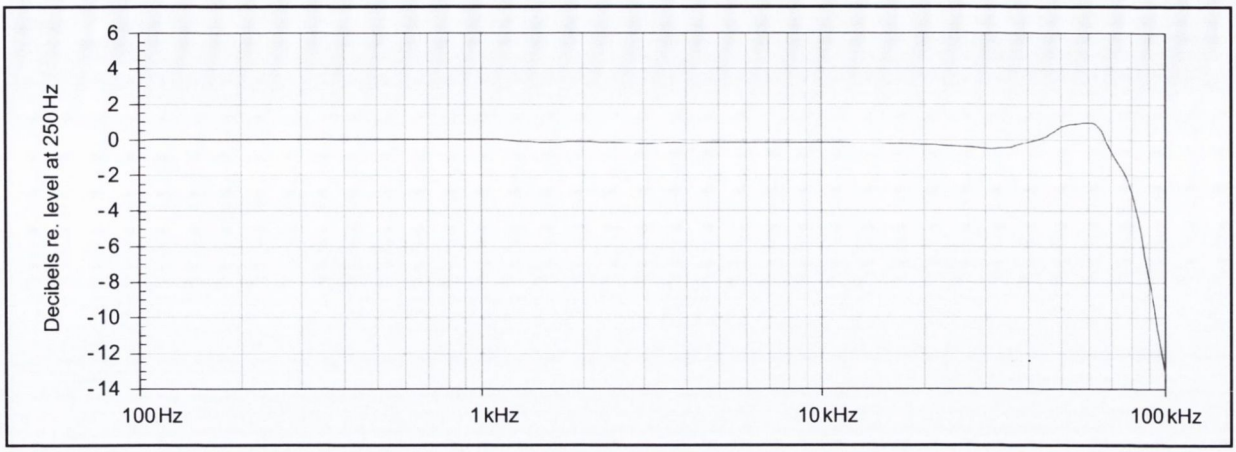

Fig. 2 Typical frequency response for Type 40BP (without protection grid)

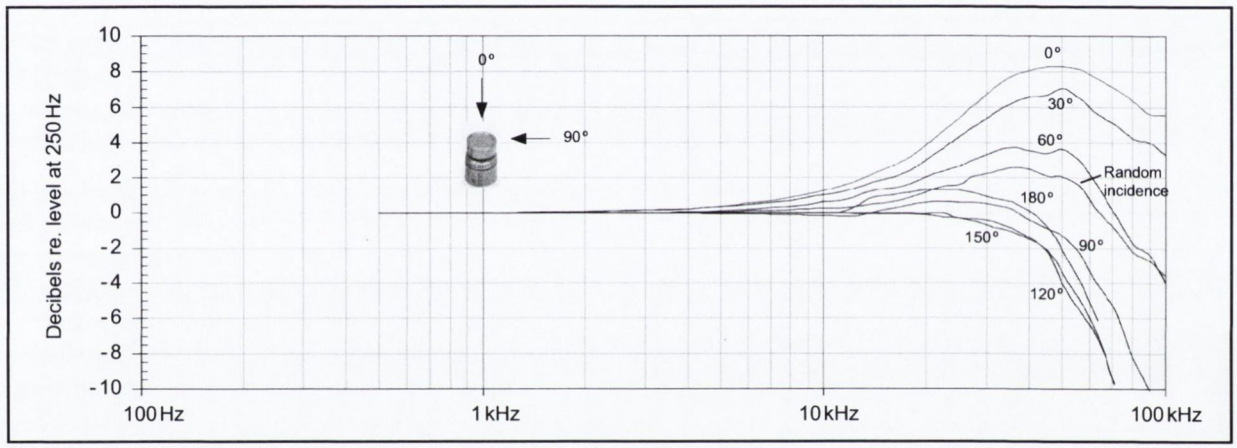

Fig. 3 Free-field corrections for various angles of incidence (without protection grid)

Specifications (continued)

Temperature:
Range:. . . . . –40 °C to +150 °C
Coeff. (250 Hz): . . . . . –0.01 dB / °C

Static-pressure coefficient:
–0.003 dB / k Pa

Humidity range:
0 - 100 % (non-condensing)

Influence of humidity (250 Hz):
< 0.1 dB (0 - 100 % RH)

Influence of axial vibration, 1 m/s²:
69 dB re. 20 µ Pa

Venting:
Rear vented

Note: for most applications, rear venting is more advantageous particularly where phase response is critical. If front venting is preferred, please add "front venting" to the Type number of the microphone when ordering.

Dimensions (with protection grid):
Length/Diameter: . . . . . 10.5 mm/6.9 mm

(without protection grid):
Length/Diameter: . . . . . 9.1 mm/6.3 mm

Diameter (diaphragm ring):
5.9 mm

Threads:
Protection Grid: . . . . . 6.35 mm - 60 UNS
Preamplifier Mounting: . . . . . 5.7 mm - 60 UNS

Weight:
2 g

G.R.A.S. Sound & Vibration reserves the right to change specifications and accessories without notice

G.R.A.S.
Sound & Vibration

Skovlytoften 33
2840 Holte, Denmark
Tel +45 45 66 40 46 Fax +45 45 66 40 47
e-mail: gras@gras.dk www.gras.dk

¼" Preamplifier Type 26AC, General-purpose

Product Data

Typical Applications

- General-purpose preamplifier
- High-frequency measurements
- High-pressure measurements

Special Properties

- Wide Frequency Range
- Low Noise Level
- Very Small

Description

The G.R.A.S. ¼" Preamplifier Type 26AC is a small robust unit optimised for acoustic measurements using condenser microphones. It has a very low inherent noise level, a wide dynamic range and a frequency response from below 2 Hz to above 200 kHz.

Design

All G.R.A.S. microphone preamplifiers are based on a small ceramic thick-film substrate with a very high input impedance. The ceramic substrate is shielded by a guard ring to minimise the influence of stray capacitance and microphonic interference. The casing is made of stainless steel for maximum strength and durability. The small dimensions of this preamplifier ensure reliable operation under humid conditions owing to the heat generated by internal power dissipation.

Dynamic Range

Type 26AC can handle both single and dual-sided power supplies. The supply can vary between 28 V_{DC} and 120 V_{DC} single-sided or ±14V_{DC} and ±60 V_{DC} dual-sided. When using the high supply voltage (120V_{DC} or ±60V_{DC}), the dynamic range exceeds 140 dB.

Noise

The electrical circuit in Type 26AC is built on a ceramic substrate using selected low-noise components to gain very low self-noise. The electrical self-noise is so low that system noise is mainly determined by the microphone capsule's thermal noise.

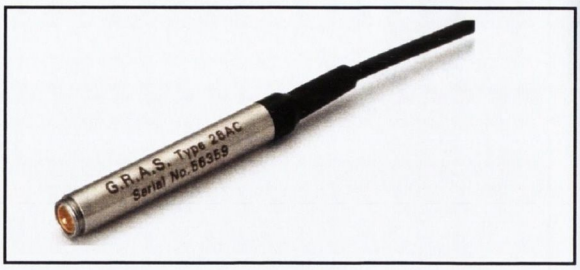

Fig. 1 ¼" Preamplifier Type 26AC

Frequency response

The low-frequency cut-off of the Type 26AC preamplifier is mainly determined by the input impedance of the preamplifier and the capacitance of the microphone capsule (see Fig. 3). The capacities 20 pF, 6.5 pF and 3 pF equal the typical capacitances of ½", ¼" and ⅛" microphone capsules respectively.

The high-frequency cut-off is determined by the preamplifier's ability to drive capacitive loads (slew rate), caused by the cable. For large-signals, the effects of these parameters must be accounted for when measurements are performed. Fig. 4 shows the large-signal response for Type 26AC for various capacitive loads corresponding to different cable lengths. The output level is in decibels relative to 1 Volt. Typical capacitance for the cable is 100pF/m (30pF/foot).

Connector

Preamplifier Type 26AC (Fig. 1) is provided with a 3-m lightweight cable terminating in a 7-pin LEMO series 1B plug (Fig. 2). The cable is only 2.5 mm in diameter and will withstand temperatures from -40 °C to +150 °C. An adaptor (GR0010) for G.R.A.S. ½" microphones is included.

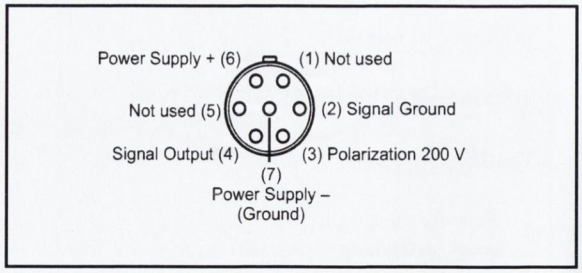

Fig. 2 7-pin LEMO plug 1B male (ext. view)

G.R.A.S.
SOUND & VIBRATION

Skovlytoften 33,
2840 Holte, Denmark
www.gras.dk gras@gras.dk

Specifications

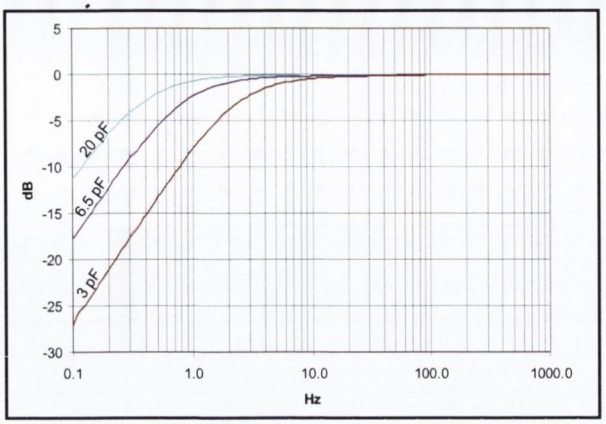

Fig. 3 Typical low-frequency response of Type 26AC for ½" (20 pF), ¼" (6.5 pF) and ⅛" (3 pF) microphones

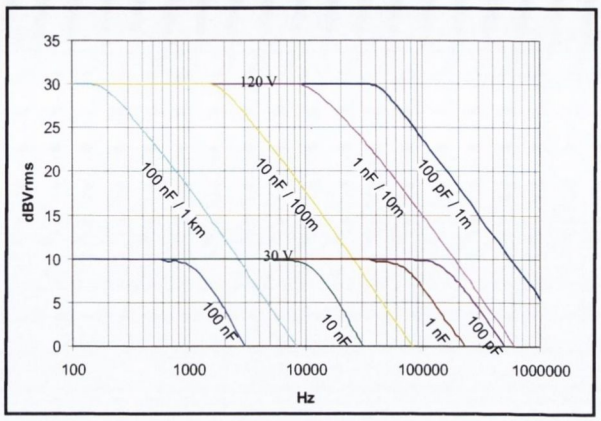

Fig. 4 Typical max. rms output signal with 120 V and 30 V supply

Technical Data

Frequency response (18pF/small signal):
2 Hz - 200 kHz . . . . . ±0.2 dB

Slew rate:
20 V/µs

Input impedance:
20 GΩ, 0.4 pF

Output impedance (Cs = 20 pF, f = 1000Hz):
Typical . . . . . 55 Ω

Noise (measured with 20 pF ½" dummy mic.):
A-weighted: . . . . . ≤2.5 µV rms
(typically 1.8 µV rms)
Linear (20 Hz - 20 kHz): . . . . . ≤6 µV rms
(typically 3.5 µV rms)

Gain:
Typical: . . . . . -0.25 dB

Power supply:
Single: . . . . . 28 V (0.7 mA) to 120 V (2.5 mA)
Dual: . . . . . ±14 V (0.7 mA) to ±60 V (2.5 mA)

Maximum signal-output voltage (peak):
from ±10 V to ±50 V

Temperature:
Operation: . . . . . -30 °C to +70 °C
Storage: . . . . . -40 °C to +85 °C

Relative humidity:
Operation: . . . . . 0 to 95 %
Storage: . . . . . 0 to 95 %

Dimensions and Weight:
Diameter: . . . . . 6.35 mm (¼")
Length: . . . . . 43 mm (1.7")
Weight (without cable): . . . . . 6 g (0.2 oz)
Weight (with cable + LEMO conn.): 50 g (1.8 oz)

Accessories

Included

GR0010:	¼" to ½" adapter for use with G.R.A.S. ½" microphones

Optional

RA0001:	Right-angled (90°) Adapter for ½" microphone and ¼" preamplifier
RA0003:	Adapter for ½" microphone and ¼" preamplifier
RA0006:	Angled (90°) Adapter ¼" to ¼".
AA0008:	Extension cable, 3 metres
AA0009:	Extension cable, 10 metres
AA0012:	Extension cable, 30 metres
AA0014:	Extension cable, 100 metres
AA0020_XX:	Extension cable, XX metres (customer-specified length)
AA0013:	Tripod adapter for ¼" preamplifier
RA0096:	Tripod adapter for ¼" preamplifier with angular adjustment

G.R.A.S. Sound & Vibration reserves the right to change specifications and accessories without notice.

G.R.A.S.
SOUND & VIBRATION

Skovlytoften 33,
2840 Holte, Denmark
www.gras.dk gras@gras.dk

Power Module Type 12AN

Product Data and Specifications

Typical applications and features

- ***General-purpose measurements***
- ***Precision measurements***
- ***Acoustic monitoring***
- ***Microphone calibration***
- ***Four channels***
- ***0 V or 200 V polarization***

Fig. 1 Power Module Type 12AN

The G.R.A.S. Power Module Type 12AN (Fig. 1) is a four-channel power supply for preamplifiers used with condenser microphones. It is for general use in acoustic measurements; both in the laboratory and in the field.

The Type 12AN can be powered either by internal standard batteries or an external DC supply (6 V - 20 V), e.g. the supplied mains/line adapter. It is built into a sturdy anodized aluminium cabinet.

The polarization voltage for the microphones fitted to the preamplifiers can be set to:

- 0 V — for prepolarized microphones, or
- 200 V — for externally polarized microphones

The Type 12AN also supplies ±15 V to power the preamplifiers. With four G.R.A.S. preamplifiers, it will run for approximately 25 hours on fresh standard alkaline batteries. A **Low Batt** LED indicates the condition of the batteries.

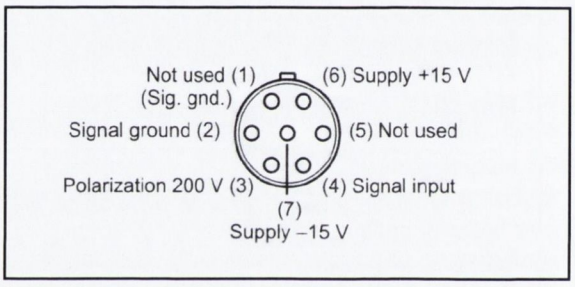

Fig. 2 7-pin LEMO female socket 1B (external view)

The inputs are 7-pin LEMO sockets on the front panel, which are wired up (see Fig. 2) for G.R.A.S. microphone preamplifiers, e.g. Types 26AB, 26AC, 26AJ and 26AK, but are also compatible with other available makes of similar microphone preamplifiers.

The signals from the preamplifiers are AC coupled to their respective outputs which are standard BNC sockets also on the front panel.

Vers.07-01-03

G.R.A.S.
Sound & Vibration

Skovlytoften 33
2840 Holte, Denmark
Tel +45 45 66 40 46 Fax +45 45 66 40 47
e-mail: gras@gras.dk www.gras.dk

Specifications

Input/Output sockets:
4 x Inputs: ..... 7-pin LEMO 1B female
4 x Outputs: ..... BNC coaxial

Output voltages:
Preamplifier supply: ..... ±15 V
Polarization voltage: ..... 0 V or 200 V

Frequency response:
0.05 Hz - 200 kHz: ..... ±0.2 dB

Output impedance:
30 Ω

Power supply:
4 x LR6 (AA) standard alkaline cells, or
Mains/line adapter: ..... 6 V - 20 V DC

Power consumption using an ext. power supply:
With 4 G.R.A.S. preamps.: ..... 135 mA

Fuse:
200 mA (Slow), 250V

Battery life (valid for 23 °C and alkaline cells):
With 4 G.R.A.S. preamps.: .....≈25 hours

Operating temperature range:
–10 °C to +50 °C

Dimensions:
Height: .....44 mm (1.73 in)
Width: ..... 210 mm (8.27 in)
Depth: ..... 194 mm (7.64 in)

Weight:
Without batteries ..... 1.2 kg (2.65 lbs)

Accessories included:
EL0001: ..... 4 x LR6 (AA) batteries
Mains/line adapter supply regulated to 15 V DC
AB0002: ..... for 230 V AC
or
AB0003: ..... for 120 V AC

G.R.A.S. Sound & Vibration reserves the right to change specifications and accessories without notice

G.R.A.S.
Sound & Vibration

Skovlytoften 33
2840 Holte, Denmark
Tel +45 45 66 40 46 Fax +45 45 66 40 47
e-mail: gras@gras.dk www.gras.dk

mks
Technology for Productivity

MKS Instruments UK Limited - Telvac Engineering

Certificate of Calibration

Certificate Number:	090265827		
Date:	12-Jan-2009		
Calibration Data:	Final		
Mfg:	MKS		
Instrument Model:	1179A24CS1BVAB		
Serial number:	090265827		
Identifier:			
Test Gas:	N2	**GCF**	1.00
Nameplate Gas:	Air	**GCF**	1.00
Range (sccm):	20000		
Accuracy (%fsd):	1.00%		

Setpoint %	STD sccm	DUT sccm	Error sccm	Error mV	Error %
0%	0.00	0.00	0.00	0.00	0.00%
25%	5000.00	4964.00	-36.00	-9.00	-0.18%
50%	10000.00	10020.00	20.00	5.00	0.10%
75%	15000.00	15004.00	4.00	1.00	0.02%
100%	20000.00	19980.00	-20.00	-5.00	-0.10%
110%	22000.00	21844.00	-156.00	-39.00	-0.78%

The above calibration data was measured on the MKS Mass Flow Standard identified below:

UK Ref.:	FS111
Range (sccm):	20000
Nameplate Gas:	N2
Serial Number:	477879
Part number:	1179A24CS1BV
Commissioned:	03-Apr-2001
Last cal date :	16-Jun-2008
Cal by:	MKS-UK
Technique:	ROR
Cal Gas:	N2

Leak Check: **Valve** <0.5% FS **Ext:** <1.0E-9 mb/L/s

Data By: GD **Comment:** MANUFACTURE

Checked By: **Next Cal. due date:** 12-Jan-2010

MKS Instruments UK Limited - Telvac Engineering., Pegasus Court, Stafford Park 7, Telford TF3 3BQ
Tel: +44 (0) 1952 200664 Fax: +44 (0) 1952 200341 www.mksinst.com

Registered in England No: 6391618

CERTIFICATE No: 0964508

Task 05|03

RdF Corporation
23 Elm Avenue
Hudson, New Hampshire 03051-0490
Tele: (603) 882-5195 1-800-445-8367
Fax: (603) 882-6925
E-mail: sensor@rdfcorp.com

ISO 9001 CERTIFIED

Q-116-01 REV A
Q-116-03 REV A
Q-116-13 REV A

MICRO-FOIL™ HEAT FLUX SENSOR

CALIBRATION

RdF PART NO. 27036-1

SERIAL NO. 02106802

HEAT FLUX SENSOR:

Output at 70°F: .161 μVBTU/ ft² hr

Polarity: (For heat flow into the surface)
White - Positive (+)
Red - Negative (–)

Temperature Multiplication Factor: See Attached Graph

*Thermal Resistance: .003 °F/BTU/ft² hr (Typ)

*Heat Capacity: .01 BTU/ft² hr/°F (Typ)

Response Time: .070 sec (62% response to step function) (Typ)

THERMOCOUPLE:

ANSI TYPE	MATERIAL	POLARITY	COLOR
T	Copper Constantan	Pos. (+) Neg. (–)	Blue Red

Output per ANSI MC96.1-1975 and NBS Monograph 125

*Thermal resistance is the temperature difference between the front surface and rear mounting surface of the sensor per unit of heat flow through the sensor. Heat capacity is the amount of heat required to raise the mean temperature of the sensor 1°F. Typical values of these two properties are given primarily to indicate sensor capabilities and are required for heat flow calculations only in very rare instances.

BY: Elaine Tardif DATE: 10-29-02

RdF Corporation
Specialists in Temperature Measurement

RdF

ISO 9001 CERTIFIED

MICRO-FOIL HEAT FLUX SENSOR

OUTPUT MULTIPLICATION FACTOR VS RECEIVING SURFACE TEMPERATURE (70^{0}F)

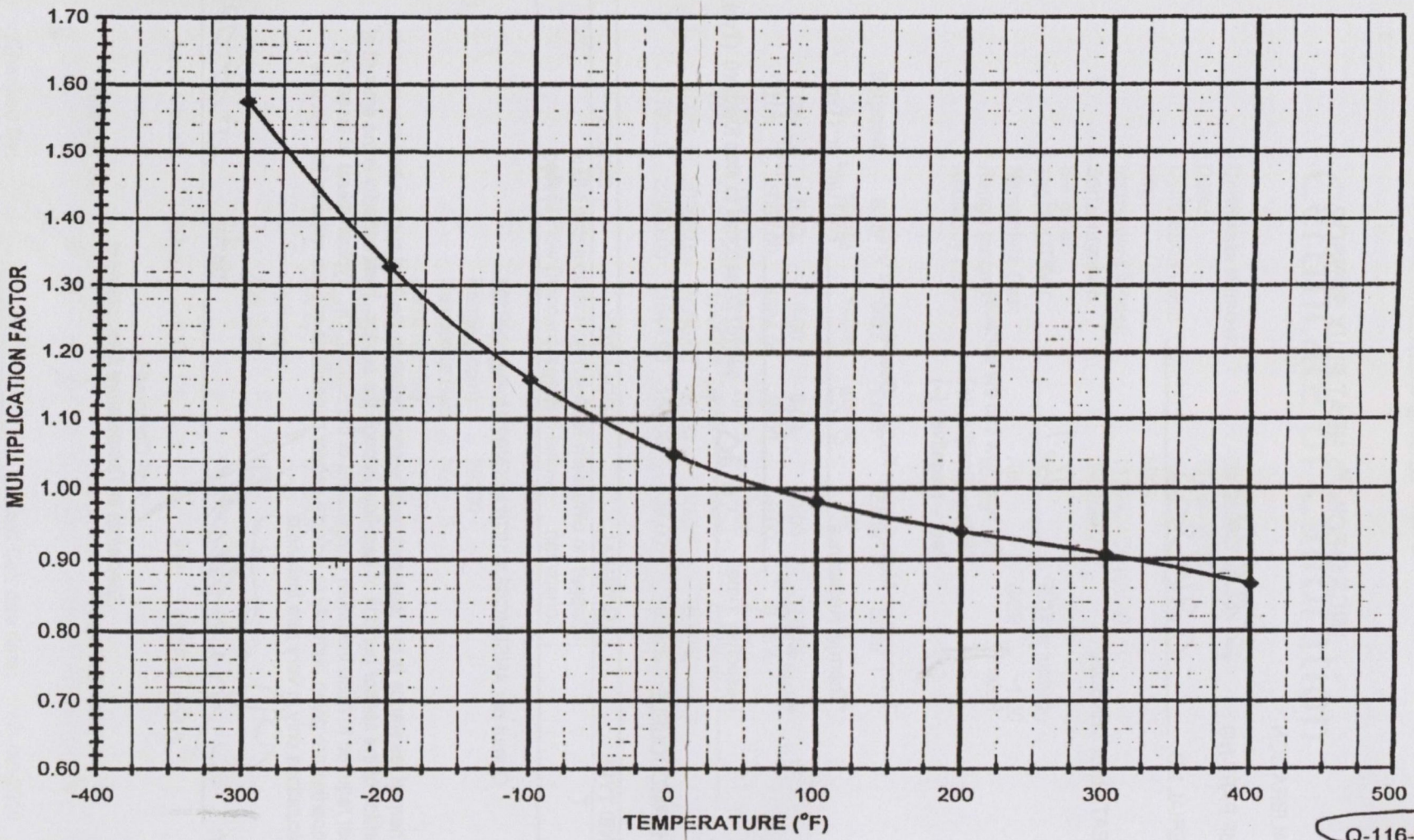

RdF Corporation
23 Elm Avenue
Hudson, NH 03051-0490
1-800-445-8367
INTERNET: sensor@rdfcorp.com

Q-116-03 REV A
Q-116-04 REV A
Q-116-08 REV A
Q-116-11 REV A
Q-116-12 REV A

OMEGA ENGINEERING LIMITED
ONE OMEGA DRIVE
RIVER BEND TECHNOLOGY CENTRE
NORTHBANK
IRLAM
MANCHESTER
M44 5BD
UNITED KINGDOM

Tel: +44 (0)161 777 6611
Fax: +44 (0)161 777 6622

FREEPHONE SALES 0800 488 488 (UK ONLY)

Website:

ISO 9002 REGISTERED COMPANY

NEWPORT OMEGA® omega.co.uk

V.A.T. REG No. GB 620 0439 89

COMPANY REG No. 2564017

Certificate of Calibration

Certificate Number: M04481 **Issue Date:** 14-04-2003

Customer.: University of Dublin
Description.: RTD Probe **S. O. No.:** 09971
Type No.: PR-11-2-100-M30-200-1/10DIN **Serial No.:** 4

The above instrument has been calibrated. All measurements made were referenced to standards of the laboratory whose values are traceable to UK National Standards. Copies of tests performed are on file at Omega Engineering Limited, Irlam, Manchester and are available upon request.

STD Temperature °C	Recorded Probe Temperature °C	Uncertainty of Measurement °C
0.00	0.05	0.15
49.95	50.10	0.18
99.90	100.05	0.20
200.20	200.20	0.27
300.20	300.1	0.37

Test Conditions	Humidity	35 %
	Temperature	22 °C

Instruments Used:	OE01, OE204, OE52
Calibrated By:	S. C. Roach

Signed: _____

Quality Manager

Ref: RTD.doc

The expanded uncertainties are based on the standard combined uncertainty multiplied by a coverage factor of K=2 providing a confidence probability of 95%

OMEGA ENGINEERING LIMITED
ONE OMEGA DRIVE
RIVER BEND TECHNOLOGY CENTRE
NORTHBANK
IRLAM
MANCHESTER
M44 5BD
UNITED KINGDOM

Tel: +44 (0)161 777 6611
Fax: +44 (0)161 777 6622

FREEPHONE SALES 0800 488 488 (UK ONLY)

Website:

ISO 9002 REGISTERED COMPANY

NEWPORT® OMEGA® omega.co.uk

V.A.T. REG No. GB 620 0439 89 COMPANY REG No. 2564017

Certificate of Calibration

OMEGA ENGINEERING, INC.

One Omega Drive, Box 4047, Stamford, CT 06907
(203) 359-1660 – http://www.omega.com – e-mail: info@omega.com

CERTIFICATE OF CALIBRATION

Model CL26 **Serial Number** T-218386

Omega Engineering, Inc., certifies that the above listed instrument has been calibrated using standards whose accuracy is traceable to the U.S. National Institute of Standards and Technology, and meets or exceeds its published specifications. Calibration traceability of the above listed instrument is in full compliance with ANSI/Z540-1-1994 standards and requirements.

6-22-00
DATE

RE
TESTED BY

mck
AUTHORIZED SIGNATURE

MD-4 ©Copyright 1998 Omega Engineering, Inc.